The Statistics and Evolution of Cosmological Density Fluctuations

Stuart Leonard Lumsden

Presented for the Degree of Doctor of Philosophy

at the University of Edinburgh

1989

This thesis is my own composition, except where otherwise indicated in the text.

October, 1989

Contents

List of Tables

List of Figures

Abstract

The theory of linear fluctuations in an expanding universe is now a well established subject. This thesis will concentrate on two aspects of this theory: the evolution of small perturbations in a cosmological framework and the statistics of the peaks in such a density field. Following the evolution of small fluctuations exactly is not possible analytically and is also a difficult numerical task. It is desirable both to check the accuracy of the solutions obtained and to understand the physics behind these solutions. This has particular relevance for modelling anisotropies in the cosmic background radiation. The constraints provided by the observational non-detection (and the possible tentative detection) of any anisotropy at a significant level have consistently tightened in the past few years. For this reason, much attention has focussed on universes dominated by exotic dark matter particles, which generally have small anisotropies. It is not clear, however, that plain baryonic universes cannot satisfy the constraints. This thesis re-examines $\Omega = 1$ baryon dominated universes. The procedures followed in constructing these models are an advance on most of those previously published since new, approximate, post-recombination solutions are used, the normalisation applied is conservative and well established and the model includes all the *known* species of particle in its framework. The solutions also vary from those previously published. With the preferred normalisation scheme ($J_3(10h^{-1}\mathrm{M}pc)$), an isocurvature model with initial power spectrum, $|\delta_k| \propto k^{-1}$, agrees with the constraints, whilst if biasing is introduced a scale-invariant adiabatic model is also marginally acceptable.

The other major topic tackled is the statistics of the fluctuations. It is a common assumption that the initial fluctuations are a random Gaussian field. The properties of such a field can be compared with the observations. Two possible areas are examined. The first is the form of the correlation function for peaks in a Gaussian field, motivated by the assumption that peaks may be related to the observed structure. This is examined in both one and three dimensions and certain general trends are identified. In particular, the amplitude of the peak-peak correlation function is considerably amplified when compared to the autocorrelation function of the density field. A major new feature though is that the location of the zeroes of the peak-peak correlation function do not coincide in general with those of the autocorrelation function, in contrast to previ-

ous approximate calculations. A new approximate method of calculating the peak-peak correlation function in three dimensions is derived from the one dimensional case and this is found to agree well with accurate numerical simulations, and is much easier to calculate. The techniques developed are used to discuss the observed cluster-cluster correlation function, and, with the assumption that clusters can be suitably modelled by filtering the power spectrum on some scale, the peak-peak correlation function is compared with the observations. This test favours low density cold dark matter models, and appears to exclude the favoured scale-invariant, $\Omega = 1$, adiabatic cold dark matter model and also a scale invariant baryonic model.

The second area relates to the observations of large scale peculiar velocities in the universe. The assumption that we lie near a maximum in the density field leads to a different answer from that obtained if we were to lie at an arbitrary point. The velocity field near peaks is shown to differ by a small factor from points in the field. A statistic is derived that reflects the probability of obtaining two peculiar velocities when the velocity field is filtered on two separate scales. When combined with the constraint of lying at a peak, this statistic is used to test various models. Using the latest published all-sky surveys, this technique rules out mostly models with too much power. A low density, cold dark matter model fits the data well, as it did for the clustering test.

Acknowledgements

Firstly, I would like to thank my supervisors, Alan Heavens and John Peacock, for their help and perseverance over the last four years. Others guilty of helping at times include Chris Collins and Lance Miller, but no blame should be attached to them.

The people who've also managed to make the last four years at the ROE (barring the last few months) relative fun include Paul Mitchell (and Linda and the camel), who has managed to successfully not share an office, Phil and Tobes for being the lads in the porta, Neil for being a management consultant, and of the relative weenies, Schmeve, Keith, Claire and Bob (from Wolverhampton). Mention must, of course, also be made of the old lads – James Dunlop for being such a consistent bluenose, James More for many crushed lifts in the orangemobile, Mark Yates for playing the Englishman abroad and Andrew Mead for his athleticism and willingness to go to the pub – some of whom are long gone.

Special thanks go to Andrew and Lorna, for putting up with complete mayhem from me for the past year. I'm also grateful to my parents and family for their support in the last few years.

Lastly, I'd like to thank the SERC for the studentship.

Preface

Much of this thesis is based around the framework provided by general relativity. No attempt will be made to re-derive basic results since these are already well documented. In particular the reference used here for general relativity and basic cosmology is Weinberg's *Gravitation and Cosmology* (1972). Detailed derivation of fundamental results can be found there. However, since the conventions and notation involved here are sometimes different, the basic definitions are presented in Appendix A.2.1.

Chapter 1 gives an introduction to the observational results on which the theory rests, and an introduction to the actual themes of this thesis. Chapters 2 and 3 discuss the calculation of anisotropies in the microwave background and other general features of baryonic models. Chapter 4 discusses the possibility that large scale clustering can be explained within the framework of random Gaussian fields. Chapter 5 applies the same framework to constrain models of peculiar velocities on large scales.

Chapter 1

Introduction

1.1 Historical Perspective

1.1.1 The Expanding Universe

Modern theoretical cosmology dates largely from the introduction of the general theory of relativity. Initially, the attempts to find solutions to the field equations were hampered by the fact that there were very few cosmological observations. Although the structure of galaxies had been discovered last century, it was not until Hubble observed Cepheids in M31 in 1923, and later, in 1925, in the irregular galaxy NGC 6822, that it was finally proved that these 'nebulae' lay outside our own galaxy. Shapley had already estimated the distance to NGC 6822 in 1923 on purely morphological grounds by comparison with the Magellanic Clouds. Before that, no one had been able to adequately differentiate between the two most common models of the universe: the correct one, that the observed spiral 'nebulae' were extragalactic, and the other, that they were merely outlying parts of our own galaxy. In 1920 Shapley and Curtis had held a famous debate at the AAAS in which Shapley contended that there was no proof that any of the 'nebulae' were extragalactic. The fact that both sides were able to make reasonable cases emphasises the poor state of observational extragalactic astronomy at that time.

The original basis for most cosmological models was founded on Einstein's conviction that the large scale structure of the universe should be relatively simple. The other fundamental hypothesis was that our location in the universe was in no way special: this is known as the *cosmological principle.* In fact, Einstein initially believed that the universe was isotropic, homogeneous and composed solely of our galaxy. Although this was later shown to be false, his basic premise of homogeneity and isotropy still seemed accurate when the structure in the universe was averaged on large enough scales. Clearly such a universe must satisfy the cosmological principle. Indeed, if the cosmological principle is accepted, then a universe which is seen as being isotropic to a fundamental observer must also be homogeneous. This is true because the observer's position could be shifted arbitrarily in line with the cosmological principle and the

universe must still appear isotropic. Any universe that is isotropic about every point is manifestly homogeneous. The converse, however, is not true. A simple three dimensional analogue would be to consider an infinite sphere. Clearly if the interior of the sphere is homogeneous it would appear isotropic. However, an infinite cylinder which was also homogeneous would not.

Einstein had originally sought a static universe as a solution to the field equations but was forced to introduce the *cosmological constant*, Λ, to do so. This gave rise to field equations of the form:

$$R_{\alpha\beta} - \frac{1}{2}g_{\alpha\beta}R - \Lambda g_{\alpha\beta} = \frac{8\pi G}{c^4}T_{\alpha\beta}\,, \tag{1.1}$$

where $R_{\alpha\beta}$ is the Ricci tensor, R, is the curvature scalar and $T_{\alpha\beta}$ is the stress tensor for the material content of the universe (see appendix A). The cosmological constant effectively exerts negative pressure to stop the universe collapsing under its own gravity. Unfortunately a static universe is inherently unstable to any small perturbation. In 1922 Friedmann offered an alternative: the universe could be expanding and satisfy the basic field equations without recourse to the cosmological constant. Such a model has for its line element the Robertson-Walker metric:

$$ds^2 = c^2dt^2 - R^2(t)\left(\frac{dr^2}{1-kr^2} + r^2(d\theta^2 + sin^2\theta d\phi^2)\right)\,. \tag{1.2}$$

Clearly, the spatial element at a fixed time is manifestly that of a homogeneous, isotropic space. The *scale factor*, $R(t)$, represents the expansion of the universe. An alternative form is to use $a(t) = R(t)/R(t_0)$ (where the subscript, zero, refers to the current epoch), so that a is dimensionless. It is this form that will be used generally here. Some attention has recently been paid to the role of the cosmological constant in an expanding universe but this will not be considered here in great detail.

Friedmann's model gained extra credence in 1929 with Hubble's observation that distant galaxies were receding from us with velocities that appeared to be proportional to distance. Hubble used the techniques that had been developed for measuring distances to galaxies and compared these with their spectra to show that there was a consistent trend of increasing redshift of the spectral lines with distance. This result was probably the most fundamental observation in cosmology in the early part of this century. Lemaitre and Robertson had expanded on Friedmann's model and it was known that the redshift-distance relationship occurred naturally in this model when the distances being considered were small.

Further observations only confirmed the redshift-distance relationship and that the universe appeared to be homogeneous on large scales. Furthermore, in 1935 Robertson and Walker had independently shown that the metric (equation A.16) was the unique metric for a homogeneous, isotropic and expanding universe. Although other solutions to the field equations have been found (see *e.g.* Weinberg 1972), the basis for most of modern theoretical cosmology remains the Robertson-Walker metric.

1.1.2 The Microwave Background

Within the framework provided by the Robertson-Walker metric however two contending theories were advanced. The simpler of these involves extrapolating the basic Friedmann universe back to its initial state, $a = 0$. Although general relativity is no longer valid at this epoch since the solutions arrived at are singular, the basic picture of a very hot and dense initial state gave its name to this model which became known as the *hot big bang* model. In particular, Gamow and others in the 1940's showed how this model could account for the observed helium fraction in the universe by nucleosynthesis during the hot dense phase. The hot big bang model also gave another prediction that could be tested. Since the early universe was hot and radiation dominated, there should be a relic of that radiation now: this would take the form of a low temperature background radiation. The other model returned to Einstein's appeal to aesthetics. Bondi & Gold and Hoyle separately proposed in 1948 that the universe should exist in a *steady state* so that it would appear the same at all times as well as being homogeneous in space. This implies that the expansion rate of the universe must also be the same at all times leading to a scale factor that has an exponential form similar to that for a DeSitter universe.

Although the specific predictions of the steady state model appeared to be in conflict with the observations of the time, it was not until Penzias and Wilson discovered the microwave background in 1965 (though they had not actually been looking for it: another group (Dicke, Peebles, Roll and Wilkinson) who had planned to conduct such an observation realised the significance of this result) that the steady state model could be finally excluded. Further observations of the background radiation (hereafter, the CBR) at different wavelengths seemed to confirm that the background was a black-body radiation at a temperature of about 3K.

The standard model in theoretical cosmology therefore became the hot big bang

model in a homogeneous, isotropic and expanding universe. Within this framework, work had already been carried out to see how the structure that is seen today in the universe could have arisen. Lifshitz pioneered this work in 1946 by investigating how small fluctuations would grow in a Friedmannian universe. A summary of basic linear perturbation theory in general relativity is given in Appendix A.2.3. Further references for both the history of this period in cosmology, and the work referred to in sections 1.1.1 and 1.1.2 can be found in either Peebles (1971) or Weinberg (1972).

1.2 Observational Data

1.2.1 Observing the Microwave Background

1.2.1.1 Spectral Distortions in the CBR

Extensive observations have been carried out since the original Penzias and Wilson experiment to test the spectral shape of the CBR. The observations can be split into two classes: long wavelength studies ($\lambda \gtrsim 1$cm) which can be carried out from the ground and short wavelength studies ($\lambda \lesssim 3$mm) which because of the poor atmospheric transparency at these wavelengths must be carried out at altitude or by using indirect methods.

The short wavelength part of the spectrum lies in the mm and sub-mm regions. At these wavelengths, there are two distinct methods of measuring the CBR. The first involves direct observation of the CBR from high altitude balloons or rockets. Observations between about 1mm and 3.5mm have been carried out by Peterson, Richards & Timusk (1985), using a balloon borne bolometer, which confirm the black-body form of the CBR spectrum at a temperature of about 2.7K. Matsumoto *et al.* (1988) used a rocket borne bolometer to measure the flux at six wavelengths (1.16mm, 0.71mm, 0.48mm, 0.26mm, 0.14mm and 0.1mm) and showed a significant distortion at wavelengths shorter than about 0.3mm. If confirmed this would represent the first significant spectral distortion seen in the CBR. However, another recent measure of the CBR using a balloon borne bolometer (Halpern *et al.* 1988) failed to detect this feature, though the technique used (in fact the group were measuring the dipole moment in the CBR) was not specifically designed for measuring the spectral shape of the CBR. All the measurements for balloon or rocket borne bolometers are calibrated on the ground using a uniform black-body source.

The other possibility at this wavelength is the observation of interstellar CN. The CBR is the major source of photons at the wavelength of 2.64mm and 1.32mm in the CN clouds. These wavelengths correspond to transitions between the rotational angular momentum levels $J = 0 \rightarrow J = 1$ and $J = 1 \rightarrow J = 2$ in the ground state of CN. Observations of interstellar CN in clouds which are on the line of sight of stars give a measure of the CBR temperature as follows. The cloud causes absorption in the optical (all the transitions are about 387nm) part of the stellar spectrum corresponding to transitions from the ground state to an excited state. Comparison of the strengths of the absorption lines for the same electronic transition but corresponding to different rotational transitions (all these transitions are dipole, $\Delta J = \pm 1$) gives the relative populations of the different angular momentum levels in the ground state. Since the excitations between these ground states is primarily caused by the CBR, with which the cloud is assumed to be in equilibrium, the relative populations of the $J = 0$ and $J = 1$ states and the $J = 1$ and $J = 2$ states gives a measure of the temperature of the CBR. Of the two, the former is the easier to measure since the $J = 0$ to $J = 1$ electronic transition is weak and the result it gives is consequently much less significant. Meyer & Jura (1985) and Crane *et al.* (1986) report recent measurements of the CBR using these techniques. Both find that this technique gives results consistent with the CBR being a black-body at about 2.7K. Further improvements in observing the transition corresponding to excitation at 1.32mm or by using other molecular transitions (see Crane (1988) for a discussion of the advantages and problems with this method, including the possibility that other sources such as collisional excitation could cause the rotational transitions) would help constrain the CBR spectrum especially since it is at about this wavelength that the observations of Matsumoto *et al.* (1988) start to find a significant distortion in the black-body form of the CBR. The most recent measurement at this wavelength by Meyer, Roth & Hawkins (1989) find a temperature of 2.83 ± 0.09K, which is consistent with the Matsumoto *et al.* data at this wavelength (2.799 ± 0.018K). This seems to indicate that the Matsumoto *et al.* result may in fact be correct. Although the discrepancy from the black-body fit derived from longer wavelengths is not large (< 0.1K), since 1mm is near the peak of the black-body it does represent a significant difference in the flux. Further measurements at this wavelength are still desirable.

At longer wavelengths, the CBR can be observed from the ground. However, galac-

tic background can be a problem. Synchrotron emission dominates the background beyond a few cm and galactic dust dominates shortwards of a few mm. The minimum in this galactic emission occurs at about 3mm (see figure 3 in Lubin & Villela 1986). Most of the observations described previously were taken near this minimum. Some of the longer wavelength observations were taken well away from this dip however and must consequently be treated with some caution. Unfortunately, the spectrum of the galactic synchrotron emission is only well known at wavelengths outside the range of interest: it is necessary to extrapolate the known spectrum to create a model of the galactic emission at CBR wavelengths. This factor is more of a problem for anisotropy experiments and will be discussed more fully in section 1.2.1.2. Recent observations in this regime have been made by De Amici *et al.* (1985), Mandolesi *et al.* (1986), Sironi & Bonelli (1986), Smoot *et al.* (1987) and De Amici *et al.* (1988). All these observations were carried out in fundamentally the same way using ground based radiometers. Johnson & Wilkinson (1987) used a balloon borne radiometer but otherwise used a similar technique. This involves comparing the observed background temperature with a calibrating source (usually kept at the temperature of liquid helium). All the groups found temperatures in the range 2.7K to 2.8K for wavelengths between about 1cm and 21cm.

Smoot *et al.* (1987) summarise all the recent observations. The CBR in the Rayleigh-Jeans portion of the spectrum is well fitted by a black-body with a temperature of 2.74 ± 0.017K. A discussion of the Wien part of the spectrum will be left to section 1.3.3.4. Figure 1.1 shows the spectral form of the CBR for all the measurements discussed in this section.

1.2.1.2 Anisotropies in the CBR

Observational searches for anisotropies in the CBR can be classed in four groups: anisotropies on the scales of a few arcseconds, on the scale of a few arcminutes, on the scale of a few degrees and finally on large scales (the dipole and quadrupole moments). On the scale of a few arcseconds the sources of the anisotropy are probably discrete. Knoke *et al.* (1984) and Fomalont, Kellerman & Wall (1984) both used the VLA to observe on these scales. Wilkinson (1988) reports that there is a possibility that partially resolved sources in the observations are correlated with faint CCD images of clusters of galaxies. In any case, the limits set ($\Delta T/T \lesssim 10^{-4}$ for scales of 10 - 30

arcseconds) do not constrain the models in a useful way.

Many observations have been made since the CBR was discovered on the scale of a few arcminutes. No confirmed detection has ever been made but stringent upper limits on possible anisotropies have been set. In particular, the work of Uson & Wilkinson (1984a,1984b,1985) and Readhead *et al.* (1988a,1988b) has set the 95% confidence upper limits of $\Delta T/T < 5 \times 10^{-5}$ at $4.5'$ and $\Delta T/T < 1.5 \times 10^{-5}$ at $7.15'$ (though the latter project is not yet complete). Uson & Wilkinson used the 43m telescope at the National Radio Astronomy Observatory (at a wavelength centred on 1.5cm) in a three-beam experiment (where the secondary beams were $4.5'$ on either side of the field point and the half-power beamwidth (FWHM) was $1.5'$). Readhead *et al.* used the 40m at the Owens Valley Radio Observatory in a similar experiment (FWHM $1.8'$, beam separation $7.15'$ and wavelength 1.5cm). Uson & Wilkinson (1984b,1985) and Readhead *et al.* (1988a,b) both give fuller details of the observing procedure involved.

The method of estimating a limit on the level of true sky fluctuations relies on some form of statistical test. There are also two fundamental assumptions involved in deriving the limits. These are that the beam pattern of the telescope is Gaussian (not entirely true but a reasonable approximation) and that the distribution of the fluctuations on the sky is also Gaussian. The currently most favoured method is a likelihood analysis. This requires constructing the probability of obtaining the observed temperatures given that there are intrinsic fluctuations on the sky of some given value.

With the assumptions given, the probability of obtaining any one measurement, $T \pm \sigma$, is:

$$p(T,\sigma) = \left(2\pi\left(\sigma^2 + \theta_{\rm sky}^2\right)\right)^{-1/2} \exp\left(\frac{-T^2}{2\left(\sigma^2 + \theta_{\rm sky}^2\right)}\right) ,$$

where $\theta_{\rm sky}^2$ is the variance of the observed values T. The likelihood function, $L(\{T_i\}|\theta_{\rm sky})$, is the product of such individual probability densities for the set of observations, $\{T_i\}$. It represents the relative probability of obtaining the observed measurements given the assumed value of $\theta_{\rm sky}$. Maximising this function would give the 'most likely' value for $\theta_{\rm sky}$. Deriving an upper limit if there is no significant detection is fairly straightforward though the variety of possible methods do not always give consistent answers. The original method used (see *e.g.* Uson & Wilkinson 1984b) was effectively a weighted χ^2 test. Basically, the procedure was designed to test the hypothesis that the intrinsic fluctuations were non-zero. Lawrence, Readhead & Myers (1988) give a useful introduction

to this subject, as well as indicating why the likelihood test is the more fundamentally stable technique (see also the discussion in Kaiser & Silk 1986).

On the scale of a few degrees there are again two basic observations: Melchiorri *et al.* (1981) and Davies *et al.* (1987). The Melchiorri *et al.* observation is a fairly straightforward two-beam experiment (with FWHM being 5° and the switching angle 6°) and gives an upper limit of $\Delta T/T < 4.8 \times 10^{-5}$. The Davies *et al.* observation gives a possible detection of fluctuations on the scale of 8° (FWHM 8°) of $\Delta T/T \sim 4 \times 10^{-5}$. Confirmation of this result (again see the discussion in Wilkinson 1988) would give the first detection of CBR anisotropies on such scales. However, the Davies *et al.* result was obtained at a wavelength of 3cm where galactic emission is problematical. Wilkinson (1988) gives other possible sources of confusion in this experiment.

The observed radiation pattern can be decomposed into multipole moments (effectively spherical harmonics on the sky). The monopole moment of the anisotropy is, by definition, unobservable. The next two higher orders are often considered separately however. The quadrupole moment reflects anisotropies separated by 90°. The dipole reflects anisotropies separated by 180°.

Observations of the quadrupole moment have been carried out by Fixsen, Cheng & Wilkinson (1983) (λ = 12mm), Lubin, Epstein & Smoot (1983) (λ = 3cm) and, more recently, Strukov *et al.* (1988) (λ = 8mm). Because the problem of galactic emission is greater at longer wavelengths, careful modelling has to be carried out to produce an upper limit on intrinsic fluctuations. The results of Lubin & Villela (1986) are a combination of the 1.2cm and the 3mm data. The experiment described in Strukov *et al.* was carried on a satellite and should have the greatest sensitivity, since integration times are not a problem. However, the quoted upper limit has been revised upwards already and the currently stated value may also be somewhat low: $\Delta T/T < 3 \times 10^{-5}$. The most stringent limit from the other work is that of Lubin & Villela: $\Delta T/T < 7 \times 10^{-5}$.

The only definite observation of an anisotropy in the CBR is that of the dipole moment. The three groups given above as references for the quadrupole anisotropy also give measures of the dipole moment which are in substantial agreement (note that it is easier to be confident in the values obtained for the dipole as opposed to the possible doubt in setting upper limits). Halpern *et al.* (1988) also give a value for the dipole and, under the assumption that the dipole is caused by our motion relative to the frame of the CBR, give spectral measurements of the CBR also as has already been

noted. This assumption seems justified, since the quadrupole limit is much lower than the dipole, whereas for intrinsic fluctuations these would be much closer in magnitude: the major anisotropy seems to be almost purely dipolar and hence probably a result of our motion relative to the CBR. As a result, the dipole does not constrain the initial fluctuation spectrum as far as the CBR is concerned, but it is of importance for the streaming velocities described in section 1.2.3.

As was stated in the previous section, the role of galactic emission is important in setting these upper limits, especially in large angle experiments. Possible anisotropies due to galactic emission must be removed before the signal can be tested for any cosmological fluctuations. This process requires some model for the galactic emission: any errors in this model could result in true signal being removed along with the galactic sources. For this reason, observations which are made at short wavelengths are preferable (since emission from the galaxy has a radiation temperature that goes roughly as λ^2 (Wilkinson 1988)). However, at very short ($\sim$ 1mm) wavelengths the contribution to any signal by dust remains problematical. Therefore, most observations for anisotropies are made at about 1cm. The extreme possibility does exist though that real cosmological anisotropies in the CBR are rejected as contamination. Table 1.1 shows the limits on the anisotropy of the CBR from the references given above.

1.2.2 Large Scale Clustering

1.2.2.1 The Abell Catalogue

The existence of clusters of galaxies was recognised in the mid 1930's: the Shapley-Ames catalogue of bright galaxies was published in 1932 and clustering was clearly evident even in this early survey. The first quantitative attempt to catalogue clusters was made by Abell (1958) (hereafter the Abell catalogue). This catalogue contained some 2700 clusters, largely in the northern hemisphere, all of which were identified by manually scanning optical plates taken for the Palomar Sky Survey. Abell also attempted to classify clusters by their *richness* and *distance*. These parameters are defined in table 1.2. A similar survey of the southern sky using plates taken by the UK Schmidt in Australia has also been completed (Abell, Corwin & Olowin 1989), and this includes corrections to the original catalogue. In particular, the distance classification system breaks down for the last two classes in the original survey. For those clusters with

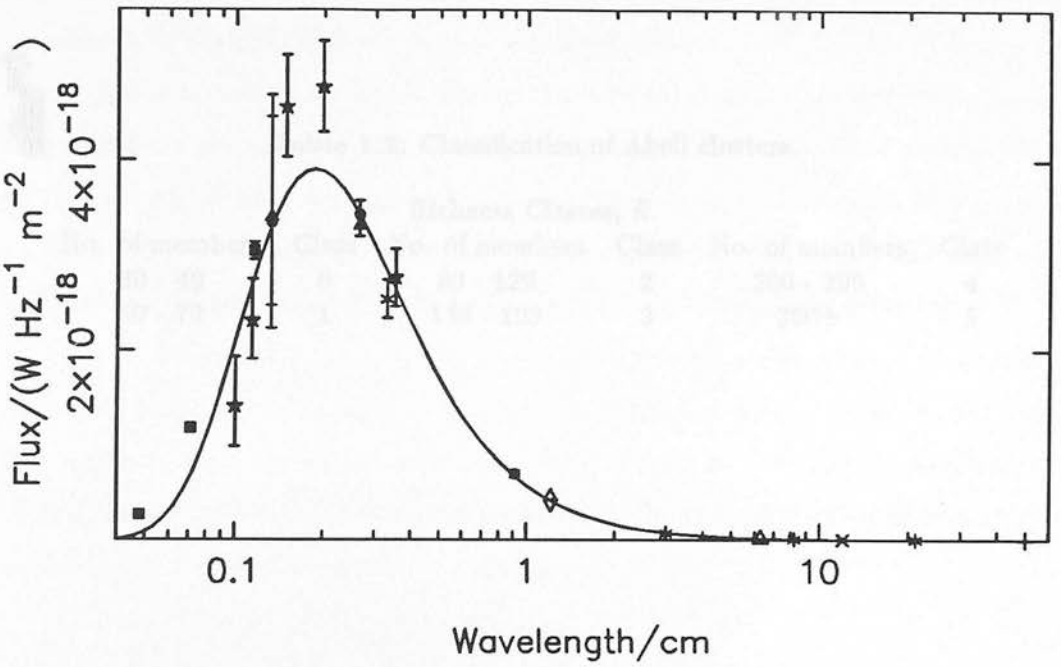

Figure 1.1: The spectrum of the CBR. The data is taken from: ■ - Matsumoto *et al* (1988), ⋆ - Peterson *et al.* (1985), ▲ - Meyer & Jura (1985), • - Crane *et al.* (1986), + - Sironi *et al.* (1987), △ - Mandolesi *et al.* (1986), ∗ - Smoot *et al.* (1987), ◇ - Johnson & Wilkinson (1987), × - Sironi & Bonelli (1986), o - De Amici *et al.* (1988).

Table 1.1: Limits on the anisotropies in the CBR

Reference	Angular Scale	Beamwidth	Anisotropy
UW (1985)	$4.5'$	$1.5'$	$< 5 \times 10^{-5}$
OVRO (1988)	$7.15'$	$1.8'$	$< 1.5 \times 10^{-5}$
Mea (1981)	6°	5°	$< 4.8 \times 10^{-5}$
Dea (1987)	8°	8°	$\sim 4 \times 10^{-5}$
LV (1986)	quadrupole		$< 7 \times 10^{-5}$
Sea (1988)	quadrupole		$< 3 \times 10^{-5}$

The references are as follows: UW - Uson & Wilkinson, OVRO - Readhead *et al.* , Mea - Melchiorri *at al.* , Dea - Davies *et al.* , LV - Lubin & Villela, Sea - Strukov *et al.* The dipole measurement of 3mK (see Lubin & Villela) is excluded since it is not believed to be intrinsic. The Dea detection is tentative.

Table 1.2: Classification of Abell clusters.

Richness Classes, R.

No. of members	Class	No. of members	Class	No. of members	Class
30 - 49	0	80 - 129	2	200 - 299	4
50 - 79	1	130 - 199	3	300+	5

Distance Classes, D.

m_{10}	Class	m_{10}	Class
<13.3	0	15.7 - 16.4	4
13.3 - 14.0	1	16.5 - 17.2	5
14.1 - 14.8	2	17.3 - 18.0	6
14.9 - 15.6	3	>18.0	7

The number of members in a cluster is defined as the number which are brighter than $m_3 + 2$, where m_3 is the blue magnitude of the third brightest cluster member, and which are within $1.5h^{-1}$ Mpc of the cluster centre. This distance translates to an apparent distance on the plate material using m_{10} as a distance indicator, where m_{10} is the magnitude of the tenth brightest galaxy. This was thought to be a stable indicator of distance.

measured redshifts, the distance classification scheme is a reasonable fit to the actual redshift distances for classes 1-4. For 5 and 6 however, the m_{10} distances were not in agreement, in general, with the actual measured redshifts. Abell, Corwin & Olowin discuss this matter in more detail. The southern survey contains another 1400 clusters. It should be noted that some of the cluster members identified in these surveys could be either foreground or background objects. Future large scale surveys will not rely on such techniques. There are already projects underway to identify and catalogue galaxies using machine based methods (see *e.g.* Heydon-Dumbleton 1989).

In order to quantify the strength of clustering on any scales some statistical test is needed. The standard method involves using the two-point correlation function. This basically measures an excess in the number of pairs in a catalogue over a uniform random catalogue. It is defined by the probability, dP, of finding two objects in sample volumes, dV_1 and dV_2, separated by a distance, r:

$$dP = n_1\, n_2\, dV_1\, dV_2\, (1 + \xi(r))\,, \tag{1.3}$$

where n is the number density of objects in the sample.

Another variation on this is the two-point angular correlation function: this requires only angular positions and is easily calculated from surveys of the kind already mentioned. The angular correlation function does contain information on structure in the universe: however, the theoretical work to be described later is best compared to three dimensional surveys. In order to produce such surveys, redshifts for the candidate objects are needed. This is as true for clusters as it is for galaxies. Although the distance to clusters can be estimated from the magnitudes of the brightest members (see section 1.2.3 and Abell 1958), this technique is not of much use for the correlation function since an *accurately* known distance is required.

1.2.2.2 The Cluster-Cluster Correlation Function

Hoessel, Gunn & Thuan (1980) measured redshifts for all but one of the Abell clusters of richness class $R \geq 1$ and distance class $D \leq 4$ at high galactic latitude. This subsample of the Abell catalogue contains 104 clusters. Bahcall & Soneira (1983) used this sample to produce a three dimensional two-point cluster-cluster correlation function. They also show that the Abell's distance class system is in error by as much as 25% in giving the redshifts of the clusters. The resulting correlation function is well fitted by:

$$\xi_{cc}(r) = \left(\frac{r}{25h^{-1}\mathrm{Mpc}}\right)^{-1.8} . \tag{1.4}$$

The value of h is defined by: $H_0 = 100h$ km s^{-1} Mpc^{-1}, where H_0 is the Hubble constant.

Ling, Frenk & Barrow (1986) reanalysed the Bahcall & Soneira result using a bootstrap analysis. This technique gives a measure of the errors on the correlation function but not the function itself. The resulting errors were found to be larger than the Poissonian errors given by Bahcall & Soneira. As well as this, the mean correlation length (the separation at which $\xi = 1$) for the sample was found to be $21.9h^{-1}$ Mpc instead of $25h^{-1}$ Mpc.

Struble & Rood (1987) catalogue all the measured Abell cluster redshifts (including those with $R = 0$ and $D > 4$). This sample contains 588 clusters but there appear to be biases towards clusters in apparent 'superclusters' (*i.e.* structures that appear in the two dimensional surveys without necessarily being real, three dimensional structures). Sutherland (1988) attempts to correct for these biases by comparing the angular correlation function for the $R \geq 0$, $D \leq 4$ part of the Struble & Rood sample (231 clusters at redshifts less than 0.3) with the angular correlation function of a similarly defined subsample of the Abell catalogue. Sutherland also finds strong line-of-sight selection effects in the Abell catalogue and tries to correct for these also. Although the procedures he uses are not necessarily completely accurate (especially that for correcting for the bias towards 'superclusters'), the resulting correlation function is probably accurate for the sample considered. The correlation length given is $14h^{-1}$ Mpc and the correlation function has the same spectral index as for the Bahcall & Soneira result.

Although the angular correlation function as such will not be further considered it is interesting to note that the southern Abell catalogue (Abell, Corwin & Olowin 1989) has a similar angular correlation function to the original northern catalogue (Couchman, McGill & Olowin 1989). However, the selection effects in any manual survey must necessarily leave the results open to doubt. Only when the machine based surveys are completed, and complete redshift samples for these catalogues compiled, will it be possible to check the spatial correlation functions described here.

1.2.3 Large Scale Streaming Motions

1.2.3.1 Distance Measures

If the universe on large (*i.e.* greater than about $30h^{-1}$ Mpc) scales were to move with the Hubble flow, the only deviation from uniform expansion would be on small scales, such as the infall of the Local Group to Virgo. In order to test whether or not this is true, methods for determining distance independent of redshift were needed. For studies of perturbations in the Hubble flow it is not necessary to have a distance scale that is calibrated absolutely. Since all the methods of determining distances on scales greater than a few Mpc are secondary, this means that the problematical issue of calibrating the primary methods (such as Cepheids: Aaronson & Mould (1986) give a useful overview of this subject) can be ignored. All that is required is a constant calibration for whatever technique is used.

The Tully-Fisher relation: the infrared Tully-Fisher relation (or IRTF) is based on the correlation between the velocity width of the 21cm neutral hydrogen emission line in a spiral galaxy and its infrared (H-band or 1600nm) magnitude. The original basis for this technique was the apparent correlation between line width and diameter, and especially between line width and luminosity when observed in the optical (blue) regime (see Tully & Fisher 1977). The procedure is limited to spirals which are almost edge-on or else the velocity width must be corrected for the inclination (which is a problem if the spiral is more face-on than edge-on). However, for optical purposes an edge-on system suffers extinction and the luminosity must be corrected for this. With this in mind Aaronson, Huchra & Mould (1979) proposed that H-band magnitudes should be used instead of blue band magnitudes. This overcomes the problem of extinction and also has the advantage that the stellar component of the galaxy's light peaks in this waveband. Aaronson *et al.* (1986) summarise the accuracy of this technique. Ideally, the galaxies considered should be of similar Hubble type: Aaronson (1986) claims that the type will not have a significant effect on the results for IRTF if the type is limited to the range Sab-Sdm). The scatter in the relation is about 0.45 mag which corresponds to an error in the measured distance of about 25-40% for each individual galaxy. Bothun & Mould (1987) summarise the contributing factors to the scatter in the H-band technique. It is possible to reduce this error by combining the results for several galaxies in every cluster (which reduces the error by $1/\sqrt{N}$). However, it is desirable to reduce the

individual errors as much as possible also. Bothun & Mould (1987) show that by using I-band photometry and a slightly modified technique that the individual scatter can be reduced to 0.2 mag. Collins, Joseph & Robertson (1986) offer the alternative solution of using another free parameter (in their case an infrared-optical colour magnitude relation) to constrain the errors on the sample.

The Faber-Jackson relation: the Tully-Fisher relation allows distances to spirals to be measured. The Faber-Jackson relation does the same for ellipticals (see Faber & Jackson 1976). Basically, the luminosity of the galaxy, L, is related to the line-of-sight central velocity dispersion, σ according to $L \propto \sigma^4$. This relation suffers as IRTF does from a large intrinsic scatter. Dressler *et al.* (1987a) propose a new correlation based on the determination that ellipticals describe a plane in a three dimensional parameter space of L, σ and an effective surface brightness (see also Djorgovski & Davis 1987). The effect of considering a third parameter is to reduce the scatter in the distance measures. Dressler *et al.* combine the luminosity and effective surface brightness into a new parameter, D_n, defined such that D_n is the diameter in arcseconds of a circular aperture within which the integrated surface brightness is 20.75 blue mag s^{-2}. D_n effectively describes the variation in the plane of the parameter space described by the luminosity and effective surface brightness, and hence the scatter in the new relation is minimised. The effective scatter is from about 20% for individual galaxies and hence as little as 10% for groups. This new relation is therefore comparable to IRTF in its accuracy.

Other secondary methods have been proposed for estimating distances but most of these are somewhat doubtful (*i.e.* large scatter and little or no physical basis to them). Aaronson & Mould (1986) summarise some of these methods. One of the other most popular methods is to use colour-magnitude relations. Collins, Joseph & Robertson (1986), for example, use this method along with Tully-Fisher to try and minimise the distance errors. However, IRTF (or other Tully-Fisher methods) and Faber-Jackson (and their improved variants) have become the standard methods used by most groups.

1.2.3.2 Deviations from the Hubble Flow

Even with an accurate indicator of distance (recession velocity), some frame of reference is needed to calculate whether or not the distant galaxies show deviations from the

Hubble flow. A suitable reference frame is provided by the CBR. Not all of the actual observed streaming motion is of interest however: some of the dipole in the CBR is caused by the motion of the Local Group within the Virgo supercluster. The remaining component represents a genuine large scale deviation in the Hubble flow. The motion of our galaxy with respect to the CBR is well known since this is just the dipole component of the anisotropy in the CBR. Observations of this feature have already been referred to in section 1.2.1.2. Once a reference frame has been chosen the data can be compared with a given model: a simple and popular choice has been a bulk flow model. Lynden-Bell *et al.* (1988) show how the data is used to calculate any possible deviation from the Hubble flow. At its simplest, for a bulk flow model, it involves comparing the predicted streaming motion ($V_{pred} = H_0 r - \Delta \mathbf{V} \cdot \hat{\mathbf{r}}$) with the observed velocity as derived from the redshift and minimising the result with respect to the components of $\Delta \mathbf{V}$.

The first comprehensive attempt to map large scale streaming motions was made by Rubin *et al.* (1976) using a sample of 96 spirals. All these spirals belonged to the classes ScI-II, and were believed to be standard candles (*i.e.* each galaxy would have the same absolute magnitude). This sample has been reanalysed by Collins, Joseph & Robertson (1986) using IRTF and an infrared-optical colour magnitude relation. Their preferred solution is the latter (though the two methods give similar results within the errors). The resulting streaming motion is effectively equivalent to the original Rubin *et al.* (1976) study, a motion of about 900 ± 300 km s^{-1} . The mean depth of this sample is close to $50h^{-1}$Mpc.

The Rubin-Ford result was placed in doubt however by the work of Hart & Davies (1982) who used a Tully-Fisher method on a sample of galaxies extending out to $60h^{-1}$Mpc (though the mean depth is only about $25h^{-1}$Mpc). Similarly, de Vaucouleurs & Peters (1984) found no evidence for any streaming beyond about $40h^{-1}$ Mpc, though they did find evidence for some motion within that scale. These results have been superseded since then. The Hart & Davies work has been redone by Staveley-Smith & Davies (1989). They use Tully-Fisher on a sample of small mean depth and find evidence for at least some large scale motions.

The other major survey using IRTF is that of Aaronson *et al.* (1986), which samples ten clusters accessible from Arecibo. They find that the clusters (ranging in distance from $40h^{-1}$Mpc to $110h^{-1}$Mpc and with a mean depth of about $60h^{-1}$Mpc) are effectively at rest with respect to the CBR. A further survey carried out at Parkes of

another six clusters in the direction of the Hydra-Centaurus Supercluster and its extension on the opposite side of the galactic plane (Aaronson *et al.* 1988a,1988b) found a significant deviation from the smooth Hubble flow however corresponding to an rms streaming motion with an upper limit of 400 km s^{-1}. However, the lack of any form of complete sky coverage in these two surveys is a problem.

Dressler *et al.* (1987b) use their modified Faber-Jackson technique to survey ellipticals of mean depth $30h^{-1}$Mpc. This shows a streaming motion of about 600 km s^{-1} in a similar direction to the Collins, Joseph & Robertson (1986) survey. Further work by the same group (Faber *et al.* (1988), Lynden-Bell *et al.* 1988) has led them to suggest that the streaming motion is caused by a very large mass concentration in the direction of Hydra-Centaurus. However, since the depth of their survey is much less than any of the others and the Aaronson *et al.* (1988b) result finds much less streaming in the direction of Hydra-Cen, this conclusion must be viewed with some suspicion.

Work on the motions of southern clusters has also been carried out by Lucey & Carter (1988b). They use similar methods to Dressler *et al.* and find that for most of the clusters in common with Lynden-Bell *et al.* and Aaronson *et al.* (1988b), the motions agree. Their are some quite radical differences for some clusters however and these remain to be explained.

On much larger scales, the picture is still confused. James, Joseph & Collins (1987) examined a sample of 60 first ranked cluster elliptical galaxies (assumed to be standard candles) of mean depth 75 h^{-1}Mpc. The sky coverage of this sample was limited but did allow any component of the streaming motion along the direction of the CBR dipole to be found. This produced a streaming motion of about 600 km s^{-1} in the direction of the dipole, in contradiction with the Aaronson *et al.* (1986) result. However, Lucey & Carter (1988a) found that by removing some of the clusters to produce a more homogeneous sample this motion disappeared.

Although the initial attempts to model the streaming motion by a dipole was possibly too simplistic, only further work will finally determine whether or not this is really true. In particular, further deep surveys are needed to go beyond Hydra-Cen to discover whether the 'Great Attractor' model of Faber *et al.* and Lynden-Bell *et al.* is wrong. Also, much more work is needed to give a sky coverage which allows the velocity field to be mapped more accurately. Lastly, further tests must be made to ensure that the properties of galaxies used to estimate distance through techniques such

as IRTF are not dependent on environment. The state of all the current observations used in chapter 4 are summarised in table 1.3. The other work referred to earlier has either been superceded by the references given in the table or is regarded as potentially unreliable. The results are given in terms of the relative motions of the Local Group and the samples, and the relative motions of the CBR (as given by the dipole) and the samples, and are taken from the literature.

Table 1.3: Streaming Flows.

Streaming with respect to the Local Group.

Reference	Mean Depth (h^{-1}Mpc)	v(kms^{-1})	l°	b°
SSD(1989)	25	154 ± 54	247 ± 51	54 ± 25
Lea(1988)	30	406 ± 91	202 ± 13	31 ± 11
CJR(1986)	50	680 ± 330	184 ± 35	-36 ± 30
Aea(1986)	60	780 ± 188	255 ± 17	18 ± 13
VL(1986)		610 ± 50	272 ± 5	30 ± 5

Streaming with respect to the CBR.

Reference	Mean Depth (h^{-1}Mpc)	v(kms^{-1})	l°	b°
SSD(1989)	25	487 ± 68	273 ± 11	20 ± 7
Lea(1988)	30	521 ± 89	307 ± 11	9 ± 8
CJR(1986)	50	970 ± 300	305	45
Aea(1986)	60	0	0	0

The references given are for: SSD - Staveley-Smith & Davies (1989), Lea - Lynden-Bell *et al.* (1988), CJR - Collins, Joseph & Robertson (1986), Aea - Aaronson *et al.* (1986), VL - Lubin & Villela (1986) (this is the CBR dipole). The CJR result is that obtained using the correlation between absolute H magnitudes with observed $B - H$. Where no errors are quoted, none are given in the original reference. Aaronson *et al.* do not give a solution in the CBR frame, but it must be near zero. The velocities with respect to the CBR may vary slightly from those used in chapter 4 since the velocities there are derived from the motions with respect to the Local Group and are not taken from the literature. Note: b is galactic latitude and l galactic longitude.

1.2.4 Other Observational Constraints

1.2.4.1 The Density Parameter and the Hubble Constant

The density parameter, Ω, is defined to be the ratio of the actual density of the universe and the 'critical' density (the density for which the curvature, K, of the universe is zero) at the present epoch. There are two tests of this quantity: direct observations of structure in the universe and, indirectly, by using arguments relating to nucleosynthesis and the age of the universe. The direct observations can take many forms. Dekel & Rees (1987) sum up the results that methods such as virial analysis of clusters give. They conclude that dynamical arguments constrain $\Omega \lesssim 0.3$. Much of this mass must be 'dark', since the luminous matter in the universe constitutes only a small fraction of the dynamical mass. This dark matter could be baryonic but much attention has focussed on universes dominated by collisionless particles, since this overcomes the standard nucleosynthesis constraints described next. This allows $\Omega = 1$ if it is accepted that the dark matter is distributed far more evenly than the luminous matter.

The nucleosynthesis constraint actually applies to the density of baryons in the universe under the assumption that the light elements (deuterium, ^{3}He, ^{4}He and ^{7}Li) are primordial and are not stellar products. Yang *et al.* (1984) predict that in the standard model $1 \times 10^{-2} \lesssim \Omega_b h^2 \lesssim 3.5 \times 10^{-2}$. Thus, for the range of values of h described below, $\Omega_b < 0.25$. More recently, non-standard models of nucleosynthesis have been proposed to allow a higher Ω_b (Applegate, Hogan & Scherrer 1987, Dimopoulous *et al.* 1988) though the validity of these models is not absolutely clear since they often rely on the parameters of other theories such as inflation.

The Hubble constant, H_0, is directly related to the expansion rate of the universe. Therefore, observations of the recession velocity of distant galaxies and their distances should give a value for H_0 from the redshift-distance relation ($v = H_0 r$ for $z \ll 1$). As has already been described in the section on streaming flows however, distance measures for galaxies outside the Local Supercluster requires the use of secondary indicators. Whereas for streaming flows an absolute distance is unnecessary (since it is the perturbation in the Hubble flow, $\delta H/H$, that is required), for measures of H_0 itself accuracy is essential. In practice, the problem in measuring H_0 is that various groups cannot agree on a consistent primary calibration. The values for H_0 lie either in the range $H_0 = 40$-50 km s^{-1} Mpc^{-1} (see *e.g.* Sandage & Tammann (1988) and references

therein) or in the range $H_0 = 90$-100 km s^{-1} Mpc $^{-1}$ (see *e.g.* de Vaucouleurs 1986).

The age of globular clusters gives another bound on the values of Ω and h, since the age of the universe in the standard model depends on these two parameters (see equations B.7 and B.11). Sandage (1988) reports that the best prediction of the age of globular clusters are 13.5 ± 1Gyr. However, this value has changed considerably in recent years (previous work had given the ages as nearer 20Gyr: see the references in Sandage 1988) and it is possible that the models of the evolution of stellar populations in globular clusters is still not entirely accurate. Even with this low value a model with $\Omega \sim 1$ and a large value of h would probably be in trouble since $t_{univ} = \frac{2}{3}H_0^{-1}$ for $\Omega = 1$ and hence $t_{univ} = 6.52h^{-1}$Gyr.

1.2.4.2 Superclusters and Filaments

There is also evidence for structures on larger scales than clusters. Superclusters (groups of clusters) can extend over scales of $50h^{-1}$Mpc. Equally, there appear to be large voids in the distribution of luminous matter in the universe. Oort (1983) gives a useful summary of the well studied superclusters. The Local Supercluster, for example, contains both the Local Group and the Virgo cluster.

There is also some evidence for other forms of structure on these scales. De Lapparent, Geller & Huchra (1988) (and earlier papers referred to therein) report the results of the CfA redshift survey of all galaxies with $m_B \leq 15.5$ in two slices covering an angle of about 0.4sr in total. The depth of this survey is about $100h^{-1}$Mpc. The sample reveals the presence of at least one large void of extent $50h^{-1}$Mpc as well as showing that the galaxies often lie in 'filaments' linking clusters and even superclusters. The significance of this structure is not absolutely clear however. Although it appears to extend across scales larger than superclusters, whether or not power exists in the density fields on these scales is still questionable.

Tests for inhomogeneities on larger scales are hampered by the problem of incompleteness of any catalogue over these distances. One possible probe that has been used are radio source catalogues. Webster (1977) shows that there is little (if any) fluctuation on the scale of 1Gpc from one such catalogue.

1.3 Theoretical Models

1.3.1 Linear Perturbation Theory

1.3.1.1 Introduction

The observed structure in the universe is assumed to have grown from initially very small fluctuations. These fluctuations evolve according to linear perturbation theory as long as the overdensity, δ (defined such that the density field $\rho = \rho_b(1+\delta)$, where ρ_b is the unperturbed background field), is much less than one. As has already been mentioned, Lifshitz (1946) pioneered this work. A detailed review of the mechanics of linear perturbation theory within the framework of general relativity is provided in appendix A.2.

Once $\delta \sim 1$ linear perturbation theory breaks down. Non-linear theory is extremely complicated: modelling the growth of structure under non-linear growth is at best an approximate process. Therefore, if it is possible to compare the results of the purely linear perturbation theory with the observations this would have the advantage of at least being reasonably accurate. Clearly, anisotropies in the CBR offer one such possibility. Since the fluctuations in the CBR are frozen out at the time of decoupling, which was still well within the linear regime in standard theory, the anisotropies that are seen now are a direct constraint on the linear theory. Another possibility is offered by the matter density field on large scales. If the density field on such scales is still approximately linear, the properties of the field on these scales will still be well described by linear theory. In this section the basis of these possible direct constraints on the theory will be discussed more fully.

1.3.1.2 Model Components

The evolution of fluctuations in any given model depends on the constituents of that model. Clearly, any model must contain a baryonic element since the luminous matter seen in the universe is baryonic. Equally, there must be a large photon contribution. The simplest model would consist only of baryons and photons: however, as was stated in section 1.2.4.1, there is a possibility that the mass density of the universe at the present epoch is dominated by some other form of matter. Two candidates are 'hot' dark matter (HDM) and 'cold' dark matter (CDM), so called because the former is initially relativistic in character and the latter non-relativistic. An example of a possible

candidate for HDM is the massive neutrino. Only a small mass is needed to achieve a closure density for the universe in neutrinos ($m_\nu \sim 98h^2$ev: Bond & Szalay 1983). The known species of massless neutrinos should also be included in any model. These behave like the photons except that they are truly collisionless whereas the photons can be coupled to the matter through Thomson scattering. There are many proposed candidates for CDM but none with any observed basis: one favoured species is the axion whose mass is generated during the phase transition associated with the Peccei-Quinn symmetry in QCD. Their mass is not well constrained by any particle physics theory.

Given that the CBR has a cosmological origin, the universe must once have been radiation dominated (see equations A.27a and A.27b for the evolution of matter and radiation densities respectively). The behaviour of the fluctuations will be different in the radiation dominated epoch form that in the matter dominated era. Equation A.25b together with equation A.27 shows that the scale factor behaves like $a(t) \propto t^{1/2}$ in the radiation dominated era and like $a(t) \propto t^{2/3}$ during the matter dominated era (assuming that the curvature contribution is negligible). The expansion rate of the universe ($\dot{a}/a$) is faster in the radiation dominated era. This has important consequences for the fate of the matter perturbations as outlined in section 1.3.1.4.

1.3.1.3 Initial Conditions

It has already been stated that the structure in the universe grows from initially small fluctuations. However, the form of these initial fluctuations also has to be specified. Traditionally, it was assumed that the initial fluctuations could be characterised by a single parameter, n, and a power law. The *power spectrum* of the fluctuations can be defined as:

$$P(k) = |\delta(k)|^2 \,. \tag{1.5}$$

Then, $|\delta(k)|^2 \propto k^n$, and n is a spectral index. This form was adopted for simplicity (it represents the minimum parameterisation given our lack of knowledge of the true initial state). However, as will be shown in section 1.3.2, inflationary models of the universe lead naturally to a Gaussian random field for the initial fluctuations, and to just this form for the initial fluctuation spectrum. The actual form of the fluctuation spectrum for all the perturbed quantities still has to be defined however. Two possibilities exist: the adiabatic mode in which the perturbation in the entropy

is zero and the isocurvature mode in which the fluctuation in the total curvature (the metric perturbations) is zero (and hence there is no net fluctuation in the total energy). The so-called 'isothermal' mode often referred to in early papers is a mixture of the isocurvature mode and the adiabatic mode. It only strictly becomes purely isocurvature at infinite redshift. The definitions of these modes will be discussed in more detail in chapter 2. The favoured values for n are $n = 1$ (adiabatic) and $n = -3$ (isocurvature) since these spectra then have equal power on all scales when the relevant scale comes within the horizon. These are called *scale invariant* spectra. Other values of n have a well defined scale given by the horizon size within which $\langle(\delta\rho/\rho)^2\rangle = 1$.

1.3.1.4 Simple Cases

Several simple limiting cases can be derived from the full perturbation equations. Consider, for example, the behaviour of matter perturbations during the matter dominated era and neglecting the effect of the radiation. Then the set of equations A.68 simplifies to give one second order differential equation for δ_m which has as its solutions $\delta_m \propto t^{2/3}$ and $\delta_m \propto t^{-1}$. This is the model for dust with no pressure that is often found in the literature (see *e.g.* Weinberg 1972).

If the universe is still affected by the radiation contribution through its mass density driving the expansion but in no other way the behaviour of the matter perturbation is significantly modified. The fluctuations grow at a slower rate than the universe actually expands, since the expansion rate is still partly determined by the radiation density whereas the growth rate for the fluctuations is purely determined by the matter density. This is known as the Mészáros effect (Mészáros 1975). Basically, until well into the matter dominated era when $a/a_{eq} \gg 1$ (where a_{eq} denotes the value of the scale factor for which the densities of matter and radiation are equal), the fluctuations will undergo little growth.

This also affects CDM dominated models during the radiation dominated era: since the CDM is not prevented from collapsing as the baryons are by radiation pressure, it might be naively thought that sub-horizon perturbations could collapse. However, perturbations in a non-relativistic component cannot grow as long as the universe is radiation dominated.

For the case of baryonic perturbations at high redshifts (greater than the decoupling epoch), sub-horizon fluctuations are suppressed by another mechanism as well. As

demonstrated by Peebles (1980) equation 93.25, the fluctuations oscillate due to the competing forces of gravity and radiation pressure. In fact the limit is determined by the *Jeans* wavelength defined such that $\lambda_J = v_s t$, where v_s is the sound speed of the medium ($v_s^2 = dp/d\rho$). In the radiation dominated era this is effectively equivalent to the horizon scale for baryonic fluctuations;

$$\lambda_J \simeq \frac{ct}{\sqrt{3}} .$$

For CDM, the Jeans' length is much less, since the radiation pressure has no effect on the dark matter. Since the baryons and the radiation are strongly coupled in this regime, the radiation fluctuation cannot grow on scales much smaller than the horizon either. In the matter dominated regime, the Jeans wavelength is given by

$$\lambda_J \sim \frac{a}{a_{eq}} \lambda_{Jeq} .$$

Note that these are proper wavelengths. The comoving Jeans wavelength does not change between equality and recombination. After recombination only the matter pressure is important and λ_J drops dramatically. Since the comoving Jeans wavelength is constant between equality and recombination (as long as $\Omega h^2 \geq 0.036$: otherwise equality occurs after recombination) those modes that enter the horizon after equality can grow. All these limiting cases show that there are various length scales which characterise any given model. These are discussed in section 1.3.1.6.

The evolution of fluctuations on super-horizon scales is strongly dependent on gauge effects. These are discussed in appendix A.2.4. In the standard choice of gauge (the *synchronous* gauge), the fluctuations appear to grow on super-horizon scales in both the matter and radiation dominated eras ($\delta \propto t^{2/3}$ and t respectively) for adiabatic perturbations. There is no growth in the isocurvature perturbations on super-horizon scales.

Finally, a simple argument can be given to define the form of the power spectrum in the radiation dominated era for adiabatic perturbations. The comoving wavelength just coming within the horizon at any time is $\lambda_h \propto ct/a(t) \propto a$. Therefore, if a_k is defined to be the scale factor at which the wavelength with corresponding comoving wavenumber k comes within the horizon, $k \propto a_k^{-1}$. Since δ grows as a^2 on super-horizon scales in the radiation dominated era but experiences no growth on sub-horizon scales, the growth factor for any mode is given by $\delta \sim a_k^2 \delta_i$, or $\delta \sim k^{-2} \delta_i$. Hence, at a given

epoch, the power spectrum is tilted from k^n to k^{n-4} as the modes come within the horizon.

1.3.1.5 Recombination

At high redshifts, the photons and the baryons are tightly coupled by Thomson scattering of photons from electrons in the plasma as long as the temperature is greater than about 3000K. At lower temperatures, the matter and radiation slowly decouple. As long as the two are coupled however, the fluctuations cannot grow since the radiation pressure prevents collapse as noted above. Peebles (1968) was the first to model the decoupling process accurately. Jones & Wyse (1985) showed that a more realistic model gave answers that were almost identical to the Peebles solutions. Bond (1988*a*) gives a neat summary of this process. The ionisation fraction drops from unity to a very small level ($\sim 10^{-5}$) as the redshift goes from about 2000 to about 800. If the effect of helium is taken into account, then a fraction of the electrons decouple at slightly higher temperatures (since the helium recombines in a straightforward manner whilst the hydrogen doesn't). The total effect is to create a last scattering shell from which all the CBR photons that are seen originate. The visibility function (which measures the probability that a photon seen at the present was last scattered at a given redshift) is well modelled by a Gaussian centred on $z \sim 1070$ with $\sigma \sim 80$ (see Jones & Wyse and chapter 3).

With this accurate model of the decoupling regime, Peebles & Yu (1970) created an accurate model of the growth of fluctuations in the universe. This model gives a set of differential equations (see appendix A) that must be solved numerically. This was also the first attempt to model the expected anisotropies in the CBR. Previous models had consisted of a simplified model of the radiation (see *e.g.* Silk 1968) and had not been very accurate. The Peebles & Yu model was based on the assumption that the universe is currently dominated by baryons. Unfortunately, the observational limits of the time were too poor to usefully constrain the theory. Work since that time can be split into two classes: those that are primarily interested in the anisotropies in the CBR and those that are concerned mainly with the form of the matter distribution as given by linear theory. Most of the latter follow computational techniques which are quite similar to those of Peebles & Yu since the final form of the radiation distribution is not accurately required. These include the original work done on universes dominated by

non-baryonic matter. Peebles (1982) and Bond & Szalay (1983) considered the case of a universe dominated by collisionless particles. These models included massive neutrino dominated universes and CDM dominated universes.

1.3.1.6 Characteristic Length Scales

The fundamental properties of all these models with regard to both the CBR and large scale structure can be understood in terms of the characteristic length scales inherent in each model. These scales vary according to the dominant form of mass in the universe and the parameters Ω and h. These are defined below. Almost all the scale lengths inherent in the models can be seen to depend on the quantity ct/a (see section B.2.2.1). This is related to the horizon scale at time t but is not strictly equal to it. The actual comoving horizon radius is given by

$$r_h = \int_0^t \frac{cdt}{a} ,$$

which gives $r_h = 3ct/a$ for the matter dominated era and $r_h = 2ct/a$ for the radiation dominated era. (See appendix B.1 for the relation between t and a). The comoving horizon can be more simply expressed in terms of the *conformal time*, τ, defined by

$$d\tau = \frac{dt}{a} .$$

Then, $r_h = c\tau$, at all times. The comoving horizon wavelength is then $\lambda_h = 2r_h$.

The comoving horizon scale at the epoch of matter-radiation equality when the mass densities of the matter and the radiation are equivalent is:

$$\lambda_{eq} = 2c\tau_{eq} \sim 32\Omega^{-1}h^{-2}\mathrm{Mpc} .$$

The comoving horizon scale at recombination is:

$$\lambda_{rec} = 2ct_{rec} \sim 257\Omega^{-1/2}h^{-1}\mathrm{Mpc} .$$

The comoving Jeans' wavelength is:

$$\lambda_J = v_s t/a .$$

The comoving Silk wavelength: in baryonic universes, when the radiation diffuses during recombination, the perturbation in the matter density is washed out on scales below this wavelength:

$$\lambda_{Silk} \sim 2(\Omega h^2 + 0.036)^{-1}\,\mathrm{Mpc} .$$

(See Peebles 1980).

The comoving scale length for free streaming of massive neutrinos in an HDM model: when the neutrinos are relativistic they free stream, erasing all structure on scales smaller than the horizon; when they become non-relativistic the comoving free streaming path length becomes finite so this no longer occurs. The neutrinos become non-relativistic when $kT \sim m_\nu c^2$: hence on all scales smaller than the horizon at this epoch structure will be erased. Bond & Szalay (1983) find that the actual value from numerical results is

$$\lambda_\nu \sim 13(\Omega_\nu h^2)^{-1}\,\mathrm{Mpc}\,.$$

Note that this is reasonably close to λ_{eq}, since the number density of massive neutrinos and photons is roughly similar.

Other scales also come into play in a detailed consideration of the processes involved but these are the main ones. CDM models are then determined only by λ_{eq}. This scale is dependent only on Ω, h and the number of species of massless collisionless particles (generally assumed to be only three types of massless neutrino). Lowering Ω or h or increasing the number of collisionless species increases λ_{eq}. Hence, in general, for an initially scale invariant adiabatic spectrum ($n = 1$), the form of the final spectrum is (very approximately) $|\delta_k|^2 \propto k^{-3}$ for $k > k_{eq}$ and $|\delta_k|^2 \propto k$ for $k < k_{eq}$.

For baryonic models, the fundamental length scales are set by Silk damping and by the horizon scales at equality and recombination (since after equality the baryon fluctuations can grow if they are outside the Jeans length, which is similar to the horizon at equality, but will not grow completely unhindered by radiation pressure except on scales outside the horizon at recombination). Therefore, the final spectrum appears like the initial spectrum for wavelengths larger than λ_{rec}, turns over slowly between there and λ_{eq} and then there is a plateau between this wavelength and λ_{Silk} where the spectrum tilts over to k^{n-4}, and below λ_{Silk} the spectrum is strongly damped. Isocurvature baryonic models tend to depend more on λ_{eq} since the radiation and matter are not so strongly coupled initially. Chapter 3 discusses general features of baryonic models in more detail.

For massive neutrino models only λ_ν is important, since this is roughly equivalent to λ_{eq}. The form of the power spectrum for an HDM model is therefore almost a Gaussian filtered power law.

One other factor must be taken into account: both the HDM and CDM models allow the possibility of smaller fluctuations in the baryonic component at recombination than in a purely baryonic model. In models dominated by collisionless particles the baryons will fall into the potential wells formed by these particles after recombination. The HDM model is not as beneficial in this respect for reducing the final baryon perturbation. Since, for adiabatic models, the fluctuation in the baryons and the dark matter must be roughly equivalent outside the horizon and most scales within the horizon at equality are damped out the only portion that gains is near the horizon scale at recombination. Only in this small range of scales will the baryonic fluctuation in a HDM model be lower than in an equivalent standard baryonic model.

With these basics, it can be seen that CDM models tend to favour structure on galactic scales (the peak in the power spectrum of the baryons is on sub-galactic scales for $\Omega = 1$) but has less power on large scales. Since the most stringent constraints on small scales are the small angle CBR limits, CDM stands the best chance of agreeing with these limits. HDM models tend in the opposite direction, favouring large scale structure. However, since both allow the baryonic component to be 'small' at recombination, the CBR limits are not necessarily violated in any case. Baryonic models suffer severe difficulties since there the matter is tightly coupled to the radiation at recombination. There is power on large scales in baryonic models, so galaxies form from fragmentation of large pancakes (the same is true for HDM). Thus both baryonic models and HDM models are examples of large scale damping in which clusters or superclusters form first. CDM is an example of a hierarchical model, since structure builds from the very smallest (baryonic Jeans' length) scales upwards.

1.3.2 Gaussian Random Fields

1.3.2.1 Biased Galaxy Formation

One possible way to reconcile the desire for a $\Omega = 1$ universe with the observed values of $\Omega \sim 0.2$ is to infer that the light (galaxies, clusters etc.) does not trace the underlying density field. The theory of 'biased' galaxy formation tries to provide a framework for this possibility. There are various possible methods for achieving this. Some of the more exotic models to be discussed in section 1.4.2 naturally give rise to biased models. Dekel & Rees (1987) review some of the possible mechanisms.

The method of most interest here is that of 'high-peak' biasing. The basic concept

is to identify the structure in the universe with the maxima (or at least regions above a given threshold, where the threshold is defined as being $\nu = \delta/\sigma_0$ and σ_0 is the *rms* value of the density field) of the density field rather than with arbitrary points in the density field. The properties of these maxima will then modify the predicted observational results arising from any model.

Having chosen to identify high peaks with proto-objects in the universe, the only remaining choice is to define how the density field is distributed. The standard choice is to assume that the density is distributed like a random Gaussian field. A density field of this type can arise within models of the very early universe, when particle physics processes play a large part. Turner (1986) gives a useful review of the role of particle physics models in cosmology. The inflationary model for the early universe in particular gives rise to a density field of the this form. This model stems from the desire to solve some of the major problems with the standard model: viz, the *flatness* problem (why Ω should be so close to unity), the horizon problem (why causally unconnected regions in the early universe should appear so similar) and the problem with the expected number density of magnetic monopoles (which particle physics GUT's predict should be large when none are observed).

Inflation solves these problems by showing that if the energy density of the universe at early times is dominated by a vacuum energy (which is constant and hence from equation A.25, $a(t)$ grows exponentially), initially very small volumes grow to encompass all the universe seen within the horizon. This could occur during a phase transition in the early universe as predicted by the various particle physics gauge theories: the universe becomes 'stuck' in a vacuum state that is not stable and which has a non-zero energy density. This solves the problems mentioned above since the whole observable universe was once causally connected, encompassed a small initial volume (where few monopoles would be expected) and the exponential growth 'flattens' the observable universe (the vacuum energy is transferred to the matter once inflation stops, leaving the matter density with a value which is virtually identical to the critical density).

Perturbations arise within this model from pre-inflation quantum fluctuations. These grow during inflation to give a random Gaussian field. Two basic types of fluctuation are possible: scale-invariant adiabatic or isocurvature. The basic fluctuation type is adiabatic: all forms of inflation give rise to adiabatic fluctuations of some form. Isocurvature perturbations require slightly more contrived conditions for their creation. For

example, if the axions acquire their mass during the inflationary phase then the fluctuations become isocurvature. Turner (1986) gives more details of fluctuations in inflation. Bardeen *et al.* (1986) (hereafter BBKS) show that any homogeneous, isotropic Gaussian field has a power spectrum which is a function of k only. For the reasons previously described, this leads to the power law initial conditions given in section 1.3.1.3.

1.3.2.2 The Statistics of Random Gaussian Fields

Peacock & Heavens (1985) and BBKS both considered the statistics of Gaussian random fields. Both calculated the number density of maxima in such a field, as well as considering the shapes of maxima and their clustering properties. Whilst the number density of maxima can be calculated numerically in a fairly straightforward manner, the clustering problem is only tractable analytically for a restricted set of cases. In particular, if the correlation function of the underlying density field falls off quickly enough so that its derivatives can be ignored, an analytical solution can be found. In practice, this solution is useful for modelling galaxy correlations but not cluster correlations. Chapter 4 discusses this particular issue in more detail.

Both BBKS and Peacock & Heavens found that the shape of the maxima was non-spherical for all but the very highest peaks. The shape of the maxima could crucially affect the form of the evolved structure: non-spherical maxima will tend to collapse along the shortest axis first, akin to the 'pancake' model of galaxy formation. Filaments and other such features could thus arise largely out of the form of the initial density maxima.

Although the statistical properties of the field are general, for modelling structure in the universe some particular choice for the density field must be made. The most common approach is to filter the density field on some appropriate scale (*e.g.* with a filter radius that is comparable to the size of the proto-object) with a Gaussian filter function, $F(r) \propto \exp(-r^2/2R_f^2)$, where R_f is the filter radius. Then a threshold ($\nu_t = \delta/\sigma_0$) is chosen so that the number density of peaks in the filtered field is equivalent to that observed for the real objects. Again, chapter 4 discusses the issue of the choice of filter in more detail.

1.3.3 Anisotropies in the CBR

1.3.3.1 Calculating the Angular Correlation Function of the CBR

The better limits set on anisotropies required a more detailed calculation of the residual fluctuations in the CBR. Appendix A covers the derivation of the actual equations needed. The computational methods involved are discussed in chapter 2. It is usual to decompose the fluctuation in the radiation energy density, $\delta(\hat{\mathbf{q}}, \mathbf{x}, t)$, into a set of spherical harmonics on the sky. The spatial dependence of these functions can be separated into the eigenfunctions of the 3-subspace: in practice, for a flat universe, this is a plane wave expansion, $\delta(\mathbf{x}, t) = \delta(t)\exp(i\mathbf{k}.\mathbf{x})$. Section A.6 outlines the general case for a space of any curvature. The models presented in chapter 2 consider flat spaces only. Given the isotropy requirements the fluctuation in the radiation energy density can be expressed in terms of a Legendre polynomial expansion (for the case of a flat space only though: an open universe has a similar expansion in terms of rather more complicated functions). Hence,

$$\delta(\mu, t) = \sum \delta_l(t) P_l(\mu)\,, \qquad \mu = \hat{\mathbf{k}}.\hat{\mathbf{q}}\,. \tag{1.6}$$

What is actually needed for comparison with the observations is the actual angular correlation function (ACF) of the CBR. This is defined by:

$$C(\theta) = \frac{1}{16}\langle \delta(\hat{\mathbf{q}}, \mathbf{x}, t)\delta(\hat{\mathbf{q}}', \mathbf{x}, t)\rangle\,, \qquad \cos\theta = \hat{\mathbf{q}}.\hat{\mathbf{q}}'\,. \tag{1.7}$$

Wilson & Silk (1981) calculated the form of the ACF for a $\Omega = 1$ baryonic universe with $h = 0.42$. Wilson (1983) did the same for a low density ($\Omega = 0.1$) universe. Unfortunately, both these papers give results for isothermal modes and not isocurvature modes. The adiabatic mode was calculated accurately however. Vittorio & Silk (1984) and Bond & Efstathiou (1984) both expanded on the basis of the Bond & Szalay paper to give the ACF for universes dominated by non-baryonic matter; both CDM and HDM models were considered.

Efstathiou & Bond (1986) modelled the evolution of isocurvature fluctuations in a CDM dominated universe (and also give a useful summary of the nature of isocurvature fluctuations). Bond & Efstathiou (1987) continued this work and also produced 'maps' of the expected sky fluctuation patterns. Peebles (1987) recalculated the baryonic model with the correct isocurvature initial condition, as did Efstathiou & Bond (1987).

Gouda, Sasaki & Suto (1987) repeated the calculations of Wilson & Silk (1981) and Wilson (1983).

1.3.3.2 Modelling the Observational Data

Having calculated an ACF for a given model, it is necessary to normalise it in some manner. The natural fluctuation to match with the observations is that in the baryons. Since the initial conditions for all the other particles in the model can be related to the baryons, this allows the ACF to be normalised. However, the manner in which this can be done allows some choice. Section 2.3 considers this in detail. As a rough guide however, the basic concept usually involves matching the observed galaxy distribution to a predicted model distribution. For example, the galaxy-galaxy correlation function could be compared to the autocorrelation function of the density field. Another popular choice is the volume integral of the correlation function, J_3 (see equation 2.11a). All the possible choices described in chapter 2 do involve some problems however. These will be considered in detail there.

There is another important element that must be considered before the models can be compared with the observations. As well as the intrinsic sky fluctuations, every observation is also dependent on the experimental set up. The ACF must be modified to take account of this. For most of the observations considered in section 1.2.1.2, the effect of the antenna can be modelled by convolving the ACF with a Gaussian of the same FWHM. Then the nature of the experiment must also be considered. For example, Uson & Wilkinson (1985) used a three-beam method. Section 2.3 again considers this problem in detail. A discussion of the results of previous work will also be deferred till then since it relies heavily on the concepts of normalisation and beam smearing to be described there.

1.3.3.3 Secondary Anisotropies

As well as the primary anisotropies that arise from the primeval fluctuations, there are also secondary anisotropies that arise in the post-decoupling era. Any process that reionises a significant fraction of the universe at redshifts such that the optical depth to us is unity will wipe out all the intrinsic fluctuations on small scales. An early generation of very massive stars could perhaps cause this effect. However, as Vishniac (1987) showed, the resultant anisotropies on intermediate scales are larger

than the intrinsic fluctuations. Therefore, whilst reionisation could explain why the observations on small scales have not as yet found anything, the limits on intermediate scales provide a severe constraint on any model which invokes this process.

A much more likely secondary anisotropy is that generated by the Sunyaev-Zel'dovich effect. Hot gas in clusters will distort the spectrum of the CBR (and also cause anisotropies if the gas is distributed in an inhomogeneous manner as seems likely). Inverse Compton scattering of the CBR photons from hot electrons causes an energy transfer from the electrons to the photons. Since the number of photons is conserved in such a process, the net effect is to shift more photons into the Wien part of the spectrum and out of the Rayleigh-Jeans portion. Searches for such distortions are useful probes of the contents of the intergalactic medium in clusters. Bond (1988a) and references therein give detailed predictions for this effect. It is important when considering the observations that are looking for primary fluctuations.

Finally, there is the possibility of distortions in the sub-mm regime caused by primeval dust. Bond, Carr & Hogan (1986) show that any early (formed at redshifts between 5 and 10) generation of stars which generate a significant dust content will cause all the optical light to be reprocessed into the infra-red. This could cause significant spectral distortions in the Wien part of the CBR as referred to in section 1.2.1.1. Tests of the Matsumoto *et al.* (1988) result could validate this model. Equally, such dust will cause anisotropies in the CBR in the same part of the spectrum ($\lesssim$ 1mm) of about 1% (see Bond 1988).

The only process that is of direct importance here is the first. Specific models that have considered reionisation as part of the process include the baryonic isocurvature models of Peebles (1987) and Efstathiou & Bond (1987). They conclude that reionisation could allow the possibility of open, purely baryonic universes.

1.3.4 Streaming Flows and Large Scale Clustering

1.3.4.1 Modelling Large Scale Streaming Motions

The discovery by Rubin *et al.* (1976) that there appeared to be large scale deviations from the Hubble flow led to some initially rather simple models. Wilson & Silk (1981) considered the peculiar velocity relative to a thin shell in the density field. They concluded that for $\Omega = 1$ and $h = 0.42$, most of the adiabatic models had sufficient

large scale power. However, since this model made no assumptions as to the distribution of the observed objects, and had an unusual normalisation (which will be discussed in greater detail in chapter 2), it is at best a guide to the large scale velocity field and not a realistic model.

Clutton-Brock & Peebles (1981) derived a more comprehensive model of streaming flows. They modelled the data by a spherical shell weighted such that a proportion of the galaxies, $W(r)$, had distances less than r. They also considered that the distribution of matter in the universe was accurately mapped by the Lick survey and used this instead of any particular model density field. With the assumption that galaxies trace the mass, since J_3 is defined in terms of ξ, it is a measure of the underlying density field. Then, convolving the window with the predicted velocities,

$$\mathbf{v} = \frac{Hfg}{4\pi G\rho} ,$$

where g is the peculiar gravitational acceleration and where $f \simeq \Omega^{0.6}$ (Peebles 1980), gives a measure of the expected *rms* streaming motions. There are however problems in this method since they were trying to construct J_3 from the angular correlation function of the Lick catalogue: the uncertainties in this imply that the quoted mean velocity for a shell of depth $60fh^{-1}$Mpc of 300 km s^{-1} is liable to be too low. They conclude that a high density universe is needed to explain the Rubin-Ford effect.

Kaiser (1983) considered the streaming motions possible in a neutrino dominated universe. He considered the streaming flow to be the underlying velocity field convolved with a Gaussian window reflecting the distribution of the sample. In linear theory, the underlying velocity field is given by:

$$\mathbf{v}(k) = \frac{-ifH\delta_k}{k^2}\mathbf{k} , \tag{1.8}$$

(note that this is equivalent to the form quoted previously). Essentially, the rest of the analysis is similar to that of Clutton-Brock & Peebles. Kaiser used the results of Hart & Davies (1982) to constrain his models: since this result has not been verified by other surveys the constraints Kaiser predicts are probably of little use. However, his prediction of streaming on the scale of $25h^{-1}$Mpc of $86(1+z_{nl})h^{-2}$ km s^{-1} (where z_{nl} is the collapse redshift) is still relevant. Vittorio & Silk (1984) follow the method of Kaiser using a combination of the Hart & Davies and the de Vaucouleurs & Peters (1984) results. They consider CDM dominated universes with $\Omega = 1$ and conclude that if light traces mass then such models can account for this data. A further model of

a similar type was that of Peebles (1987) who demonstrated that some isocurvature baryonic models could explain large streaming motions on large scales.

Vittorio, Juszkiewicz & Davis (1986) expanded this analysis by considering the motion in two shells, one local which has a comparable streaming motion to ourselves and one on the scale of the distant galaxies being studied. They then consider the probability that it is possible to obtain large scale streaming for any model given that the local motion is effectively zero. They do not find any of their models which can explain the data. These include standard CDM dominated models and HDM dominated models. A technique similar to this will be described in chapter 5 and forms the basis of that chapter. A more detailed discussion of other similar work will also be given there (section 5.5).

The most comprehensive analysis of any of the streaming motions was that of Kaiser (1988a). He used the observational data of Dressler *et al.* (1987b) and Aaronson *et al.* (1986) to construct a tensor window function: this was then convolved with the predicted model peculiar velocities and a maximum likelihood test used to show that standard unbiased CDM was in agreement with the data used. He also tested a set of generic power spectra with a Gaussian form, with a coherence length, R_c. Since one of the problems with modelling streaming flows is the non-linear form of the density field on small (*i.e.* galaxy) scales, he clumped all the data into 'clusters' which are still well described by linear theory to circumvent this. He then considered the likelihood function arising from the probability of obtaining the observed streaming motions given a predicted model velocity and coherence length. He found that there is no strong constraint on the coherence length.

The latest approach to this problem relies on determining the form of the velocity correlation tensor. This is defined in a somewhat similar manner to the correlation function of the density field, viz:

$$\xi_{\alpha\beta}(\mathbf{r}) \equiv \langle v_\alpha(\mathbf{x}) v_\beta(\mathbf{x}+\mathbf{r}) \rangle \, . \tag{1.9}$$

This tensor can be calculated directly from the observational data-sets. Groth, Juszkiewicz & Ostriker (1988) use this tensor to show that the standard biased CDM ($\Omega = 1$) model is statistically inconsistent with the observations. A discussion of some other more recent results from methods of this type is given in section 5.5.

1.3.4.2 *The Cluster-Cluster Correlation Function*

Modelling the cluster-cluster correlation function leads back to the question of whether or not mass traces the light again. Given that ξ_{cc} is well defined by the results of Bahcall & Soneira (1983) and Sutherland (1988), and that the galaxy-galaxy correlation function, ξ_{gg}, is given by $\xi_{gg}(r) = (r/r_0)^{-1.8}$, where the correlation length r_0 is about 5 - $8h^{-1}$ Mpc (Davis & Peebles 1983, de Lapparent, Geller & Huchra 1988), then clearly both the clusters and the galaxies cannot trace the underlying density field since their correlation lengths are so different.

There are a variety of possible solutions to this problem. Firstly, there is the chance that the correlation functions as stated are badly determined. The galaxy-galaxy correlation functions may be derived from samples that are not a fair representation of the universe, and the cluster-cluster correlation function was determined from a very small number of objects. However, if the results are accepted some physical process must be invoked which causes clusters and galaxies to cluster in a different manner. Section 1.4.2 discusses some of the more exotic galaxy formation theories which can give rise to structure like this. One simple possibility was outlined by Kaiser (1984) when he showed that if clusters formed preferentially in overdense regions, and galaxies trace the mass, then $\xi_{cc} \sim A\xi_{gg}$ where A is some amplification factor. This can arise naturally within the framework of Gaussian random fields giving rise to a fairly natural explanation for this problem.

With this in mind Kaiser (1984) calculated the correlation function of all *regions* of a Gaussian density field above a given threshold, ν_t, in the limit that $\nu_t \to \infty$. If the scaled autocorrelation function is given by $\psi(r) = \xi(r)/\sigma_0^2$, the correlation function of all regions above the threshold in this limit is simply $\xi_\nu = \nu_t^2\psi(r)$. Politzer & Wise (1984) give another approximate answer to the same problem, $\xi_\nu = \exp(\nu^2\psi(r)) - 1$. The true result was derived by Jensen & Szalay (1986) and is given by:

$$\xi_\nu = \sum_{m=1}^{\infty} \frac{\psi(r)^m}{m!} A_m^2 \,,$$

where $A_m = 2xH_{m-1}(x)2^{-m/2}/\sqrt{\pi}x\exp(x^2)\mathrm{erfc}(x)$ ($x = \nu/\sqrt{2}$, and the H_m are Hermite polynomials). From the simple expression of Kaiser it is clear that the overdense regions are more clustered than the underlying field.

If it is assumed that the proto-objects (whether galaxies, clusters or whatever) form at the maxima of the density field then the clustering of peaks must be considered,

rather than that of regions. BBKS gave the solution to this problem for a restricted limiting case which was however useful for matching to the galaxy-galaxy correlation function. They showed that purely linear theory would give a quasi power-law ξ_{gg} for the standard CDM model, in line with the numerical non-linear N-body predictions of Davis *et al.* (1985) (see section 1.4.1.2). One of the major conclusions of BBKS was that although the clustering of peaks could also be described by an equation of the form $\xi_{pk-pk} = \langle\tilde{\nu}\rangle^2\psi(r)$, the value of $\langle\tilde{\nu}\rangle$ is in general much less than ν_t. Hence, the amplification that comes about by considering the clustering of peaks in the density field is not as large as once seemed likely. Further discussion of this work is deferred to chapter 4.

Some authors have modelled the cluster-cluster correlation function using the results given by Politzer & Wise or Kaiser. Some results have also been derived using the approximate formulas given in BBKS. In general this is done by filtering the density field on some 'appropriate' scale (chosen to match with the presumed size of a proto-cluster), and then choosing ν_t in some manner. The most formally correct solution is to match the number density of peaks (regions) to that observed for the Abell clusters used to give the observational result.

1.4 Non-Linear Models and Exotic Models

1.4.1 Introduction

This section will deal with those other aspects of theory which, although not of direct relevance to the work presented in this thesis, are still important for constraining various models of galaxy formation. The most important of these topics is the growth of fluctuations in the non-linear regime. Because of the difficulty of obtaining analytic solutions to this problem, much attention has been paid to numerical methods. The major exception to this is the *Zel'dovich approximation* applicable when $\delta \sim 1$. This gives a quantitative representation of the structure and allows checks to be made on any numerical methods. The major numerical method considered in recent years has been the use of N-body simulations to model the growth of large scale structure. Therefore, the two methods described here represent only two of the possible routes to analysing the growth of structure but do give a reasonably complete guide as to how non-linear theory can constrain any model.

The other aspect considered here are those models which I have grouped together under the term 'exotic'. This has been taken to mean any model which requires either a highly speculative physical process, growth of fluctuations dominated by forces other than their own self-gravity or which invokes more than a minimal set of free parameters. The first type is typified by the cosmic string model described below, the second by the explosion model (also described below) and the last by the 'hybrid' models which invoke more than one kind of dark matter or other extra features in the power spectrum (see *e.g.* Bardeen, Bond & Efstathiou 1987 or Turner *et al.* 1987). Again, no attempt at completeness is made. Those models considered do show how such models can account for many of the observed features and the problems associated with them.

1.4.2 Non-Linear Evolution of Fluctuations

1.4.2.1 The Zel'dovich Approximation

The modelling of the non-linear growth of fluctuations in the universe presents problems. Approximations are needed before the problem becomes tractable. Since non-linear effects are assumed to be important only on sub-horizon scales (since the initial fluctuations in the universe are assumed to be homogeneous and isotropic, but see section 1.4.3 below), ordinary Newtonian theory suffices. Further simplification is obtained since the coupling of matter and radiation is not important. Hence, the motion of any component can be well described by a simple set of partial differential equations.

$$\frac{\partial \delta}{\partial t} + \frac{1}{a}\nabla.(1+\delta)\mathbf{v} = 0 \,, \tag{1.10a}$$

$$\frac{\partial \mathbf{v}}{\partial t} + \frac{\dot{a}}{a}\mathbf{v} + \frac{1}{a}(\mathbf{v}.\nabla)\mathbf{v} = \mathbf{g} \,, \tag{1.10b}$$

$$\nabla.\mathbf{g} = -4\pi G \rho_b a \delta \,. \tag{1.10c}$$

Here, $\mathbf{v}$ is the proper peculiar velocity. However, even this set of equations can only be solved given more restrictive assumptions.

One approach to this problem was derived by Zel'dovich (1970). He assumed that linear theory would still accurately model the density field in terms of a Lagrangian coordinate frame if $\delta \sim 1$. Then, the actual position, $\mathbf{r}$, of a trace particle would be a function of its Lagrangian coordinate $\mathbf{q}$ and the time, t.

$$\mathbf{r} = a(t)\mathbf{q} + b(t)\mathbf{p}(\mathbf{q}) \,. \tag{1.11}$$

Here, a is simply the scale factor so the first term represents the expansion of the universe. The other term is a combination of the dominant linear growing mode, b, and the initial conditions, $\mathbf{p}(\mathbf{q})$.

The density at any time in terms of its Eulerian coordinates would then be given by the Jacobian of the transformation between the coordinate systems, r and $\mathbf{q}$:

$$\rho(t) = \rho(t_i) \det\left(\frac{\partial q_i}{\partial r_j}\right)$$

$$= \rho(t_i) \det\left(a(t)\delta_{ij} + b(t)\frac{\partial p_i}{\partial q_j}\right)^{-1} .$$

Hence, whenever $\det(\partial r_j/\partial q_j) = 0$, the density will tend to infinity. The collapse will tend to be along the shortest axis, leaving pancake like structures. After this point is reached the approximation breaks down since particle paths will cross each other.

Numerical simulations of the Zel'dovich approximation show evidence for sheets and filaments similar to those actually observed. Frenk, White & Davis (1983) examined the behaviour of a neutrino dominated universe. They found that the correlation function steepens with time, since pancake models in general do not evolve in a self similar fashion. One of the main problems with such a model is that galaxies are presumed to form only after the pancakes have collapsed: the epoch of pancake collapse in their model was only at $z \sim 2$. Klypin & Shandarin (1983) found similar behaviour.

The major problem with the Zel'dovich approximation is that it *is* only an approximation. For example, Grinstein *et al.* (1987) show that the approximation does give different answers from a more correct non-linear theory for the first four moments of the mass density fluctuations. This leads them to predict that the Zel'dovich approximation will give the wrong estimates for models of large scale streaming velocities. Similarly, N-body simulations show how the approximation breaks down at the caustic surfaces. Efstathiou & Silk (1983) review this subject in more detail.

1.4.2.2 N-Body Simulations

The main alternative method to the analytic techniques described above is to use a truly numerical simulation. The principle method is to use an N-body code. This involves placing test particles on a grid and calculating their mutual interactions under various simplifications. Efstathiou *et al.* (1985) describe the technical aspects in more detail. The important features of any such model are as follows. The simulation can

follow the evolution of density fluctuations well into the non-linear regime. However, because of the limits placed by the practical amount of storage space on a computer, the dynamic range of such simulations tends to be small. This implies that no one model can accurately describe the evolution of structure on both small and large scales. This limited resolution means that the results of N-body simulations should be treated with some caution: it is possible that they may be in error in some details by large amounts.

Having noted these reservations however, it should be noted that the general features seen in the simulations agree well with the predictions of the Zel'dovich approximation when the overdensity is not much greater than one. Therefore the *trends* seen in N-body simulations will be treated as being reliable.

Since N-body codes were designed for modelling dissipationless systems, they are especially useful for testing the non-linear behaviour of hierarchical models. In particular, CDM dominated universes have been studied in detail. Frenk (1988) summarises many of the features of these models. He concludes that the standard ($\Omega = 1$) CDM model can account for the galaxy-galaxy correlation function if biasing is introduced (see also White *et al.* 1987a). The model also correctly predicts many of the observed properties of galaxies that are beyond the scope of this thesis. One other significant feature is that structure on scales up to that including galaxies collapses relatively quickly whilst on larger scales the process is much slower. However, the median redshift for galaxy formation is about 3.

The conclusions of N-body simulations with regard to large scale clustering will be considered further in chapter 4. White *et al.* (1987b) try to use an N-body simulation to model the cluster-cluster correlation function but their procedure is open to error as will be shown later. It is still unclear whether or not a standard biased CDM model can explain the observed large scale clustering. The success of the model in other ways implies that it should still be studied further.

1.4.3 Non-Gaussian Galaxy Formation Models

1.4.3.1 Galaxy Formation by Strings

Cosmic strings are topological defects in space. Certain grand unification theories in particle physics give rise to symmetry breaking that leaves a string that is still in the false vacuum (see section 1.3.2.1) surrounded by space that is in the true vacuum. These strings have a mass density (defined per unit length) and in principle could dominate

the mass density of the universe. However, this is not of particular interest in theories of galaxy formation. It is the strings' role as possible seeds for sites of galaxy formation that is important.

The dynamics of the string network determines the locations at which galaxies form in this picture. At any given time only one infinite (straight) string can exist within the horizon, although many closed loops are possible. Where the strings intersect they reform: loops which cross can subdivide into two smaller closed loops for example. The closed loops radiate and shrink so that eventually they will disappear. As the horizon expands, the infinite string can also cross itself to form closed loops which break off from the remaining straight string. There is some evidence that the loops cluster in a self-similar fashion (Turok 1985). This could explain the form of both the galaxy-galaxy and cluster-cluster correlation function, which have a similar form. In this model ξ_{gg} would be influenced mainly by the gravitational interactions between galaxies but ξ_{cc} would be determined by the correlations of the closed loops.

Since galaxy formation in the string scenario is non-Gaussian, the large scale structure that is observed is less of a problem than with traditional models. String models have been proposed that can account for very large peculiar velocities on the Rubin-Ford scale for example (Zurek & Hoffman 1988). Also, since the initial amplitude of the matter density could in principle be very small (since the density field accretes around the string), the constraints provided by CBR measurements are not as useful. However, the string itself causes a discontinuity in the CBR, which should have been detected if the mass density of the strings was too large (Kaiser & Stebbins 1984).

In order to provide a useful seed, the mass density of the strings must be relatively large. Standard GUT's predict such values but the existence of the millisecond pulsar provides an observational test (Hogan & Rees 1987). The closed loops should emit gravitational radiation which, if it lay across the line of sight to the quasar, would distort the frequency of the pulsar. At the present, the observations limit the mass density of strings to be of about the correct amplitude for acting as seeds for galaxy formation but such values may well be ruled out within a few years. Also, there appears to be some problems with more accurate numerical models of strings, leading to results that are not as straightforward as originally seemed possible.

It would seem that string models should still be regarded with caution therefore until either some direct evidence for their existence is found or the simpler standard

models are shown to be inadequate. Press & Spergel (1987) give a review of many of these topics.

1.4.3.2 Explosive Models

Another example of non-Gaussian fluctuations is provided by the explosive models of galaxy formation. The general idea in all these models is to create the large scale structure from small scale perturbations. These small scale fluctuations give rise to explosions which sweep up shells in the surrounding density field leading to collapse in the shock fronts. The new generation of objects are far more massive than their precursors. In principle, this process could occur many times, leading to structure on scales much larger than the original seeds. This model was first proposed by Ostriker & Cowie (1981). Their suggested initial seeds were either a generation of supermassive stars or even clusters of such objects. Ikeuchi (1981) proposed a similar origin to the large scale structure, though in his case the initial seeds were quasars.

The benefits of this scenario are as follows. The structure will form in thin sheets where the shock front is, giving rise to a structure that is similar to that observed (section 1.2.4.2). The intrinsic fluctuations in the CBR will be small since all the initial fluctuations are on very small scales. However, there are distinct problems. As noted by Peebles (1988b), if structures on scales of the local supercluster were produced by explosions, then the observed peculiar velocities of galaxies are a problem. Supposing that the plane of the supercluster is the shell around an explosion, then the velocities of galaxies in the shell and off it need not be the same. Indeed, it might be thought that galaxies near the supercluster but off the plane (and hence, presumably part of another shell formed by a different explosion) would have systematic differences between their peculiar velocities and that of galaxies in the plane which are not seen. Also, in order to form structures on these scales, the size of the explosion is such that either very small initial seeds were formed very early (soon after recombination) or else single exotic events took place (such as those represented by cosmic strings).

Hogan (1984) and Vishniac & Ostriker (1986) showed that if such structure formed only relatively recently ($z < 10$), then the induced Sunyaev-Zel'dovich effect will give give rise to anisotropies larger than those currently observed. However, Yashioka & Ikeuchi (1987) and Ostriker & Thompson (1987a) showed that very large explosions at redshifts greater than 40 will not distort the CBR in this way. Instead it would

produce an isotropic frequency shift, giving rise to a feature similar to that found by Matsumoto *et al.* (1988).

Ostriker (1988) and Ostriker & Thompson (1987b) review these topics in more depth. The explosive model for galaxy formation remains of interest despite the criticisms but its *necessity* is not readily apparent if the simpler Gaussian models can be shown to explain the observed structure in the universe.

Chapter 2

Anisotropies in the CBR

2.1 Introduction

In all standard models of galaxy formation, the initial fluctuations in the density field are very small. Observationally, it is known that the rms value of the density field is at least unity at the present (on scales $\lesssim 10h^{-1}$ Mpc). In linear theory in the matter dominated regime after recombination, $\delta_m \propto a$, so at the time of recombination $\delta_m \sim 10^{-3}$. Since the photon field is coupled to the matter field until recombination and after that is almost unchanged up to the present, there should still be fluctuations at approximately this level in the radiation. The observations indicate that such fluctuations do not exist. In order to test any model correctly however, an accurate calculation of the expected temperature anisotropies is needed. As noted in the introduction, work in this field was pioneered by Peebles & Yu (1970). Since then many others (Wilson & Silk 1981; Wilson 1983; Efstathiou & Bond 1987; Gouda, Sasaki & Suto 1987 (for baryon dominated universes); Vittorio & Silk 1984; Bond & Efstathiou 1984; Efstathiou & Bond 1986 (for CDM and HDM dominated universes)) have calculated the expected anisotropies on small angular scales. However, some of the techniques applied to baryonic models in the past are slightly dubious. There is therefore a need for a more formally accurate solution, just as Bond & Efstathiou (1987) did for CDM models.

The basic components of any of these models are essentially similar. The evolution of the perturbed quantities (the matter density, the matter peculiar velocity, the radiation density, the gravitational field and the densities of any collisionless particles included in the model) is described by a set of coupled linear differential equations. Appendix A outlines the derivation of these equations for the case of a baryon dominated universe. Although there are some limiting solutions to these equations (appendix B gives some examples), there is no exact analytical solution for the most general case. Therefore, the problem must be solved numerically. Section 2.2 discusses this aspect in detail. A discussion of the initial conditions is also given there.

There are various 'short-cuts' which can be adopted in carrying out these calcu-

lations. In particular, Wilson & Silk (1981) and others consider only temperature anisotropies on small angular scales. In this limit, it is possible to follow the evolution of the radiation distribution after recombination (when scattering processes are unimportant) without recourse to complicated (and time consuming) numerical calculations. Similarly, the form of the angular correlation function (ACF) on large angular scales can be approximated by computing only the Sachs-Wolfe contribution. This latter aspect is considered in the next chapter. The former is discussed later in section 2.4.

Even if a completely accurate ACF were to be produced, the final predictions of expected temperature anisotropies are crucially dependent on the choice of normalisation scheme. The natural fluctuation to match with the observations is that in the baryons. Since the initial conditions for all the other particles in the model can be related to the baryons, this allows the ACF to be normalised. However, the manner in which this can be done allows some choice. The effects of different normalisation schemes are considered in section 2.3. In particular, attention is paid to the concept of biasing and the effect this has on the problems of normalisation. The necessity of introducing biasing into a purely baryonic model might be questioned, but the principle is no different from the inclusion of biasing in an $\Omega = 1$ CDM model.

Although in general purely baryonic models have been well studied in the past, there have been no published attempts to calculate the ACF properly. The most recent results for adiabatic models (Wilson & Silk 1981; Wilson 1983; Gouda, Sasaki & Suto 1987) have all been for the small angle approximation and none consider the possible effect of biasing. Similarly, the isocurvature models considered previously all assumed standard normalisation schemes (Efstathiou & Bond 1987; Gouda, Sasaki & Suto 1987). For these reasons (and also for simplicity when trying to calculate approximate ACF's in chapter 3) the two models considered in detail here are purely baryonic. Accurate, $\Omega = 1$, CDM models are discussed in detail in Bond & Efstathiou (1987). The results derived here are discussed in section 2.4 and comparisons with previous work is also given there.

Although a completely general derivation is given in appendix A, only the restricted case for $\Omega = 1$ is discussed in this chapter. This is due mostly to the constraints of available cpu time on a VAX 11/780 or microVAX. Each model took *many* days of cpu time. The small angle approximation of Wilson & Silk considerably speeds up the time required since the evolution need not be followed through the time consuming

post-recombination epoch accurately. To produce results from this approximate model would take tens of hours of cpu time. It is easy to see why most models considered in the past adopted this approach.

2.2 Numerical Methods

2.2.1 Overview

The derivation of the complete set of equations describing the evolution of small fluctuations is given in appendix A. Although the derivation is given for the independent variable being time for the set of ordinary differential equations (equation A.72), in practice the scale factor is used for this purpose. This removes the necessity of solving for a as a function of t. This implies multiplying all the right hand sides by $1/\dot{a}$. Only the case applying to $\Omega = 1$ will be discussed in this chapter. As well as this, h is assumed to be 0.5 throughout. Despite this, most of the numerical code used was designed with the more general case in mind. The problem can be split into several components:

(i) the initial conditions

(ii) the set of equations used at high redshifts when the mean free time between collisions for photons tends to zero

(iii) the set of equations used for intermediate redshifts when this quantity is no longer small and the full equations must be solved numerically

(iv) the set of equations used when the effect of the radiation can be ignored.

These four areas are discussed separately later.

The basic model adopted has a flat spatial section, and the synchronous gauge is used throughout (see appendix A for a fuller discussion). Hence, the metric perturbation is described by the quantity h_{ij}. Since the spatial section is flat, a plane wave decomposition of the equations A.68 is possible (see appendix A.6). The problem reduces therefore to a set of first order ordinary differential equations. For example, $h_{ij}(\mathrm{x}, t)$ is given by:

$$h_{ij}(\mathrm{x}, t) = \left(\frac{1}{3}(h(t) + H(t))\delta_{ij} - H(t)\hat{k}_i\hat{k}_j\right) e^{i\mathrm{k}.\mathrm{x}} .$$

The radiation fluctuation $\delta(\hat{\mathrm{q}}, \mathrm{x}, t)$ can also be decomposed into a series of Legendre polynomials, so that

$$\delta(\mu,t) = \sum \delta_l(t) P_l(\mu)\,, \qquad\qquad \mu = \hat{\mathbf{k}}.\hat{\mathbf{q}}\,.$$

In order to simplify the presentation, the symbols used are defined here.

a - the scale factor

a_g - the epoch at which matter and photon densities are equal

a_ν - the epoch at which matter and neutrino densities are equal

$a_{eq} = a_g + a_\nu$

k - comoving wavenumber

n_e - electron density

σ_T - Thomson scattering cross section

δ_m - the baryon density fluctuation

δ_l - the coefficients of the Legendre expansion of the fluctuation in the photon density

v - the dimensionless proper baryon velocity

$\dot{h}$ - the trace of the metric fluctuations

$\delta_{\nu l}$ - the coefficients of the Legendre expansion of the fluctuation in the neutrino density

2.2.2 The Evolution Equations

2.2.2.1 The Initial Conditions

A very simple set of equations apply in the limit that $a \ll a_{eq}$ and $kct/a \ll 1$ (high redshift, modes outside the horizon). Then the first order equations presented in the next section reduce to a zeroeth order set. As described in appendix B.2, there are two possible sets of initial conditions. The first (and predominant) type is adiabatic. Here, a small initial fluctuation in the matter density, δ_{mi}, is reflected by a corresponding fluctuation in the radiation and the gravitational field (as given by the metric). Then, (remembering that the independent variable is a and not t),

$$\delta_0 = \delta_{\nu 0} = \frac{4}{3}\delta_{mi} \tag{2.1a}$$

$$v = 0 \tag{2.1b}$$

$$\dot{h} = 4\frac{\dot{a}}{a}\delta_{mi} \tag{2.1c}$$

$$\delta_{\nu 2} = 2\delta_{\nu 0} \, . \tag{2.1d}$$

Note that the initial conditions assume that the initial particle distribution is static so $v = 0$.

The other type of initial condition is isocurvature, in which the local energy density is conserved (and hence the local curvature is also unperturbed). In order to achieve this the fluctuation in the baryon density creates a fluctuation of the opposite sign, and much smaller amplitude in the radiation (both photons and neutrinos). This mode is the same as the isothermal mode of Wilson & Silk (1981) if the perturbation is laid down at $t = 0$. Only in this limit is the isothermal mode correct however. The conditions given here differ from those of Wilson & Silk (1981), who consider only the fluctuation in the baryonic component and assume that the fluctuation in the radiation is negligible. This 'isothermal' (since there is no fluctuation in the radiation) condition is a mixture of adiabatic and isocurvature conditions. The problems which they experienced in carrying out the numerical calculation (they found that the isothermal mode tended to turn into pure adiabatic prematurely due to small errors in the numerical calculation mimicking an adiabatic element) is partly due to this mixture. Only pure isocurvature modes are considered here. Then,

$$\delta_0 = \delta_{\nu 0} = -\frac{a}{a_{eq}}\delta_{mi} \tag{2.2a}$$

$$v = 0 \tag{2.2b}$$

$$\dot{h} = 0 \, . \tag{2.2c}$$

The form of the initial baryon perturbation is taken to be

$$\delta_{mi} = k^{n/2} e^{i\phi_k} \, , \tag{2.3}$$

where ϕ_k is a random phase. The special case of scale invariant power spectra are given by $n = 1$ (adiabatic) and $n = -3$ (isocurvature).

2.2.2.2 *The Second-Order Calculation*

The accuracy of the numerical solution at large redshifts is partly dependent on the mean free time between collisions for the photons, $t_c = (n_e \sigma_T c)^{-1}$. When $t_c \sim 0$, the full equations can be expanded in terms of varying orders of t_c. Peebles & Yu (1970) and Wilson & Silk (1981) both give details of this calculation. The work presented here

follows Wilson & Silk (1981) in keeping terms up to second order in t_c. The derivation (given in appendix B.2) differs in that the massless neutrinos are also included. However, since the behaviour of the massless neutrinos at high redshifts is well described by the standard equations, the essence of the derivation is the same.

The set of equations used is:

$$\dot{\delta}_m = -\frac{ikc}{a}v + \frac{1}{2}\dot{h} \tag{2.4a}$$

$$\dot{\delta}_0 = \frac{4}{3}\dot{\delta}_m - \frac{1}{3}\frac{ikc}{a}t_c\Delta \tag{2.4b}$$

$$\ddot{h} = -2\frac{\dot{a}}{a}\dot{h} + 8\pi G\rho_{b0}a^{-3}\left(\delta_m + 2\frac{a_g}{a}\delta_0 + 2\frac{a_\nu}{a}\delta_{\nu 0}\right) \tag{2.4c}$$

$$\dot{v} = -\frac{\dot{a}}{a}v + \frac{1}{3}\frac{a_g}{a}\Delta \tag{2.4d}$$

$$\dot{\delta}_{\nu 0} = -\frac{1}{3}\frac{ikc}{a}\delta_{\nu 1} + \frac{2}{3}\dot{h} \tag{2.4e}$$

$$\dot{\delta}_{\nu 1} = -\frac{ikc}{a}\left(\delta_{\nu 0} + \frac{2}{5}\delta_{\nu 2}\right) \tag{2.4f}$$

$$\dot{\delta}_{\nu 2} = -\frac{ikc}{a}\left(\frac{2}{3}\delta_{\nu 1} + \frac{3}{7}\delta_{\nu 3}\right) - \frac{4}{3}\dot{H} \tag{2.4g}$$

$$\dot{\delta}_{\nu l} = -\frac{ikc}{a}\left(\frac{l}{2l-1}\delta_{\nu l-1} + \frac{l+1}{2l+3}\delta_{\nu l+1}\right), l > 2 \tag{2.4h}$$

In addition to this set, which must be solved numerically, the following quantities are also given:

$$\begin{aligned}\Delta = &\left(1 + \frac{4}{3}\frac{a_g}{a}\right)^{-1}\left(4\frac{\dot{a}}{a}v - \frac{ikc}{a}\delta_0\right) \quad + \\ &\left(1 + \frac{4}{3}\frac{a_g}{a}\right)^{-1} t_c\left(\frac{16}{27}\frac{ikc}{a}\left(\dot{H} + 2\frac{ikc}{a}v\right) \quad + \right. \\ &\left(1 + \frac{4}{3}\frac{a_g}{a}\right)^{-1}\left(\frac{4}{3}\frac{k^2c^2}{a^2}v + \frac{2}{3}\frac{ikc}{a}\dot{h} - 4\frac{d}{dt}\left(\frac{\dot{a}}{a}\right)v \quad - \right. \\ &\left.\left. 2\frac{\dot{a}}{a}\left(4\frac{\dot{a}}{a}v - \frac{ikc}{a}\delta_0\right)\left(1 + \frac{4}{3}\frac{a_g}{a}\right)^{-1}\left(1 + \frac{8}{3}\frac{a_g}{a}\right)\right)\right)\end{aligned} \tag{2.5a}$$

$$\dot{H} = -\dot{h} + \frac{24\pi Gi}{kc}\rho_{b0}a^{-2}\left(\left(1 + \frac{4}{3}\frac{a_g}{a}\right)v + \frac{1}{3}\frac{a_\nu}{a}\delta_{\nu 1}\right) \tag{2.5b}$$

$$\delta_1 = 4v + t_c\Delta \tag{2.5c}$$

$$\delta_2 = -\frac{40}{27}t_c\left(\dot{H} + 2\frac{ikc}{a}v\right) \tag{2.5d}$$

$$\delta_l = 0\ , l > 2 \tag{2.5e}$$

This 2nd order set is used to follow the evolution from the initial redshift of 10^8 until a redshift of 10000 as described in section 2.2.3.

2.2.2.3 Recombination

The free electron number density in the universe changes rapidly during recombination. As the universe cools, the free electrons and protons combine to form neutral hydrogen. The ionisation fraction, x_e, is defined to be the fraction of electrons which are still free. The simplest solution to this problem is given by the Saha equation but this assumes that recombination occurs direct to the ground state. Highly energetic background photons inhibit such a process through reionisation. In practice, recombination occurs via the first excited level. Peebles (1968) gave the accurate solution to the evolution of x_e. Jones & Wyse (1985) modified this analysis to include the effect of line transitions not considered by Peebles and to take account of a possible dark matter component in the total mass density. Bond (1988a) also gives a neat summary of the processes involved.

The equations solved to give an accurate model of the ionisation in the universe were equation 2 of Jones & Wyse and equation 39 of Peebles.

$$\frac{dx_e}{dt} = \frac{R_{2c}(1-x_e)\exp(-h\nu_\alpha/kT)\,(1+K\Lambda n_e(1-x_e))}{1+K\Lambda n_e(1-x_e)+KR_{2c}n_e(1-x_e)+KR_{c2}x_e^2n_e^2} - \frac{x_e^2 n_e R_{c2}\left(1+K\Lambda n_e(1-x_e)+KR_{c2}n_e^2x_e^2\right)}{1+K\Lambda n_e(1-x_e)+KR_{2c}n_e(1-x_e)+KR_{c2}x_e^2n_e^2} \tag{2.6a}$$

$$\frac{dT_m}{dt} = \frac{8\sigma_T \mathcal{E}_b c}{3m_e}x_e(T-T_m) - \frac{2T_m}{a}\dot{a}\,. \tag{2.6b}$$

Again, the independent variable used in the actual computation was a, so that both equations must be multiplied by $1/\dot{a}$. In the above equations, T is the radiation temperature, T_m is the matter temperature, R_{c2} is the rate of transitions from higher levels (assumed to act like a continuum) to the first excited state for which the value $2.84 \times 10^{-17}\ T_m^{-1/2}$ m^3 s^{-1} is adopted, R_{2c} is the rate of radiative transitions in the opposite direction for which the value $R_{c2}(2\pi m_e kT/h^2)^{3/2}\exp(-B_2/kT)$ (where B_2 is the binding energy of the excited state, 3.4 eV, and h here is Planck's constant and k Boltzmann's constant) is used (Peebles equation 26), ν_α is the frequency of a Lyman-α photon, Λ is the decay rate from the $2S$ level of hydrogen to the ground state (8.227 s^{-1}) and $K = c^3a/8\pi\nu_\alpha^3\dot{a}$ (Peebles equation 29). All values are taken from Jones & Wyse unless otherwise indicated. Note that the numerous typographical mistakes in Jones & Wyse have however been corrected.

This set of coupled differential equations is solved using the techniques described in section 2.2.3 below. The solutions were checked against those of Peebles and Jones & Wyse and no major discrepancy found. These solutions were used as a look-up table for the main routines, and interpolation between points used where necessary. Since the solutions are stable and monotonic functions of scale factor this does not give rise to unnecessary errors.

2.2.2.4 The Complete Equations

The set of equations derived in appendix A are also given here for the particular case of $\Omega = 1$. They are,

$$\dot{\delta}_m = -\frac{ikc}{a}v + \frac{1}{2}\dot{h} \tag{2.7a}$$

$$\dot{v} = -\frac{\dot{a}}{a}v + \frac{1}{3}\frac{a_g}{a}n_e\sigma_T c\left(\delta_1 - 4v\right) \tag{2.7b}$$

$$\ddot{h} = -2\frac{\dot{a}}{a}\dot{h} + 8\pi G\rho_{b0}a^{-3}\left(\delta_m + 2\frac{a_g}{a}\delta_0 + 2\frac{a_\nu}{a}\delta_{\nu 0}\right) \tag{2.7c}$$

$$\dot{\delta}_0 = -\frac{1}{3}\frac{ikc}{a}\delta_1 + \frac{2}{3}\dot{h} \tag{2.7d}$$

$$\dot{\delta}_1 = -n_e\sigma_T c\left(\delta_1 - 4v\right) - \frac{ikc}{a}\left(\delta_0 + \frac{2}{5}\delta_2\right) \tag{2.7e}$$

$$\dot{\delta}_2 = -\frac{9}{10}n_e\sigma_T c\delta_2 - \frac{ikc}{a}\left(\frac{2}{3}\delta_1 + \frac{3}{7}\delta_3\right) - \frac{4}{3}\dot{H} \tag{2.7f}$$

$$\dot{\delta}_l = -n_e\sigma_T c\delta_l - \frac{ikc}{a}\left(\frac{l}{2l-1}\delta_{l-1} + \frac{l+1}{2l+3}\delta_{l+1}\right), l > 2 \tag{2.7g}$$

$$\dot{\delta}_{\nu 0} = -\frac{1}{3}\frac{ikc}{a}\delta_{\nu 1} + \frac{2}{3}\dot{h} \tag{2.7h}$$

$$\dot{\delta}_{\nu 1} = -\frac{ikc}{a}\left(\delta_{\nu 0} + \frac{2}{5}\delta_{\nu 2}\right) \tag{2.7i}$$

$$\dot{\delta}_{\nu 2} = -\frac{ikc}{a}\left(\frac{2}{3}\delta_{\nu 1} + \frac{3}{7}\delta_{\nu 3}\right) - \frac{4}{3}\dot{H} \tag{2.7j}$$

$$\dot{\delta}_{\nu l} = -\frac{ikc}{a}\left(\frac{l}{2l-1}\delta_{\nu l-1} + \frac{l+1}{2l+3}\delta_{\nu l+1}\right), l > 2 \tag{2.7k}$$

As well as these equations, which must be solved numerically, $\dot{H}$ is given by

$$\dot{H} = -\dot{h} + \frac{24\pi Gi}{kc}\rho_{b0}a^{-2}\left(v + \frac{1}{3}\frac{a_g}{a}\delta_1 + \frac{1}{3}\frac{a_\nu}{a}\delta_{\nu 1}\right). \tag{2.7l}$$

2.2.2.5 *The Post Recombination Epoch*

After recombination, two effects allow a simplification of the problem. At late redshifts, when the effect of the radiation is confined to the universal expansion, the massless neutrinos can be excluded, since they no longer affect the behaviour of the other components. Similarly, once the universe has no significant ionisation fraction the photons and the baryons are only coupled through the gravitational influence of the matter on the radiation.

Appendix B.2.3 outlines the derivation of the solution to the equations 2.7 under these circumstances. The solutions are

$$\delta_m = c_1 \left(1 + \frac{3}{2}y\right) + c_2 f(y) \tag{2.8a}$$

$$v = c_3 a^{-1} \tag{2.8b}$$

$$h' = 3c_1 + 2c_2 f'(y) + 2\frac{ikc}{a^2}\frac{a_{eq}}{\dot{a}}c_3 \,, \tag{2.8c}$$

where

$$f(y) = \left[\left(1 + \frac{3}{2}y\right)\log\left(\frac{\sqrt{1+y}+1}{\sqrt{1+y}-1}\right) - 3\sqrt{1+y}\right] \tag{2.8d}$$

and

$$y = \frac{a}{a_{eq}} \,. \tag{2.8e}$$

The behaviour of the photons can also be described in a simple form if the dominant contribution to the evolution of h' is the effect of the growing matter mode ($\propto c_1$). For adiabatic initial conditions this is true as long as the universe is matter dominated. Even if the background radiation still makes a significant contribution to the expansion of the universe, this can be allowed for as long as $a > a_{eq}$. The situation for isocurvature initial conditions is somewhat more complicated since the dominant contribution to h' can be a decaying velocity mode. Until this mode is overtaken by the growing mode the solution must be determined numerically by directly solving equations 2.7. If $h' \propto c_1$ then

$$\tilde{\delta}_l(x_0) = \left(\frac{2l+1}{2}\right)\sum_{n=0}^{\infty}\sum_{p=0}^{\min(l,n)} \tilde{\delta}_n(x_1) c_{lnp} (-i)^{l+n-2p} j_{l+n-2p}(2A(x_0 - x_1)) \,. \tag{2.8f}$$

where

$$\tilde{\delta} = \delta + -3\frac{c_1}{A^2} + 6i\frac{c_1}{A}x\mu \,, \tag{2.8g}$$

$$A = kcH_0^{-1} a_{eq}^{1/2} ,$$

$$c_{lnp} = \left(\frac{2l + 2n - 4p + 1}{2l + 2n - 2p + 1} \right) \frac{a_{l-p} a_{n-p} a_p}{a_{l+n-p}}$$

and

$$a_n = \frac{(2n-1)!!}{n!} .$$

The double summation is much quicker in terms of cpu time than directly solving equations 2.7. The upper limit on the summation over n can be truncated at $n \sim 2A(x_0 - x_1)$ because of the properties of the spherical Bessel functions.

2.2.3 The Numerical Method

2.2.3.1 General Techniques

The equations given above (equations 2.4, 2.6 and 2.7) were all solved in a similar fashion. In all three cases, the independent variable for the numerical solution was the scale factor (as previously mentioned). If the original equations are thought of as a set (with the dependent variables denoted by $\{y_i\}$)

$$\frac{d\mathbf{y}}{dt} = \mathbf{g}(\mathbf{y}(\mathbf{t}), \mathbf{t})$$

then the equations to be solved have the form

$$\frac{d\mathbf{y}}{da} = \frac{\mathbf{g}(\mathbf{y}(t(a)), t(a))}{\dot{a}} .$$

In practice, the functions g are more simply expressed as functions of scale factor anyway, as they have been in the previous section. The set of equations to be solved can then be taken to have the generic form

$$\mathbf{y}' = \mathbf{f}(\mathbf{y}, a) \qquad \text{where} \quad \mathbf{y}' = \frac{d\mathbf{y}}{da} \ , \ \mathbf{f} = \frac{\mathbf{g}}{\dot{a}} .$$

These equations are 'stiff', in the sense that some of the components on the right hand sides have greatly different time-scales from the others. For example, consider equation 2.6b. The timescale for the second term on the right hand side is roughly proportional to the expansion timescale for the universe. The first term has a much shorter timescale since the ionisation changes rapidly between redshifts of 2000 and 1000. This equation is at least partly stiff therefore. Many of the others show similar behaviour. In particular, the equations (2.6) governing recombination are very stiff.

If the massless neutrinos are excluded from the problem, the equations (excluding 2.6, which is very stiff) can be solved using basic methods. Four of the five numerical routines tried are part of the NAG library (a commercial numerical applications package): the other was a very simple and basic Runge-Kutta routine. The results from tests carried out by comparing the routines were all in agreement, suggesting that the routines selected for the actual problem are accurate. The four NAG routines used were: a Runge-Kutta method, an Adams-Moulton method, and two methods for solving stiff equations, one adopting a backwards differentiation method and the other a variant of the Gear method. The basic principles of these routines are discussed below.

In general, the solutions are known at a point a_n, where they have a value $\mathbf{y}_n$. To advance the solution to a point a_{n+1}, the functions $\mathbf{f}$ are evaluated. The simplest (but impractical) solution is to use Euler's method, where

$$\mathbf{y}_{n+1} = \mathbf{y}_n + h\mathbf{f}$$

and $h = a_{n+1} - a_n$ is some suitably chosen step-size. This method can be improved upon greatly, simply by evaluating the functions, f_i, not only at the initial point but also at some midpoints in the range. The fourth-order (since the error is proportional to h^5) Runge-Kutta routines used need four such function evaluations (see, for example, Press *et al.* 1986, equation 15.1.3). The accuracy of the solution can be checked either by halving the step-size, h, or by considering a routine with a higher order. The NAG routine (D02BBF) uses the second method (also known as Runge-Kutta-Merson), the version written to check the NAG routines uses the first.

The Adams-Moulton method (NAG routine D02CBF) is a predictor-corrector method, which utilises previous values of the solution ($\mathbf{y}_{n-2}$, $\mathbf{y}_{n-1}$ etc.) to predict forwards. This information is used to calculate the value of $\mathbf{f}$ at the end-point, and a 'corrector' formula takes this information as well as the values from previous steps, and uses it to calculate $\mathbf{y}_{n+1}$. The routine used is variable-order (that is, when the solution is smooth a low order formula is used, when it is less well behaved a higher order solution).

All three of the routines already described will solve most problems. However, the equations given in the last section are stiff. If the massless neutrinos are excluded all three routines give a solution. The two Runge-Kutta routines are however rather slow (since they compensate for the stiffness by taking very small steps), even compared to the Adams-Moulton routine.

Routines for solving stiff equations overcome the problem of small step-sizes by considering a backwards differencing scheme. The concept in this method is to use the derivatives at the end point of the required range rather than the starting position, giving an implicit equation for the $y_{i,n+1}$. The simplest example of this type of scheme involves the following implicit equation

$$\mathbf{y}_{n+1} = \mathbf{y}_n + h\mathbf{f}(a_{n+1}, \mathbf{y}_{n+1}) \, .$$

If this equation is simplified by expanding around $\mathbf{y}_n$, then the following equation results

$$\mathbf{y}_{n+1}\left(1 - h\left.\frac{\partial \mathbf{f}}{\partial \mathbf{y}}\right|_{\mathbf{y}_n}\right) = \mathbf{y}_n + h\left(\mathbf{f}(a_{n+1}, \mathbf{y}_n) - \left.\frac{\partial \mathbf{f}}{\partial \mathbf{y}}\right|_{\mathbf{y}_n}\mathbf{y}_n\right) \, .$$

It can be seen from this that this method requires the inversion of the matrix

$$1 - \frac{\partial \mathbf{f}}{\partial \mathbf{y}}$$

Hence, routines for solving 'stiff' equations would for most problems be slower than the more straightforward routines described previously. With the exception of equations 2.6 however this matrix has a band structure for the problems considered here. The NAG routines D02NCF, D02NTF and D02NVF allow for this possibility explicitly. The NAG routine D02EBF, which in the form used utilised a Gear method (see, for example, Gear 1971), was modified to taken account of the fact that the matrix has this structure. This considerably improved its performance in terms of cpu time used without compromising its accuracy.

As stated above, for the tests carried out all the routines agreed to within 10%. The main discrepancies were between the crude Runge-Kutta methods and the other three. The Adams-Moulton routine and the two 'stiff' methods were in close agreement. However, when the massless neutrinos were included, the Adams-Moulton routine, whilst it gave results in agreement with the other two, was much slower in terms of cpu time. The other two routines were therefore used to solve all the sets of equations. D02EBF was used for solving equation 2.6. D02NCF, D02NTF and D02NVF were used for the evolution equations in the work described below since they allowed greater control of the error checking performed.

2.2.3.2 Outline of Basic Method

For both the adiabatic and isocurvature initial conditions the bulk of the numerical procedure is similar. Those aspects which are different are dealt with in the next two

sections below. The initial conditions are taken to apply at a redshift of 10^8. This starting value is chosen so that all the modes of interest are outside the horizon at that redshift. This avoids the problems of attributing a phase to any oscillating component which may be present for modes within the horizon. The first order set of equations are used to provide a solution at a redshift of 10000. This redshift was chosen as providing a stable mid-point for the solution. Lower redshifts give rise to spurious solutions (caused by inaccuracies in the neutrino components) and higher redshifts contain essentially the same information but leave a longer integration range for the full set of equations. Since the full set are not useful at redshifts much greater than 10^5 (because of the problems outlined in section 2.2.2.2), it is in any case inadvisable to use them at these redshifts.

The solution at a redshift of 10000 is then fed in as the initial conditions for the full set of equations. The numerical evolution is followed at least as far as a redshift of 300. This ensures, for $\Omega = 1$, $h = 0.5$, that the radiation component in the universe is no longer significant except as a background. Therefore, the massless neutrinos can be excluded at lower redshifts. Similarly, for a normal recombination scheme, the ionisation fraction in the universe has fallen sufficiently by this time that the effects of Thomson scattering can also be ignored, except for very long wavelengths where the mean free path for photons is still less than the scale of interest. Very long wavelengths are followed numerically all the way to the present epoch. (In practice, the mean free path for photons after recombination rapidly increases to about one hundred times the current horizon. Even for the longest wavelength modes required the scattering effect can be ignored.) Other modes can be traced using the schemes outlined in section 2.2.2.5 if certain other conditions are met.

The number of equations to be solved is determined by the parameter $kc\tau$ (the conformal time, τ, is defined by equation B.12) since the number is effectively determined by the two radiation modes. The number of significant modes in the Legendre decomposition is largest when the radiation is free streaming (as the neutrinos do all the time). Since any mode cannot probe angles smaller than that wavelength subtends on last scattering ($\theta \sim \lambda/c\tau_0$: see section 2.4.2.1) and the order of the Legendre expansion is roughly an inverse angle, the highest order polynomial required is $kc\tau_0$. Mathematically, equation B.44b demonstrates that there is a cut-off in the number of significant modes caused by the properties of Bessel functions, which is set by $kc\tau$. To ensure a complete solution the number of equations solved was $\max(2kc\tau + 100)$ for

both the first order and the full set of equations. In practice, this adequately counted all the significant elements of the Legendre decompositions for both the neutrinos and the photons. For large wavenumbers ($k \sim 1$), this implies that over 10000 differential equations would have to be solved using the direct method. Clearly, the solution given by equation 2.8f is to be preferred if it can be applied.

2.2.3.3 The Adiabatic Mode

Controlling the growth of any error component for the adiabatic mode is relatively easy. A single global relative and absolute tolerance could in principle be set (and was when the routine D02EBF was used). However, since the scaling of the various components is quite disparate (the value of $\dot{h}$ is consistently less than that of the dominant term δ_m, as are many of the terms in the Legendre expansion for the radiation), control of the individual errors is an advantage. The routines used (D02NCF, D02NTF, D02NVF) allowed that possibility.

The initial value chosen was $\delta_{mi} = 10^{-10}$. This was found to allow the calculation to proceed without fear of overflow or underflow. In this case the individual tolerances were set as follows: all the relative tolerances (which controls the relative error but not overall stability) were set at a level of 10^{-7}, except for those for $\dot{h}$ where the relative tolerance was 10^{-18} and the neutrino modes where it was 10^{-13}. The absolute tolerances (which control the global error in the solution) were set as 10^{-10}, except for those for $\dot{h}$ where the absolute tolerance was 10^{-18} and $\delta_{\nu 0}$ and $\delta_{\nu 1}$ where it was 10^{-14}. Both checks were satisfied by complying with the stricter of the two. The extra controls on the important neutrino modes and the gravitational fluctuation ensure a stable solution since the largest errors were found to be in these components during testing. As well as setting these internal parameters, the solution was checked by increasing the required tolerance for all the components. This gave effectively the same solution for the modes tested to within 1% in most cases (the variation was larger for some of the less significant radiation modes near the cut-off point described in section 2.2.3.2 above but it is not important there).

At a redshift of 300 the solutions were used as the starting conditions for the set of equations 2.8. These equations give the solutions for all later times. The exception was for modes with wavelengths longer than about 120 Mpc, for which the numerical solution was followed all the way until the present. The match between these two

distinct forms of solution was found to be smooth with no sign of any discontinuity between them. The series solution 2.8f was also checked by calculating some shorter wavelength modes directly and the answers found agreed well. Another check is found by considering equation B.43c. This implies a conservation equation

$$\sum_{l=0}^{\infty} \frac{\left|\tilde{\delta}_l(k,x_0)\right|^2}{2l+1} = \sum_{l=0}^{\infty} \frac{\left|\tilde{\delta}_l(k,x_1)\right|^2}{2l+1} \,. \tag{2.9}$$

This check also showed that the series solution was accurate.

2.2.3.4 The Isocurvature Mode

Unlike the adiabatic mode, the isocurvature mode requires a strict control of the errors generated, since any error term will grow rapidly whilst the components of the solution are constant, swamping the desired solution. The intial value selected for δ_{mi} was 10^{-5}. Since there is little growth in any of the components, a larger initial value than used in the adiabatic case is suitable. The following tolerances were found to give a stable solution. For the first order calculation, all relative tolerances were set to 10^{-10} except for δ_0 and $\delta_{\nu 0}$ where the value 10^{-14} was used and for $\dot{h}$ where the value 10^{-20}. The absolute tolerances were set relative to the starting values for δ_m, δ_0, $\dot{h}$ and $\delta_{\nu 0}$: $10^{-5}|\delta_{mi}|$, $10^{-5}|\delta_{0i}|$, $10^{-17}|\delta_{mi}|$ and $10^{-5}|\delta_{0i}|$ respectively. The other components all had the simpler absolute tolerance of 10^{-7}.

Solving the full set of equations for isocurvature initial conditions was not as simple as for the adiabatic initial conditions. The integrating range (from an upper redshift of 10000 to a lower redshift of 0 for most modes) was split into twenty parts to force the routines to use small enough step-sizes to give a controllable error. With the NAG routines being used this was accomplished by calling the routines on twenty separate occasions. The relative tolerances used were 10^{-10} except for δ_0, $\dot{h}$ and $\delta_{\nu 0}$ where the values 10^{-13}, 10^{-20} and 10^{-13} were used. The absolute tolerances were set at 10^{-12}, except for $\dot{h}$ where the value $10^{-10}|\dot{h}|$ was used (and again this value is recalculated at the start of each of the twenty integrals). This time-varying approach to the absolute tolerances gives a reliable solution.

2.3 Correlation Functions and Normalisation

2.3.1 Correlation Functions

The properties of the matter and radiation fields can be characterised by a set of correlation functions. These are also important when comparing the theoretical predictions with the observations. The definitions of these functions (and where necessary their derivations) are given in the first part of this section. Their application in terms of comparison with the observations is given in the second part. The last part is devoted to modelling the actual observations.

2.3.1.1 The Autocorrelation Function

The autocorrelation function is defined as the Fourier transform of the power spectrum, $|\delta_m(k)|^2$.

$$\xi(r) = \langle \delta_m(\mathbf{x}) \delta_m(\mathbf{x}+\mathbf{r}) \rangle \ . \tag{2.10a}$$

Hence, since

$$\delta(\mathbf{x}) = \frac{V}{(2\pi)^3} \int d^3k \, \delta_{\mathbf{k}} \, e^{i\mathbf{k}.\mathbf{x}} \qquad \text{and} \quad \delta_{\mathbf{k}} = \frac{1}{V} \int d^3x \, \delta(\mathbf{x}) \, e^{-i\mathbf{k}.\mathbf{x}} \ ,$$

for an isotropic density field (as a Gaussian field is), this gives

$$\xi(r) = \frac{4\pi V}{(2\pi)^3} \int k^2 \, |\delta_m(k)|^2 \, \frac{\sin(kr)}{kr} dk \ . \tag{2.10b}$$

The autocorrelation function is a direct measure of the strength of clustering in the underlying field on any given scale. If the density field is thought of as a series of test particles rather than a smooth continuum, strong correlations are equivalent to an excess in the number of pairs on that scale (*cf.* equation 1.3) when compared to a purely random (Poissonian) distribution. Similarly, anti-correlations reflect a lack of clustering.

2.3.1.2 $J_3(r)$

Other quantities related to the autocorrelation function can be generated by considering integrals of $\xi(r)$. In practice, the most commonly used is the volume integral of the autocorrelation function, J_3, defined by:

$$J_3(r) = \int_0^r s^2 \xi(s) ds \ . \tag{2.11a}$$

This equation can be cast in terms of the initial density field using equation 2.10 above and integrating out the r dependence.

$$J_3(r) = \frac{4\pi V}{(2\pi)^3} \int \left\{ \frac{\sin(kr)}{k} - r\cos(kr) \right\} |\delta_k|^2 \, dk \, . \tag{2.11b}$$

2.3.1.3 The Mass Variance in an Arbitrary Sphere

Another useful quantity that can be generated from the matter density field is the variance $\delta M/M$ for the mass contained within an arbitrarily placed sphere, or, more usefully, the mean square mass fluctuation. With the definition of the Fourier transform as given above this is, for a sphere of radius R

$$\left\langle \left(\frac{\delta M}{M} \right)^2 \right\rangle = \frac{1}{V} \int d^3x \left(\frac{\delta M}{M} \right)^2 \, . \tag{2.12a}$$

The mass fluctuation, δM is related to the density fluctuation by

$$\delta M = \int d^3r \, \rho \, \delta(\mathbf{r}) \, ,$$

so

$$\left\langle \left(\frac{\delta M}{M} \right)^2 \right\rangle = \left(\frac{3}{4\pi R^3} \right)^2 \int d^3r \int d^3r' \left\langle \delta(\mathbf{r}) \delta(\mathbf{r}') \right\rangle \, . \tag{2.12b}$$

The averaged quantity in this integral is easily recognised from equation 2.10a as the autocorrelation function. But the correlation function is also simply the Fourier transform of the power spectrum. Hence,

$$\left\langle \left(\frac{\delta M}{M} \right)^2 \right\rangle = \frac{V}{(2\pi)^3} \left(\frac{3}{4\pi R^3} \right)^2 \int d^3r \int d^3r' \int d^3k \, |\delta_{\mathbf{k}}|^2 \, e^{i\mathbf{k}.(\mathbf{r}'-\mathbf{r})} \, . \tag{2.12c}$$

The integrals over $\mathbf{r}$ and $\mathbf{r}'$ are straightforward and give

$$\left\langle \left(\frac{\delta M}{M} \right)^2 \right\rangle = \frac{9V}{(2\pi)^3} \int k^2 \, dk \, |\delta_{\mathbf{k}}|^2 \, \frac{(\sin kR - kR\cos kR)^2}{(kR)^6} \, . \tag{2.12d}$$

2.3.1.4 The Angular Correlation Function for the Radiation

In a similar manner to the way in which the spatial correlation function of the mass is defined, an angular correlation function (ACF) for the radiation can also be defined.

$$C(\theta) = \frac{1}{16} \langle \delta(\hat{\mathbf{q}}, \mathbf{x}, t) \delta(\hat{\mathbf{q}}', \mathbf{x}, t) \rangle \, , \qquad \cos\theta = \hat{\mathbf{q}}.\hat{\mathbf{q}}' \, . \tag{2.13}$$

The factor of 1/16 is included so that $C(\theta)$ is directly related to the fluctuation in the observed temperature. The vectors $\mathbf{q}$ and $\mathbf{q}'$ give the direction of the incoming radiation. The method presented here (as in Peebles & Yu, 1970, or Wilson & Silk,

1981, or any of the more recent papers) determines the evolution of the radiation field at a fixed point.

This average can be simplified. Firstly, note that

$$\langle \delta(\hat{\mathbf{q}},\mathbf{x},t)\delta(\hat{\mathbf{q}}',\mathbf{x},t)\rangle = \frac{1}{V}\int d^3x\, \delta(\hat{\mathbf{q}},\mathbf{x},t)\,\delta^*(\hat{\mathbf{q}}',\mathbf{x},t)\,.$$

With the definition of the Fourier transform given previously, and using the Legendre decomposition for the radiation distribution, this becomes

$$\langle \delta(\hat{\mathbf{q}},\mathbf{x},t)\delta(\hat{\mathbf{q}}',\mathbf{x},t)\rangle = \frac{V}{(2\pi)^3}\sum_m\sum_n \int d^3k\, \delta_m(k,t)\,\delta_n^*(k,t)\,P_m(\cos\alpha)\,P_n(\cos\gamma)\,,$$

where $\cos\alpha = \hat{\mathbf{k}}.\mathbf{q}$ and $\cos\gamma = \hat{\mathbf{k}}.\mathbf{q}'$. A co-ordinate system can be set up such that $\mathbf{q}$ points along the k_z-axis and $\mathbf{q}'$ lies in the $k_x - k_z$ plane. Then, $\mathbf{q}'$ has the co-ordinates $(\sin\theta, 0, \cos\theta)$ and $\hat{\mathbf{k}}$ is $(\sin\alpha\cos\phi, \sin\alpha\sin\phi, \cos\alpha)$. It is straightforward to see that in this co-ordinate frame

$$\cos\gamma = \sin\theta\sin\alpha\cos\phi + \cos\theta\cos\alpha\,.$$

The angular integral is equivalent to integrating over α and ϕ. In order to re-express $P_n(\cos\gamma)$ in terms of these variables, the addition theorem for spherical harmonics is used (see Arfken, 1970, section 12.8),

$$P_n(\cos\gamma) = \frac{4\pi}{2n+1}\sum_{j=-n}^{n}(-1)^j Y_n^j(\alpha,\phi)Y_n^{-j}(\theta,0)\,.$$

The spherical harmonics are given by

$$Y_n^j(\alpha,\phi) = (-1)^j\left\{\frac{2j+1}{4\pi}\frac{(n-j)!}{(n+j)!}\right\}^{1/2} P_n^j(\cos\alpha)e^{ij\phi}\,.$$

Substituting for $P_n(\cos\gamma)$ and using the fact that $P_m(\cos\alpha) = (4\pi)^{1/2}Y_m^0(\alpha,\phi)$ gives an integral over α and ϕ of two spherical harmonics, which by the orthonormality relation gives

$$\int d\Omega Y_m^0(\alpha,\phi)Y_n^j(\alpha,\phi) = \delta_{mn}\delta_{j0}\,.$$

Hence the sums over j and m disappear and rewriting $Y_n^0(\theta,0)$ in terms of $P_n(\cos\theta)$ gives the desired result:

$$\langle \delta(\hat{\mathbf{q}},\mathbf{x},t)\delta(\hat{\mathbf{q}}',\mathbf{x},t)\rangle = \frac{4\pi V}{(2\pi)^3}\int dk\,k^2\sum_n \frac{|\delta_n(k,t)|^2}{2n+1}P_n(\cos\theta)\,. \qquad (2.14)$$

In practice, the monopole and dipole terms are subtracted from the sum in equation 2.14 since the monopole is inherently unobservable (contributing only to a global increase in the background temperature) and the dipole is usually attributed to possible streaming motions and will be dealt with separately in chapter 5. The sum should therefore be taken to be for values of $n \geq 2$. An angular power spectrum corresponding to this correlation function can be defined:

$$P(k,\theta) = \sum_n \frac{|\delta_n(k,t)|^2}{2n+1} P_n(\cos\theta) \,. \tag{2.15}$$

This power spectrum is not a two-dimensional power spectrum on the sky (which will be introduced in chapter 3) but a full three-dimensional quantity reflecting the contribution of any wavenumber to the correlation function on a given angular scale.

2.3.2 Normalisation

So far, only the mechanics of calculating the values of the fluctuations for the various components have been described. In order to compare these calculations with observations, the fluctuations must be normalised in some way. The simplest approach is to match the linear density field for the baryons, δ_m, with some observed property. Since the initial conditions all scale with δ_{mi}, this gives an overall normalisation for all the components.

There are various possible choices for an observable quantity though all have problems. Most of these methods have been used previously. A detailed comparison however, for the same initial set of data, allows the possibility of discriminating between them.

2.3.2.1 The Galaxy-Galaxy Correlation Function

If light traces the mass, then the galaxy-galaxy correlation function, ξ_{gg}, is a reliable measure of clustering in the underlying density field. Therefore, knowing ξ_{gg} at a point at which linear theory applies allows us to normalise the autocorrelation function of the baryonic contents of the universe. The autocorrelation function is defined above (equation 2.10).

Wilson & Silk (1981) modified this method by considering some form of non-linear evolution of the density field before calculating the autocorrelation function. This allowed them to compare to ξ_{gg} at smaller separations where it is better known. In

particular, previous surveys had been consistent with $\xi_{gg}(4.3h^{-1}\ \mathrm{Mpc}) = 1$. Wilson (1983) shows how their non-linear corrections affect the normalisation. Only linear constraints will be considered here.

Two problems occur with this method. The first is non-linearity of the density field where ξ_{gg} is best known. Matching the theory to the observations at points where the density field is even mildly non-linear is prone to error. The other problem is entirely observational. The measured form of the correlation function is generally found to be

$$\xi_{gg}(r) = \left(\frac{r}{r_0}\right)^{-\gamma} .$$

The earliest measurements of the correlation function were derived from the galaxy-galaxy two-point angular correlation function, $w(\theta)$. Limber's equation (see Peebles 1980, section 51-53) which gives $w(\theta)$ as a function of ξ can be inverted to give ξ if $w(\theta)$ is known. Groth & Peebles (1977) found that $r_0 = 4.7h^{-1}$ Mpc and $\gamma = 1.77$ from the Lick survey. For the Center for Astrophysics (CfA) survey, Davis & Peebles (1983) found the slightly different values $r_0 = 5.4h^{-1}$ Mpc and $\gamma = 1.77$.

More recently, redshift surveys have been carried out for complete samples of brighter galaxies. For example, DeLapparent, Geller & Huchra (1988) report one such survey using the CfA. They use a different method from the previous groups. In essence, they calculate the galaxy-galaxy correlation function in redshift space. This will be comparable to the true spatial correlation function where the peculiar velocities of the galaxies are negligible. Their sample of galaxies, complete to a depth of 14.5 m_B (and a sample complete to a depth of 15.5 m_B in a smaller area), gives $\gamma \sim 1.6$ and $r_0 = 7.5h^{-1}$ Mpc .

Another recent survey has also suggested different results. Collins, Heydon-Dumbleton & MacGillivray (1988) find that, for the machine based Edinburgh-Durham Southern Galaxy Catalogue (EDSGC), the break scale (where ξ_{gg} deviates from a power-law) is different from that found by Groth & Peebles. If the two correlation functions scale in a similar way this would indicate that the correlation length of the EDSGC sample is also larger.

Although the earlier results may be correct (since there are uncertainties in the level to which peculiar velocities affect the recent CfA result and the results for the EDSGC are preliminary), this disparity indicates that any normalisation based on ξ_{gg} should be used cautiously. Future surveys based on much larger areas using a sparse sampling technique (Kaiser 1986) should clarify these matters.

2.3.2.2 $J_3(r)$

Since the observed $J_3(r)$ is the volume integral of ξ_{gg}, it is much less dependent on the non-linear fluctuations at small scales as long as r is chosen to be large enough. This statistic has gained popularity in recent years, and has to a large extent superceded the correlation function. It is best to consider the normalisation at a point where ξ_{gg} is still well enough known that J_3 is accurately determined. Davis & Peebles (1983) tabulate J_3 for various values of r as determined from the 14.5 m_B CfA survey. The value that will be used here is

$$J_3(10h^{-1}\ \mathrm{Mpc}) = 277h^{-3}\mathrm{Mpc}^3\ .$$

Many of the criticisms of the galaxy-galaxy correlation function can also be applied here since the two statistics rely on the same data sets. Since there are varying estimates of ξ_{gg}, these will be reflected to some extent in the observed values for J_3. DeLapparent, Geller & Huchra (1988) report that values of J_3 derived from their velocity space correlation function can be substantially larger than those given by Davis & Peebles. Again, it is not clear to what extent peculiar velocities contaminate their results on scales less than $5h^{-1}$ Mpc.

2.3.2.3 *Number Counts of Galaxies*

The variance, $\delta M/M$, can be related observationally to number counts of bright galaxies. This is found to be equal to unity for a sphere of radius $8h^{-1}$ Mpc from the CfA survey (Davis & Peebles 1983). Since this method is related to the correlation function most of the comments made previously still apply.

2.3.2.4 *The Collapse Epoch*

At some point in the past, the *rms* value of the density field when smoothed on some scale must have been unity. At this time, the linear fluctuations would have started to collapse and go non-linear. There are some observational indications that the number density of sources falls off at high redshifts. Dunlop (1987) found that powerful radio sources were less common at redshifts above 3 and Mitchell (1989) and Warren, Hewett & Osmer (1989) both find that the number of high redshift quasars found by multi-colour selection techniques is less than expected.

However, these observations do not strongly constrain the collapse epoch. In a hierarchical universe (such as a CDM dominated one), an early generation of stars would form at quite high redshifts and larger more powerful objects such as quasars would not form until much later. It does provide a *lower* limit to the collapse epoch of galaxies though, since the existence of powerful sources at higher redshifts suggests that late collapse epochs (say at redshift unity) could be wrong. The value of this technique is to invert the problem and ask what the observed upper limits on the temperature anisotropies predict for the latest possible collapse epoch.

2.3.2.5 Biasing

All of the foregoing discussion has been based on the assumption that light traces mass: *i.e.* the concept that the tracer particles in the underlying density field can be compared directly to the observed galaxy distribution. However, since the observational constraints on the density parameter, Ω, imply that it is about 0.2, if the universe were actually flat then the mass in the universe must be less clustered than the light. This leads naturally to the concept of biased galaxy formation, since, whatever the biasing mechanism, tracers of the mass and the light in the universe are no longer equivalent.

In biased models of galaxy formation the concepts of normalisation of the density field must be altered (see, for example Kaiser, 1988c). In the simplest picture of biasing, in the linear regime, $\delta_{gal} = b\delta_m$. The predicted correlation function for galaxies is simply multiplied by some biasing factor b^2. Although this is not strictly correct for more complex models of biasing (compare this with the predicted correlation function for peaks, in one dimension, at small separations, equation C.23, as opposed to the large separation limit, equation C.30), for use with the J_3 method of normalisation it is adequate.

Various values for the bias, b, can be obtained. By comparing N-body simulations of galaxy evolution for an $\Omega = 1$ universe against the observed values, b can be obtained simply by requiring the simulations to have the same correlation length as is actually seen. Also, number counts of the 'galaxies' in such simulations can be compared with the observational measures and then the bias is just the number required to give $(\delta N/N)/(\delta M/M)$ correctly. Both these methods have been applied in the past to CDM models. Values for the bias are usually about $b \sim 2$.

More directly, the cosmic virial theorem (Peebles, 1980) gives a direct measure of

Ω_0. To reconcile this value with a flat universe it is necessary to invoke a bias factor of about 2. This applies whatever type of matter dominates the universe. It is for this reason that biasing should not be regarded as unnatural in purely baryonic models. The desire to have $\Omega_0 = 1$ forces this choice. Later in this chapter biasing will be considered and the value of $b \simeq 2$ derived from observations will be used as a reasonable test.

2.3.3 Modelling the Observations

Observations of CBR anisotropies are made with telescopes which have finite beam sizes. The standard assumption is that the telescope's beam profile can be accurately approximated by a Gaussian. Structure on scales smaller than the beam size will then be smoothed. The observations are also rarely simple measures of the temperature anisotropy. Therefore, the theoretical calculations must also take account of the observational set-up involved. These two factors are discussed in this section.

2.3.3.1 The Effect of Finite Beam Size

The correlation function as described is not what is actually observed. Any real telescope has a finite beam size which must also be taken into account. The beam pattern of the telescope is generally taken to be a Gaussian. Although this need not be strictly true, for most cases it is a reasonable assumption. The beam is characterised by one parameter, σ, which can be related to the observational FWHM since for a Gaussian

$$\sigma = \frac{\mathrm{FWHM}}{\sqrt{8 \ln 2}} .$$

The response of the telescope is then given by

$$f\left(\left|\mathbf{q} - \mathbf{q}'\right|\right) = \frac{1}{2\pi\sigma^2} e^{-|\mathbf{q}-\mathbf{q}'|^2/2\sigma^2} . \tag{2.16a}$$

The effect of this beam smearing on the radiation is then

$$\delta(\hat{\mathbf{q}}, \mathbf{x}, t; \sigma) = \int d\Omega_{\mathbf{q}'} f\left(\left|\mathbf{q} - \mathbf{q}'\right|\right) \delta(\hat{\mathbf{q}}', \mathbf{x}, t) . \tag{2.16b}$$

Substituting this formula back into equation 2.13 and following the rest of the procedure for calculating the angular correlation function leads to a double convolution of the correlation function,

$$C\left(|\mathbf{q}_1 - \mathbf{q}_2|; \sigma\right) = \int d\Omega_{\mathbf{q}_1'} d\Omega_{\mathbf{q}_2'} f\left(\left|\mathbf{q}_1 - \mathbf{q}_1'\right|\right) f\left(\left|\mathbf{q}_2 - \mathbf{q}_2'\right|\right) C\left(\left|\mathbf{q}_1' - \mathbf{q}_2'\right|; 0\right) . \tag{2.16c}$$

There are two approaches to this problem. One is to assume that only small angles will be considered. In this case points near an arbitrarily chosen pole on the unit sphere will appear like a flat plane. In this case, if θ is the angle between $\mathbf{q}$ and $\mathbf{q}'$, $\left|\mathbf{q}-\mathbf{q}'\right|^2 = \theta^2$. Another approach is to consider a co-ordinate transformation (see also Bond & Efstathiou 1987). The elements of solid angle $d\Omega$ are defined by $d\Omega = sin\theta\, d\theta d\phi$. Suppose a new variable, ω, is defined such that $\omega = 2\sin(\theta/2)$. Then $d\Omega = \omega d\omega d\phi$. The unit sphere defined by θ and ϕ have now been mapped onto a polar co-ordinate system in which ω is bound by the limits $\omega \in [0,2]$. The rest of this derivation is the same whichever of the two methods is used. The notation throughout will follow that of Bond & Efstathiou. A Fourier transform of $C(\omega)$ can be defined such that

$$C(\omega) = \frac{1}{(2\pi)^2}\int P_\kappa e^{i\kappa.\omega} d^2\kappa\,.$$

If convolution is denoted by $*$ and a Fourier transform by $\tilde{f}$ or $\mathcal{F}$, then the integral, equation 2.16c, can be thought of symbolically as

$$C * f_1 * f_2 = (C * f_1) * f_2 = \mathcal{F}^{-1}\left(\tilde{C}\tilde{f}_1\right) * f_2 = \mathcal{F}^{-1}\left(\mathcal{F}\mathcal{F}^{-1}\left(\tilde{C}\tilde{f}_1\right)\tilde{f}_2\right)$$

$$= \mathcal{F}^{-1}\left(\tilde{C}\tilde{f}_1\tilde{f}_2\right).$$

The smoothing function f can be rewritten as

$$f = \frac{1}{2\pi\sigma^2} e^{-\omega^2/2\sigma^2}\,.$$

since $\omega^2 = 2(1-\cos\theta)$. The Fourier transform of this is simply

$$\tilde{f} = e^{-\kappa^2\sigma^2/2}\,.$$

Hence, the convolved correlation function is

$$C(\omega;\sigma) = \frac{1}{(2\pi)^2}\int\int C(s) e^{-i\kappa.\mathbf{s}} e^{-\kappa^2\sigma^2} e^{i\kappa.\omega} d^2\kappa d^2 s\,.$$

The integral over κ is then straightforward and gives

$$C(\omega) = \frac{1}{4\pi^2\sigma^2}\int C(s) e^{-(\omega-\mathbf{s})^2/4\sigma^2} d^2 s\,.$$

If the axes are chosen such that $\omega.\mathbf{s} = \omega s\cos\phi$ then the integral over ϕ gives rise to

$$\int_0^{2\pi} d\phi\, e^{\omega s\cos\phi/2\sigma^2} = 2\pi \mathrm{I}_0\left(\frac{\omega s}{2\sigma^2}\right)\,.$$

The I_0 is a modified Bessel function. The final result is then

$$C(\omega;\sigma) = \frac{1}{2\sigma^2}\int_0^\infty ds C(s)\theta(2-s)e^{-(\omega^2+s^2)/4\sigma^2} \mathrm{I}_0\left(\frac{\omega s}{2\sigma^2}\right) . \tag{2.17}$$

The limits on this integral are strictly $(0,\infty)$ but since C is only defined on the region $[0,2]$, the theta function, $\theta(2-s)$, has been included for clarity. In the alternative small angle approximation, $\omega \to \theta$, and s will similarly represent a true angle. The limits can also be taken as $(0,\infty)$ since the effect of the Gaussian means the integrand is negligible when θ or s are larger than ϕ. It is not clear that the more formally accurate method of Bond & Efstathiou reveals any more than the small angle approximation since the distortion near $\omega = 2$ is large. Since the mapping is not conformal, the correlation function in the transformed space will not bear much resemblance to the correlation function in real space. Only the case $\omega \ll 2$ will be used in this chapter.

2.3.3.2 The Observational Arrangement

The simplest observations use a beam-switching approach. All of Uson & Wilkinson (1985), Readhead *et al.* (1988a) and Melchiorri *et al.* (1981) use variations on this method. The Davies *et al.* (1987) experiment will not be modelled here. Their result is roughly equivalent to the Melchiorri *et al.* one in any case. In a three beam experiment as used by Uson & Wilkinson, the telescope is moved from the target field to two reference fields an angle θ away on either side, so that half the time is spent on the target field and a quarter on each of the reference fields.

Their measured *rms* temperature fluctuation is therefore given by,

$$\delta T_{rms} = \left\langle \left| T_1 - \frac{1}{2}(T_2+T_3)\right|^2 \right\rangle^{1/2} . \tag{2.18a}$$

In terms of the angular correlation function this is:

$$\left(\frac{\Delta T}{T}\right)^2 = 2(C(0,\sigma) - C(\theta,\sigma)) - \frac{1}{2}(C(0,\sigma) - C(2\theta,\sigma)) , \tag{2.18b}$$

where the correlation function has been convolved with a Gaussian beam as described above. The Melchiorri *et al.* experiment used an even simpler two-beam method for which

$$\delta T_{rms} = \left\langle |T_1 - T_2|^2 \right\rangle^{1/2} . \tag{2.19a}$$

Hence,

$$\left(\frac{\Delta T}{T}\right)^2 = 2(C(0,\sigma) - C(\theta,\sigma)) . \tag{2.19b}$$

For the Caltech experiment, a three-beam approach was used, but the reference fields were averaged over arcs of extent $2\psi_R = 30°$ on either side of the target field. This adds a correction term to the form already given. Bond (1988b) gives this correction term as,

$$-\int_0^{\psi_R} \frac{d\psi}{\psi_R}\left(1-\frac{\psi}{\psi_R}\right)\{C(0,\sigma)-C(2\theta\sin\psi,\sigma)+C(2\theta,\sigma)-C(2\theta\cos\psi,\sigma)\}\ .$$

2.4 Results

2.4.1 Introduction

All the techniques required for calculating accurate temperature anisotropies have now been described. In this section, the results generated when these methods were applied to two particular models will be discussed. Both of these models had $\Omega = 1$ and $h = 0.5$, but varied in their initial conditions. The easier of the two to calculate (and in this case also the more complete) was the adiabatic fluctuations. The isocurvature fluctuations as presented are not fully completed but are accurate for the restricted cases discussed below.

The results for these two separate modes are described below. A discussion of some of the features of both these models will be deferred until chapter 3. The basic data for both models consists of values for the various perturbed quantities calculated at discrete points in k-space.

2.4.2 Power Spectra

2.4.2.1 Adiabatic Fluctuations

The power spectrum for the matter is defined by 357 points in k-space. 289 of these points are calculated using the techniques described in the previous section. The other 68 short wavelength modes are calculated in an approximate manner since only the values of δ_m, v and $\dot{h}$ are required. The first order equations are solved as before but the set of full equations are truncated at the same Legendre component as given by the maximum from the first order routine rather than the limit outlined in section 2.2.3.2. This decreases the cpu time required markedly (since time is roughly proportional to the number of equations) without significantly affecting the results for the three required components. The values for the radiation components do diverge radically from the correct solutions but by the time this occurs they are no longer dynamically important.

Figure 2.1(a) shows this power spectrum for the canonical scale invariant model with $n = 1$. The normalisation is arbitrary. The minimum wavelength considered using the full set was 5 Mpc. The minimum using the 'fudged' solutions was 1 Mpc. This is far enough into the damped portion of the power spectrum as to leave negligible power at shorter wavelengths. The maximum was 100000 Mpc. Again this left negligible power on larger scales. The reasoning behind this choice of maximum wavelength is not in fact related to the sampling of the matter power spectrum, which can be seen to be negligible for $n = 1$ when $\lambda = 3000$ Mpc, but to correctly model the large angle distribution of the radiation to be described later. The points are not spread uniformly in k-space since this would require far too many to give an adequate sampling near the Silk damping scale. Instead the range was split into bins and the points arranged uniformly within the bins. The resulting power spectrum is well enough sampled to show all the major oscillatory features even at the Silk scale.

The power spectrum shown is in reasonable agreement with the results of Wilson & Silk (1981). Perfect agreement is not expected since their power spectrum was derived without the presence of massless neutrinos, so the matter-radiation equality time was at higher redshifts. Since the amplitude of the bump in the power spectrum at 200 Mpc is a reflection of the ratio a_{rec}/a_{eq}, the large bump in the Wilson & Silk power spectrum is consistent with the smaller feature found here. The results are also reasonably consistent with those of Gouda, Sasaki & Suto (1987) (the power spectrum for an $\Omega = 0.2$ model is shown in figure 3.1, similar to their figure 1), despite their claims that using non gauge-invariant methods leads to errors on large scales.

The angular power spectrum for the radiation is shown in figure 2.2. Again, the normalisation is arbitrary, but is internally consistent. The radiation fluctuations are far more attenuated than the matter on small scales. Because of this the minimum wavelength for which the ACF was needed was about 20 Mpc. To ensure that all the power in the radiation was well sampled however, the minimum for full sampling (calculating the full radiation fluctuations for every point where the matter is sampled) was taken as 13 Mpc and three points near 10 Mpc were included as a further check. There are 208 points in the complete angular power spectrum for the radiation. The excluded points all lie at wavelengths below 13 Mpc. The points sampled are naturally the same as those for the matter. Again the results are in reasonable agreement with what might be expected from the Wilson & Silk model if they had included the massless

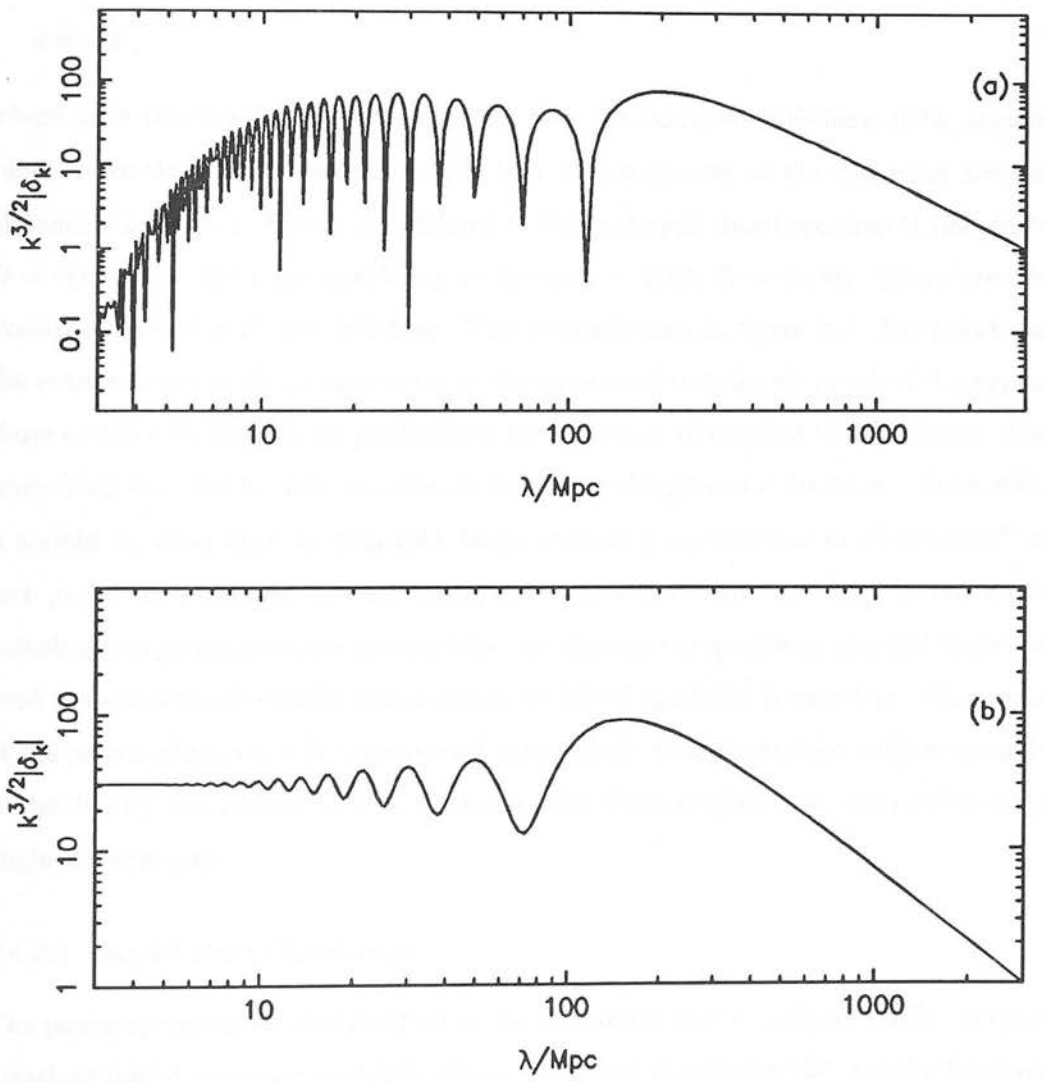

Figure 2.1: Power spectra for a baryonic, $\Omega = 1$, $h = 0.5$ model with (a) adiabatic and (b) isocurvature initial conditions. $n = 1$ for (a) and $n = -3$ for (b). The normalisation is arbitrary.

neutrinos.

Increasing the value of θ in the angular power spectrum (equation 2.15) is equivalent to smoothing the structure on wavelengths which subtend an angle smaller than θ subtends on the surface of last scattering. The comoving distance subtended by an angle θ is given simply by

$$d = D\theta \ ,$$

where D is the angular diameter distance (see, for example, Weinberg 1972, section 14.4). Note that this distance is defined in a similar manner to the comoving horizon distance when $\Omega = 1$. Hence, D is related to the conformal time (equation B.12a) since $D = c(\tau_0 - \tau_1)$. For a last scattering surface at $z \sim 1000$, $D \sim 2c/H_0$. Therefore, for example, when $\theta = 1^\circ$, $d \sim 200$ Mpc. This is clearly seen in figure 2.2. The points on the extreme right of all the figures are at the same amplitude for all values of θ, whereas those on the extreme left are gradually more and more attenuated as θ increases. The smoothing can also be seen to move to larger wavelengths as θ increases. From this, it should be clear that, in principle, beam switching experiments at angles of 5° in fact probe the structure on very large, and even super-horizon, scales. Small angle anisotropy experiments are a probe of the complete power spectrum, and will therefore tend to sample much smaller scales unless the initial spectrum is very flat. Since most of the power when $n = 1$ is concentrated into a single peak, contained within an angle subtended by the horizon at last scattering, this feature is not well sampled in large angle experiments.

2.4.2.2 Isocurvature Fluctuations

The power spectrum for the isocurvature fluctuations is shown in figure 2.1(b). A scale invariant initial spectrum is shown: this is equivalent to plotting the transfer function against k. The maximum wavelength considered was about 10000 Mpc. The minimum considered for the matter component was about 2 Mpc. Below this wavelength the power spectrum tends asymptotically to a constant value until the effect of matter pressure on small scales leads to a damping similar to Silk damping in the adiabatic case. The upper wavelength was chosen of necessity, since an accurate solution to the evolution equations 2.7 was not possible. This may be partly due to the use of gauge-dependent variables: Bond (1988a) asserts that use of gauge-invariant variables on

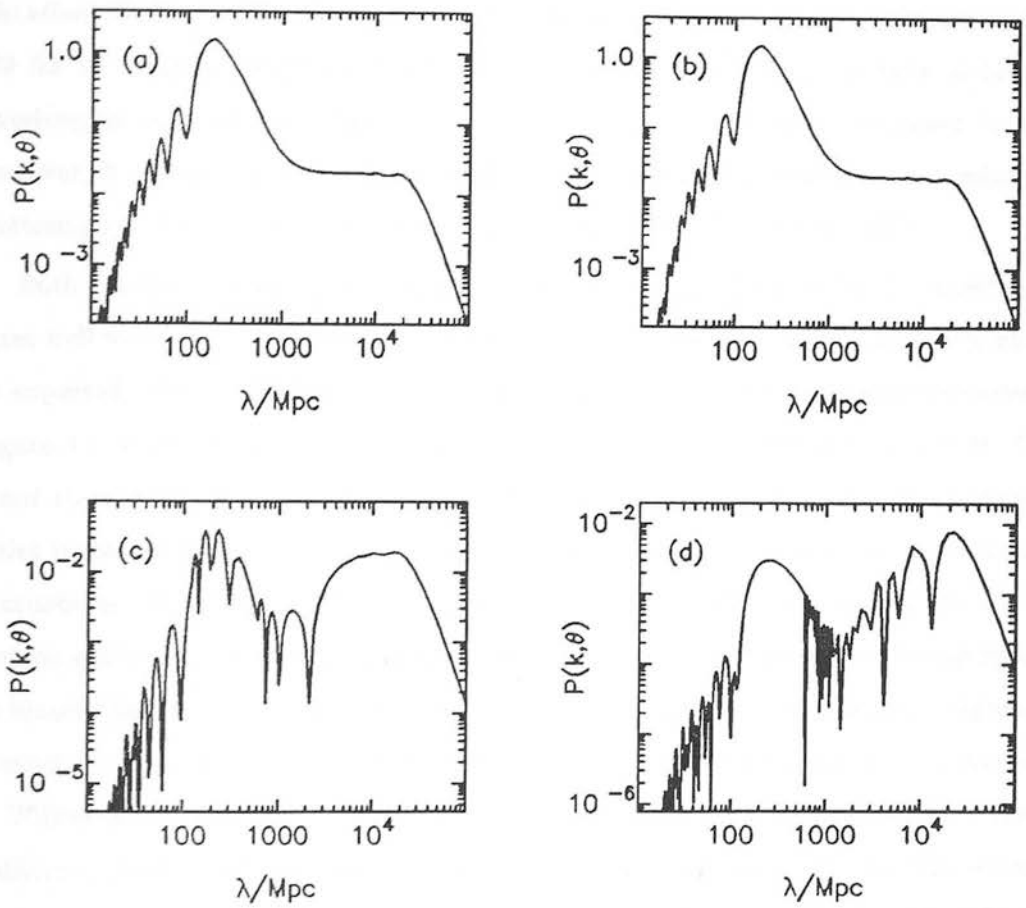

Figure 2.2: Angular power spectra for the adiabatic model. Again, $n = 1$. The angular power spectrum is defined by equation 2.15. The figures represent (a) $\theta = 0$, (b) $\theta = 1.5'$, (c) $\theta = 6^\circ$ and (d) $\theta = 30^\circ$. The normalisation is arbitrary.

super-horizon scales improves the accuracy. Despite this, Efstathiou & Bond (1987) do not consider wavelengths on any larger scales than those considered here. Their figure 1 is directly comparable to figures 2.1(b) and 2.3 here. The angular power spectrum is only modelled down to $\lambda \sim 25$ Mpc. Again, this is similar to the limits shown in Efstathiou & Bond. There are 198 points defining the matter power spectrum and 123 for the angular power spectrum. Because of the lack of accurate data at long wavelengths only the restricted cases of $n = 0$ and $n = -1$ will be discussed here. However, it is these spectra that are required to be compatible with observed galaxy clustering (see the discussion in Efstathiou & Bond, 1987, and Peebles, 1987).

Both the matter power spectrum and the angular power spectrum for the radiation agree well with those of Efstathiou & Bond (1987). It is also comparable to what might be expected from the Gouda, Sasaki & Suto (1987) work on lower density universes (figure 3.1 shows the matter fluctuations for an isocurvature model with $\Omega = 0.2$). It is not clear however if their model shows less power than might be expected on large scales in the radiation. An interesting comparison can be made with the isothermal fluctuations considered by Wilson & Silk (1981). The results seem similar on sub-horizon scales but there would appear (and their figure 2 is somewhat confusing with its bizarre choice of units for k) to be extra power on scales above the horizon. Again, it must be remembered that the lack of massless neutrinos makes the $\Omega = 1$ model of Wilson & Silk appear as if $h > 0.5$. Direct comparison is therefore tricky. The isothermal model will not perfectly match the isocurvature model in any case since at least some adiabatic component will be mixed in. The slight fixing of the initial conditions evident in the appendix of Wilson & Silk would appear to be an attempt to single out the isocurvature component, but it is clear that since their results are different that it was not successful.

2.4.3 Angular Correlation Functions

2.4.3.1 The Wilson & Silk Approximation

The exact angular correlation function for the radiation is calculated using equation 2.14. It is also possible to construct an approximate correlation function instead. Indeed, this is what Wilson & Silk used in practice, since they did not follow the evolution of the radiation moments until the present epoch. It is useful to consider how this ap-

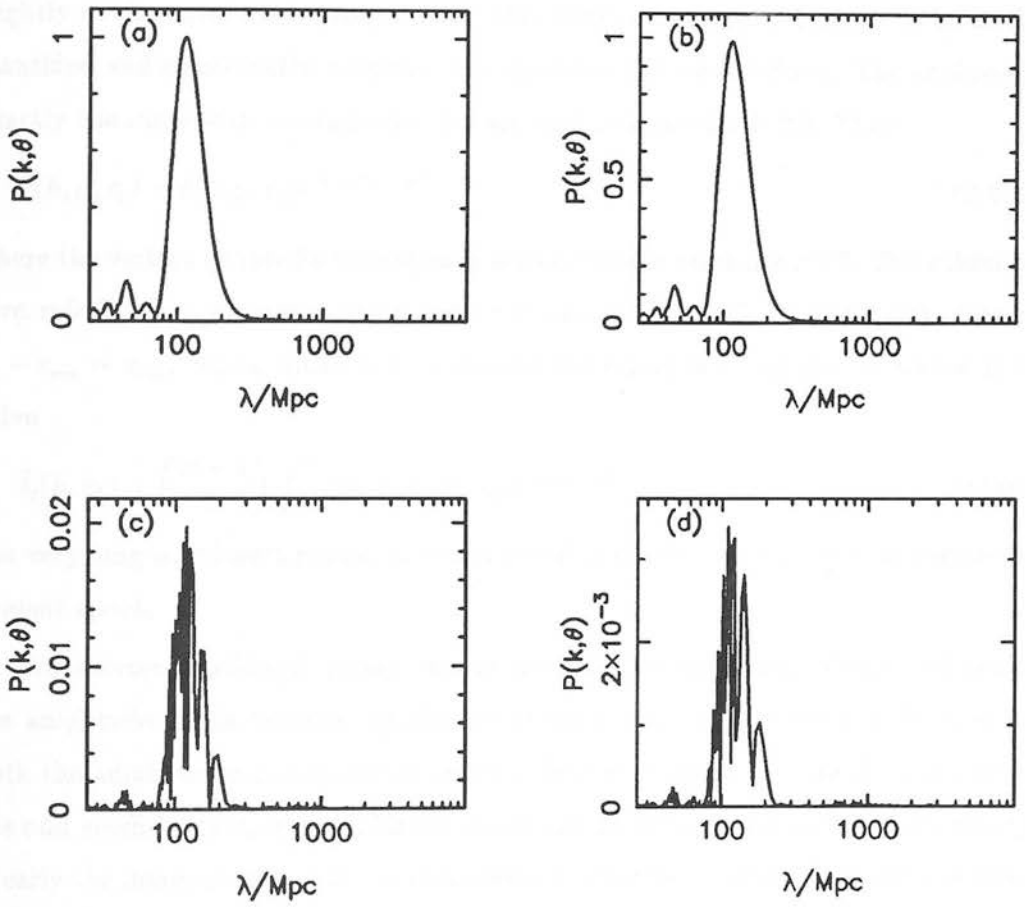

Figure 2.3: Angular power spectra for the isocurvature model. The spectrum shown is $n = 0$. The angular power spectrum is defined by equation 2.15. The figures represent (a) $\theta = 0$, (b) $\theta = 1.5'$, (c) $\theta = 6°$ and (d) $\theta = 30°$. The normalisation is arbitrary.

proximate correlation function fares compared to the more formally accurate version. Bond & Efstathiou (1987) show how the Wilson & Silk approximation can be derived. In the matter dominated era, after recombination, the radiation evolves according to equation B.43b. It is convenient here to change the form of the solution to this equation slightly so that conformal time is used. This allows certain scale lengths to be easily identified and considerably simplifies the appearance of what follows. The analysis is exactly the same with the variables that are used in appendix B.2.3. Then,

$$\tilde{\delta}(k,\mu,\tau_0) = \tilde{\delta}(k,\mu,\tau_1)e^{ikc\mu(\tau_1-\tau_0)} \; . \tag{2.20a}$$

where the various quantities have already been defined in section 2.2.2.5. The subscript zero refers to the present, and the subscript one to a redshift of about 300. Hence, $\tau_1 - \tau_{rec} \sim \tau_{rec}$. Since, equation 2.14 requires the values of δ_l, all that is needed is to solve

$$\tilde{\delta}_l(k,\tau_0) = \left(\frac{2l+1}{2}\right)\int_{-1}^{1} \tilde{\delta}(k,\mu,\tau_1)P_l(\mu)e^{ikc\mu(\tau_1-\tau_0)}d\mu \; . \tag{2.20b}$$

For very long wavelength modes, it is best to follow the radiation numerically until the present epoch.

For shorter wavelength modes this integral can be simplified. Figure 2.4 shows the amplitude of the Legendre coefficients at the present time when $\lambda = 25$ Mpc for both the adiabatic and isocurvature models. Only even values of l are shown in both: the odd coefficients show a similar behaviour and have only been excluded for clarity. Clearly the dominant terms in the expansion are all at large values of l, and it is these components that must be calculated using any approximate method. For adiabatic models, the function $\tilde{\delta}(k,\tau_1,\mu)$ is a single peaked function of μ, very similar to the function shown in figure 2.2. Unfortunately, a scale invariant isocurvature model would have power over a much larger range. For the restricted cases considered here for isocurvature initial conditions ($n = 0$ and $n = -1$), the single peaked behaviour is still evident (see figure 2.3). The width of $\tilde{\delta}(k,\tau_1,\mu)$ for any value of k is given by the angle subtended by that wavelength at last scattering. The comoving distance to last scattering from a point at a redshift corresponding to τ_1 is simply $c(\tau_1 - \tau_{rec})$. Hence, the angle subtended at last scattering is roughly $1/kc\tau_{rec}$ (see the end of section 2.2.3.2). The function is single peaked and dies off rapidly at angles greater than $1/k_{rec}c\tau_{rec}$. It follows that, for modes with $kc\tau_{rec} > 1$, the width of this function is $1/kc\tau_{rec}$.

If equation 2.18b is recast as

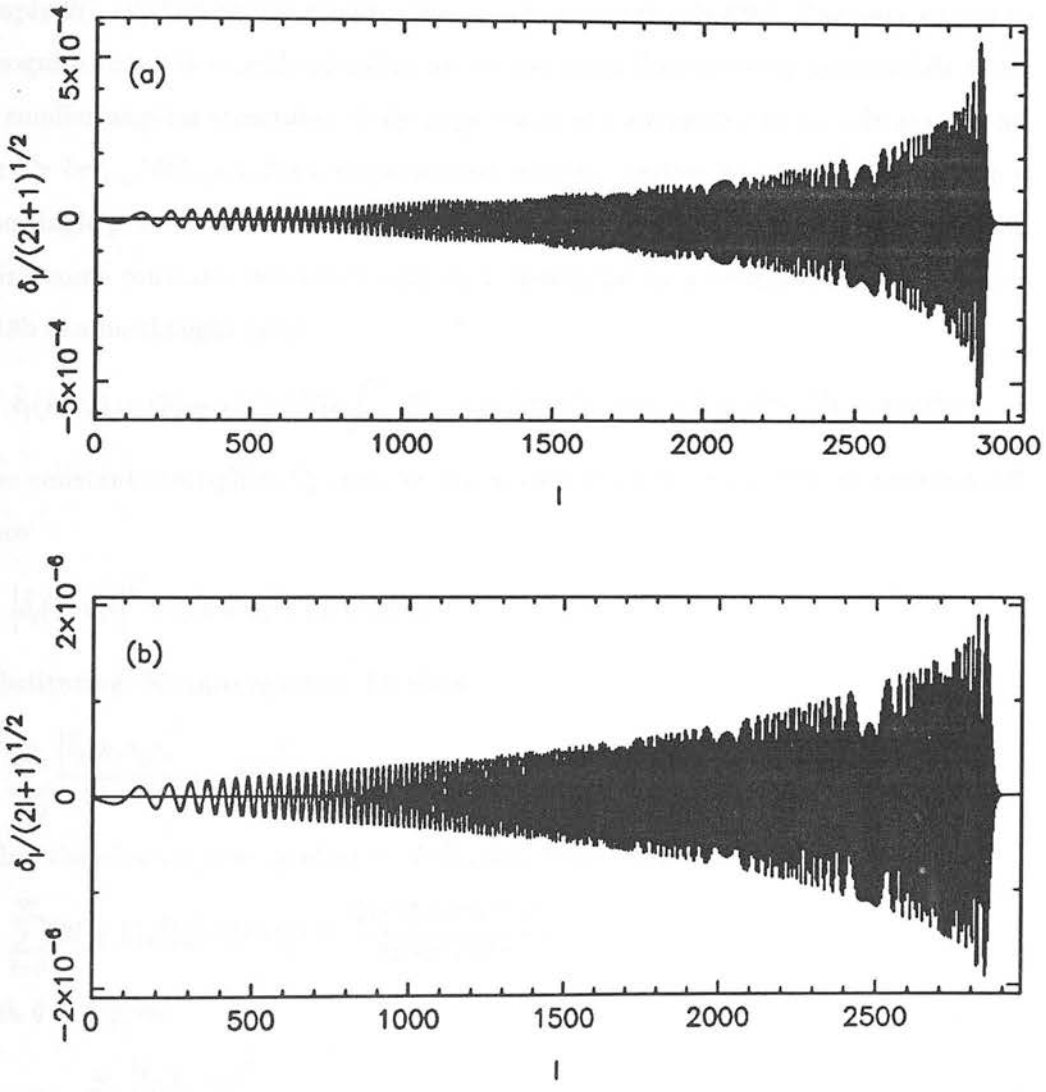

Figure 2.4: The amplitude of the coefficients of the Legendre expansion for the radiation. $\lambda \sim 25$ Mpc for both figures. (a) the adiabatic model: only even values of l are shown. (b) the isocurvature model: only even values of l are shown. The scale has been normalised so that the current value of the matter density, δ_m, is unity.

$$\tilde{\delta}_l(k,\tau_0) = \left(\frac{2l+1}{2}\right)\int_{-\infty}^{\infty} \tilde{\delta}(k,\mu,\tau_1)P_l(\mu)\theta(1-\mu)\theta(1+\mu)e^{-ikc\mu\Delta\tau}d\mu\ ,$$

where the θ functions are step functions and $\Delta\tau = \tau_0 - \tau_1$, it is fairly easy to see that this is the convolution of the Fourier transforms of $\tilde{\delta}(k,\mu,\tau_1)$ and P_l, where the conjugate variables are μ and $kc\Delta\tau$. The Fourier transform of $\theta(1-\mu)\theta(1+\mu)P_l(\mu)$ is simply $2(-i)^l j_l(k\Delta\tau)$ (see the identity preceding equation B.43b). The next step is to recognise that l is roughly speaking an inverse angle (higher order polynomials relate to smaller angular structure). Only large values of l are needed as already stated. So, for $l > kc\tau_{rec}$, $\tilde{\delta}(k,\mu,\tau_1)$ is a single peaked, narrow, function of μ, and its transform is also single peaked and a narrow function of $kc\Delta\tau$. In particular, it can be regarded as being some constant, dependent only on k, multiplied by a δ-function. Then equation 2.18b can be thought of as

$$\tilde{\delta}_l(k,\tau_0) = (2l+1)\,(-i)^l C_k \int_{-\infty}^{\infty} \delta(y - kc\Delta\tau)j_l(y)dy = (2l+1)(-i)^l C_k j_l(kc\Delta\tau)\ .$$

The constant multiplier, C_k, can be determined using the conservation equation 2.9, since

$$\left|\tilde{\delta}_l(k,\tau_0)\right|^2 = (2l+1)^2 C_k^2 j_l^2(kc\Delta\tau)\ .$$

Substituting this into equation 2.9 gives

$$\sum_{l=0}^{\infty} \frac{\left|\tilde{\delta}_l(k,\tau_0)\right|^2}{2l+1} = C_k^2 \sum_{l=0}^{\infty}(2l+1)j_l^2(kc\Delta\tau)\ .$$

Using the identity (see Gradshteyn & Ryzhik, 1980, equations 8.533)

$$\sum_{l=0}^{\infty}(2l+1)j_l^2(y)P_l(cos\theta) = \frac{\sin(2y\sin(\theta/2))}{2y\sin(\theta/2)}\ ,$$

with $\theta = 0$ gives

$$C_k^2 = \sum_{l=0}^{\infty} \frac{\left|\tilde{\delta}_l(k,\tau_0)\right|^2}{2l+1}\ ,$$

or, by the conservation theorem,

$$C_k^2 = \sum_{l=0}^{\infty} \frac{\left|\tilde{\delta}_l(k,\tau_1)\right|^2}{2l+1}\ .$$

Hence,

$$\left|\tilde{\delta}_l(k,\tau_0)\right|^2 = (2l+1)^2 \sum_{n=0}^{\infty} \frac{\left|\tilde{\delta}_n(k,\tau_1)\right|^2}{2n+1} j_l^2(kc\Delta\tau)\ . \qquad (2.21)$$

Finally, equation 2.14 gives

$$C(\theta) = \frac{2\pi^4}{V} \int dk\, k^2 \left[\sum_{n=0}^{\infty} \frac{\left|\tilde{\delta}_n(k,\tau_0)\right|^2}{2n+1} P_n(\cos\theta) - \left|\tilde{\delta}_0(k,\tau_0)\right|^2 - \frac{1}{3}\cos\theta \left|\tilde{\delta}_1(k,\tau_0)\right|^2 \right] .$$

The sum over $\tilde{\delta}_n(k,\tau_0)$ can now be replaced using equation 2.19. Further using the same identity to replace the dependence on $P_n(\cos\theta)$ this results in

$$C(\theta) = \frac{2\pi^4}{V} \int dk\, k^2 \left[\sum_{n=0}^{\infty} \frac{\left|\tilde{\delta}_n(k,\tau_1)\right|^2}{2n+1} j_0\left(2kc\Delta\tau \sin\frac{\theta}{2}\right) \right.$$

$$\left. - \left|\tilde{\delta}_0(k,\tau_0)\right|^2 - \frac{1}{3}\cos\theta \left|\tilde{\delta}_1(k,\tau_0)\right|^2 \right] . \qquad (2.22)$$

Finally, in terms of the variables used in appendix B.2, this equation holds if $kc\Delta\tau$ is replaced by $2A\Delta x$, where $x = \sqrt{1 + a/a_{eq}}$. The other approximate method considered by Bond & Efstathiou (1987), derived from Doroshkevich, Zel'dovich & Sunyaev (1978), will not be used here. Bond & Efstathiou find that it gives poorer results for the CDM model: it is unlikely that it will do any better for a purely baryonic model.

2.4.3.2 Results

Figure 2.5 shows the angular correlation functions for some adiabatic models with different values of n, and the two selected isocurvature models. All these models have been normalised by matching the density field to $J_3(r)$ at $r = 10h^{-1}$ Mpc. The density field was pre-filtered with a Gaussian of radius $0.35h^{-1}$ Mpc, which is roughly the size expected for protogalaxies (see BBKS). This makes little difference to the normalisation for adiabatic models but does offer a means of truncating the isocurvature matter spectrum at short wavelengths without having to insert an *ad hoc* damping on very small scales (even here, the filtering had little effect on the normalisation of the $n = -1$ model). The solid line is the correlation function as calculated using equation 2.14. The dot-dash line is calculated using the approximate correlation function of Wilson & Silk (equation 2.20). Most of the oscillatory behaviour seen in some of the figures is real. There is also, however, some points at which either the exact correlation function or the approximate one are rather badly defined (where this is chosen to mean that the error in calculating the respective integrals is greater than a tenth of the actual answer). Such points in general occur where $C(\theta)$ is near zero. They have all been left in the

final version of $C(\theta)$ since they will not have a major effect on calculating temperature anisotropies. The points which fail this test increase as n increases since the portion of the angular power spectrum that is important shifts to higher k and consequently to the portion of the function that is oscillating strongly. A more accurate correlation function at large angular separations could be achieved by calculating the angular power spectrum at more points in this regime. Since the main comparisons with observations to be made here are all at small separations, the sampling is designed to give $C(\theta)$ very accurately in this regime only. This is purely a computing decision though, and does not reflect further limitations in the calculation of $C(\theta)$ to those already discussed.

The agreement between the exact and approximate methods is remarkably good in the regime of interest. The deviation in the $n = 0$ model is tiny and that in the $n = 1$ case almost as small. However, as n increases the differences do increase. There is a large section beyond $50'$ in the $n = 4$ model that is not well defined in the exact correlation function. This is due to the fact that power on scales near the upper limit in k of the exact angular power spectrum contributes markedly in this model. The approximate method takes account of this since the upper limit in k is set at a wavelength of 5 Mpc for reasons discussed in section 2.4.2.1. Values of n less than zero are not considered since anisotropies in such models are dominated by fluctuations on scales above the present horizon. This issue will be discussed later in terms of the use of gauge dependent variables compared to the gauge independent methods of Gouda, Sasaki & Suto (1987). The deviation of the approximate method from the exact $C(\theta)$ as n increases might be thought to be against the principles outlined above for deriving the Wilson & Silk approximation. There, it was stated that the method was accurate for high values of k. This is still true. The accuracy of the approximation when $n = 1$ or $n = 2$ is due to the fact that the angular power spectrum is a simple, single peaked function of θ. For higher (or lower) n this is no longer true. The angular power spectrum for $n = -1$ has a double humped feature due to the importance of power on super-horizon scales and that for $n = 4$ has similar complicated structure on small scales. It is the single-peaked appearance that is primary in deriving the approximate method above all else.

The approximate method also holds up well when the isocurvature models are considered. In one sense this is not surprising. The chosen values of n both correspond to an angular power spectrum that is sharply peaked as required. However, as was

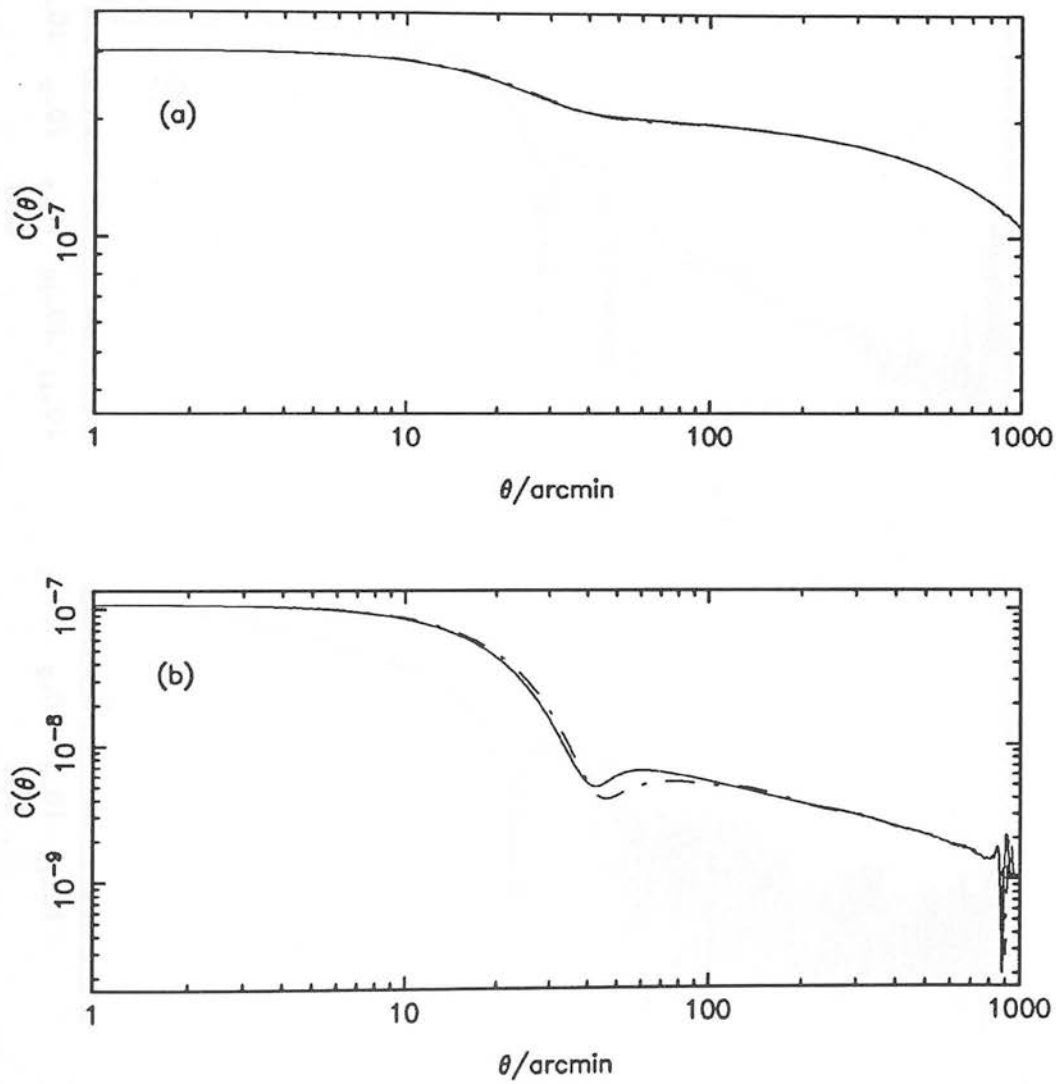

Figure 2.5: Angular correlation functions for adiabatic models. (a) $n = 0$. (b) $n = 1$. (c) $n = 2$. (d) $n = 4$. Isocurvature models: (e) $n = -1$. (f) $n = 0$.

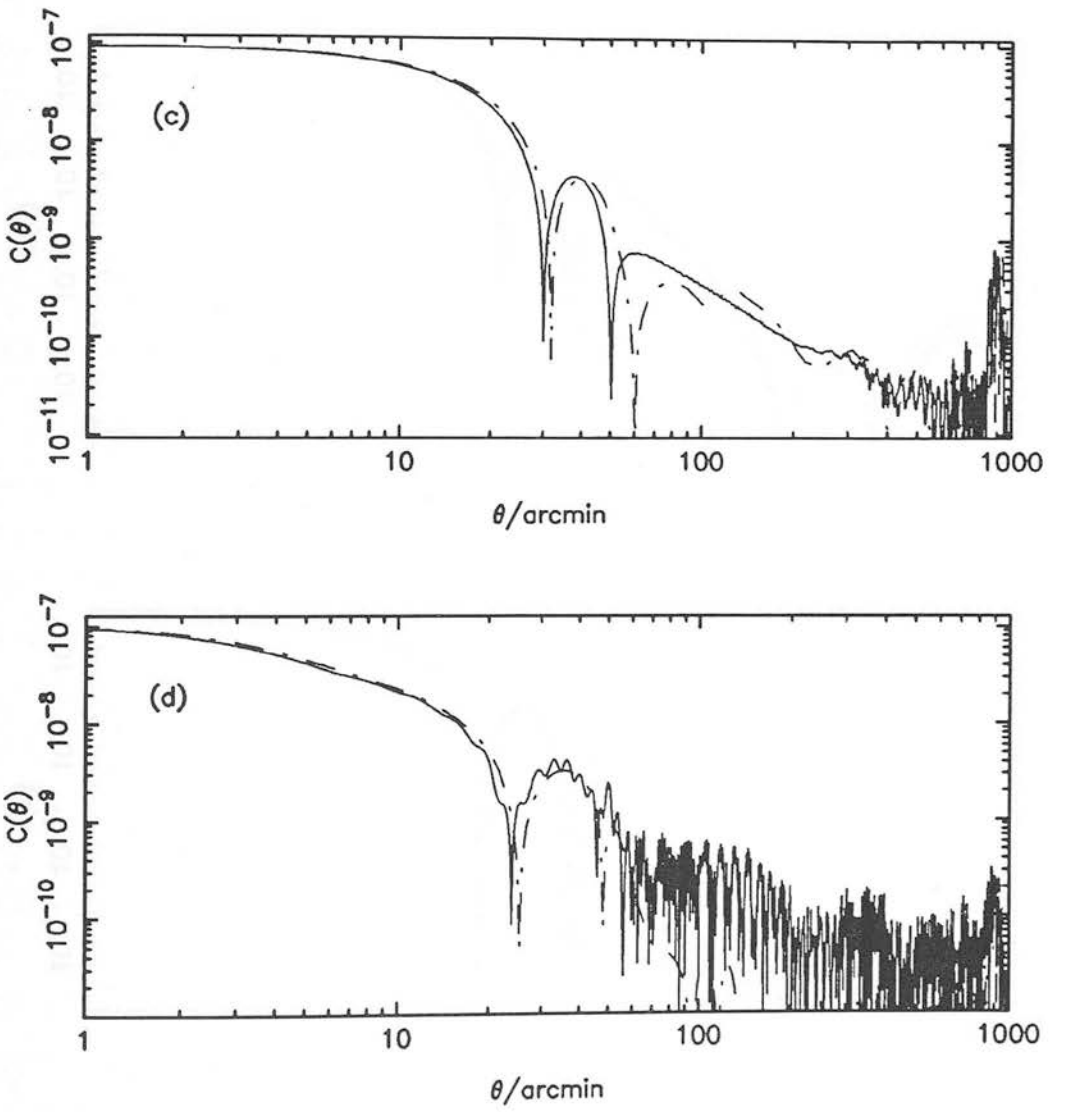

Figure 2.5: (*cont.*)

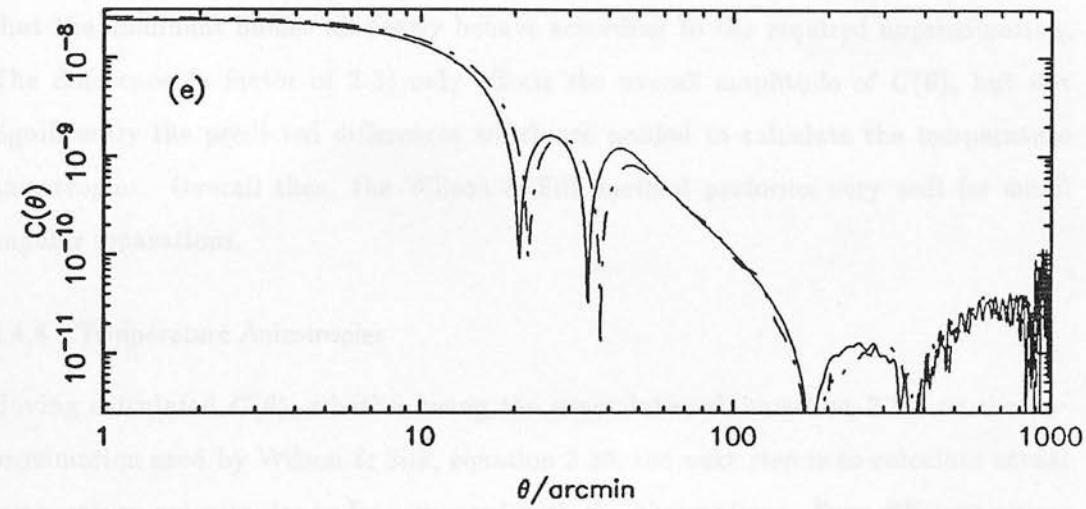

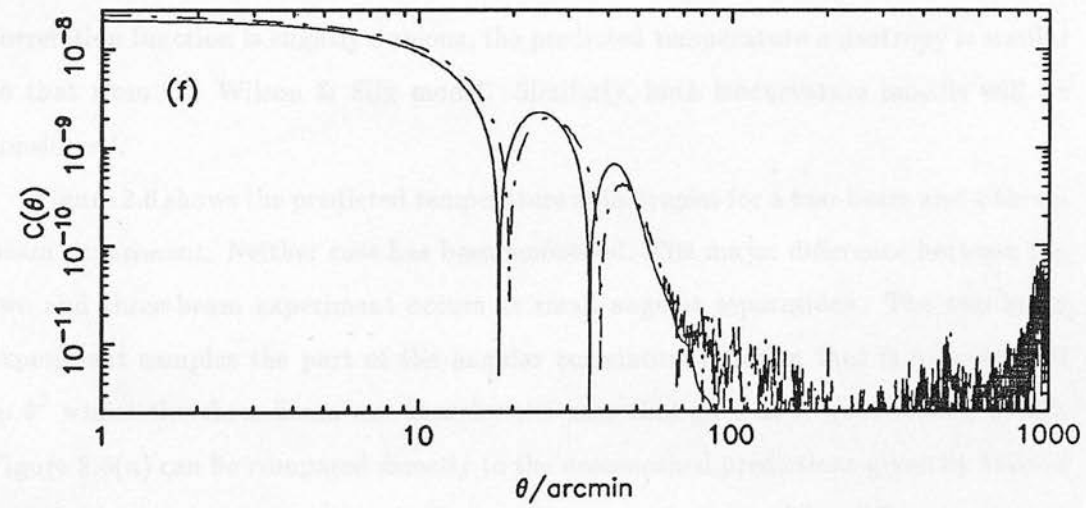

Figure 2.5: (*cont.*)

noted in section 2.2.2.5, the isocurvature model is not well suited to the techniques described there, and hence the Wilson & Silk method should also be flawed. Indeed, if the angular power spectra for the approximate models are compared to the exact versions some differences are seen. The amplitude of the main peak is not as large for $\theta = 0$ as is seen in the exact case. The reason for the accuracy of the approximation is that the dominant modes all nearly behave according to the required approximation. The difference (a factor of 2-3) only affects the overall amplitude of $C(\theta)$, but not significantly the predicted differences which are needed to calculate the temperature anisotropies. Overall then, the Wilson & Silk method performs very well for small angular separations.

2.4.4 Temperature Anisotropies

Having calculated $C(\theta)$, whether using the exact integral, equation 2.14, or the approximation used by Wilson & Silk, equation 2.20, the next step is to calculate actual temperature anisotropies to be compared with the observations. Four different observations will be considered, as discussed in section 2.3.3.2. Although the exact $n = 4$ correlation function is slightly dubious, the predicted temperature anisotropy is similar to that from the Wilson & Silk model. Similarly, both isocurvature models will be considered.

Figure 2.6 shows the predicted temperature anisotropies for a two-beam and a three-beam experiment. Neither case has been smoothed. The major difference between the two and three-beam experiment occurs at small angular separations. The two-beam experiment samples the part of the angular correlation function that is proportional to θ^2 whilst the three-beam one samples the part that goes as θ^4 (see section 3.3.5). Figure 2.6(a) can be compared directly to the unsmoothed predictions given by Wilson & Silk, figure 4, which shows similar two-beam predictions. The difference that is immediately obvious is that the normalisation scheme chosen by Wilson & Silk tends to favour models with high values of n, whereas the more conservative scheme used here shows that the intrinsic anisotropies on small angular scales are least when n is smallest. However, as the angular scale increases, these same models start to have the largest intrinsic fluctuations. This is just a reflection of the lack of power on small scales when $n \lesssim 1$ and the corresponding increase in power on large scales. Models with $n \gtrsim 2$ show the opposite behaviour: the dominant power shifts to small scales so

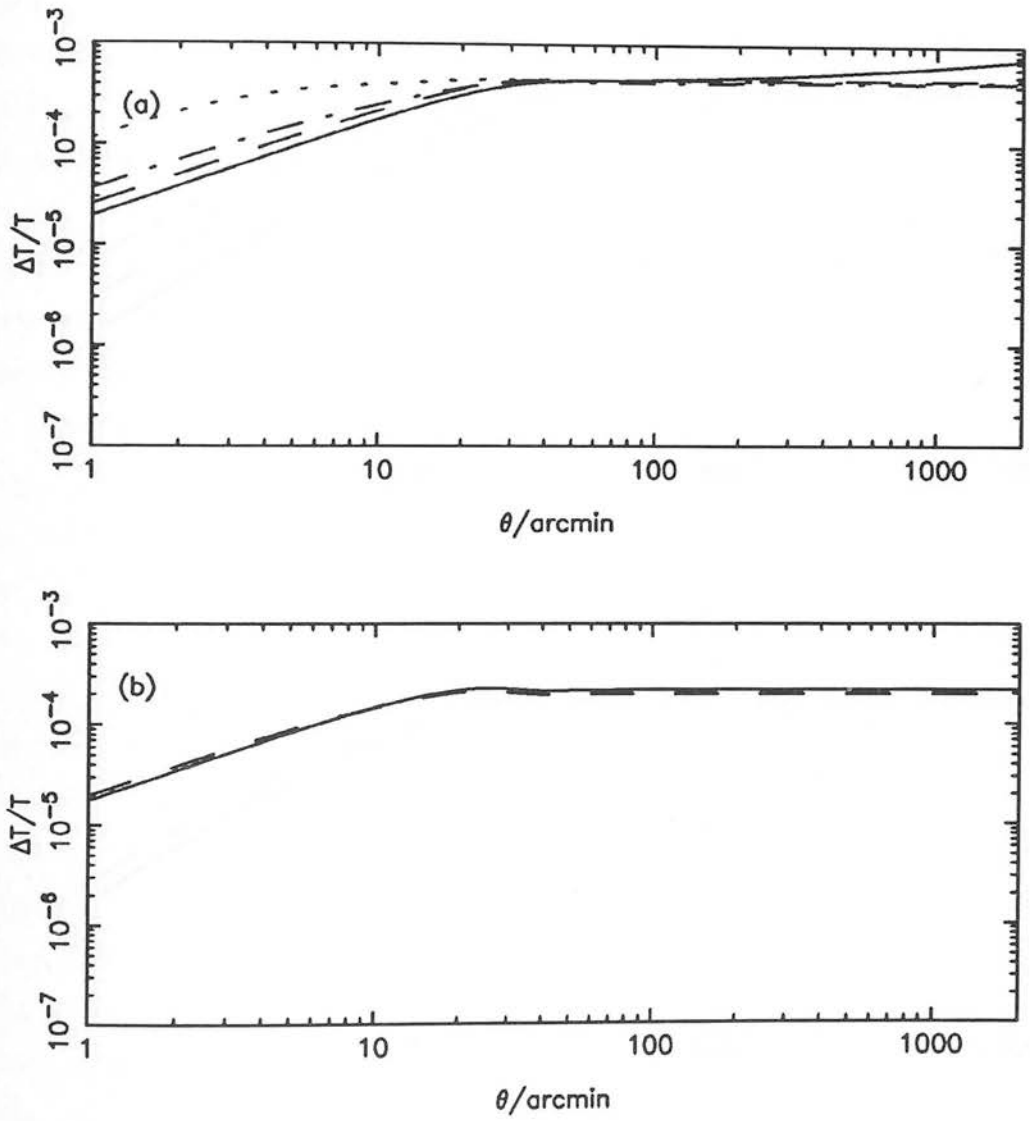

Figure 2.6: Predicted temperature anisotropies for: (a) adiabatic models ($n = 0$ solid line, $n = 1$ dashed line, $n = 2$ dot-dash line and $n = 4$ dotted line), two-beam experiment, (b) isocurvature models ($n = -1$ solid line and $n = 0$ dashed line), two-beam experiment, (c) adiabatic models, three-beam experiment and (d) isocurvature models, three-beam experiment. No smoothing has been applied ($\sigma = 0$).

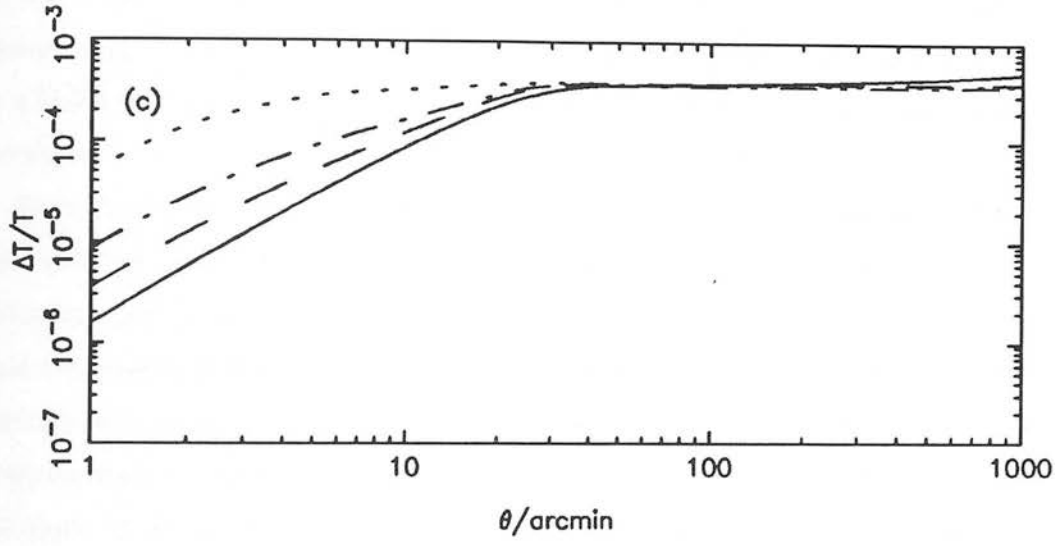

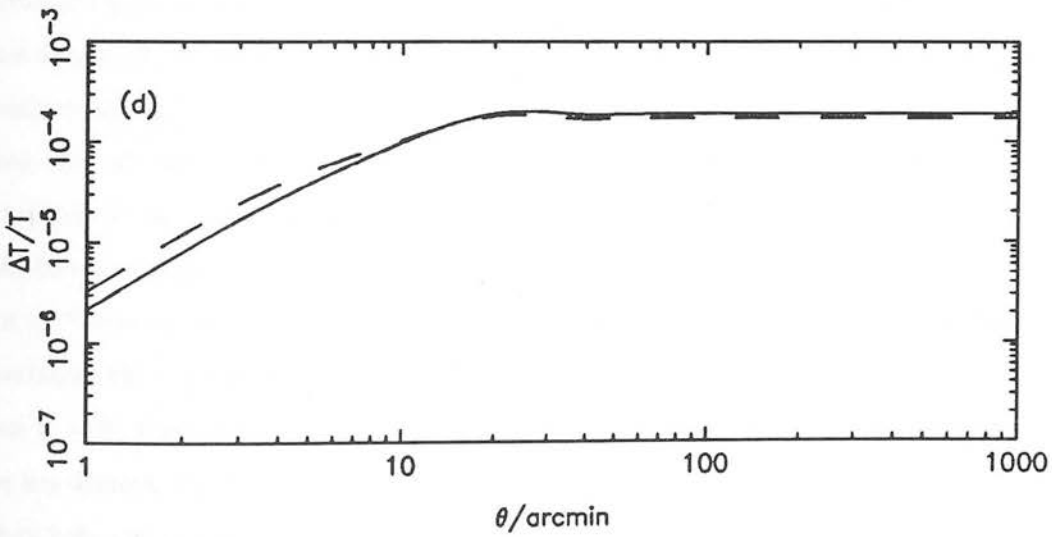

Figure 2.6: (*cont.*)

large intrinsic fluctuations in the CBR will also be expected there in these models. The normalisation apart, the general features of the adiabatic anisotropies here and those shown in Wilson & Silk are very similar.

The next three figures all relate to the observations discussed in section 2.3.3. Figure 2.7 shows the predicted temperature anisotropies for a Uson & Wilkinson type experiment, figure 2.8 that for a Readhead *et al.* type experiment and figure 2.9 that for a Melchiorri *et al.* type experiment. The upper limits found by all these groups are also shown.

From these results, it can be seen quite clearly that the most stringent constraint is provided by the Readhead *et al.* result. This excludes *all* flat baryonic models with a standard recombination history. However, if this observation were laid aside, the other two observations do not provide nearly as powerful constraints. This might seem arbitrary, but it was initially believed that the Uson & Wilkinson result excluded all adiabatic baryonic models. Instead, it only excludes adiabatic models with $n > 1$. The Melchiorri *et al.* result excludes all adiabatic models with $n < 2$. Clearly, since no adiabatic model satisfies even any two of the observations they can be ruled out with some degree of confidence. If the Readhead *et al.* result were wrong, then isocurvature models could still be allowed by the other two results. These predictions are of course based only on one particular form of normalisation. In terms of previous work, only Efstathiou & Bond use the same method. Their results are in excellent agreement with those obtained here. For the Melchiorri *et al.* experiment they predicted $\Delta T/T = 1.4\times10^{-5}$ when $n = -1$ and $\Delta T/T = 0.7\times10^{-5}$ when $n = 0$. For the Uson & Wilkinson experiment their values were $\Delta T/T = 2.8\times10^{-5}$ when $n = -1$ and $\Delta T/T = 3.6\times10^{-5}$ when $n = 0$. From figure 2.7 and figure 2.9, it can be seen that the values predicted here are almost identical. Other types of normalisation will be considered next to see if they help salvage purely baryonic models.

2.4.5 Normalisation

All the models shown have been normalised by using the value of $J_3(10h^{-1}\ Mpc)$ taken from Davis & Peebles (1983). This is of course not the only possible choice as was noted in section 2.3.2. Some of the other methods described there have also been considered here. Table 2.1 gives the factors which the angular correlation functions must be multiplied by using these methods. The predicted temperature anisotropies

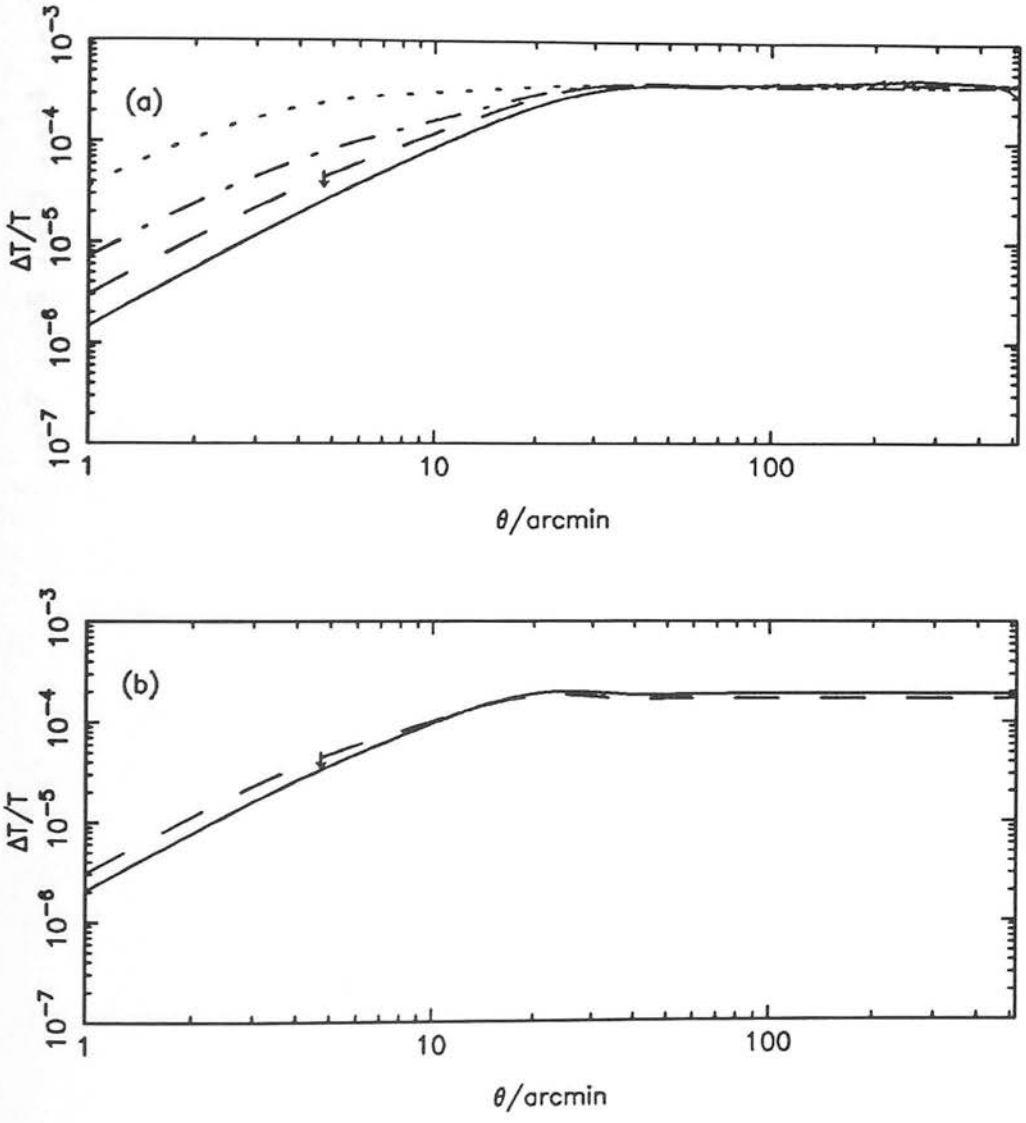

Figure 2.7: Predicted temperature anisotropies for the Uson & Wilkinson experiment. The beamwidth $\sigma = 0.64'$. (a) adiabatic models ($n = 0$ solid line, $n = 1$ dashed line, $n = 2$ dot-dash line and $n = 4$ dotted line). (b) isocurvature models ($n = -1$ solid line and $n = 0$ dashed line). The upper limit from Uson & Wilkinson is shown by the top of the arrow.

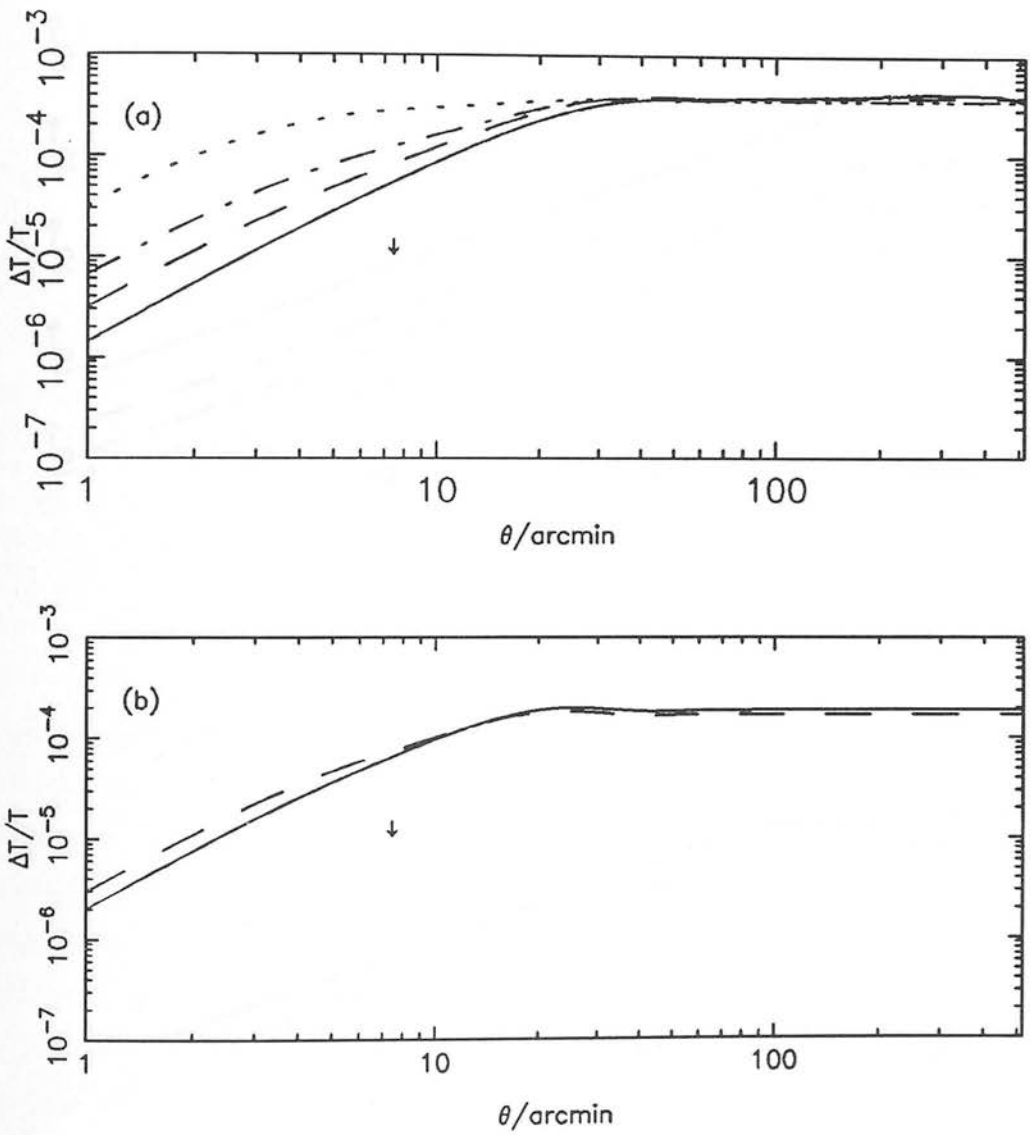

Figure 2.8: Predicted temperature anisotropies for the Readhead *et al.* experiment. The beamwidth $\sigma = 0.77'$. (a) adiabatic models ($n = 0$ solid line, $n = 1$ dashed line, $n = 2$ dot-dash line and $n = 4$ dotted line). (b) isocurvature models ($n = -1$ solid line and $n = 0$ dashed line). The upper limit from Readhead *et al.* is shown by the top of the arrow.

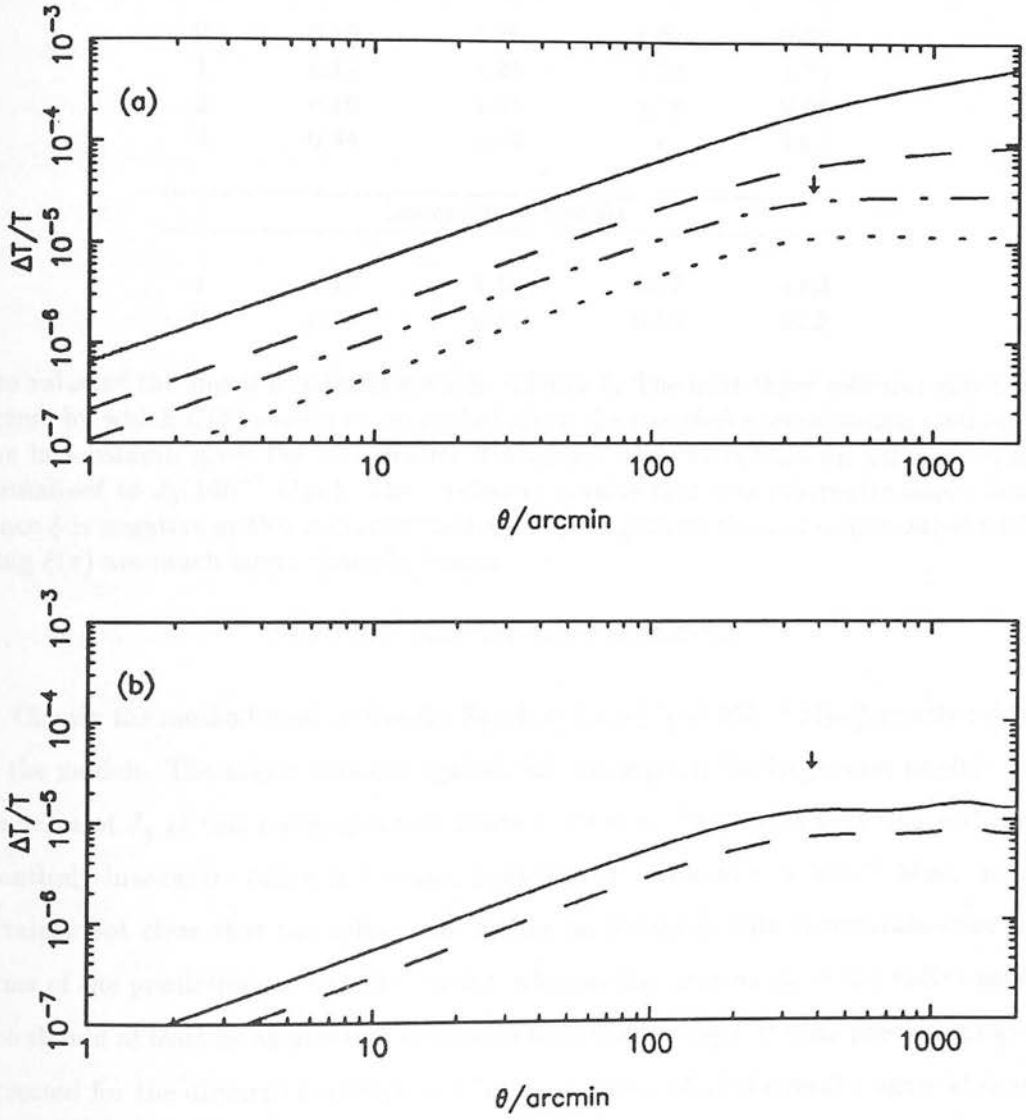

Figure 2.9: Predicted temperature anisotropies for the Melchiorri *et al.* experiment. The beamwidth $\sigma = 128'$. (a) adiabatic models ($n = 0$ solid line, $n = 1$ dashed line, $n = 2$ dot-dash line and $n = 4$ dotted line). (b) isocurvature models ($n = -1$ solid line and $n = 0$ dashed line). The upper limit from Melchiorri *et al.* is shown by the top of the arrow.

scale according to the square root of this factor.

n	$J_3(25h^{-1}$ Mpc)	$\delta M/M$	$\xi(5.4h^{-1}$ Mpc)	σ_{0g}
		adiabatic models		
0	0.10	1.26	1.21	0.94
1	0.12	1.25	1.12	1.14
2	0.16	1.35	0.98	2.08
4	0.44	0.63	*	14.4
		isocurvature models		
−1	0.19	1.15	1.07	14.3
0	0.15	0.83	0.19	91.8

The value of the spectral index is given in column 1. The next three columns give the factors by which $C(\theta)$ should be multiplied given the specified normalisation methods. The last column gives the *rms* density fluctuation when smoothed on galaxy scales, normalised to $J_3(10h^{-1}$ Mpc). The $*$ refers to a value that was inherently unphysical (since ξ is negative at this radius for that model). In general the errors associated with using $\xi(r)$ are much larger than the others.

Table 2.1: Alternative normalisations.

Clearly the method used by Gouda, Sasaki & Suto (J_3 at $25h^{-1}$ Mpc) greatly helps all the models. The major criticism against this technique is the large error implicit in the value of J_3 at this radius given by Davis & Peebles. They state that this statistic is entirely inaccurate (since it becomes negative) at values of $r > 30h^{-1}$ Mpc. It is certainly not clear that the value used by Gouda, Sasaki & Suto is accurate even in terms of the predictions of the CfA survey (whereas the error on J_3 at the radius used here should at least be an accurate prediction from that survey). If their predictions are corrected for the different normalisation technique their adiabatic results agree almost exactly with those presented here. Note that their definition of n for isocurvature models is slightly different and they do not consider the models presented here for that case. The general trend of their results with n however is consistent with the values obtained here ($n = -1$ is equivalent to $n = 3$ in their definition) when the normalisation has been corrected. Were their normalisation to prove accurate then none of the models could be excluded by the observational constraints. In general, with their normalisation the predicted values of $\Delta T/T$ are about a third smaller than those here.

Using $\delta M/M$ results in very little difference to the predicted anisotropies (at most

a factor of about 1.1 either way). This is as would be expected since this method should in principle give almost identical answers to an accurate application of the J_3 method. By contrast, the predictions from using $\xi(r)$ are extremely mixed. Since $\xi(r)$ can be negative at the matching radius (where in reality $\xi_{gg} = 1$), it is not a very useful method in principle. Wilson & Silk noted this behaviour themselves but still used the method. Wilson (1983) gives correction factors from their unique normalisation scheme back into two standard methods (either the linear prediction for $\xi(r)$ or a value of J_3). When this is applied to their adiabatic results they are similar to those found here, though slightly lower since they did not include the massless neutrinos. Their isothermal results are of limited usefulness.

Finally, suppose a general biasing factor of about 2 were applied to the standard model presented here. This will reduce the predicted values of $\Delta T/T$ by a factor of 2 when the J_3 normalisation is used. This would allow both the isocurvature models (though the $n = 0$ case is marginal) and also possibly the $n = 1$ adiabatic model (though it would just be excluded at the 95% level by the Readhead *et al.* result). The $n = 0$ adiabatic model is still excluded by the Melchiorri *et al.* result and the $n > 1$ models are definitely excluded by the Readhead *et al.* result. The last item of interest is the predicted redshift of galaxy formation. This can be derived from the values of σ_{0g} given in table 2.1 since $z_g \sim \sigma_{0g} - 1$. With biasing, the marginal adiabatic model has a low mean redshift of galaxy formation ($z \sim 0.5$). This would seem to imply that a biased model is only undergoing its main phase of galaxy formation now. Indeed, for any of these adiabatic models to truly satisfy the observational constraints, the current value of σ_{0g} would probably have to be less than unity. This is clearly nonsense in terms of the standard model since galaxies do exist, though in a top-down model (which the $n = 1$ model is to a certain extent), galaxies can form from 3σ peaks in the pancakes (see Peacock & Heavens, 1985). The isocurvature models both have rather large values of z_g. Also, since structure in such models initially forms on much smaller scales than galaxies it is possible that recombination could never have occurred. Efstathiou & Bond consider non-standard ionisation histories but their predicted temperature anisotropies are only slightly smaller than calculated here for $\Omega = 1$.

2.5 Conclusions

There have been several reasons for recalculating the expected temperature fluctuations in a purely baryonic universe. Although similar models have been considered by Wilson & Silk (1981), Gouda, Sasaki & Suto (1987) and Efstathiou & Bond (1987) amongst others, there are several features which still make these models interesting. The first is the problem of achieving a stable solution. Although accurate baryonic models have existed since Peebles & Yu (1970), the problem is sufficiently difficult to merit checking the accuracy of the solutions obtained with different techniques. Section 2.2.3 dealt with this question in some depth. All the different methods used for solving the differential equations numerically were found to give very similar results. It would appear then that the numerical methods used, both here and elsewhere, are stable and accurate. The exception to this was the difficulty in calculating solutions for the isocurvature model for modes that are still outside the present horizon. It may be that some different choice of independent variable than scale factor would alleviate this difficulty. Certainly, in previous similar work the independent variable has been different. Wilson & Silk used time, but this necessitates solving an extra equation for a as a function of time, and Efstathiou & Bond use either conformal time or a variable of their own creation (see Efstathiou & Bond 1986). However, in tests done whilst writing the code used here, the choice of scale factor was found to be superior to using either time or redshift. Using conformal time gives identical solutions and takes a similar amount of cpu time.

The other matter relating to accuracy deals with the matter of gauge-invariance. The results derived here were calculated in the synchronous gauge. This seems the natural choice for a gauge when calculating the evolution of small fluctuations. Bond (1988a) discusses this matter and concludes that using the synchronous gauge should give essentially identical results to using gauge invariant methods. This can be tested since Kodama & Sasaki (1984, 1986) and Gouda, Sasaki & Suto (1987) have used a completely gauge-invariant analysis. Gouda, Sasaki & Suto state that the difference between their work and others can be traced to their use of gauge-invariance. The analysis here, however, gives identical results if corrected for their choice of normalisation. The one major benefit of their method may be that they can correctly model isocurvature fluctuations on large scales and hence consider scale-invariant isocurvature models (as they do). The differences are not as large as they suggest however. As a further

test of the importance of gauge-invariance, the fluctuation spectra can be truncated at the present horizon. All modes within the horizon are not affected by gauge problems. Unless there is large scale power this results in identical results. Even the adiabatic models with large scale power considered here ($n = 0$ for example) give effectively identical results to Gouda, Sasaki & Suto. It would appear that the synchronous gauge is still applicable.

The next issue to be tackled was the accuracy of the various approximate angular correlation functions used in previous work. Only Efstathiou & Bond use similar methods to the full solution described here. Both Wilson & Silk and Gouda, Sasaki & Suto use an approximate method which is described in section 2.4.3. In practice, for small angular scales, this approximation is excellent. It is unlikely that errors greater than about 10% will be generated as a result of using it. That this is true is confirmed by the excellent agreement between the predicted anisotropies found here for the adiabatic models and those obtained by Gouda, Sasaki & Suto. As well as examining the approximate model for $C(\theta)$, differing forms of normalisation were also discussed. Most gave similar answers, though that used by Gouda, Sasaki & Suto gave much lower temperature fluctuations than found elsewhere. Their method is considered to be erratic since it requires an accurate calculation of J_3 at $25h^{-1}$ Mpc from the CfA survey and Davis & Peebles (1983) do not suggest that the values derived at this radius are that precise. The much more conservative value of J_3 used here is more likely to be accurate. Only further calculations from the new galaxy catalogues that now exist will answer this point however (see section 2.3.2). Perhaps the most telling normalisation criterion for adiabatic models though was the extremely low redshift of collapse predicted for galaxies. This point remains whichever value of J_3 was used.

Lastly, the actual results obtained here would seem to exclude most baryonic models. With the normalisation chosen, *all* baryonic models are excluded by the observations of Readhead *et al.* (1988b). If this result is set aside, the constraints are not as powerful and the scale-invariant adiabatic model and both isocurvature models still fare reasonably well. Even if biasing were included, only the isocurvature model with $n = -1$ really satisfies the constraints that the Readhead *et al.* result provides. Furthermore, the work of Efstathiou & Bond shows that a non-standard recombination history, which is feasible in these isocurvature models, gives similar results. Again, only the $n = -1$ isocurvature model is saved. Figure 4 of Efstathiou (1988) does show however, that

reionisation can be of benefit to lower density universes. In particular, for $h = 0.5$, none of the models with $n = -1$ can be ruled out unless $\Omega_0 < 0.1$. It seems that whilst a flat baryonic model may well be ruled out (and chapter 4 suggests that the most favoured isocurvature model would not satisfy clustering constraints for clusters of galaxies in any case), lower density models may still be viable. The major test for these low Ω_0 models is the large scale structure constraints discussed in chapters 4 and 5.

Chapter 3

Approximate Models

3.1 Introduction

Chapter 2 dealt with an exact numerical model of the evolution of fluctuations. Some of the properties of these fluctuations were not dealt with in detail there, since they were not necessary for a discussion of anisotropies in the CBR. The first section in this chapter will cover some of these properties. The scaling of baryonic power spectra will be discussed: this matter is important to the models of baryonic power spectra used in chapter 5. Also, the time evolution of the various perturbed quantities will be discussed: this will be useful in the section half of this chapter. There, an approximate model of CBR fluctuations will be described. What the exact method discussed in chapter 2 did not show at all clearly was the underlying physical processes. Since the success or failure of any model can be traced to these, it is useful to consider other methods which highlight the different mechanisms. It is also helpful to be able to generate semi-accurate angular correlation functions for the radiation without having to use many days of cpu time.

3.2 Baryonic Fluctuations

3.2.1 The Scaling of Baryonic Power Spectra

The scaling properties of power spectra are needed if any attempt is made to create an analytical fit. Any attempt to fit the baryonic power spectra must take account of the features present there. Figure 2.1 shows power spectra for models with three species of massless neutrinos, $\Omega = 1$ and $h = 0.5$. The inclusion of the massless neutrinos would seem to set these models apart from most of those already published. Wilson & Silk (1981) and Wilson (1983) only considered models without the neutrinos, considering that they would not have a strong effect beyond the obvious one of increasing the radiation density somewhat. This should be reflected in two ways in the baryonic power spectrum. The first is an increase in the Silk damping scale, though the depen-

dence of this scale on Ω and h is not straightforward (see, for example, Peebles, 1980, equation 92.50). Note that Silk damping is still present in the isocurvature model: the small adiabatic component that arises after modes enter the horizon is still strongly damped. This is represented in the power spectra by the damping of the oscillatory portion. The second is the amplitude of the first peak which is dependent on the ratio of a_{rec} and a_{eq}, since it reflects the difference between those modes which can grow between equality and recombination since they lie outside the Jeans' wavelength and those which oscillate because of the radiation pressure. The exclusion of the massless neutrinos would probably be justified if all that was required was the power spectrum. Unfortunately, since an accurate measure of the amplitudes of all the components was sought in chapter 2, their inclusion was necessary.

As well as the two models described in chapter 2, two other power spectra were also calculated using the same techniques described there (although the corresponding, complete radiation power spectra was not followed through to the present, so they are not presented there). Both an adiabatic and an isocurvature model with $\Omega = 0.2$ and $h = 0.5$ were considered. Figure 3.1 shows their power spectra. These four models then constitute the available sample which will be used to try and derive scaling relations for the power spectra. Since only one value of h was considered, any consideration of the possible variation with h in these models is largely speculative, based on what might be expected on reasonable physical grounds rather than what is actually seen in the models. Since most model parameters are dependent on powers of Ωh^2, the scaling with h adopted here will follow this rule. No attempt will be made to try and produce a fit of the power spectrum for arbitrary Ω and h given the small size of the available database.

In order to produce scaling relations between the power spectra the following approach was used. The maxima and minima of the power spectrum (note that these are the maxima and minima, and the zeroes, respectively, of the transfer function in the adiabatic case) were found, the positions in k-space of the corresponding points were ratioed. For example, the first peak (that at the smallest k) was compared in both adiabatic models, then the first minima and so on. The resulting values, as a function of k are shown in figure 3.2(a) for the adiabatic models and figure 3.2(b) for the isocurvature models. The solid line in both figures represents a scaling $k \propto (\Omega h^2)^{1/2}$. As can be seen, deviations from this value are actually quite small ($\lesssim 10\%$), but are

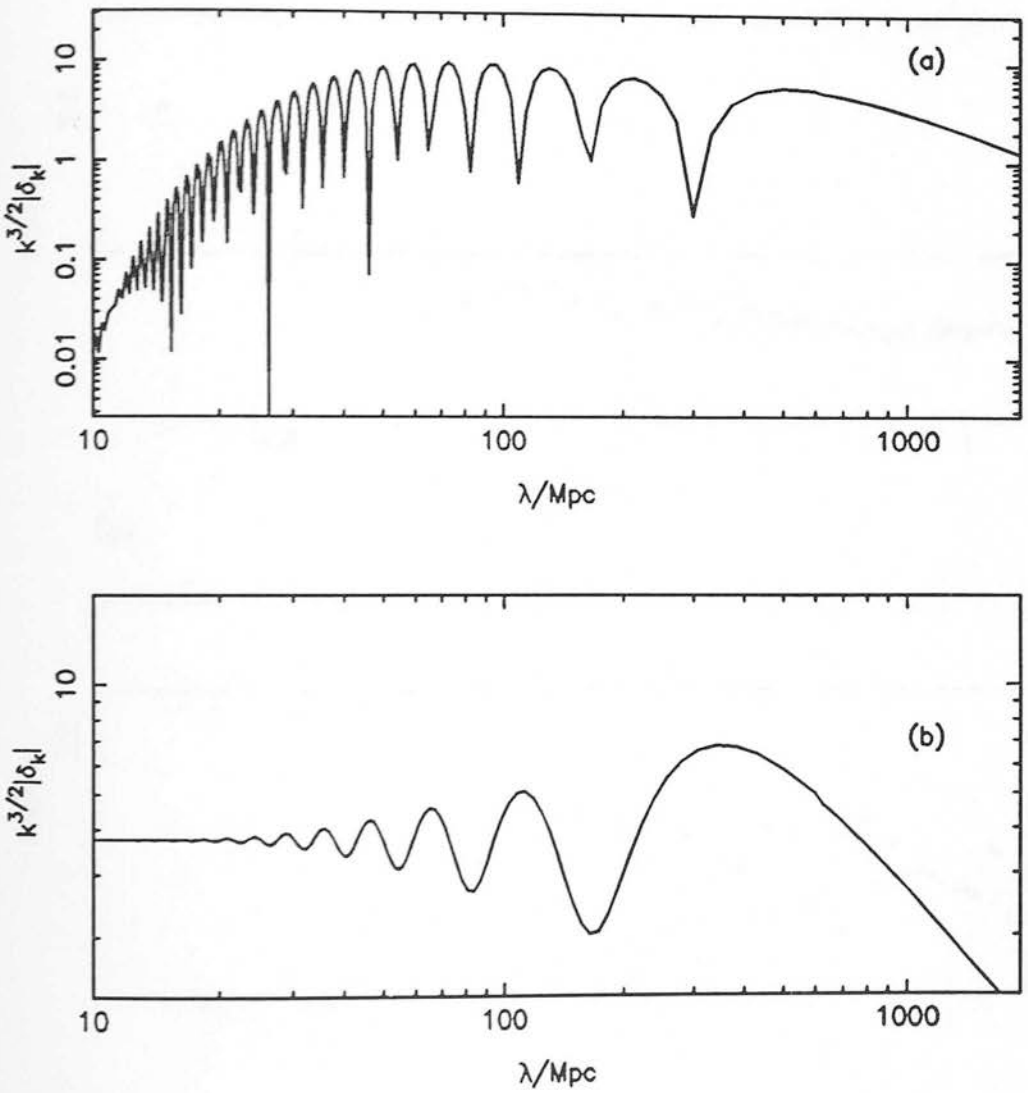

Figure 3.1: Power spectra for a baryonic, $\Omega = 0.2$, $h = 0.5$ model with (a) adiabatic and (b) isocurvature initial conditions. $n = 1$ for (a) and $n = -3$ for (b). The normalisation is arbitrary.

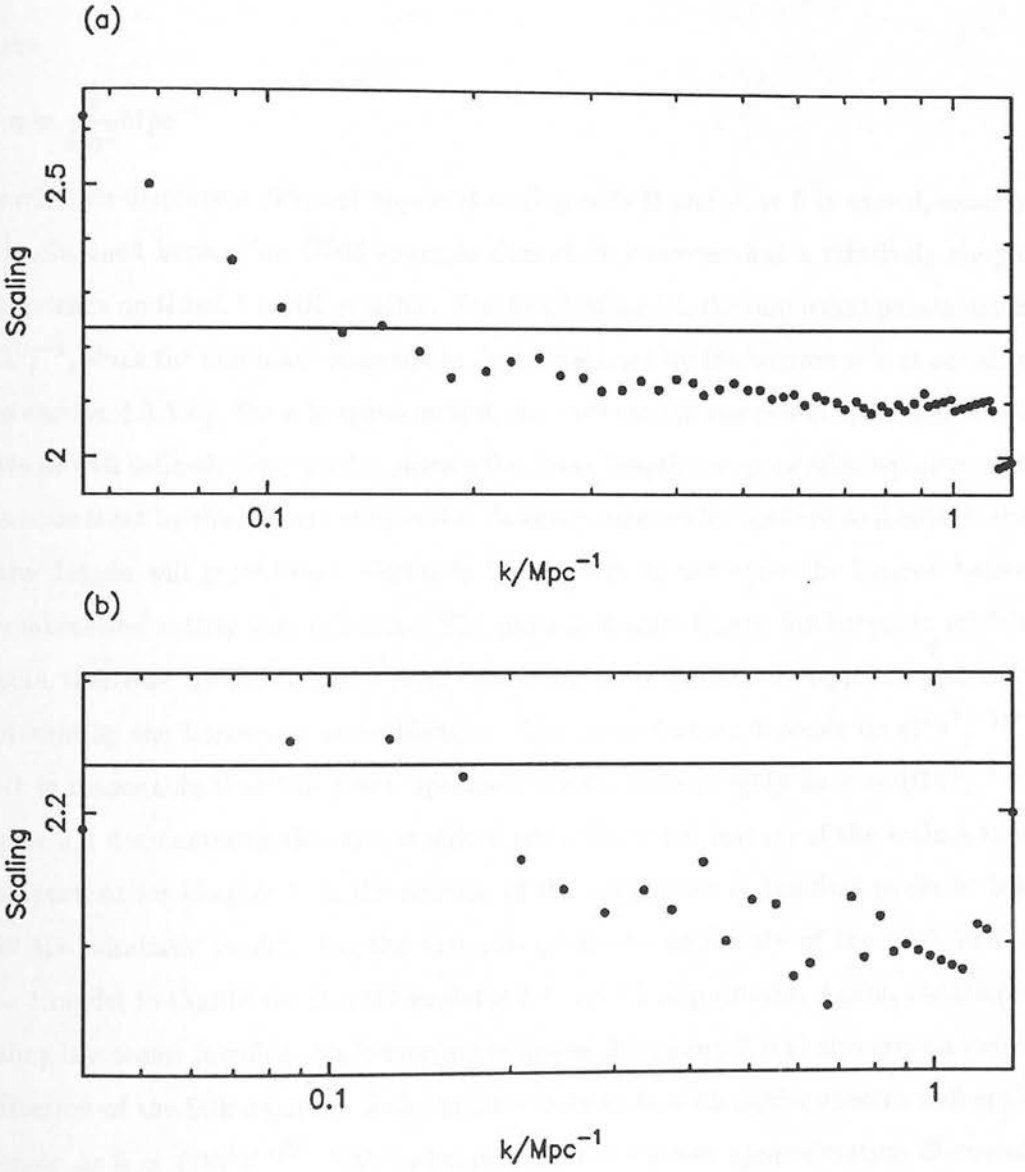

Figure 3.2: Scaling of the power spectra described in section 3.2.1. The adiabatic model is shown in (a) and the isocurvature in (b). The solid line represents a scaling law of $k \propto (\Omega h^2)^{1/2}$ for the two models considered ($\sqrt{0.2}$). The wavenumber is comoving wavenumber for the $\Omega = 1$ models. The tick-marks on the y-axis represent intervals of 0.1 in the scaling.

significant. In fact, both figures show behaviour similar to that found by BBKS for the standard CDM model. Their fit for the adiabatic model was (if $\Omega_{baryons} \ll \Omega$)

$$T_k = \frac{\ln(1+2.34a)}{2.34a}\left(1+3.89a+(16.1a)^2+(5.46a)^3+(6.71a)^4\right)^{-1/4},$$

where

$$a = \frac{k}{\Omega h^2}\mathrm{Mpc}^{-1}.$$

Clearly this displays a different apparent scaling with Ω and h as k is varied, exactly as is obtained here. The CDM example does show however that a relatively simple dependence on Ω and h is still possible. For the CDM model, the important parameter is $(\Omega h^2)^{-1}$, since the dominant scale size in the model is set by the horizon size at equality (see section 1.3.1.6). For a baryonic model, the turn-over in the power spectrum is not quite so well defined. Only modes outside the Jeans' length can grow after equality, and this scale is set by the horizon at equality. However, only modes that are well outside the Jeans' length will grow freely. Certainly those which do not enter the horizon before recombination satisfy this criterion. The dominant scale length for baryonic models should therefore lie between the scale representing the horizon at equality and that representing the horizon at recombination. The latter feature depends on $(\Omega h^2)^{-1/2}$, so it is reasonable that the power spectrum should scale roughly as $k \propto (\Omega h^2)^{-1/2}$. Figure 3.2 demonstrates that this is indeed true. The other feature of the scaling that is important for chapter 5, is the relation of the amplitudes of the first peaks at low k in the adiabatic model. For the first two peaks the amplitude of the peak in the $\Omega = 1$ model to that in the $\Omega = 0.2$ model is 2.3 and 2.2 respectively. Again, the simple scaling law seems justified. An inspection of figures 2.1(a) and 3.1(a) also gives a rough indication of the Silk damping scale. Similar features in both power spectra still scale roughly as $k \propto (\Omega h^2)^{-1/2}$. This indicates that the Peebles approximation discussed earlier is not very accurate, though it must be remembered that the definition of the Silk damping length is a somewhat contentious one.

In particular, with chapter 5 in mind, a scaling of $(\Omega h^2)^{-1/2}$ seems reasonable for the adiabatic models at small k. Since the velocity power spectrum is strongly peaked around the first maximum of the matter power spectrum, the scaling of the velocity power spectrum will therefore be treated as obeying this law.

3.2.2 Time Evolution of Baryonic Models

It is helpful when considering the physics involved in the growth of density perturbations to look at their evolution with time. Using the techniques described in chapter 2, and for the adiabatic and isocurvature models outlined there, the evolution of four separate modes (at 10 Mpc, 40 Mpc, 200 Mpc and 1000 Mpc) have been followed from a redshift of 10000 through to about 300. This covers the whole of the important epoch of recombination whilst also showing the behaviour of the fluctuations outside this period. Figure 3.3 shows the evolution for the adiabatic model and figure 3.4 for the isocurvature model. The figures are presented in order of increasing wavenumber. Each figure displays the evolution of δ_m, δ_r, $\dot{h}$ and v. The quantity δ_r represents the monopole moment (solid line), dipole (dashed line) and $P(k,0)$ (dot-dash line and see equation 2.9).

The adiabatic model shows behaviour that is relatively easy to understand in physical terms. Figure 3.3(a) shows a mode which has never entered the horizon until after recombination. In this case, the simple predictions of section B.2.2.3 apply. The growing mode dominates in both the matter and the radiation. The velocity also grows in a similar manner to the matter until recombination when it starts to decay as predicted by equation B.34b. However, the velocity is relatively unimportant at this wavelength since the perturbation is largely driven by the gravitational field. $\dot{h}$ also decays smoothly, as would be expected once the mode nears the horizon. As might be expected for such large wavelengths, the dominant contribution to the radiation distribution at this time is in the monopole moment. The simple prediction of $\delta_0 = 4\delta_m/3$ is violated however, since, as the radiation free streams, the higher order moments become more important. This is seen in both the growth of the dipole and the angular power spectrum at late times. Figure 3.3(b) shows similar behaviour, though the growth of power in the higher order moments of the radiation is reflected by a dip in the monopole. At this wavelength, the mode is within the horizon at recombination but still well outside the Jeans' length (which is set by the horizon at matter-radiation equality). Figure 3.3(c) shows a mode that is within the Jeans' length. The characteristic oscillating behaviour of sub-horizon adiabatic fluctuations in the pre-recombination epoch, caused by the balance in forces between gravitation causing collapse and radiation pressure holding the perturbation up, can clearly be seen in both the matter and the radiation. The velocity and the matter are almost perfectly out of phase as would be expected.

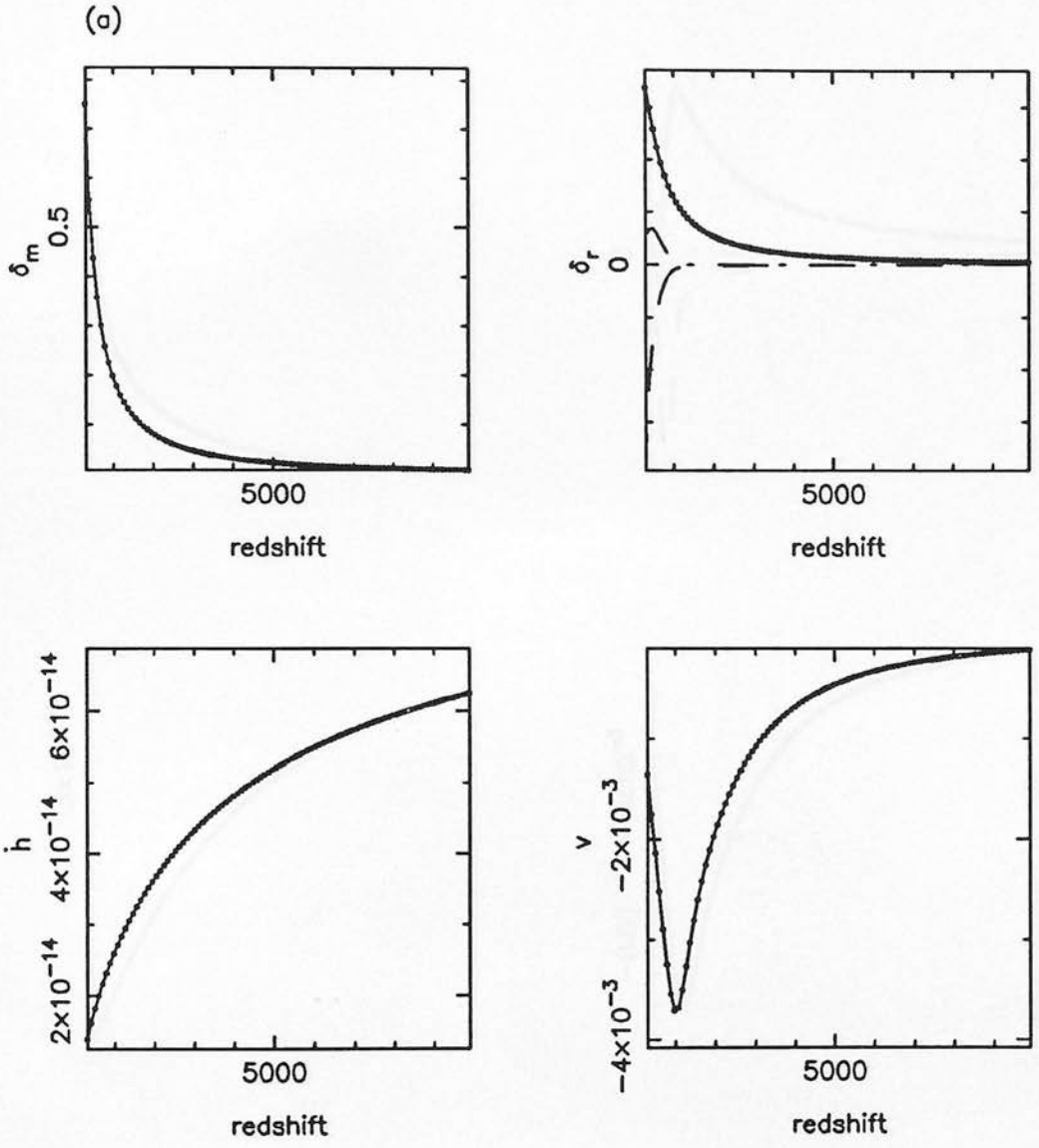

Figure 3.3: The evolution of the matter, radiation, gravitational and velocity components for the adiabatic model as described in the text. The absolute normalisation is arbitrary but the relative normalisation between the figures is fixed. The figures are (a) 1000 Mpc, (b) 200 Mpc, (c) 40 Mpc and (d) 10 Mpc. The various lines for δ_r are described in the text. The intervals on the redshift are 1000 and low redshifts lie to the left of the diagram. The tick-marks on the amplitudes of δ_m and δ_r are at the same intervals. The minor tick-marks represent multiples of powers of ten.

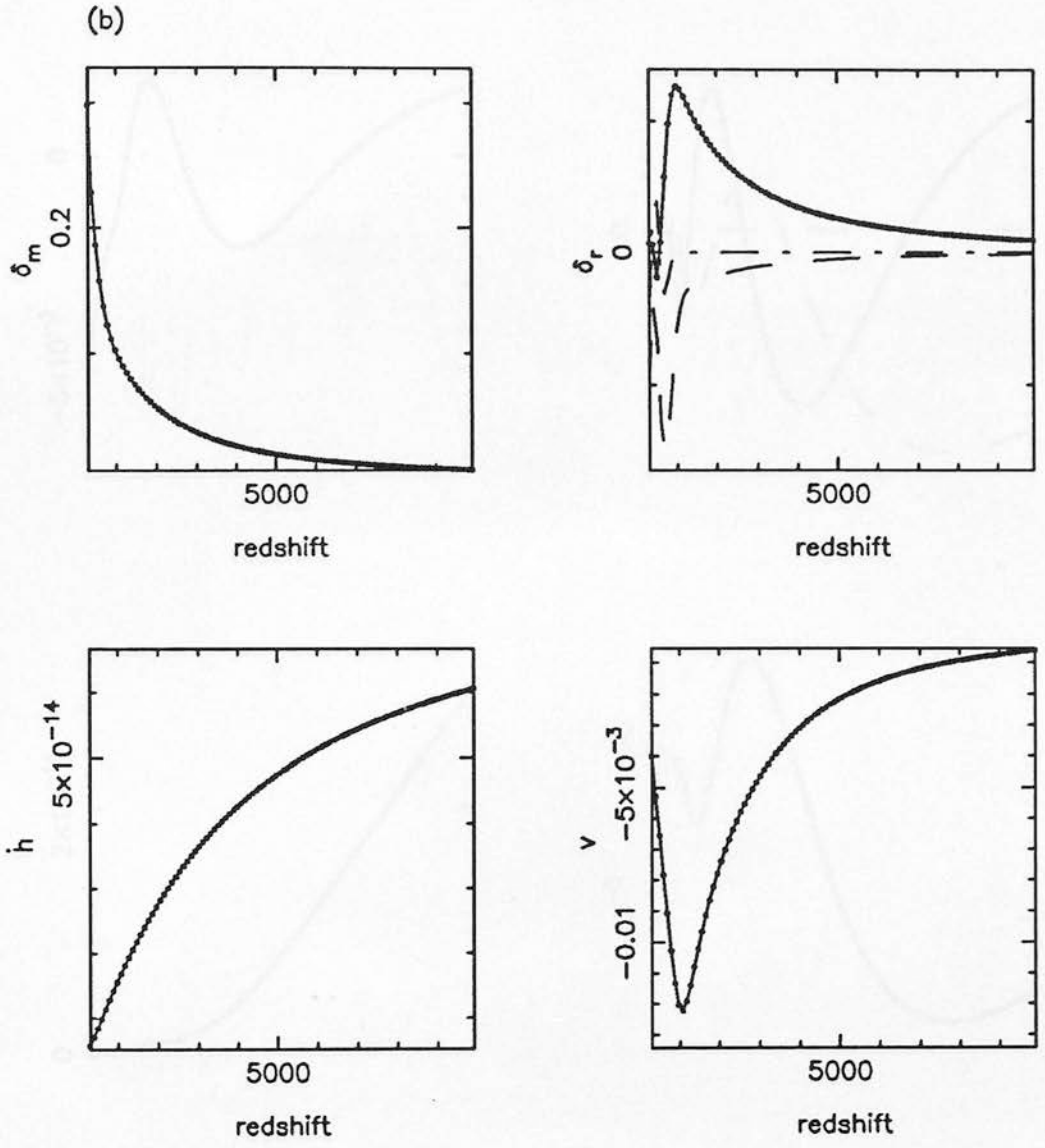

Figure 3.3: (*cont.*)

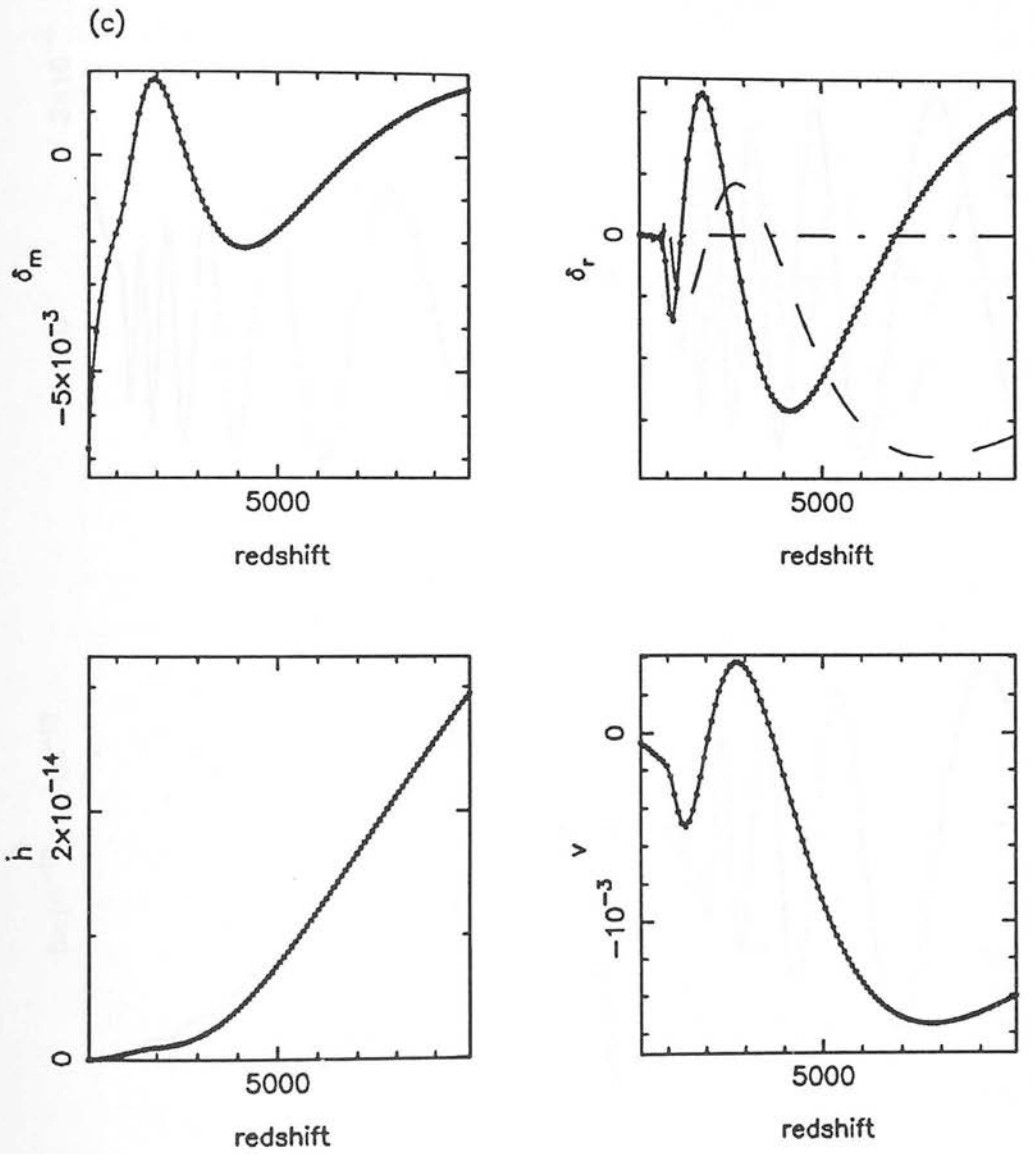

Figure 3.3: (*cont.*)

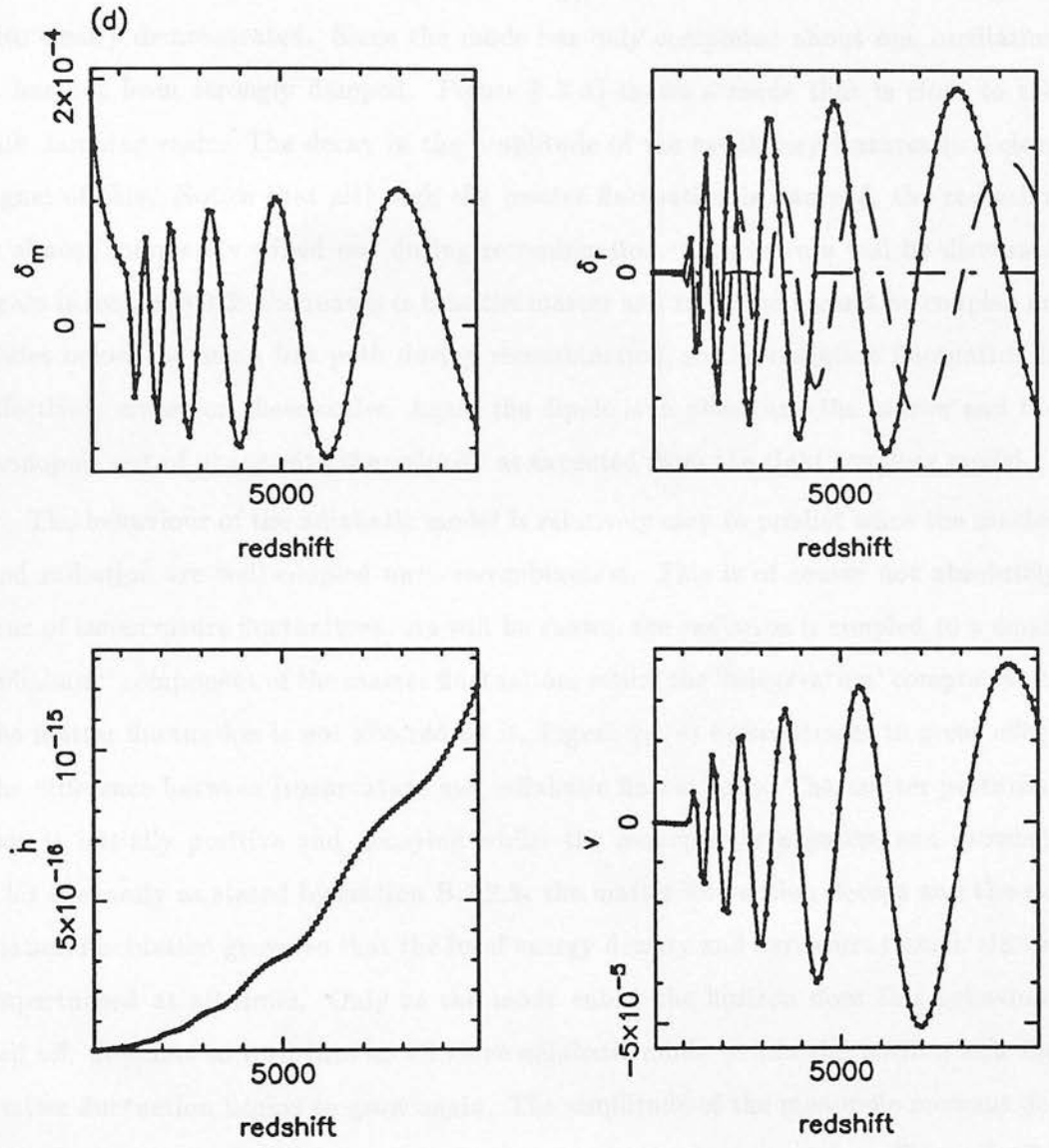

Figure 3.3: (*cont.*)

After recombination the matter displays growing mode behaviour and the radiation, which is strongly attenuated at recombination free streams. The dipole is clearly well in phase with the velocity as predicted by the simple tight coupling approximations of section B.2.1. The small contribution of the gravitational term at this wavelength is also clearly demonstrated. Since the mode has only completed about one oscillation it has not been strongly damped. Figure 3.3(d) shows a mode that is close to the Silk damping scale. The decay in the amplitude of the oscillatory features is a clear signal of this. Notice that although the matter fluctuation is damped, the radiation is almost completely wiped out during recombination. This feature will be discussed again is section 3.3.3: the reason is that the matter and radiation cannot be coupled on scales below the mean free path during recombination, so the radiation fluctuation is effectively erased on these scales. Again the dipole is in phase and the matter and the monopole out of phase with the velocity as expected from the tight coupling model.

The behaviour of the adiabatic model is relatively easy to predict since the matter and radiation are well coupled until recombination. This is of course not absolutely true of isocurvature fluctuations. As will be shown, the radiation is coupled to a small 'adiabatic' component of the matter fluctuation, whilst the 'isocurvature' component of the matter fluctuation is not affected by it. Figure 3.4(a) demonstrates to great effect the difference between isocurvature and adiabatic fluctuations. The matter perturbation is initially positive and decaying whilst the monopole is negative and growing. This is exactly as stated by section B.2.2.2: the matter fluctuation decays and the radiation fluctuation grows so that the local energy density and curvature remain almost unperturbed at all times. Only as the mode enters the horizon does this behaviour tail off. It starts to turn into an effective adiabatic mode within the horizon and the matter fluctuation begins to grow again. The amplitude of the monopole moment decays as the dipole and higher moments increase during free streaming. Figure 3.4(b) also shows similar behaviour, though since the mode entered the horizon at an earlier epoch the matter fluctuation within the horizon has stopped decaying at a much earlier redshift. In fact, by the time the mode is within the horizon in the matter dominated era, the fluctuation has effectively regained the amplitude it had at much earlier epochs. Although the matter and radiation are not strongly coupled for isocurvature fluctuations, the dipole moment still tracks the velocity. As the mode enters the horizon, the gravitational term switches from being negative (as it should be at late times

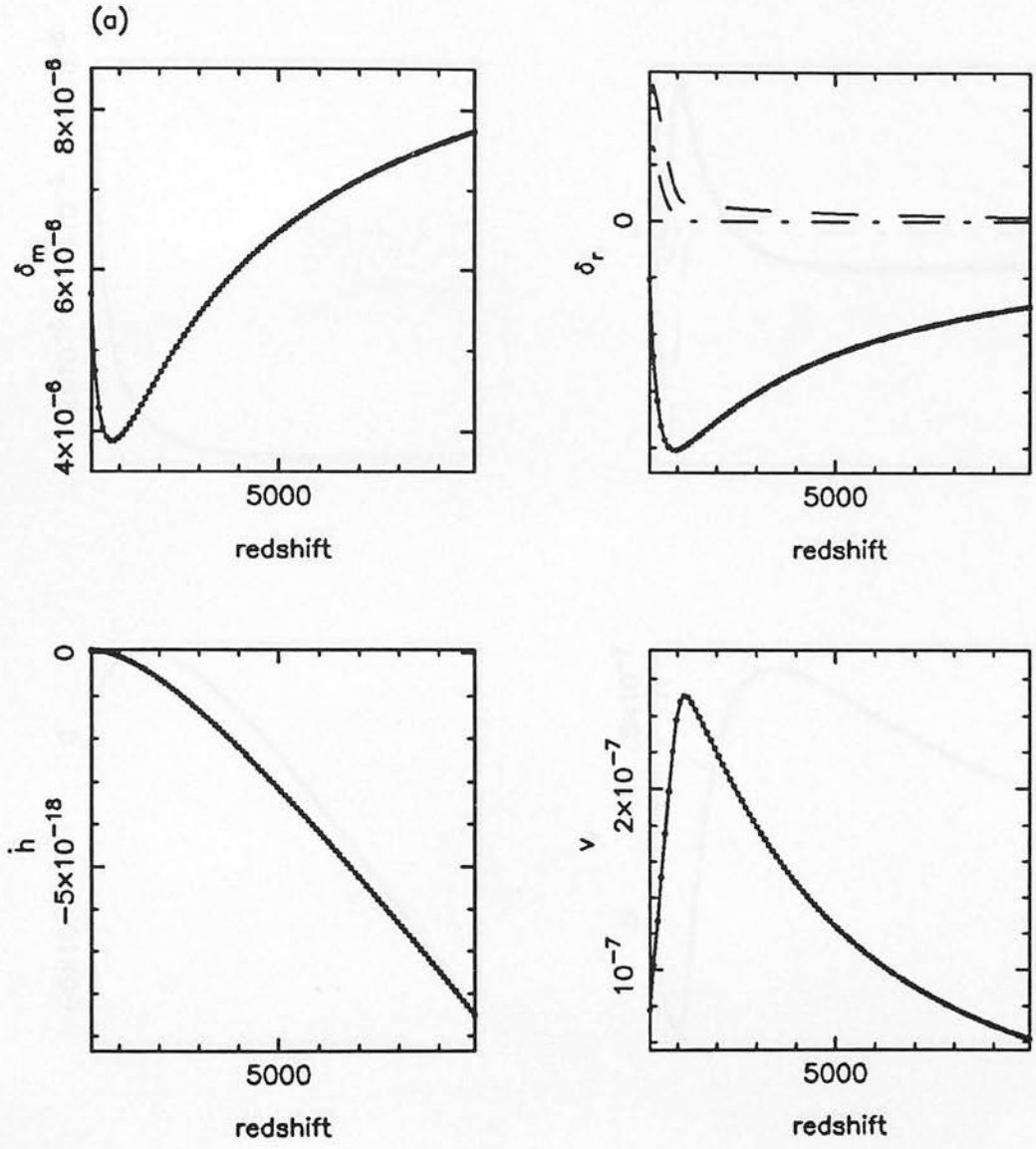

Figure 3.4: The evolution of the matter, radiation, gravitational and velocity components for the isocurvature model as described in the text. The absolute normalisation is arbitrary but the relative normalisation between the figures is fixed. The figures are (a) 1000 Mpc, (b) 200 Mpc, (c) 40 Mpc and (d) 10 Mpc. The various lines for δ_r are described in the text. The intervals on the redshift are 1000 and low redshifts lie to the left of the diagram. The tick-marks on the amplitudes of δ_m and δ_r are at the same intervals.

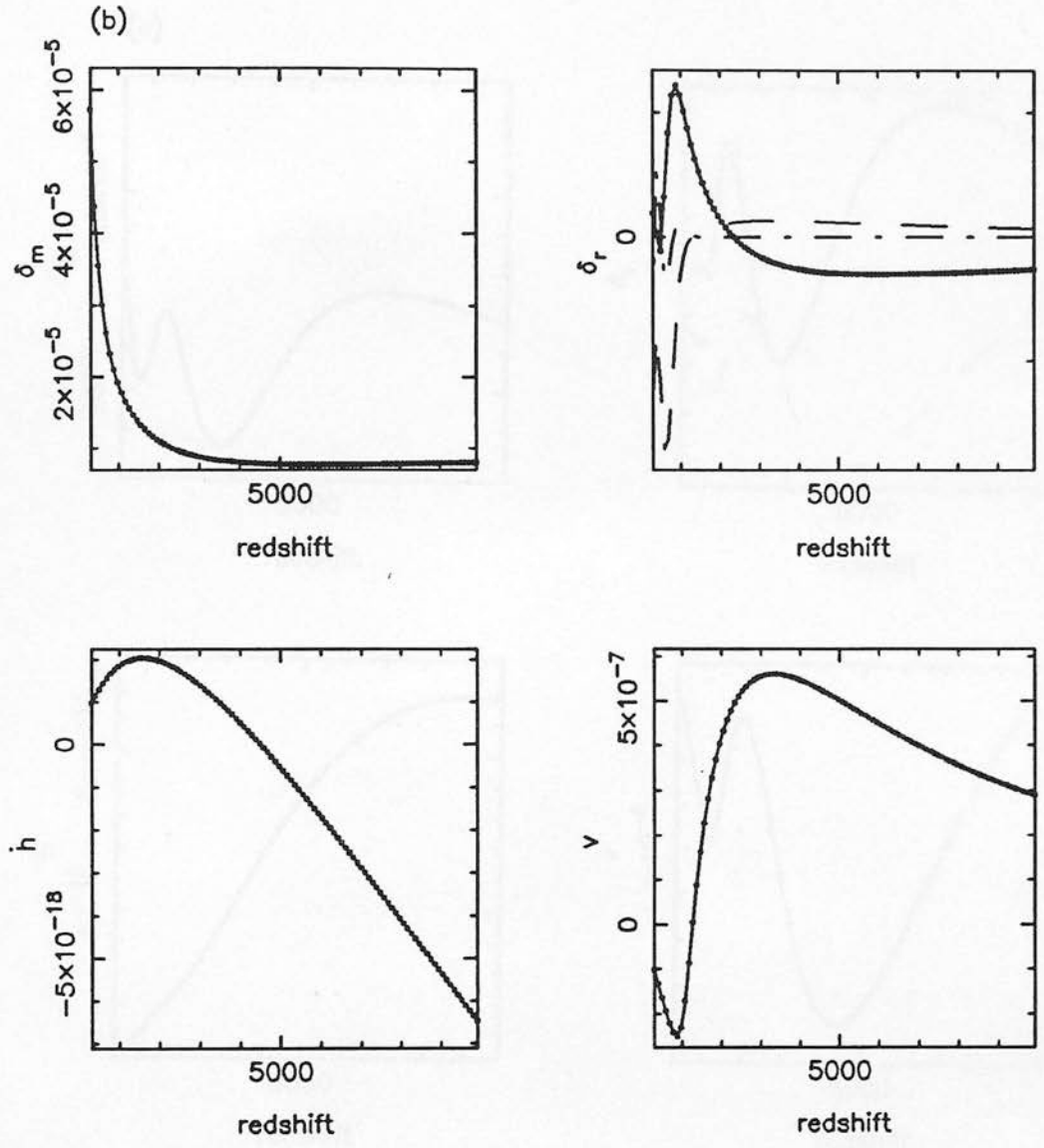

Figure 3.4: (*cont.*)

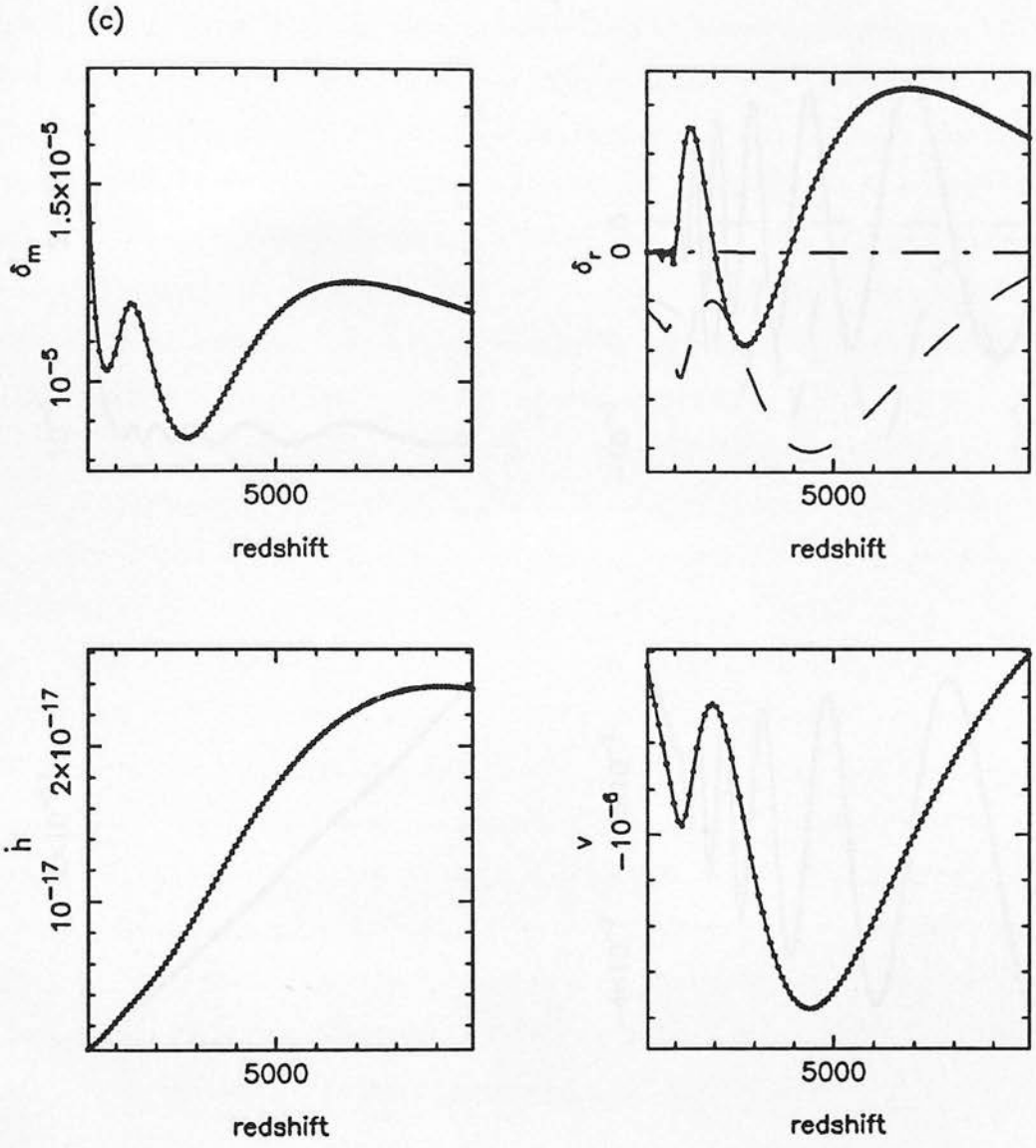

Figure 3.4: (*cont.*)

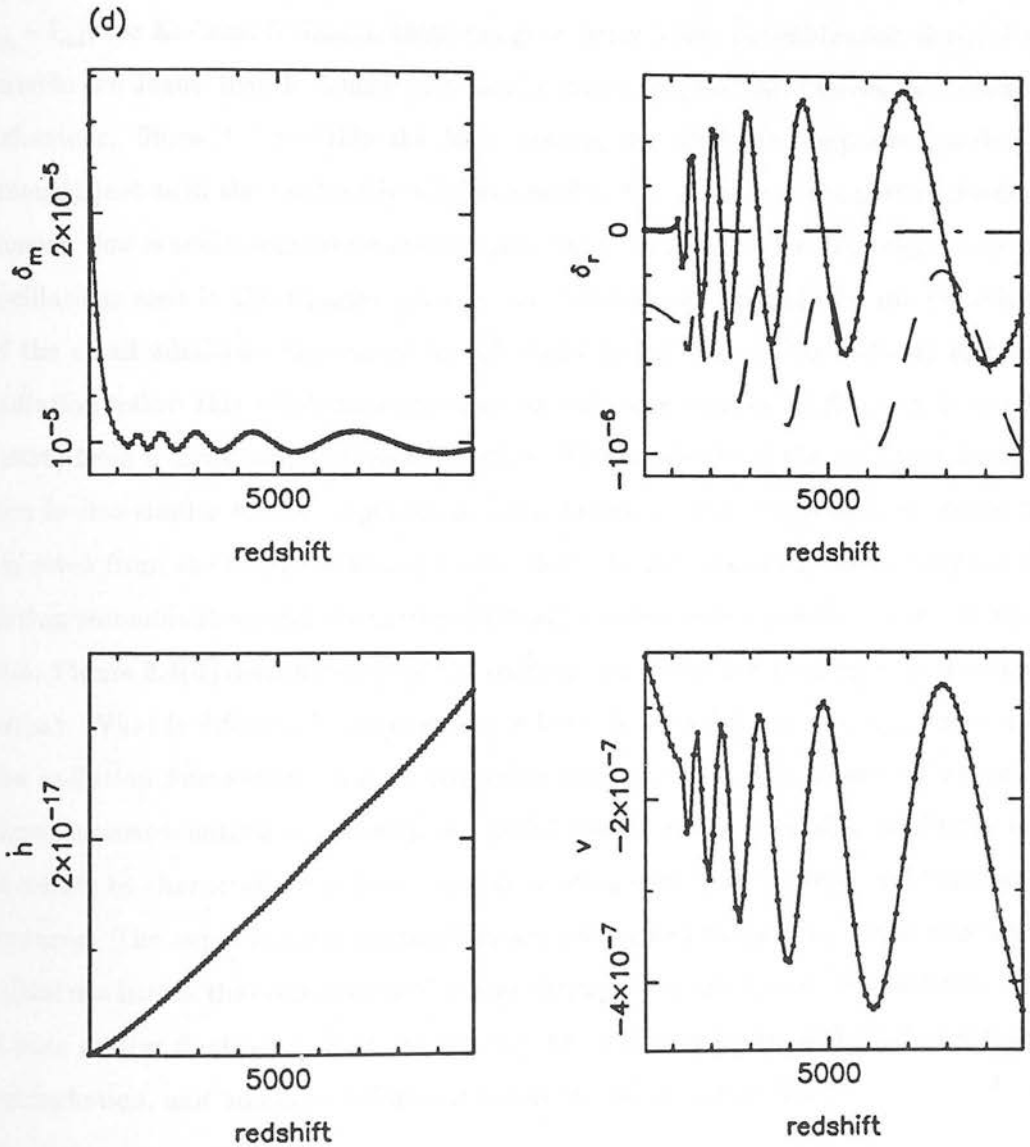

Figure 3.4: (*cont.*)

for modes outside the horizon: figure 3.4(a) also shows this behaviour), to positive as it effectively matches on to the post-recombination solutions of section B.2.3. This mode is actually near the peak in the isocurvature transfer function (figure 3.1(b)): the adiabatic component generated as it comes within the horizon (basically the difference $\delta_m - \delta_{mi}$; see Kodama & Sasaki, 1986) can grow freely before recombination since it lies outside the Jeans' length. This is also clearly shown. Figure 3.4(c) shows the opposite behaviour. Since it lies within the Jeans' length, the adiabatic component oscillates strongly just as in the completely adiabatic model. Here, however, the part of the fluctuation that is still isocurvature remains constant at its initial value. The characteristic oscillations seen in the transfer function can therefore be explained by the behaviour of the small adiabatic component on sub-Jeans' length scales. The velocity and the radiation follow this adiabatic component as well, as predicted by Kodama & Sasaki (1986) from a tight coupling approximation. The amplitude of the radiation fluctuation is also similar to the amplitude of the adiabatic matter component, as would be expected from the adiabatic model above. Both the radiation and the velocity die off during recombination and the matter fluctuation shows growing mode behaviour after this. Figure 3.4(d) demonstrates all the traits shown by the previous figure to a greater extent. What is different is the damping of both the adiabatic matter component and the radiation fluctuation prior to decoupling (compare this with figure 3.3(d) which shows almost identical behaviour). A model with isocurvature initial conditions can therefore be characterised at later times as showing both 'isocurvature' and 'adiabatic' features. The super-horizon fluctuations are determined solely from the isocurvature initial conditions that conserve local energy density. The sub-horizon fluctuations show a base matter fluctuation that has exactly the same amplitude as the initial entropy perturbation, and adiabatic behaviour superimposed on top of this.

3.3 Approximate Models of the CBR

3.3.1 Introduction

It is useful to consider a simplified model of the anisotropies in the CBR. The benefit of the approach given here is that the relative magnitudes of the mechanisms responsible for the fluctuations can be clearly seen. The major drawback is that accurate predictions for some aspects of the fluctuations are hard to obtain. The methods of chapter 2

are necessary to calculate the sizes of the anisotropies correctly: what can be achieved here is accurate only to about a factor of two. Despite this, the physical processes that create the fluctuations are more easily understood with the approach in this section.

The techniques used here are not new. Sunyaev & Zel'dovich (1970) first used a similar approach when considering only the case of isothermal perturbations and Doppler scattering mechanisms. Davis & Boynton (1980) also carried out a similar analysis. A critique of these papers is offered by Lasenby (1981), who corrected some mistakes. Most of what follows is an extension of this work to consider processes other than Doppler scattering. Bond (1988a) also gives a useful summary of this sort of analysis, though the present work was derived independently and does not attempt to use the same methods as he does. The major difference between the previous work and that presented here is that the values of all the components apart from the CBR fluctuations will be assumed to be known. In practice, all this requires is the matter power spectrum at the present. Only baryonic models will be considered, and the data for the power spectra comes from chapter 2. Given the assumptions that are required, only the $\Omega = 1$ model is considered. All actual lengths referred to in this section are comoving.

3.3.2 The Visibility of Decoupling and Temperature Anisotropies

The optical depth between the present epoch and any past epoch is given simply by

$$\zeta = \int_{\tau}^{\tau_0} x_e n_e \sigma_T c a d\tau \, ,$$

where these symbols are as defined previously in chapter 2, though it should perhaps be noted that τ is conformal time. The ionisation history as calculated using the techniques described in section 2.2.2.3 can be used to give a model for the differential visibility function. This is just the probability that a photon emitted at an epoch τ is seen at the present. The differential visibility is given by $V(\tau) = e^{-\zeta} d\zeta/d\tau$. Jones & Wyse (1985) find that V can be approximated by a Gaussian, centred on a redshift, z_m, of about 1065 with a width, σ_z of 79, independent of Ω and h, and of $\Omega_{baryons}/\Omega$. Hence, the last scattering shell for most CBR photons is a relatively narrow region and is the same region for all models in terms of redshift.

Using this simplified model of the last scattering surface, the temperature fluctuation at the present can be written as

$$\frac{\delta T}{T} = \int_0^\infty V(z)\Delta dz \,. \tag{3.1a}$$

The form of Δ will be given later: for the moment it will be assumed that it is just a general spatial function which depends on the various perturbed quantities, and which represents the contribution to $\Delta T/T$ from those photons last scattered at a given redshift. In particular, it can be replaced by its Fourier transform so that

$$\frac{\delta T}{T} = \int_0^\infty \int e^{i\mathbf{k}.\mathbf{x}'} \Delta_{\mathbf{k}} V(z) d^3k \, dz \,. \tag{3.1b}$$

In order to make the analysis here more like that of chapter 2, it is useful to express the variable $\mathbf{x}'$ as $\mathbf{x}' = \mathbf{x} + c(\tau_x - \tau')\mathbf{q}$. Then $\mathbf{q}$ is the photon propagation direction and $\mathbf{x}$ is an arbitrary point in space and $\mathbf{x}'$ will be taken to be a point centred in the last scattering shell. It is helpful to state several approximations that will be made at this point. The function, $\Delta_{\mathbf{k}}$, will be assumed to be effectively constant over the last scattering shell and will be replaced by the value at the maximum of last scattering. Since Δ is related to the perturbation components this is clearly not true, but will do if the (assumed) average values reflect the change across the shell. Also, the integral over z requires $\tau(z)$. This is given by equation B.12b but will be approximated here by (remembering that at last scattering $z \gg 1$ and assuming that recombination is after τ_{eq}, which is why $\Omega = 1$ is also assumed)

$$\tau \simeq 2H_0^{-1} z^{-1/2} \,.$$

The visibility function has the form

$$V(z) \simeq \frac{1}{(2\pi\sigma_z^2)^{1/2}} e^{-(z-z_m)^2/\sigma_z^2} \,.$$

Since this function is strongly peaked about z_m, the form of τ' will be expanded as

$$\tau' \simeq 2H_0^{-1}\left(z_m^{-1/2} - \frac{1}{2} z_m^{-3/2}(z - z_m)\right) \simeq \tau_m - H_0^{-1} z_m^{-3/2}(z - z_m) \,.$$

Hence

$$\frac{\delta T(\mathbf{x},\mathbf{q})}{T} = \frac{1}{(2\pi\sigma_z^2)^{1/2}} \int d^3k \Delta_{\mathbf{k}} \, e^{i\mathbf{k}.\mathbf{x}} \, e^{ic(\tau_z - \tau_m)\mathbf{k}.\mathbf{q}} \times$$

$$\int_0^\infty e^{icH_0^{-1} z_m^{-3/2}(z-z_m)\mathbf{k}.\mathbf{q}} \, e^{-(z-z_m)^2/2\sigma_z^2} dz \,. \tag{3.1c}$$

Since the integrand is peaked around z_m the limit can be changed from 0 to $-\infty$ with little loss of accuracy. The integral over z is then a Fourier transform of a Gaussian, so

$$\frac{\delta T(\mathbf{x},\mathbf{q})}{T} = \int d^3k \Delta_{\mathbf{k}}\, e^{i\mathbf{k}.\mathbf{x}}\, e^{ic(\tau_z-\tau_m)\mathbf{k}.\mathbf{q}}\, e^{-(\sigma \mathbf{k}.\mathbf{q})^2/2} dz\ . \tag{3.1d}$$

where $\sigma = \sigma_z c H_0^{-1} z_m^{-3/2}$. The angular correlation function at the present epoch is given by

$$\left\langle \frac{\delta T(\mathbf{x},\mathbf{q})}{T} \frac{\delta T(\mathbf{x},\mathbf{q}')}{T} \right\rangle = \frac{1}{V} \int d^3x \frac{\delta T(\mathbf{x},\mathbf{q})}{T} \frac{\delta T(\mathbf{x},\mathbf{q}')}{T}\ . \tag{3.2a}$$

The volume integral gives rise to a δ-function as usual leaving

$$\left\langle \frac{\delta T(\mathbf{x},\mathbf{q})}{T} \frac{\delta T(\mathbf{x},\mathbf{q}')}{T} \right\rangle = \frac{(2\pi)^3}{V} \int d^3k\, |\Delta_{\mathbf{k}}|^2\, e^{ic(\tau_0-\tau_m)(\mathbf{q}-\mathbf{q}').\mathbf{k}} \times$$

$$e^{-(\sigma \mathbf{k}.\mathbf{q})^2/2}\, e^{-(\sigma \mathbf{k}.\mathbf{q}')^2/2} dz\ . \tag{3.2b}$$

In order to simplify this further it will be assumed that the angle between the two lines of sight is small. Suppose $\mathbf{q}.\mathbf{q}' = \cos\psi$ and $\sin\psi \simeq \psi$. Then a co-ordinate system can be set up where the polar axis points from last scattering, midway between $\mathbf{q}$ and $\mathbf{q}'$, and the other two axes are in the plane of last scattering. Then the vectors $\mathbf{q}, \mathbf{q}'$ and $\mathbf{k}$ have co-ordinates $(-\psi/2, 0, 1), (\psi/2, 0, 1)$ and $(k\sin\theta\cos\phi, k\sin\theta\sin\phi, k\cos\theta)$ respectively. Using this co-ordinate system, and the fact that $d^3k = k^2\, dk\, d(\cos\theta)\, d\phi$,

$$(\mathbf{k}.\mathbf{q})^2 + (\mathbf{k}.\mathbf{q}')^2 = 2k^2\cos^2\theta + O(\psi^2)\ ,$$

and,

$$\left(\mathbf{q}-\mathbf{q}'\right).\mathbf{k} = -k\psi\sin\theta\cos\phi\ .$$

The integral over ϕ gives rise to a Bessel function (see section 2.3.3.1), so the final integral is

$$C(\psi) = \frac{(2\pi)^4}{V} \int k^2\, dk\, d(\cos\theta)\, |\Delta_{\mathbf{k}}|^2\, J_0(c(\tau_0-\tau_m)k\psi\sin\theta)\, e^{-k^2\sigma^2\cos^2\theta}\ . \tag{3.3}$$

3.3.3 The Form of the Source Function

So far, the source function, Δ, has not been specified. Four possible mechanisms generate temperature anisotropies. These are the adiabatic source term (the coupling between the matter and the radiation), the doppler scattering term (scattering off electrons as decoupling proceeds), the isocurvature effect (isocurvature fluctuations only: see section B.2.2.2) and the Sachs-Wolfe effect.

The Sachs-Wolfe effect will be considered here in two separate approaches. The first follows on from the techniques of appendix A, though the independent variable used

here is conformal time (for simplicity and consistency with section 3.3.2). Also, $\Omega = 1$ is assumed, so that the curvature terms present there will be ignored. When scattering processes are no longer important, the Boltzmann equation (A.68e) can be written as

$$\delta' + \frac{\partial \delta}{\partial x^i}\gamma^i = 2h'_{ij}\gamma^i\gamma^j \ . \tag{3.4a}$$

Since δ is a function of τ, x_i and γ_i, a total derivative can be defined as

$$\frac{d\delta}{d\tau} = \delta' + \frac{\partial \delta}{\partial x^i}\gamma^i \ ,$$

since $\gamma_i = dx_i/d\tau$ (equation A.53), and $d\gamma_i/d\tau = 0$. Hence,

$$\delta(\tau_0) = 2\int_{\tau_i}^{\tau_0} h'_{ij}\gamma^i\gamma^j d\tau \ . \tag{3.4b}$$

It has been assumed here that the initial fluctuation, $\delta(\tau_i)$, is effectively zero. Since all the other processes are going to be considered separately this is reasonable. After recombination, the following approximations are also reasonable (see section B.2 but note that the primes there are derivatives with respect to a)

$$a = \frac{2\pi G}{3}\rho_{b0}\tau^2 \ ,$$

$$h = -H = \frac{1}{2}c_1\tau^2 \ ,$$

$$\delta_m = \frac{1}{4}c_1\tau^2 \ .$$

All the functions can be decomposed into a spatial part and a time varying part as in appendix A.6. The spatial eigenfunctions will be denoted $Q(\mathrm{x})$ as there, though for a flat space these are simply plane wave solutions. Along the photon path, $\mathrm{x} = \mathrm{x}(\tau)$, so

$$\frac{\partial Q}{\partial \tau} = \frac{\partial Q}{\partial x^i}\gamma^i \ .$$

Allowing for the fact that space is flat, the covariant derivatives become ordinary derivatives and

$$h'_{ij}(\mathrm{x},\tau)\gamma^i\gamma^j = -k^{-2}h'(\tau)Q_{,ij}\gamma^i\gamma^j = -k^{-2}h'Q'' \ .$$

Therefore, an integration by parts will solve equation 3.4b. Writing $\delta T/T = \frac{1}{4}\delta$, equation 3.4b becomes

$$\frac{\delta T}{T} = -\frac{1}{2}k^{-2}\left\{\left[h'Q'\right]_{\tau_i}^{\tau_0} - \left[h''Q\right]_{\tau_i}^{\tau_0}\right\} \ .$$

Since $h \propto \tau^2$ there are no other terms. By above, the first term is proportional to γ_i, which is a dipole term. This will be ignored here, since only small angular separations will be considered (see section 2.3.1.4 as well). The final effect is then

$$\frac{\delta T}{T} = -\frac{1}{2}k^{-2}\left\{\left[h'Q'\right]_{\tau_i}^{\tau_0}\right\} . \tag{3.5}$$

It is usual to express this relation in terms of a Newtonian potential, ϕ. This potential is given by

$$\nabla^2\phi = 4\pi G\rho_b\delta_m a^2 .$$

Using the relationships given between h, δ_m, a and τ, this gives

$$\phi(\mathrm{x},\tau) = -\frac{3}{2}k^{-2}h''Q(\mathrm{x}) .$$

Restoring the c's that have been left out of this analysis leaves the required relationship.

$$\frac{\delta T}{T} = -\frac{1}{3c^2}\left[\phi(\tau_0) - \phi(\tau_i)\right] . \tag{3.6}$$

The observable portion of this term is the $\phi(\tau_i)$ part. This can be written as

$$\Delta_{sw} = \frac{1}{3}\frac{\phi}{c^2} = -\frac{2}{(kr_H)^2}\delta_m .$$

The horizon distance at last scattering is given by, $r_H \simeq 130\Omega^{-1/2}h^{-1}$ Mpc (see section 1.3.1.6). This is the final form required for the Sachs-Wolfe effect. A somewhat simpler approach to this problem is to consider the Sachs-Wolfe effect as being composed of two distinct parts. The first is simply the temperature fluctuation induced by the change in gravitational potential,

$$\frac{\Delta T}{T} = \frac{\delta\phi}{c^2} ,$$

and the second is caused by a time dilation effect so that the local time co-ordinates are also perturbed. Then the total effect is

$$\frac{\Delta T}{T} = \frac{\delta\phi}{c^2} - \frac{\delta a}{a} .$$

For a matter dominated universe, the latter term is simply $\frac{2}{3}\frac{\delta t}{t}$. But $\delta t/t$ is just $\delta\phi/c^2$, so the total effect is just as before, $\frac{1}{3}\frac{\delta\phi}{c^2}$.

The doppler scattering term is much easier to derive. Since the motion of the electrons in the plasma obeys $v \ll c$, the perturbation to the temperature is simply

$$\frac{\delta T}{T} = \frac{\mathbf{v}.\boldsymbol{\gamma}}{\mathbf{c}} . \tag{3.7}$$

Hence, using the notation of this section,

$$\Delta_v = \frac{v \cos\theta}{c} .$$

The form of v can be estimated from the continuity equation, 1.8, for modes within the horizon. For modes outside the horizon, this equation is modified by the presence of the gravitational field (see the correct continuity equation given in chapter 2, equation 2.4a). For simplicity, it will be assumed that the simpler continuity equation is valid. In this case,

$$\Delta_v = \frac{2}{r_H k} \cos\theta \delta_m .$$

The adiabatic source term is rather more problematical. For modes outside the horizon, it is reasonable to say that $\Delta_a = \frac{1}{3}\delta_m$. However, as can be seen from figures 2.1,2.2 and 2.3, the fluctuation in the radiation is far more attenuated than the matter. Part of this effect is taken into account by the Gaussian term in the correlation function. This represents a damping of the radiation through the shell of last scattering. Since the parameter $\sigma \simeq 4.9(\Omega h^2)^{-1/2}$ Mpc, the damping is only strong in those portions of the power spectra which are already affected by Silk damping (figure 4.2 shows the $\Omega = 1$ baryonic power spectra damped to a similar extent). One additional possibility is to introduce another damping term into the adiabatic contribution. Although the width of this term could be treated as an adjustable factor, the physical reasoning is that the matter and radiation cannot be coupled on scales smaller than the mean free photon path at last scattering. For $\Omega = 1$ and $h = 5$, this is about 15 Mpc at a redshift of 1065. As might be expected, this factor is reasonably close to the FWHM of the shell of last scattering, $10.5(\Omega h^2)^{-1/2}$ Mpc. Filtering the adiabatic source term on these scales should therefore be a reasonable approximation. Then,

$$\Delta_a = \frac{1}{3} e^{-k^2\sigma_{rad}^2/2} \delta_m .$$

The 'isocurvature effect' of Bond & Efstathiou (1987) is simply a reflection of the isocurvature condition on very large scales. Section B.2.2.2 shows that at late times, in the matter dominated era, this implies that

$$\frac{\Delta T}{T} = -\frac{1}{3}\delta_{mi} ,$$

where δ_{mi} is the initial matter perturbation. This effect only plays a part in isocurvature models. Correspondingly, the adiabatic term is not nearly as important in isocurvature

models. However, the fact that, on entering the horizon, an isocurvature fluctuation generates a small adiabatic term (see section 3.2) does imply that there is still some adiabatic terms in the radiation distribution. Since at large k the isocurvature transfer function tends to unity (figures 2.1 and 3.1), is is convenient here to couple the adiabatic and isocurvature terms into

$$\frac{\Delta T}{T} = \frac{1}{3}(\delta_m - \delta_{mi}) .$$

For very large wavelengths, δ_m is negligible compared to the initial value. For smaller wavelengths, where the adiabatic term is important, this combination is roughly what might be expected. Figure 2.4 tends to bear out this approximation. Hence, for isocurvature models

$$\Delta_a = \frac{1}{3} e^{-k^2\sigma_{rad}^2/2}(\delta_m - \delta_{mi}) .$$

In practice, since the models considered here will be compared with the accurate models calculated in chapter 2, the dipole and monopole terms must be excluded from the calculation. Although the explicit dipole terms have been removed, the power spectrum must be truncated at small k in order to avoid introducing these terms into the Sachs-Wolfe effect, which tends to be dominant at these wavelengths in adiabatic models, or the isocurvature effect for isocurvature models. This is done by truncating the power spectrum at a wavelength such that

$$\lambda_{max} \gtrsim c\tau_0 \frac{\pi}{2} .$$

Wavelengths below this scale correspond to angular separations probed by the quadrupole and higher moments on the surface of last scattering, and those above to separations probed only by the dipole or monopole contributions. Similarly, all the other terms in the source function used the same truncated power spectrum.

3.3.4 Calculating the Angular Correlation Function

The angular correlation function of the radiation is given by equation 3.3. All the source terms contributing to the power spectrum have now been described. The complete power spectrum is given by

$$|\Delta_{\mathbf{k}}|^2 = \left[f_v^2(k)\cos^2\theta + (f_a(k) + f_{sw}(k))^2\right] |\delta_m|^2 . \tag{3.8}$$

There is no cross term between the doppler and adiabatic/Sachs-Wolfe terms because of symmetry (only even functions of $\cos\theta$ contribute). The terms f_a, f_v and f_{sw} are trivially related to the Δ's defined in the previous section.

Since the form of the angular correlation function is already only an approximation, there is little additional loss of accuracy if the integral is also cast into various limiting forms. In particular, equation 3.3 can be recast in the form (notice that the limits on the angular integral have been changed since this integral is even and need only be evaluated over half its range)

$$C(\psi) = \frac{(2\pi)^4}{V} \int k^2 dk \, |\delta_m|^2 \, 2 \int_0^1 d\mu \left[f_v^2(k) \cos^2\theta + (f_a(k) + f_{sw}(k))^2 \right] \times$$
$$J_0(c(\tau_0 - \tau_m) k\psi \sqrt{1-\mu^2}) e^{-k^2\sigma^2\mu^2} \, . \tag{3.9}$$

In particular, two generic transfer functions can be defined,

$$T_1^2(k,\psi) = \int_0^1 d\mu J_0(x\sqrt{1-\mu^2}) e^{-y^2\mu^2} \, , \tag{3.10a}$$

and

$$T_2^2(k,\psi) = \int_0^1 d\mu \mu^2 J_0(x\sqrt{1-\mu^2}) e^{-y^2\mu^2} \, . \tag{3.10b}$$

where $x = c(\tau_0 - \tau_m)k\psi$ and $y = k\sigma$. Both of these functions can be approximated to a high degree of accuracy.

3.3.4.1 Small Angles: $x \ll 1$

When the argument of the Bessel function is small, a reasonable approximation is to truncate the series representation (see Gradshteyn & Ryzhik, hereafter GR, 1980, equation 8.441.1) at some low order polynomial. To take account of the possibility of modelling three-beam experiments, terms must be kept at least up to fourth order (see section 3.3.5). Then,

$$J_0(x\sqrt{1-\mu^2}) \simeq 1 - \frac{x^2}{4}(1-\mu^2) + \frac{x^4}{64}(1-\mu^2)^2 \equiv \sum_{i=0}^{2} a_i c^{2i} \, .$$

Using this approximation for the Bessel function and with the substitution, $t = y^2\mu^2$, the transfer functions can then be seen to be expressed in terms of incomplete gamma functions (GR, equation 3.381). The solution is

$$T^2 = \frac{1}{2y^{1+2m}} \sum_{i=0}^{2} \frac{a_i}{y^{2i}} \gamma(m+i+\frac{1}{2}, y^2) \, , \tag{3.11a}$$

where

$$a_0 = 1 - \frac{x^2}{4} + \frac{x^4}{64} \ , \ a_1 = \frac{x^2}{4} - \frac{x^4}{32} \text{ and } a_2 = \frac{x^4}{64} \ .$$

For T_1, $m = 0$ and for T_2, $m = 1$. The gamma functions obey a recurrence relation (GR equation 8.356),

$$\gamma(n+1, y^2) = n\gamma(n, y^2) - y^{2n}e^{-y^2},$$

and $\gamma(0.5, y^2) = \sqrt{\pi}\text{erf}(y)$. This approximation is accurate to better than 1% for $x < 1$.

3.3.4.2 Large Wavelengths: $y \ll 1$

In this case, it is reasonable to ignore the Gaussian in the transfer function altogether. A change of variables of the form $t = \sqrt{1-\mu^2}$ leaves the resulting integral in a standard form (GR 6.554, 6.567 for T_1 and T_2 respectively and using the definition of spherical Bessel functions), so that

$$T_1^2 = j_0(x) \ , \tag{3.12a}$$

$$T_2^2 = \frac{j_1(x)}{x} \ . \tag{3.12b}$$

Again, this approximation is accurate to better than 1% when $y < 0.1$.

3.3.4.3 $x \gg 1$, $y \gg 1$

When $y \gg 1$, the upper limit of the integral can be extended to infinity since the Gaussian term dominates at even moderate values of μ. Also, since this implies that the dominant contribution to integral is mostly where $\mu \sim 0$, the argument of the Bessel function is also large if $x \gg 1$. In this limit, the Bessel function has the asymptotic form

$$J_0(z) \sim \sqrt{\frac{2}{\pi z}} \cos\left(z - \frac{\pi}{4}\right) \ .$$

Since μ is small, $\sqrt{1-\mu^2} \sim 1 - \frac{1}{2}\mu^2$. Further, if the variable t is defined by $t = \mu^2$, then

$$T^2 = \frac{1}{2\pi x} \int_0^\infty (1 - \frac{1}{2}t)^{-1/2} \cos(x - \frac{\pi}{4} - \frac{1}{2}xt) e^{-y^2 t} [t] t^{-1/2} dt \ .$$

The $[t]$ is present in T_2 only. Again, since t is small, it is reasonable to say

$$(1 - \frac{1}{2}t)^{-1/2} \simeq 1 + \frac{1}{4}t \simeq e^{t/4} \ .$$

With this approximation, and expanding the cosine term, leaves integrals of the form

$$\int_0^\infty e^{-\beta t} t^{\nu-1} \begin{cases} \cos \delta t \\ \sin \delta t \end{cases} dt \,,$$

which are given by GR equations 3.944.5 and 3.944.6. Regathering all the resulting cosine and sine terms gives the required result

$$T_m^2 = \frac{1}{\sqrt{2\pi x}} \frac{\Gamma(\nu)}{(\beta^2+\delta^2)^{\nu/2}} \cos\left(\phi - \nu \arctan\left(\frac{\delta}{\beta}\right)\right) \,, \tag{3.13}$$

where $\beta = y^2 - \frac{1}{4}$, $\delta = x/2$, $\phi = x - \frac{\pi}{4}$ and $\nu = \frac{1}{2}$ for $m = 1$ and $\nu = \frac{3}{2}$ when $m = 2$.

3.3.4.4 $x \sim 1, y \sim 1$

This is the most difficult regime in which to approximate the transfer functions accurately. In practice, this regime does not contribute significantly to the radiation fluctuations however. There are two possible methods of obtaining more accurate answers than those already given. When $y \lesssim 1.7$, the Gaussian term can be expanded as a power series so that (GR, equation 6.567)

$$T^2 = \sum_{n=1}^{\infty} \frac{(-1)^n}{n!} y^{2n} 2^{n+m} \frac{\Gamma(n+\frac{1}{2}+m)}{\sqrt{\pi}} x^{-(n+m)} j_{n+m}(x) \,. \tag{3.14}$$

For T_1, $m = 0$ and for T_2, $m = 1$. The spherical Bessel functions obey a recursion relation of the form

$$j_{n+1}(x) = \frac{2n+1}{x} j_n(x) - j_{n-1}(x) \,.$$

In practice, the series can be truncated at relatively low values of n for $y \lesssim 1.7$. A reasonable value is $n \sim 8$.

When $y \gtrsim 1.7$, the approximation derived for the case $x \gg 1$ can be used. Since $y \not\gg 1$, the expansion of $\sin\theta$ in terms of $\cos\theta$ can be carried out to one higher order. Then

$$(1-t)^{1/2} \simeq 1 - \frac{1}{2}t + \frac{1}{8}t^2 \,.$$

Treating the extra term as being small gives

$$(1 - \frac{1}{2}t + \frac{1}{8}t^2)^{-1/2} \simeq 1 + \frac{1}{4}t + \frac{1}{32}t^2 \simeq e^{t/4} \,.$$

Hence, the addition of this term is solely equivalent to including

$$\cos(x(1 - \frac{1}{2}t + \frac{1}{8}t^2) - \frac{\pi}{4}) \simeq \cos(x(1-\frac{1}{2}t) - \frac{\pi}{4}) - \frac{1}{8}xt^2 \sin(x(1-\frac{1}{2}t) - \frac{\pi}{4}) \,.$$

The first term here is the same as derived previously. The second term gives rise to an additional contribution. As before the sine term can be expanded into factors depending on $\sin(xt/2)$ and $\cos(xt/2)$, and equations 3.944.5 and 3.944.6 of GR then give the solutions. Gathering together the resultant terms gives the complete transfer function as

$$T_m^2 = \frac{1}{\sqrt{2\pi x}}\left[\frac{\Gamma(\nu)}{(\beta^2+\delta^2)^{\nu/2}}\cos\left(\phi - \nu\arctan\left(\frac{\delta}{\beta}\right)\right)\right.$$
$$\left. -\frac{1}{8}x\frac{\Gamma(\nu+2)}{(\beta^2+\delta^2)^{(\nu+2)/2}}\sin\left(\phi-(\nu+2)\arctan\left(\frac{\delta}{\beta}\right)\right)\right] , \qquad (3.15)$$

where $\beta = y^2 - \frac{1}{4}$, $\delta = x/2$, $\phi = x - \frac{\pi}{4}$ and $\nu = \frac{1}{2}$ for $m = 1$ and $\nu = \frac{3}{2}$ when $m = 2$. The $\nu + 2$ factors in the additional term arise because of the presence of t^2 in the original expansion of $\cos(x(1 - \frac{1}{2}t + \frac{1}{8}t^2) - \frac{\pi}{4})$.

The approximations given here cover the entire range of the integral. If $x > 1$, then the approximation of section 3.3.4.2 is used when $y < 0.2$, section 3.3.4.4 when $0.2 < y < 3$, section 3.3.4.3 when $y > 3$, and if $x < 1$ the approximation of section 3.3.4.1 is used. These results were checked by calculating both integrals numerically and no disagreements were found at greater than the 1% level. There is a great saving in cpu time from using the approximations given here since the completely numerical calculation is not easy. The relative contributions of the various source terms to the correlation function are shown in figure 3.5 for the two models considered later. The values of $|\delta_m|^2 f_a^2 T_1^2$, $|\delta_m|^2 f_{sw}^2 T_1^2$ and $|\delta_m|^2 f_v^2 T_2^2$ are plotted separately.

3.3.5 Moments of the Radiation Power Spectrum

Just as in section 2.3.3.1, a two-dimensional Fourier transform can be defined on the sky. In terms of this, the radiation power spectrum is given by

$$C(\omega) = \frac{1}{(2\pi)^2}\int P_\kappa e^{i\kappa.\omega} d^2\kappa \, . \qquad (3.16a)$$

Here, $\omega = |\omega| = 2\sin\frac{\theta}{2}$ as before, and θ is a real angle on the sky. The corresponding inverse is

$$P_\kappa = \int C(\omega) e^{-i\kappa.\omega} d^2\omega \, . \qquad (3.16b)$$

The angular integral in both cases is trivial leaving a Hankel transform pair. In particular,

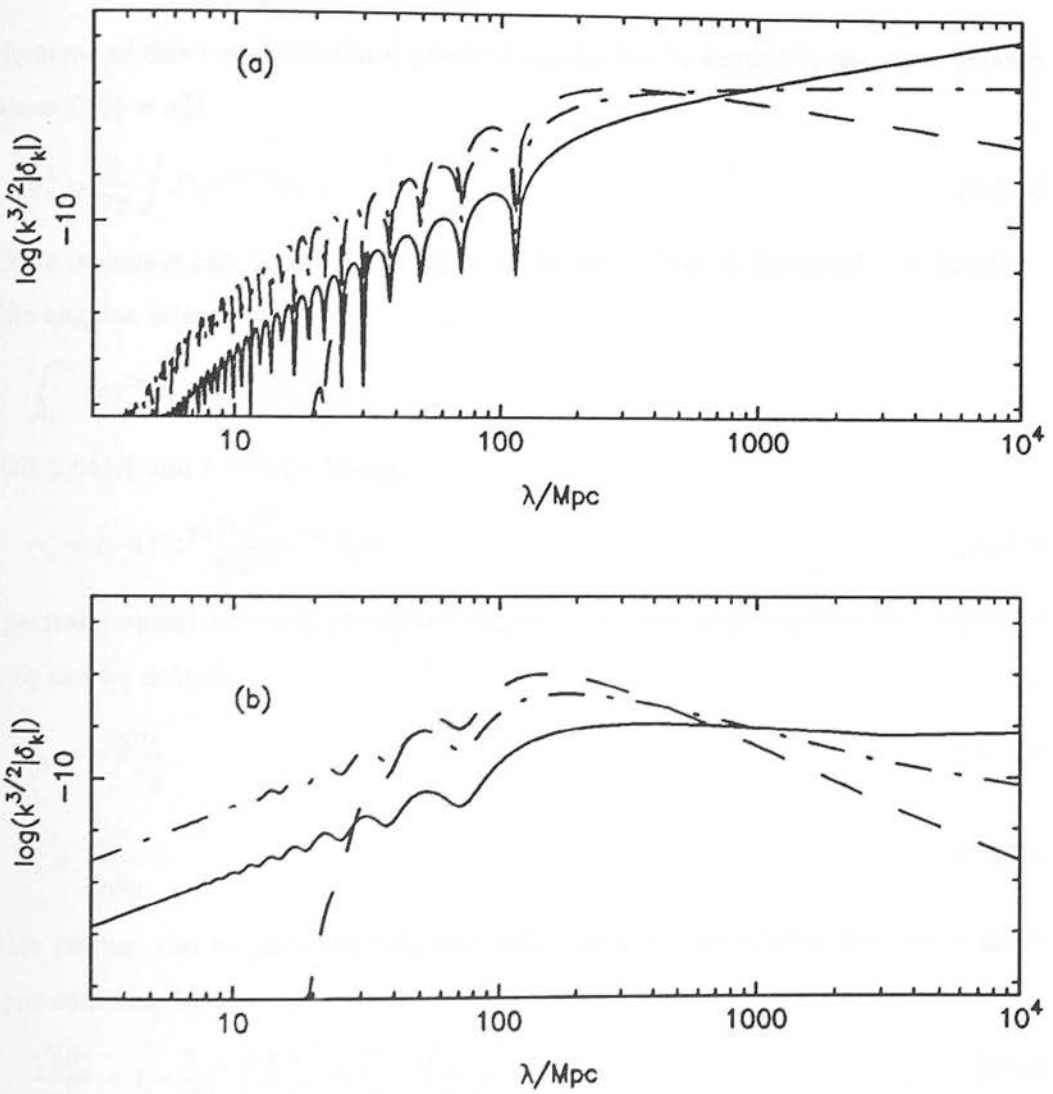

Figure 3.5: Contribution of the Sachs-Wolfe term (solid line), doppler (dashed) and adiabatic/isocurvature terms (dot-dash) to the integrand of the approximate angular correlation function (equation 3.9). Figure (a) shows an $n = 1$ adiabatic model, figure (b) an $n = -1$ isocurvature model. $\Omega = 1$ and $h = 0.5$ for both models.

$$C(\omega) = \frac{1}{2\pi} \int P_\kappa J_0(\kappa\omega) d\kappa \, . \tag{3.16c}$$

For what is required here though, this is not needed. If the $(2n)^{th}$ derivative of $C(\omega)$ with respect to ω is denoted by $C^{(2n)}(\omega)$, then

$$C^{(2n)}(\omega) = \frac{(-1)^n}{(2\pi)^2} \int P_\kappa \kappa^{2n+1} d\kappa \int_0^{2\pi} \cos^{2n} \phi d\phi \, .$$

Moments of this two-dimensional power spectrum can be defined in the usual manner (since $C(0) = \sigma_0^2$)

$$\sigma_n^2 = \frac{1}{2\pi} \int P_\kappa \kappa^{2n+1} d\kappa \, . \tag{3.17a}$$

These moments can be defined in terms of the derivatives of the correlation function. The angular integral gives

$$\int_0^{2\pi} \cos^{2n} \phi d\phi = \frac{2\pi(2n)!}{2^{2n}(n!)^2} \, ,$$

(GR 3.631.1 and 8.384.6). Hence,

$$\sigma_n^2 = (-1)^n 2^{2n} \frac{(n!)^2}{(2n)!} C^{(2n)}(0) \, . \tag{3.17b}$$

Spectral parameters (similar to those defined in either one or three dimensions, equation C.6) can be defined

$$\theta_* = \sqrt{2} \frac{\sigma_1}{\sigma_2} \, , \tag{3.18a}$$

$$\gamma = \frac{\sigma_1^2}{\sigma_0 \sigma_2} \, . \tag{3.18b}$$

This process can be inverted and, for small angles, the correlation function is given approximately by

$$\frac{C(\theta)}{\sigma_0^2} = 1 - \frac{1}{2}\gamma^2 \left(\frac{\theta}{\theta_*}\right)^2 + \frac{1}{16}\gamma^2 \left(\frac{\theta}{\theta_*}\right)^4 + \cdots \, . \tag{3.19}$$

This explains the necessity of keeping terms up to θ^4 in deriving equation 3.11a. For a two-beam experiment (see also section 2.3.3.2), the dominant term in the measured $\frac{\Delta T}{T}$ is the θ^2 term,

$$\left(\frac{\Delta T}{T}\right)^2 = \gamma^2 \sigma_0^2 \left(\frac{\theta}{\theta_*}\right)^2 \left(1 - \frac{1}{8}\left(\frac{\theta}{\theta_*}\right)^2\right) \, .$$

However, for a three-beam experiment the resultant temperature fluctuation is given by

$$\left(\frac{\Delta T}{T}\right)^2 = \frac{3}{8}\gamma^2\sigma_0^2\left(\frac{\theta}{\theta_*}\right)^4 .$$

Hence, a three-beam experiment isolates rather different behaviour in the true sky anisotropy from a two-beam one.

In practice, the moments can be calculated by considering equation 3.3. The form of this equation is very similar to that of equation 3.16c. The moments can be calculated simply by taking derivatives of the Bessel function with respect to ψ in equation 3.3. Then,

$$\sigma_n^2 = \frac{32\pi^4}{V}\int k^2 dk \int_0^1 d\mu \, |\Delta_k|^2 \left(c(\tau_0 - \tau_m)\right)^{2n} k^{2n}\left(1-\mu^2\right)^{2n} e^{-k^2\sigma^2\mu^2} . \qquad (3.20)$$

The integral over μ can be carried out using the same techniques as section 3.3.4.1, though this time the $\sin^{2n}\theta$ term is expanded in a power series. Given that,

$$\left(1-\mu^2\right)^{2n} = \sum_{i=0}^{n} a_i \mu^{2i} ,$$

then a new transfer function can be defined such that

$$\sigma_n^2 = \frac{32\pi^4}{V}\int k^{2+2n}|\delta_m|^2\left[(f_a(k)+f_{sw}(k))^2 T_3^2 + f_v^2(k)T_4^2\right]\left(c(\tau_0-\tau_m)\right)^{2n} dk , \qquad (3.21a)$$

where

$$T_m^2 = \frac{1}{2y^{1+2m}}\sum_{i=0}^{n}\frac{a_i}{y^{2i}}\gamma(m+i+\frac{1}{2},y^2) , \qquad (3.21b)$$

and $m = 0$ for T_3 and $m = 1$ for T_4.

For the real correlation function (equation 2.14), the moments are also fairly easy to calculate. The correlation function can be substituted into the integral defining the two-dimensional power spectrum, equation 3.16b, giving

$$P_\kappa = 2\pi\frac{2\pi^4}{V}\int dk k^2 \sum_{n=2}^{\infty}\frac{|\delta_n(k,\tau_0)|^2}{2n+1}\int_0^2 P_n\left(1-\frac{\omega^2}{2}\right)J_0(\kappa\omega)\omega d\omega ,$$

The solution to the angular integral is given by GR, equation 7.251.3, as

$$\int_0^2 P_n\left(1-\frac{\omega^2}{2}\right)J_0(\kappa\omega)\omega d\omega = 2\kappa^{-1}J_{2n+1}(2\kappa) .$$

Hence,

$$P_\kappa = 4\pi\frac{2\pi^4}{V}\kappa^{-1}J_{2n+1}(2\kappa)\int dk k^2\sum_{n=2}^{\infty}\frac{|\delta_n(k,\tau_0)|^2}{2n+1} .$$

Moments of this power spectrum are defined by equation 3.17a. The integral over κ gives

$$\int_0^\infty \kappa^{2m} J_{2n+1}(2\kappa) d\kappa = \frac{1}{2}\frac{(n+m)!}{(n-m)!} .$$

When $m > n$, $((n-m)!)^{-1} = 0$. Hence,

$$\sigma_m^2 = \frac{1}{16}\frac{32\pi^4}{V}\int dk k^2 \sum_{n=2}^{\infty} \frac{|\delta_n(k,\tau_0)|}{2n+1}\frac{(n+m)!}{(n-m)!} . \tag{3.22}$$

For the approximate correlation function outlined in section 2.4.3.1, a similar analysis can be carried out, but using the functions $\tilde{\delta}$ defined there. An equation like 3.22 is again the result, but the sum over the $\tilde{\delta}_n$ at the current epoch is replaced by the radiation moments at an earlier time as before. Now however, the presence of the extra factorial terms when $m \neq 0$ spoils the trick (see the steps following equation 2.21) of replacing one of the sums over the spherical Bessel functions. This sum is

$$S(m) = \sum_0^\infty (2n+1)\frac{(n+m)!}{(n-m)!} j_n^2(kc\Delta\tau) .$$

When $m = 0$ this sum is unity. Otherwise, it was calculated numerically. The resultant moments are

$$\sigma_m^2 = \frac{1}{16}\frac{32\pi^4}{V}\int dk k^2 \sum_{n=2}^{\infty} \frac{\left|\tilde{\delta}_n(k,\tau_1)\right|}{2n+1} S(m) \times$$

$$-\frac{m!}{(-m)!}\left|\tilde{\delta}_0(\tau_0)\right|^2 - \frac{1}{3}\frac{(1+m)!}{(1-m)!}\left|\tilde{\delta}_1(\tau_0)\right|^2 . \tag{3.23}$$

Since the $m = 2$ moment is largely dominated by large k values, this approximate version is useful in extending the accurate equation, 3.22, into the large k limit. The approximate equation is fairly accurate when extended over much a larger range of k than is required here.

3.3.6 Results

The approximate methods outlined so far in this chapter have been used to calculate a scale invariant adiabatic model as in chapter 2. An isocurvature model with $n = -1$ was also considered, but there are many problems in approximating the spectral parameters for this model as will be shown later. The adiabatic models used the forms for the source function described above. No attempt was made to 'fudge' any of the parameters when calculating correlation functions. As well as calculating an angular correlation function when all the source terms are included (dashed line), one was calculated for the Sachs-Wolfe contribution alone (dot-dash line). Both of these angular correlation functions are shown in figure 3.6(a), as is the 'true' correlation function from chapter 2. The error

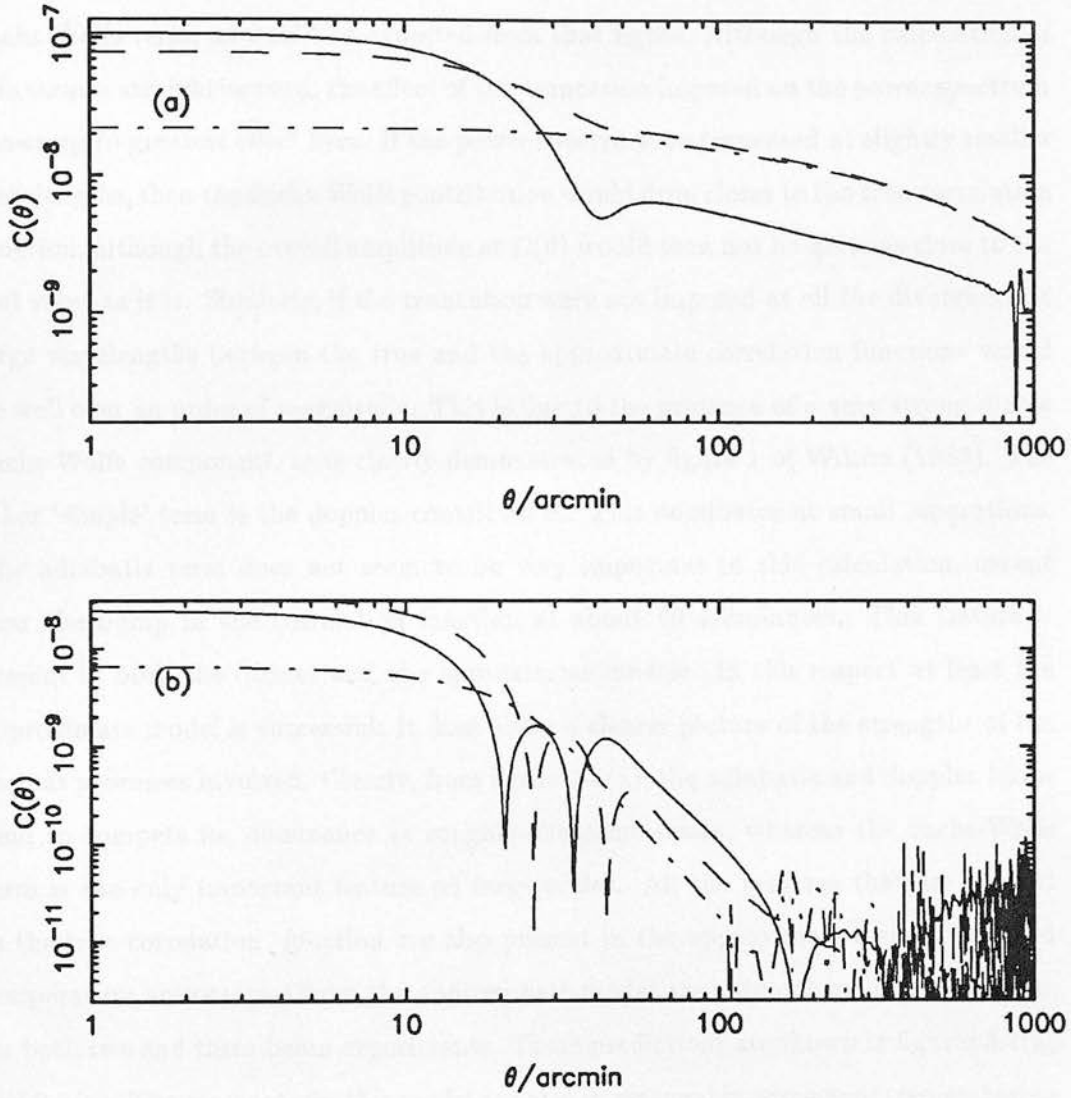

Figure 3.6: Approximate angular correlation functions. Figure (a) shows an $n = 1$ adiabatic model, figure (b) an $n = -1$ isocurvature model. The solid line represents the 'true' correlation function from chapter 2, the upper dashed line the approximate model considered here and the lower dot-dashed line the Sachs-Wolfe effect only.

in the approximate correlation function for $C(0)$ is only 35%. The divergence is greater at larger angles however. At 1000 arcminutes, the approximate correlation function is out by a factor of 2. This is still remarkably good considering the approximations that have been made in deriving this model. The relative contributions from the various source terms are shown in figure 3.5(a). The dominant term at large wavelengths is the Sachs-Wolfe term, as would be expected from that figure. Although the calculation of this term is straightforward, the effect of the truncation imposed on the power spectrum shows up to greatest effect here. If the power spectra were truncated at slightly smaller wavelengths, then the Sachs-Wolfe contribution would drop closer to the true correlation function, although the overall amplitude at $C(0)$ would then not be quite as close to the real value as it is. Similarly, if the truncation were not imposed at all the divergence at large wavelengths between the true and the approximate correlation functions would be well over an order of magnitude. This is due to the presence of a very strong dipole Sachs-Wolfe component, as is clearly demonstrated by figure 1 of Wilson (1983). The other 'simple' term is the doppler contribution. This dominates at small separations. The adiabatic term does not seem to be very important in this calculation, except near the bump in the correlation function at about 40 arcminutes. This feature is present in both the correct and the approximate models. In this respect at least the approximate model is successful: it does allow a clearer picture of the strengths of the various processes involved. Clearly, from figure 3.5(a), the adiabatic and doppler terms tend to compete for dominance at roughly the same scales, whereas the Sachs-Wolfe term is the only important feature on large scales. All the features that are present in the true correlation function are also present in the approximate form. Predicted temperature anisotropies from the approximate model are only out by a factor of two, for both two and three-beam experiments. These predictions are shown in figures 3.7(a) and 3.8(a). The moments for this model are also in reasonable agreement, remembering that neither correlation function has been smoothed. For the true correlation function, $\theta_* = 4.11'$ and $\gamma = 0.32$. For the approximate model, $\theta_* = 3.6'$ and $\gamma = 0.16$. The value of γ in the approximate model is sensitive to very small changes in the source terms. Increasing the contribution of the adiabatic term by an overall factor of 1.75 brings γ to very nearly the same value as in the real model, whilst leaving θ_* largely unchanged.

The isocurvature model considered had $n = -1$. Again, the approximate model

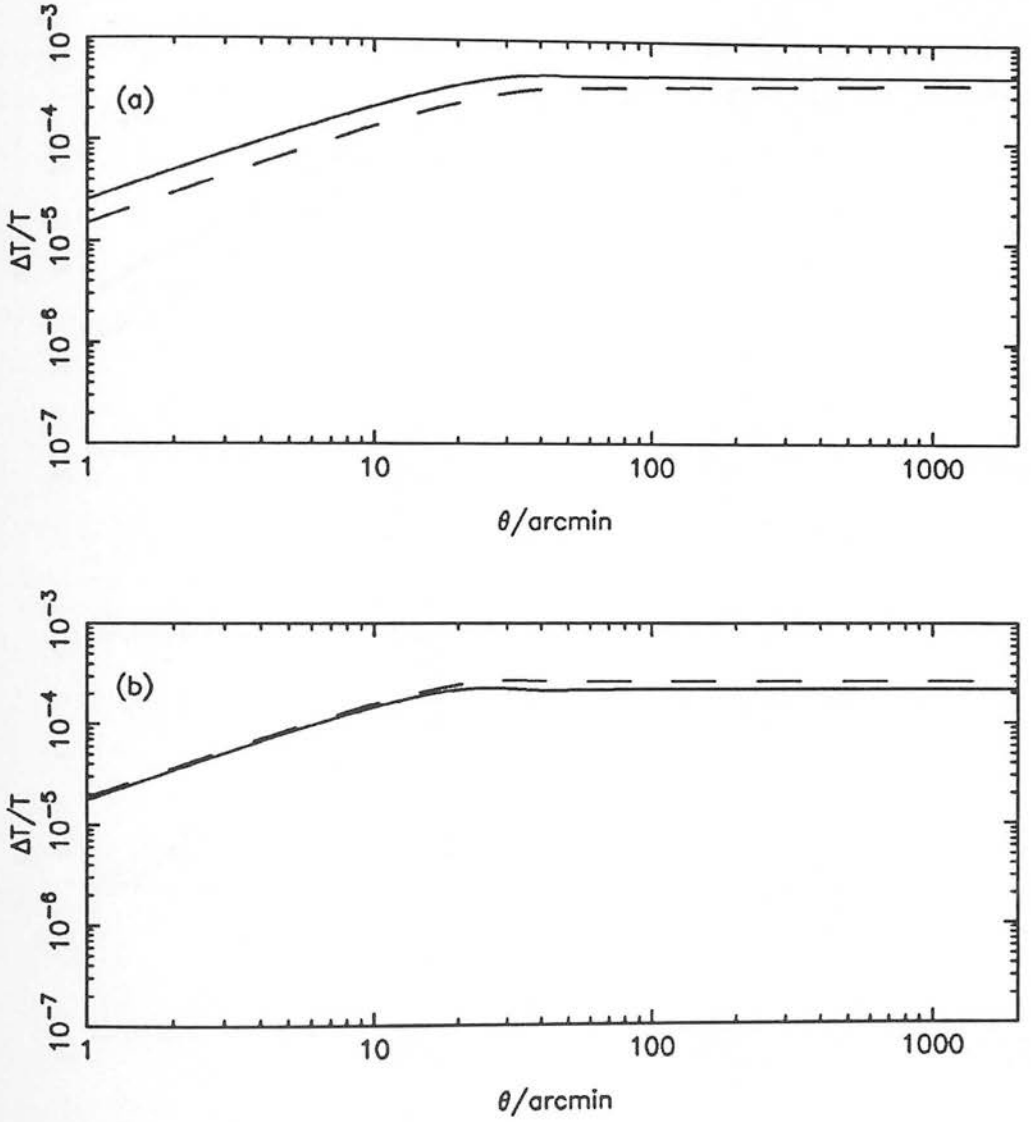

Figure 3.7: Predicted temperature anisotropies from the approximate model for a two-beam experiment. The solid line is the correct values from chapter 2 and the dashed lines the predictions from the approximate model. Figure (a) is the adiabatic model and figure (b) the isocurvature one.

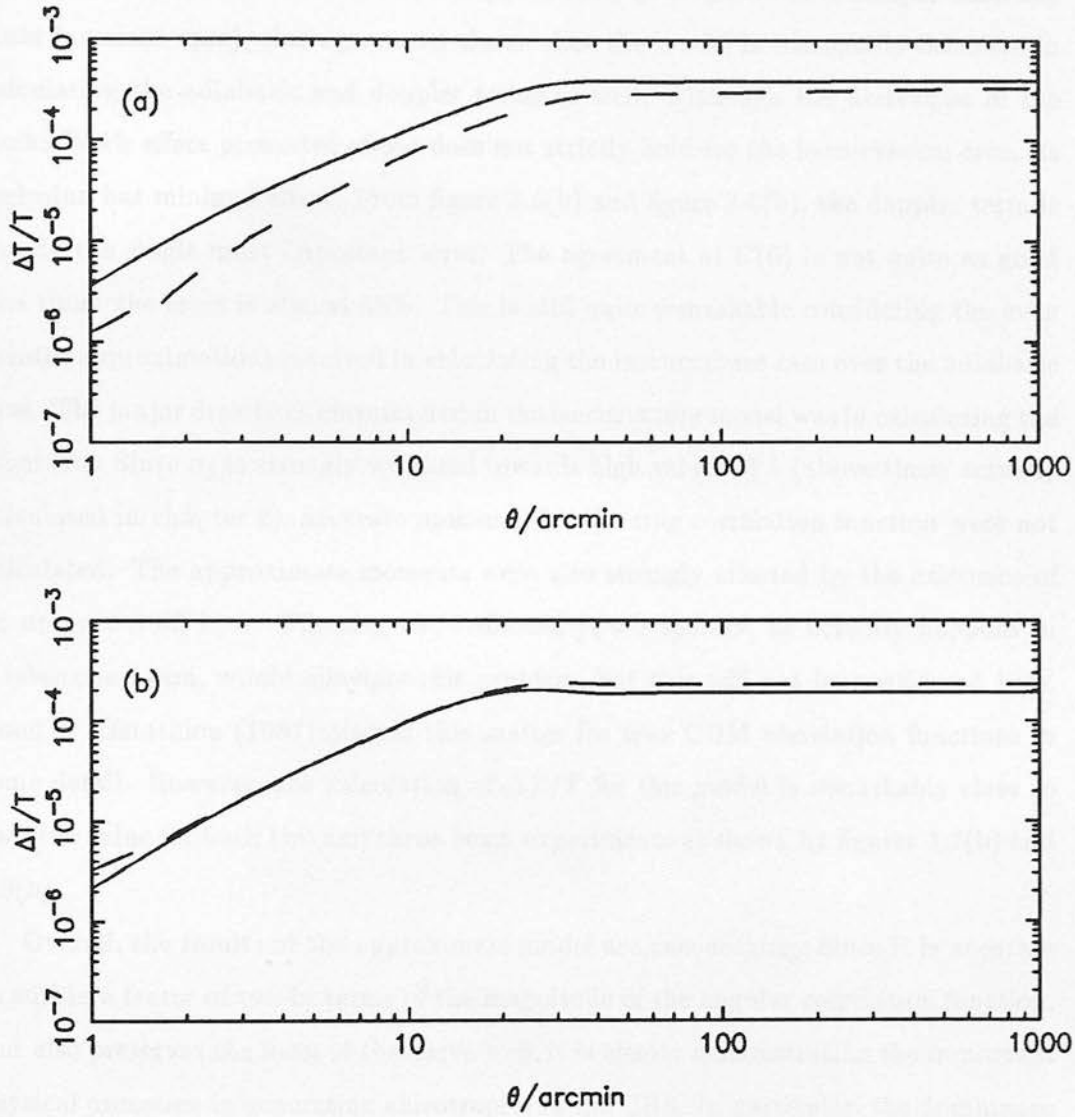

Figure 3.8: Predicted temperature anisotropies from the approximate model for a three-beam experiment. The solid line is the correct values from chapter 2 and the dashed lines the predictions from the approximate model. Figure (a) is the adiabatic model and figure (b) the isocurvature one.

(shown by the dashed line) fares quite well in comparison with the true correlation function. The excessive noise at large angles is due to small inaccuracies in calculating the approximate model. This shows up especially in the doppler component (the dot-dash line). Given that the dominant term in the isocurvature case considered was not the Sachs-Wolfe or isocurvature effects (since the power spectrum is steeper than the scale invariant case), this agreement shows that the model is reasonably accurate in calculating the adiabatic and doppler terms as well. Although the derivation of the Sachs-Wolfe effect presented above does not strictly hold for the isocurvature case, its inclusion has minimal effect. From figure 3.5(b) and figure 3.6(b), the doppler term is clearly the single most important term. The agreement at $C(0)$ is not quite as good this time: the error is almost 45%. This is still quite remarkable considering the even greater approximations involved in calculating the isocurvature case over the adiabatic case. The major drawback encountered in the isocurvature model was in calculating the moments. Since σ_2 is strongly weighted towards high values of k (above those actually calculated in chapter 2), accurate moments for the true correlation function were not calculated. The approximate moments were also strongly affected by the existence of an upper cut-off in k. Filtering the radiation power spectra, as actually happens in a telescope beam, would alleviate this problem, but this will not be considered here. Bond & Efstathiou (1987) discuss this matter for true CDM correlation functions in some detail. However, the calculation of $\Delta T/T$ for this model is remarkably close to the true value for both two and three-beam experiments as shown by figures 3.7(b) and 3.8(b).

Overall, the results of the approximate model are encouraging. Since it is accurate to within a factor of two in terms of the magnitude of the angular correlation function, and also preserves the form of the curve well, it is clearly demonstrating the important physical processes in generating anisotropies in the CBR. In particular, the dominance of the Sachs-Wolfe term at large angles is clearly shown for the adiabatic case. Equally clear is the strength of the doppler term for the isocurvature model. In short, these approximate models provide a good way of quantitatively understanding the characteristic amplitude, $C(0)$, and, in principle, the scale, θ_* of CBR fluctuations. Even for more detailed aspects such as a consideration of two or three beam experiments, much of the functional form of $\Delta T/T$ as a function of angular scale is reproduced, and this encourages a greater examination of possible improvements to this model. It may be

possible to use these techniques as a method of interpolating known accurate solutions into other models, calibrating the approximate method from the accurate one, allowing a greater sampling of parameter space than would otherwise be feasible.

Chapter 4

Large Scale Clustering

4.1 Introduction

The existence of large scale clustering poses a severe test for any theory of galaxy formation. The observed cluster-cluster two point correlation function (Bahcall & Soneira 1983; Sutherland 1988) remains positive out to at least $30h^{-1}$ Mpc and possibly to even larger scales, though the result there is not clearly significant (Ling, Frenk & Barrow 1986). It has a greater amplitude than the galaxy-galaxy two point correlation function, though there is uncertainty about the exact amplitude. The observed correlation function is well fitted by:

$$\xi_{cc}(r) \propto r^{-1.8} . \tag{4.1}$$

Sutherland gives the correlation length of ξ_{cc} as $14h^{-1}$ Mpc; Bahcall & Soneira give the larger value of $25h^{-1}$ Mpc. These values are adopted as limits to the observed cluster-cluster correlation function in this chapter.

As mentioned in section 1.3.2, recent attention in galaxy formation theory has focussed on the statistics of Gaussian random fields (Peacock & Heavens 1985; BBKS 1986), with maxima of the density field identified as the sites of proto-objects. The statistical properties of the Gaussian field then determine the properties of this set of proto-objects. Kaiser (1984) suggested that the enhanced clustering seen when moving up in scale from galaxies to clusters could have a statistical origin if clusters formed preferentially in overdense regions. Applying the model of high-peak biasing in a random Gaussian field to the correlation function of Abell clusters could thus conceivably explain the observed result in a simple manner.

All of the basic models in which structure in the universe grows from initially small fluctuations through their own self gravity can be considered as examples of Gaussian fields as long as the density field is still linear. In particular the popular Cold Dark Matter (CDM) dominated models can be considered as such a field, if the small scale power (which acts like noise) is filtered out. Non-linear evolution introduces deviations from a purely Gaussian character. Fortunately, the density field when filtered on cluster

scales is only marginally non-linear, so that the positions of the peaks (and hence the correlation function) will be only slightly perturbed away from the predictions of linear theory.

In principle, the correlation function of peaks in a three dimensional Gaussian field can be calculated, but for a given two point correlation function this involves a fourteen dimensional integral (each field point has an associated peak height, δ, its three first derivatives, $\nabla_i\delta$, and the six distinct elements of the second derivatives, $\nabla_i\nabla_j\delta$: for peaks the first derivatives are zero leaving another 2×7 terms which must be integrated over) that must be done numerically because of nonzero cross-correlations between different field points (see Section VI of BBKS). It is possible to simplify the problem in the limit that derivatives of the autocorrelation function are negligible compared to the autocorrelation function itself. This approach is not valid if clusters are being modelled, since on large scales the canonical scale-invariant power spectrum is close to a power law: $P(k) \propto k$.

In contrast, the correlation function of peaks in a simple one dimensional field can be calculated in a fairly straightforward fashion. Here, only four integrals are required. The one dimensional case will be used both as a guide, to show how the behaviour of the peak-peak correlation function might be expected to behave in the proper three dimensional case, and as an approximation to the three dimensional peak-peak correlation function, by considering one dimensional slices through a three dimensional density field. For the full three dimensional case a static Monte-Carlo simulation of the density field was created and the correlation function of the peaks in this simulation was calculated directly.

As well as the two approaches outlined above, comparisons were also sought with the various other approximate methods used in the past. Jensen & Szalay (1986) (hereafter JS) give an exact answer to the related problem of the correlation function of all *regions* of a density field above a given threshold. Obviously, in the limit that this threshold becomes infinite, these regions must be peaks in the density field. Methods similar to this have been used by Silk & Vittorio (1987) to give an estimate of the true peak-peak correlation function. Such estimates are not necessarily an accurate guide to the correlation function of the peaks. A new approximation, based on the framework given by JS, is presented here. This is more accurate than the simple application of JS type formalisms used in the past, although

not as accurate as the one dimensional slice described above.

The one dimensional case will be considered first. The derivation of the one dimensional peak-peak correlation function is presented in appendix C. The application of this result is considered in section 4.2. In section 4.3, the Monte-Carlo simulations used for the full three dimensional density field are described. Section 4.4 presents the approximations based on the JS result and comments on their accuracy. The approximation to the three dimensional correlation function based on taking a slice through a three dimensional density field is also presented here. Section 4.5 discusses the problems with the approach presented here, of calculating correlation functions using filtered power spectra.

4.2 One Dimensional Correlations

4.2.1 Overview

The n-point peak-peak correlation function in one dimension can be calculated, for small n, using simple numerical methods, since only $2n$ integrals are involved. The advantage of doing this calculation is that it allows a more detailed examination of the behaviour of the correlation function in those regimes where the approximate methods given by BBKS for three dimensions would break down. Only the two-point function will be considered here.

Two features are of particular interest: the first is the amplitude of peak-peak correlation function, ξ_{pk-pk}, compared to the autocorrelation function, $\xi(r)$; the other is the behaviour of ξ_{pk-pk} as it crosses zero. The simplest approximations all imply that $\xi_{pk-pk} = 0$ when the autocorrelation function $\xi(r) = 0$. However, as was shown by Otto, Politzer & Wise (1986), the constraint of lying at a peak introduces an anticorrelation into the final result. Therefore, ξ_{pk-pk} should cross zero (going from positive correlations to negative correlations) at a radius within that at which $\xi(r)$ crosses zero. The magnitude of this induced anticorrelation is therefore clearly important in considering the model of high peak biasing as outlined in this chapter.

The results of this section will be used to check the results found in section 4.3 from the Monte-Carlo study of the full three dimensional density field. They will also prove useful when the approximation (described in section 4.4) of considering ξ_{pk-pk} in three dimensions to be well modelled by ξ_{pk-pk} of a one dimensional slice through that field

is used.

4.2.2 Method

The derivation of ξ_{pk-pk} is given in appendix C. For convenience, the basic results are also presented here. In the calculation of ξ_{pk-pk} the values of the density field and its first two derivatives at each field point are needed. Consider the vector

$$\mathbf{y}^{\mathbf{T}} \equiv (\delta_1, \delta_1', \delta_1'', \delta_2, \delta_2', \delta_2'') \,. \tag{4.2a}$$

The indices refer to the separate field points. The covariance matrix of the set of random variables $\{y_i\}$ is M_{ij}:

$$M_{ij} \equiv \langle y_i y_j \rangle \,. \tag{4.2b}$$

Then, the joint probability distribution for a one dimensional Gaussian random field considered at two distinct field points is

$$P(\mathrm{y})\, d^6y = \frac{e^{-Q}}{[(2\pi)^6 \det M]^{1/2}}\, d^6y \,, \tag{4.3a}$$

where:

$$Q \equiv \frac{1}{2}\, \mathbf{y}^{\mathbf{T}}.\mathbf{M}^{-\mathbf{1}}.\mathbf{y} \,. \tag{4.3b}$$

The following definition for the Fourier transform pair will be used throughout:

$$\delta(x) = \frac{L}{2\pi} \int_{-\infty}^{\infty} \delta_k\, e^{ikx}\, dk \,, \tag{4.4a}$$

$$\delta_k = \frac{1}{L} \int_{-\infty}^{\infty} \delta(x)\, e^{-ikx}\, dx \,, \tag{4.4b}$$

where k is a comoving wavenumber.

Using this, the mean square density fluctuation is

$$\sigma_0^2 = \frac{L}{2\pi} \int_{-\infty}^{\infty} |\delta_k|^2\, dk \,, \tag{4.5}$$

and there is a corresponding set of spectral moments of higher order

$$\sigma_j^2 = \frac{L}{2\pi} \int_{-\infty}^{\infty} |\delta_k|^2\, k^{2j}\, dk \,. \tag{4.6}$$

It is convenient to introduce the spectral parameters γ and R_*:

$$\gamma = \frac{\sigma_1^2}{\sigma_2 \sigma_0} \,, \qquad R_* = \frac{\sigma_1}{\sigma_2} \,, \tag{4.7}$$

and the change of variables, $\nu = \delta/\sigma_0$ and $q = -\delta''/\sigma_2$.

In terms of these variables, the number density of peaks above a given threshold, ν_t, is

$$n_{pk}(\nu_t) = \frac{1}{[(2\pi)^3(1-\gamma^2)R_*^2]^{1/2}} \int_{\nu_t}^{\infty} \int_0^{\infty} q\, dq\, d\nu\, e^{-(\nu^2 - 2\gamma\nu q + q^2)/2(1-\gamma^2)} . \tag{4.8}$$

If the correlation function of peaks above a common threshold is considered, the peak-peak correlation function can be written as:

$$1 + \xi_{pk-pk}(r) = \frac{1}{n(\nu_t)^2} \int_{\nu_t}^{\infty} \int_{\nu_t}^{\infty} \int_0^{\infty} \int_0^{\infty} P(y : \delta'_{i,i=1,2} = 0)\, q_1\, q_2\, dq_1\, dq_2\, d\nu_1\, d\nu_2 . \tag{4.9}$$

One of these four integrals can be done analytically. The resulting correlation function has the form given by equation C.24. The other three integrals were calculated numerically. A standard procedure was followed for all three. Each integral can be considered to be of the general form

$$\mathrm{I} = \int e^{-t^2} f(t)\, dt , \tag{4.10a}$$

where $f(t)$ is a a smoothly varying function of t (generally involving terms such as $\mathrm{erfc}(c_1 \times t)$ and $\exp(c_2 \times t)$ with c_1, c_2 arbitrary constants). Using the substitution $y = t^2$ leaves integrals of the form

$$\mathrm{I} = \int e^{-y} f(\sqrt{y})\, \frac{dy}{2\sqrt{y}} . \tag{4.10b}$$

These integrals were solved using a Gaussian quadrature formula (see *e.g.* Press *et al* 1986, section 4.5).

$$\mathrm{I} = \sum_{i=1}^{n} w_i f(y_i) , \tag{4.11}$$

where the w_i are the weights and the y_i are the abscissae of the relevant Gauss-Laguerre quadrature. Checks were made on the accuracy of using this method by considering the solutions obtained by increasing n and also by comparing the numerical solution to the number density of peaks above a given threshold with the analytical form. A 16-point rule was found to give adequate accuracy in a reasonably small amount of cpu time for all three integrals.

The greatest source of error in calculating ξ_{pk-pk} was found to occur in calculating the set of moments given by equation C.16. For small separations ($r < R_*$), where the problems were greatest, the results could be checked against an asymptotic expansion to M_{ij}^{-1} found using the REDUCE algebraic reduction package. Careful control of

the numerical error in the calculation of the moments gave satisfactory answers. One consequence of the choice of integrator used for this however was that an upper limit to the value of k had to be imposed. For the models considered in the next section this was not a problem.

4.2.3 Results

The results can be illustrated by considering a series of generic models. The exact choice of each model is arbitrary but an attempt has been made to present a set which illustrate the range of possible behaviour. For convenience, one dimensional power spectra which have the form of a Gaussian filtered power law (note that the spectral index n should not be confused with the index in three dimensions) have been used. Each model can be defined by five parameters: the filter scale, the minimum and maximum wavelengths (the truncation at large wavelengths has no effect as long as the power on these scales is negligible: the truncation at small wavelengths mentioned previously has no effect as long as $R_f \gg \lambda_{min}$ since this is equivalent to $\lambda_{min} \sim 0$), the value of n and the threshold, ν_t. Table 4.1 shows the actual parameters chosen as well as the value of γ. Units are scaled in terms of r/R_*. Figure 4.1 shows the peak-peak correlation function and the autocorrelation function for each of the models.

Table 4.1: Model Parameters (1D)

model	R_f	λ_{min}	λ_{max}	n	ν_t	γ	$\langle\tilde{\nu}\rangle$	ν_{eff}
a	1.002	0.100	100.0	−1	1	0.447	1.185	0.774
b	1.002	0.100	100.0	−1	3	0.447	3.018	2.931
c	1.722	0.861	8.6	1	2	0.932	2.006	1.998
d	1.181	0.118	11.8	−1	1	0.824	1.018	0.888
e	1.181	0.118	11.8	−1	2	0.824	2.000	1.996
f	1.017	0.339	33.9	−1	2	0.577	2.024	1.906

Some points should be made about general features common to all of these models. The small separation behaviour can be generally described by $\xi_{pk-pk} \sim -1$ out to several times R_*. Since $R_* \sim R_f$, there is effectively no structure on scales less than this and therefore $\xi_{pk-pk} < 0$ and indeed will tend towards -1. The inversion of the covariance matrix found using the REDUCE package helps demonstrate why this should be. The solution for $r = 0$ is always singular, as can be seen from the form

of the covariance matrix. Expanding the functional form of the covariance matrix and discarding all terms of order r^3 , the behaviour of the dominant term in the inverse matrix was found to be $M_{11}^{-1} \propto 1/r^2$. If this is substituted into equation C.24, it can be seen that the small r behaviour of the peak-peak correlation function is dominated by an $e^{-R_*^2/r^2}$ term. Hence, for $r < R_*$, the peak-peak correlation function must tend towards -1 rapidly.

The persistence of this behaviour as $r > R_*$ in some models can be explained as follows. The peak-peak correlation function is *almost* like an amplified autocorrelation function: if $\xi(r) < 0$ for $r \sim R_*$, then $\xi_{pk-pk} \sim -1$. Models c and e exhibit this trend. Model d, which has the same parameters as model e but a lower threshold, shows a smaller amplification but the same general trend. Models a,b and f exhibit the counter trend where $\xi(r)$ is positive in this region and ξ_{pk-pk} tends away from -1 much more rapidly, once $r > R_*$.

The amplification of ξ_{pk-pk} relative to $\xi(r)$ is obvious from all the examples shown. The amplitude of $\xi_{pk-pk}/\xi(r)$ also scales well with the value of ν_t as would be expected from the simple arguments of Kaiser (1984). As will be shown in section 4.4 however, the scaling also depends on the value of γ, so that in model d, where $\nu_t = 1$, there is still a considerable amplification of the peak-peak correlation function.

The location of the zeroes of ξ_{pk-pk} does show the behaviour predicted in section 4.1. For those cases where the gradient of the autocorrelation function is large compared to the autocorrelation function itself, this term will have an appreciable effect on the structure of the covariance matrix, perturbing the zeroes away from the points where the autocorrelation function is zero. All models show this to some extent. The difference is slight where the autocorrelation function is 'flat' (i.e. its first derivatives are negligible compared to the autocorrelation function, $\xi' \ll \xi/R_*$) as in model b. Where the autocorrelation function is 'steep', as in model c, the difference is quite marked: almost a whole filter length separates the location of the first zeroes. Since the autocorrelation function will tend to flatten out around zero as $r \to \infty$ for most reasonable power spectra, this behaviour is important only at reasonably small r, but, in practice, it is this same region which is of most interest.

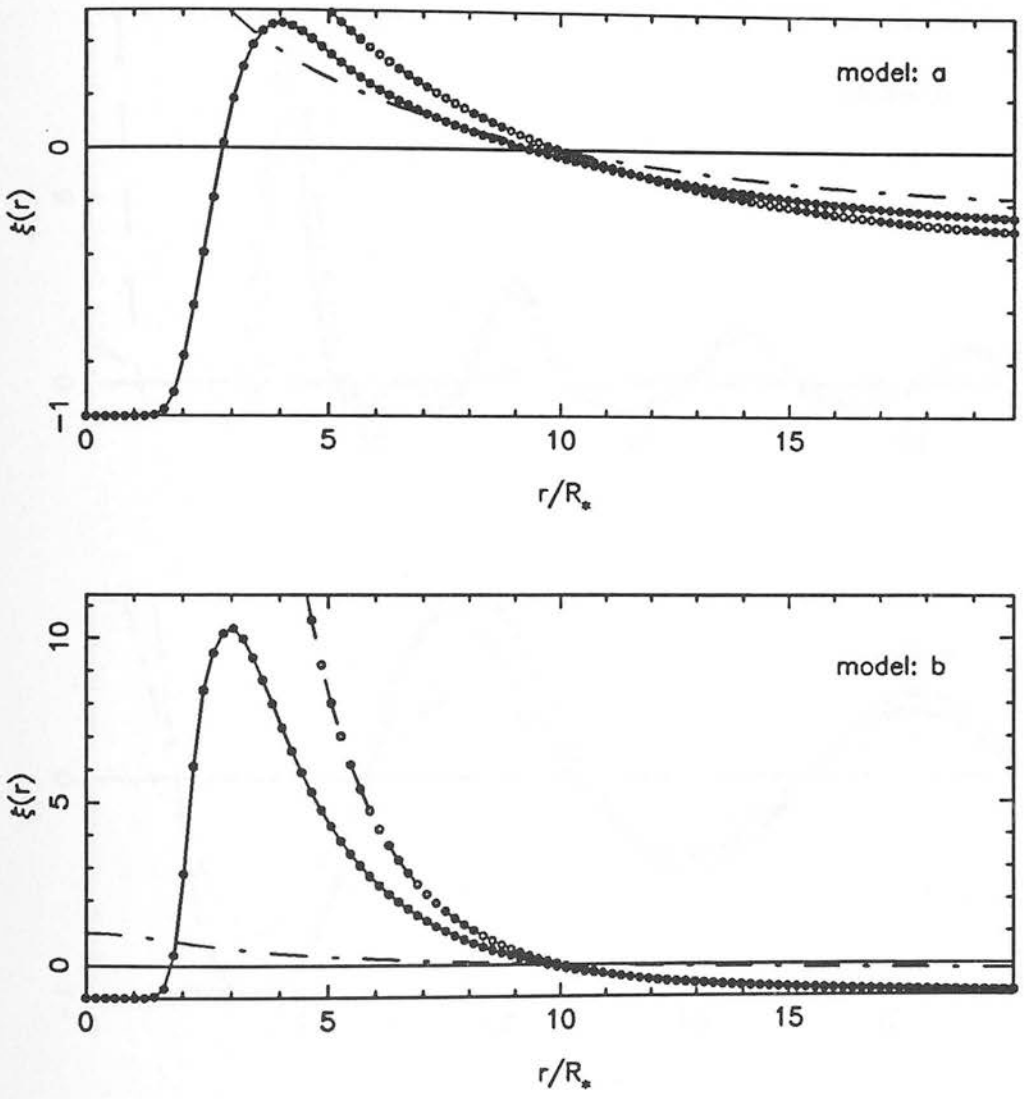

Figure 4.1: The one dimensional correlation functions. The solid line is the peak-peak correlation function, the dot-dash line the autocorrelation function and the dashed line the modification to the JS method described in section 4.4. Each model is as described in table 4.1.

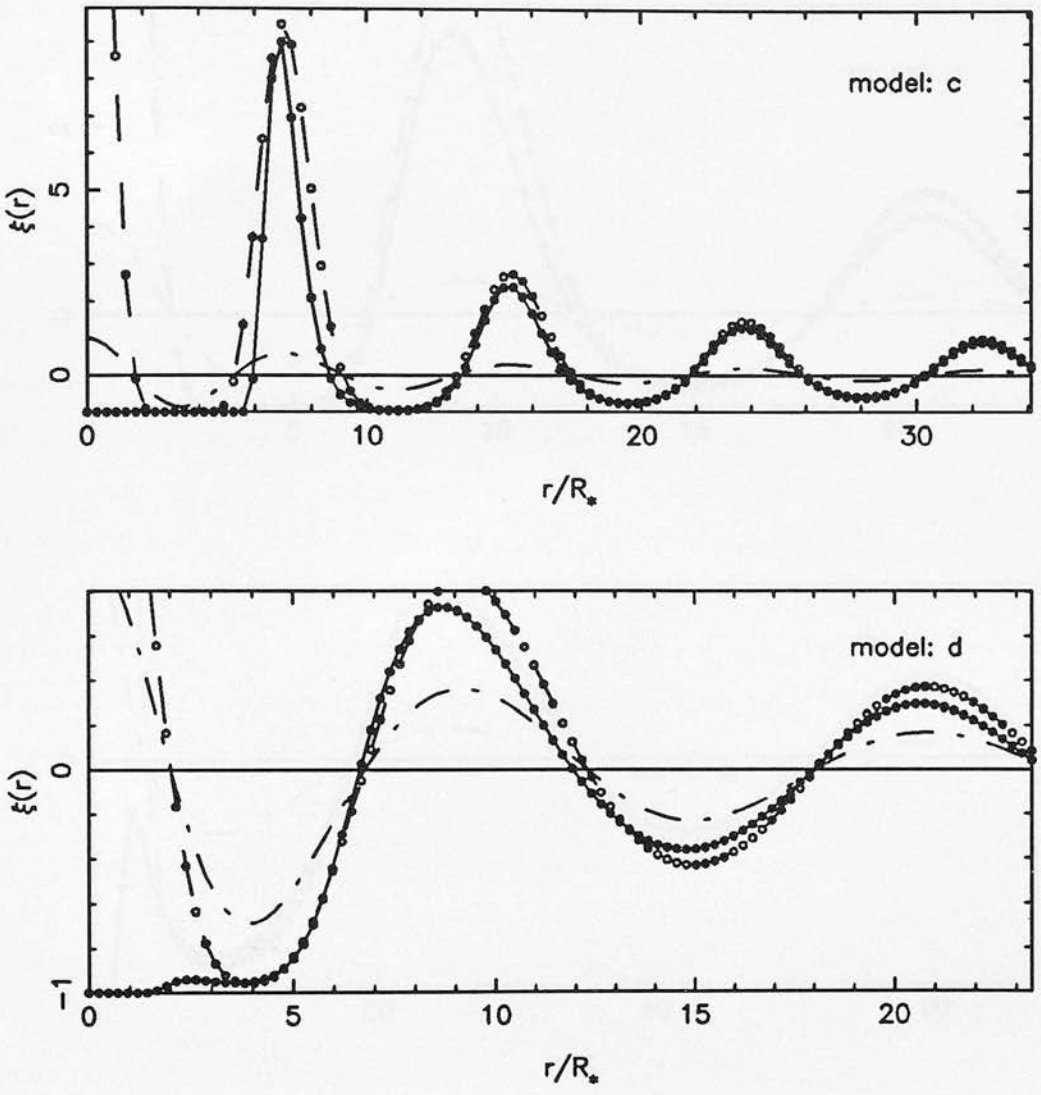

Figure 4.1: (*cont.*)

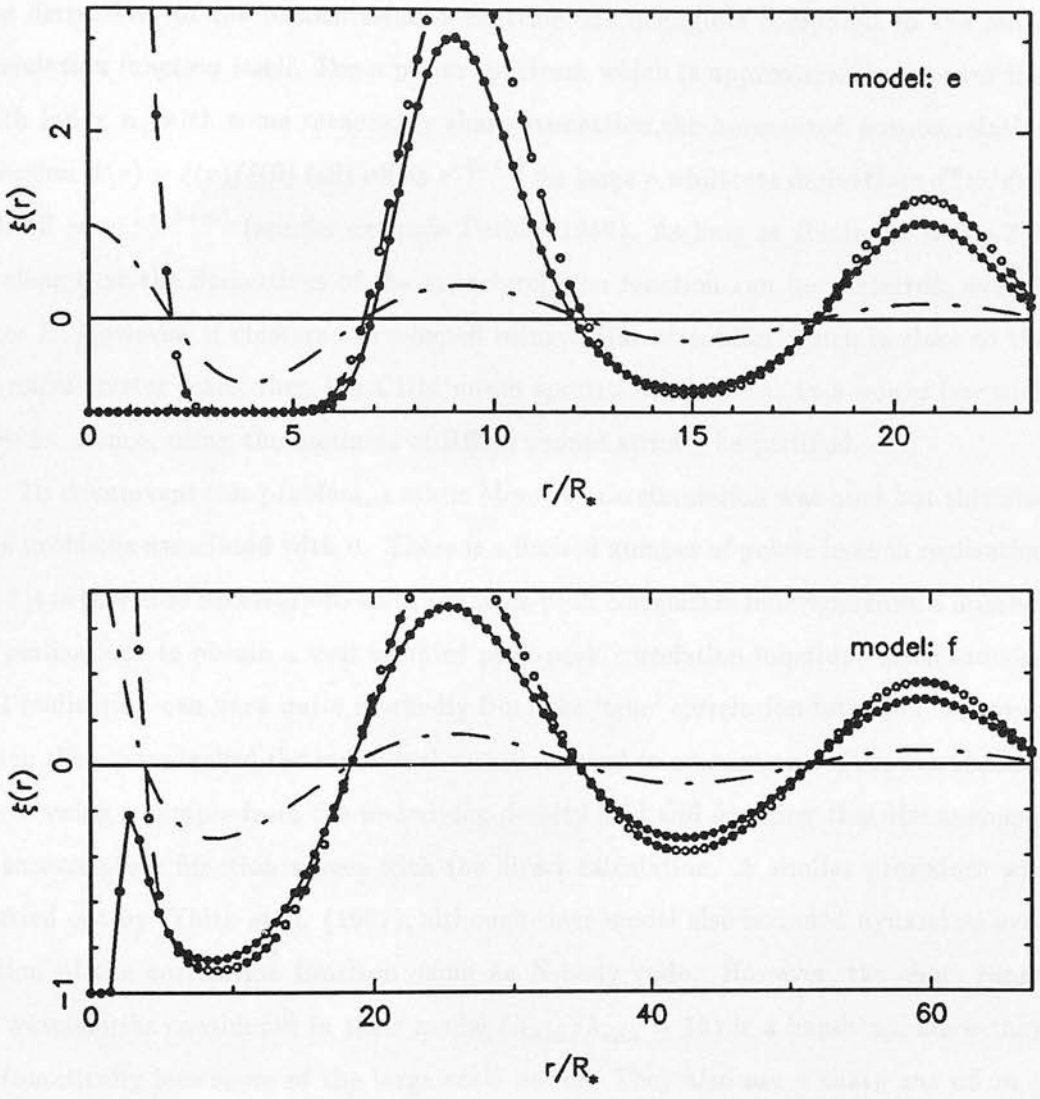

Figure 4.1: (*cont.*)

4.3 Three Dimensional Correlations

4.3.1 Overview

The methods derived by BBKS for calculating the correlation function of peaks in a three dimensional Gaussian density field are specifically for use in the limit that the derivatives of the autocorrelation function are negligible compared to the autocorrelation function itself. For a power spectrum which is approximately a power law with index n, with some reasonably sharp truncation,the normalised autocorrelation function $\psi(r) = \xi(r)/\xi(0)$ falls off as $r^{-(n+3)}$ for large r whilst its derivatives $d^m\psi/dr^m$ fall off as $r^{-(n+3+m)}$ (see for example Peebles 1980). As long as the index $n \sim -3$ it is clear that the derivatives of the autocorrelation function can be neglected, even if $\psi \sim 1$. However, if clusters are selected using a Gaussian filter which is close to the physical cluster scale, then the CDM power spectra will be close to a power law with $n \sim 1$. Hence, using the methods of BBKS cannot strictly be justified.

To circumvent this problem, a static Monte Carlo simulation was used but this also has problems associated with it. There is a limited number of points in each realisation and it is therefore necessary to stack the peak-peak correlation functions from a number of realisations to obtain a well sampled peak-peak correlation function. Each individual realisation can vary quite markedly from the 'true' correlation function: however, when these are stacked the individual variations tend to average out. This was checked by drawing a sample from the underlying density field and ensuring that the averaged autocorrelation function agrees with the direct calculation. A similar procedure was carried out by White *et al.* (1987), although their model also included dynamical evolution of the correlation function using an N-body code. However, the short range of wavelengths considered in their model ($\lambda_{max}/\lambda_{min} = 16$) is a handicap, since they automatically lose some of the large scale power. They also use a sharp cut off in k space which creates an artificial 'ringing' in the resulting correlation function. This causes their peak-peak correlation function to go negative at the artificially small scale of approximately $15h^{-1}$ Mpc. The effect of using different types of filter is considered further in section 4.5. It should be remembered that the filtering process is inherently imprecise. However, the basic choice adopted here is the same as BBKS, since a Gaussian filter balances the necessity of having to truncate the power spectrum in k space whilst suppressing grossly unphysical behaviour in the resulting correlation function.

The number density of peaks was matched to the observed number density of Abell clusters of richness class ≥ 1, $6 \times 10^{-6} h^3$ Mpc^{-3} . For a cube of volume $1.56 \times 10^7 h^{-3}$ Mpc^3 there should be approximately 94 such clusters: a close check was made to ensure that each cube had the right number of peaks for the given threshold. The selection criterion adopted was similar to that of BBKS and Kaiser (1984); in practice the filter scale used was $R_f = 5h^{-1}$ Mpc. The differential number density of peaks was integrated to get the number density of peaks above a given threshold (equation 4.11a of BBKS). Because of the nature of the problem a sharp threshold was assumed. The values of ν_t generated by this are given in table 4.2. It should be noted that any one single choice of model (R_f, ν_t) pair cannot be regarded as the only defensible one (*e.g.* Kaiser 1984). Nevertheless, the values given here are in the centre of the preferred range. The effect of altering this choice is discussed in greater detail in section 4.5.

The value $h = 0.5$ is used throughout. This value gives CDM the best chance of producing large-scale power, since physical length scales in CDM are proportional to $(\Omega h^2)^{-1}$.

4.3.2 Method

Given an initial power spectrum $P(k)$, a realisation of this density field can be created in a cube. For the CDM models, with $\Omega_B \ll \Omega$, the transfer functions, $T(k)$, of BBKS were used (see also Bond & Efstathiou 1984). The transfer functions for a standard baryonic universe were generated from the results of chapter 2. In each case the standard scale invariant initial spectrum was assumed ($n = 1$ for adiabatic, $n = -3$ for isocurvature). Each point in the cube then has an associated value $\delta_k = A\, k^{n/2}\, F(R_f, k)\, T(k)\, e^{i\phi_k}$, where $F(R_f, k)$ is a Gaussian filter, $F = e^{-k^2 R_f^2/2}$, and ϕ_k is a random initial phase. A FFT routine is then applied to the cube to give a sample of the density field in real space.

The initial cube contained 10^6 grid points; the minimum wavelength for each model was chosen in order to include all the significant power at small scales to minimise the problem of 'ringing' described above. For the flat adiabatic CDM model ($\Omega = 1$: as stated in chapter 1, the cosmological constant is assumed to be zero), the maximum wavelength was taken as $\lambda_{max} = 500$ Mpc; for the open adiabatic CDM model and the flat isocurvature model, 625 Mpc. The flat adiabatic baryonic model and the flat isocurvature baryonic model posed a problem since power extends over a much larger

range: the value λ_{max}= 500 Mpc was adopted for the adiabatic case, and 1000 Mpc for the isocurvature case. Cubes with a larger maximum wavelength were also considered; the large-wavelength truncation does cause a small amount of spurious ringing in the correlation functions, but this does not have an important effect on the results.

The grid spacing in the cubes was set by the practical requirement of being able to locate the peaks; Peacock & Heavens (1985) found that the minimum wavelength consistent with finding about 95% of all peaks in a cube was 4 cell units, ($\lambda_{max}/25$) Mpc. This is double the value given by the Nyquist criterion, ($\lambda_{max}/50$) Mpc. For large structures, such as those considered here, there is no problem in using the Nyquist value for λ_{min} when this gives a minimum wavelength that is as small as the scale of the objects. However if the Nyquist criterion gave a minimum wavelength greater than about 10 Mpc, the chosen cluster scale size, 4 cell units ([$\lambda_{max}/25$] Mpc) was imposed as the minimum. The power spectra and autocorrelation functions for the models are shown in figures 4.2 and 4.3.

Having created the density field, the peaks were isolated using the simple criterion that a cube maximum must have a greater amplitude than its 26 nearest neighbours. Using estimates of the first and second derivatives of the field at that point derived from the lattice points, the position and height of the true maxima can then be estimated. A more elegant alternative method (Hoffman 1988) is to use the initial power spectrum to calculate the first and second derivatives at each cube point and then do the FFT on these datasets as well. This unfortunately requires ten times as much storage as the method used here and would have reduced the dynamic range of our models to unacceptable levels.

The peak-peak correlation function for each cube was calculated using an algorithm (Hewett, private communication) that corrects for bias in catalogues where a small number of large objects (in the sense that they occupy a large fraction of the sample volume) are distributed in an inhomogeneous manner throughout the sample. Given a random catalogue of points, an estimator of the correlation function is:

$$\xi_{pk-pk}(r) = 2\,\frac{n_{ran}n_{pk-pk}(r)}{n_{pk}n_{pk-ran}(r)} - 1 \qquad (4.12)$$

where $n_{pk-pk}(r)$ is the number of pairs in the peak-peak catalogue, $n_{pk-ran}(r)$ is the number of pairs in the peak-random catalogue and n_{pk} and n_{ran} are the number of these objects in the catalogue. These individual correlation functions were then stacked, as

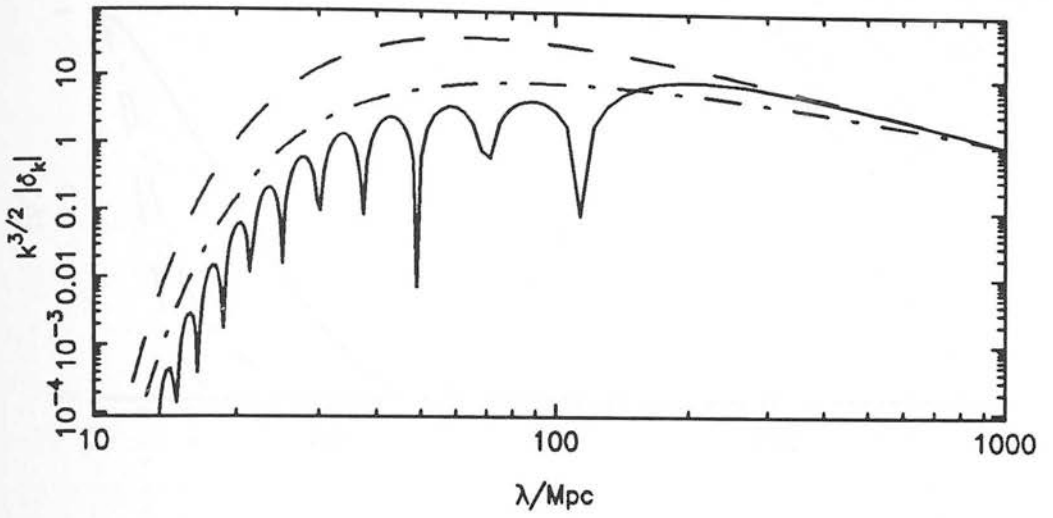

Figure 4.2: (a) The power spectra for the three dimensional adiabatic models. The solid line is the baryonic model, the dashed line the flat CDM model and the dot-dash line the $\Omega = 0.2$ CDM model. The normalisation is arbitrary.

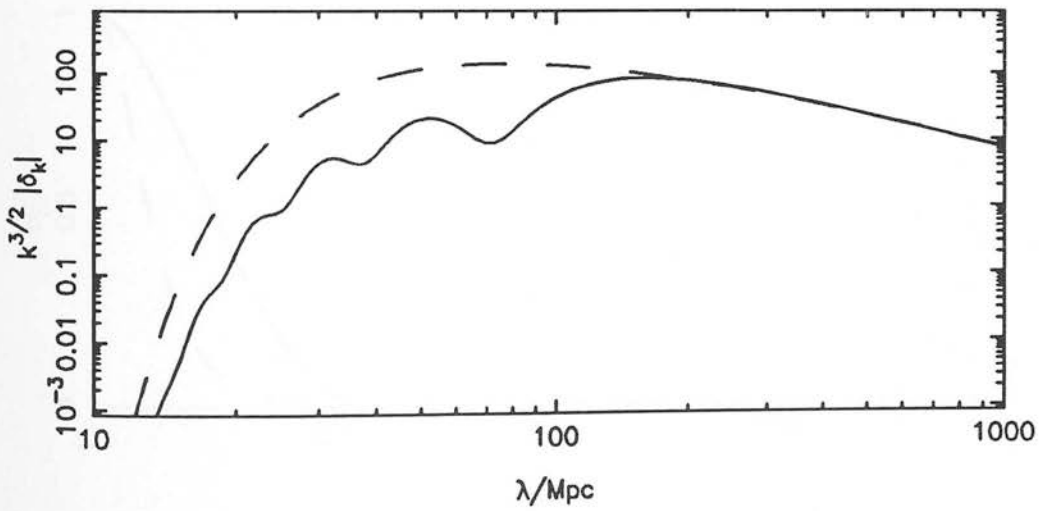

Figure 4.2: (b) The power spectra for the isocurvature models. The solid line is the baryonic model and the dashed line the flat CDM model. The normalisation is arbitrary.

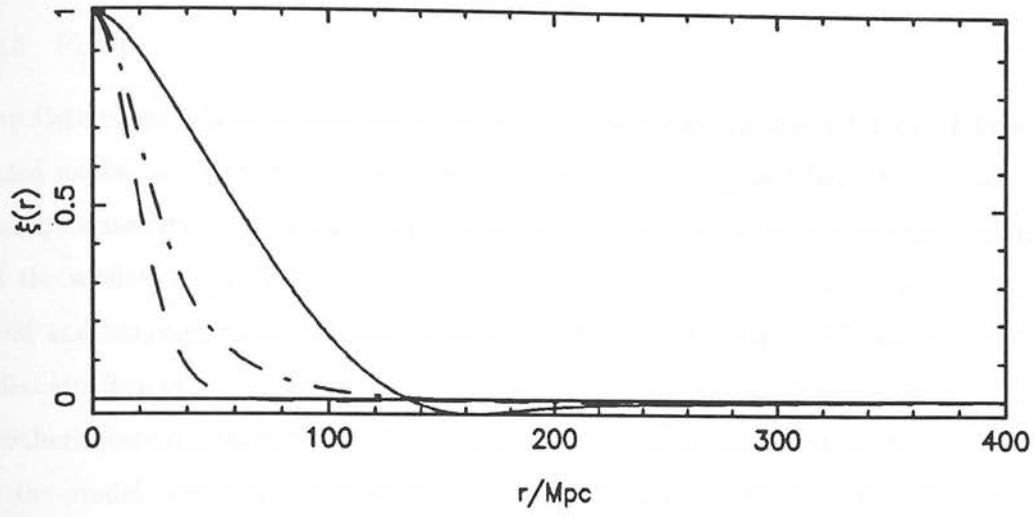

Figure 4.3: (a) The autocorrelation functions corresponding to the models shown in figure 4.2(a). All models are scaled so that $\xi(0) = 1$.

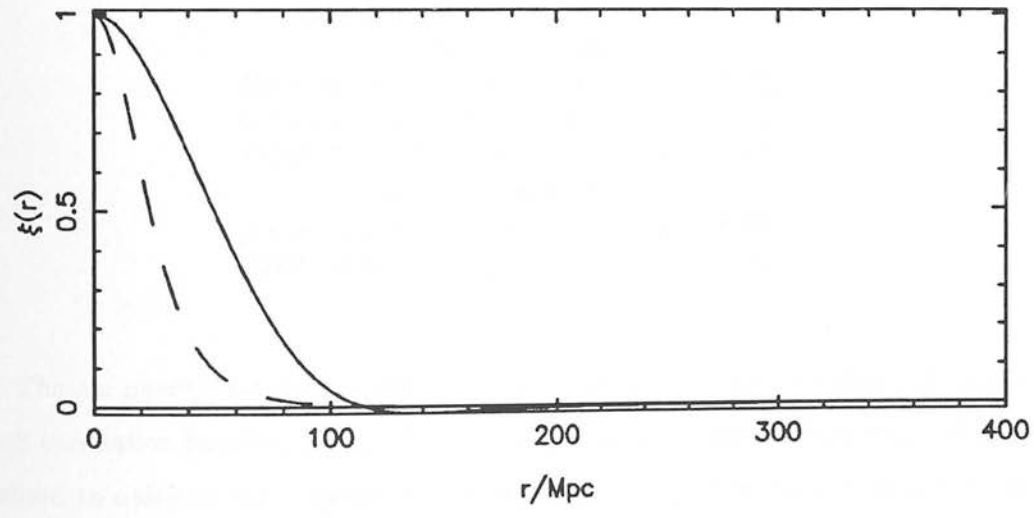

Figure 4.3: (b) The autocorrelation functions corresponding to the models shown in figure 4.2(b). All models are scaled so that $\xi(0) = 1$.

mentioned above, to give the ensemble average correlation function. The standard deviation obtained by comparing individual realisations with this average gives a measure of the uncertainty in the process.

4.3.3 Results

Five distinct models were considered: for adiabatic initial conditions, a flat CDM dominated model, an open ($\Omega = 0.2$) CDM dominated model and a flat baryon dominated model; for isocurvature initial conditions, a flat CDM model and a flat baryonic model. All the models considered had scale invariant initial conditions. The value of other CDM and baryonic models can be assessed from these. For the flat CDM model 50/40 (adiabatic/isocurvature) cubes were stacked, 15 for the open CDM model and 35/25 (adiabatic/isocurvature) for the baryonic model. It was necessary to use more cubes for the models which are calculated at smaller separations since the errors for scales within the filter scale are greater than Poissonian, and it is desirable to reduce these errors as much as possible.

Table 4.2: Model Parameters (3D) ($h = \frac{1}{2}$, $R_f = 10Mpc$)

model	γ	ν_t	$\langle\tilde{\nu}\rangle$	ν_{eff}
Adiabatic Models				
Baryons, $\Omega = 1$	0.45	1.59	1.28	0.69
CDM, $\Omega = 1$	0.74	2.81	2.15	1.73
CDM, $\Omega = 0.2$	0.66	2.48	1.85	1.39
Isocurvature Models				
Baryons, $\Omega = 1$	0.62	0.76	0.43	−0.66
CDM, $\Omega = 1$	0.71	2.61	1.95	1.51

The parameters for each model are given in table 4.2. Figure 4.4 shows the peak-peak correlation function for the 'clusters' as well as the autocorrelation function normalised to unity at zero separation. Note that all the models show a decline in the peak-peak correlation function as $r \to R_f$. As in one dimension, this indicates that the density field is being sampled near the mean cluster-cluster separation. This behaviour should not be compared to the actual ξ_{cc} since on small scales this will be dominated by dynamical evolution of the clustering, whereas here only the *statistical* part due to the biasing effect of long-wavelength modes is being considered. (see Section 4.6 for more discussion of this point). The technique as described should correctly model the

true cluster-cluster correlation function for scales larger than the filter scale and, for the reasons outlined above, cannot be expected to do the same for scales within the filter scale.

The major drawback of the flat adiabatic CDM model is that the peak-peak correlation function goes negative at about 50 Mpc compared with the simple prediction of about 80 Mpc (since this is where $\xi(r) = 0$). Similarly, the flat isocurvature baryonic model has a zero at about 70 Mpc compared to about 100 Mpc. These are the prime example of the possibility that $\xi_{pk-pk} = 0$ when $\xi(r) \neq 0$. The autocorrelation function for both models are relatively 'steep' (i.e. their first derivatives are non-negligible compared to the autocorrelation function, $|\nabla_i \xi| \not\ll \xi/R_*$) when ψ crosses the zero-line. For such a correlation function, just as in the one-dimensional models of the last section, there is no necessity that the zeroes of the two functions should coincide. In comparison, the other models, which have much 'flatter' autocorrelation functions, as $\psi \to 0$, show less evidence of this behaviour.

4.4 Approximate Methods

4.4.1 Overview

Although the methods described in section 4.3 give reliable results, they are extremely time consuming. Each single run (doing the FFT, locating and selecting the peaks and calculating the correlation function) required approximately two hours of cpu time on a VAX 11/780. Hence, the flat CDM model required about 100 hours of cpu time on its own. If an approximate method could be found that gave reliable answers it would clearly be preferable to the static Monte-Carlo method.

Two possible approaches are described in this section. The first involves an extension of the results of JS relating to the correlation function of all regions in a density field above a given threshold. An asymptotic form of the peak-peak correlation function has a very similar form to their result. One approximation is to use the density threshold given by this asymptote and substitute it into the JS formalism. The second method involves considering slices through a full three dimensional density field. The technique developed in section 4.2 can then be used on the resulting one dimensional slice. Although the peaks in this slice cannot be directly equated to the peaks in the three dimensional field, for even moderate thresholds the density contours become sim-

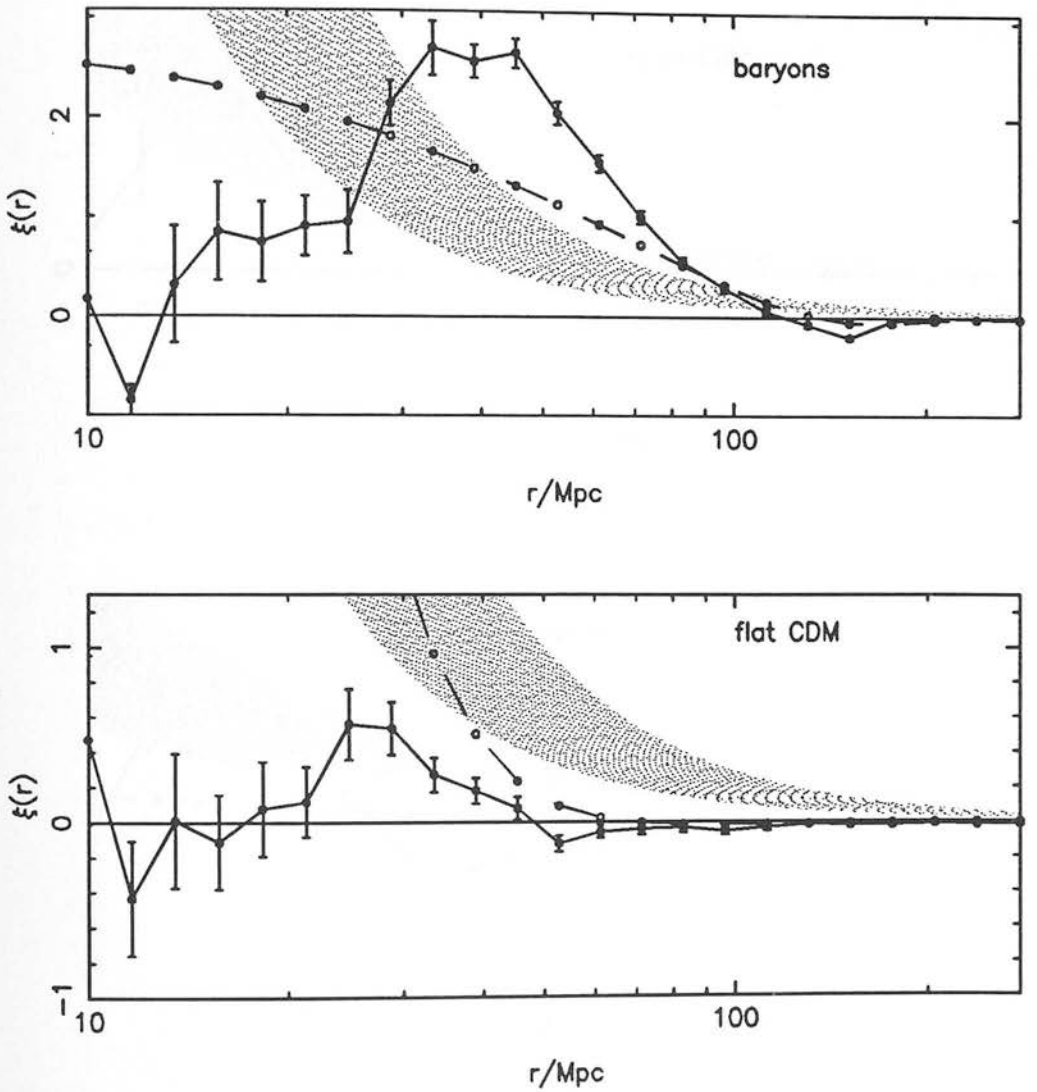

Figure 4.4: The three dimensional correlation functions. The solid line is the peak-peak correlation function and the dashed line the modified JS fit. The hatched area represents the observed cluster-cluster correlation function. Note that $h = \frac{1}{2}$ for these models.

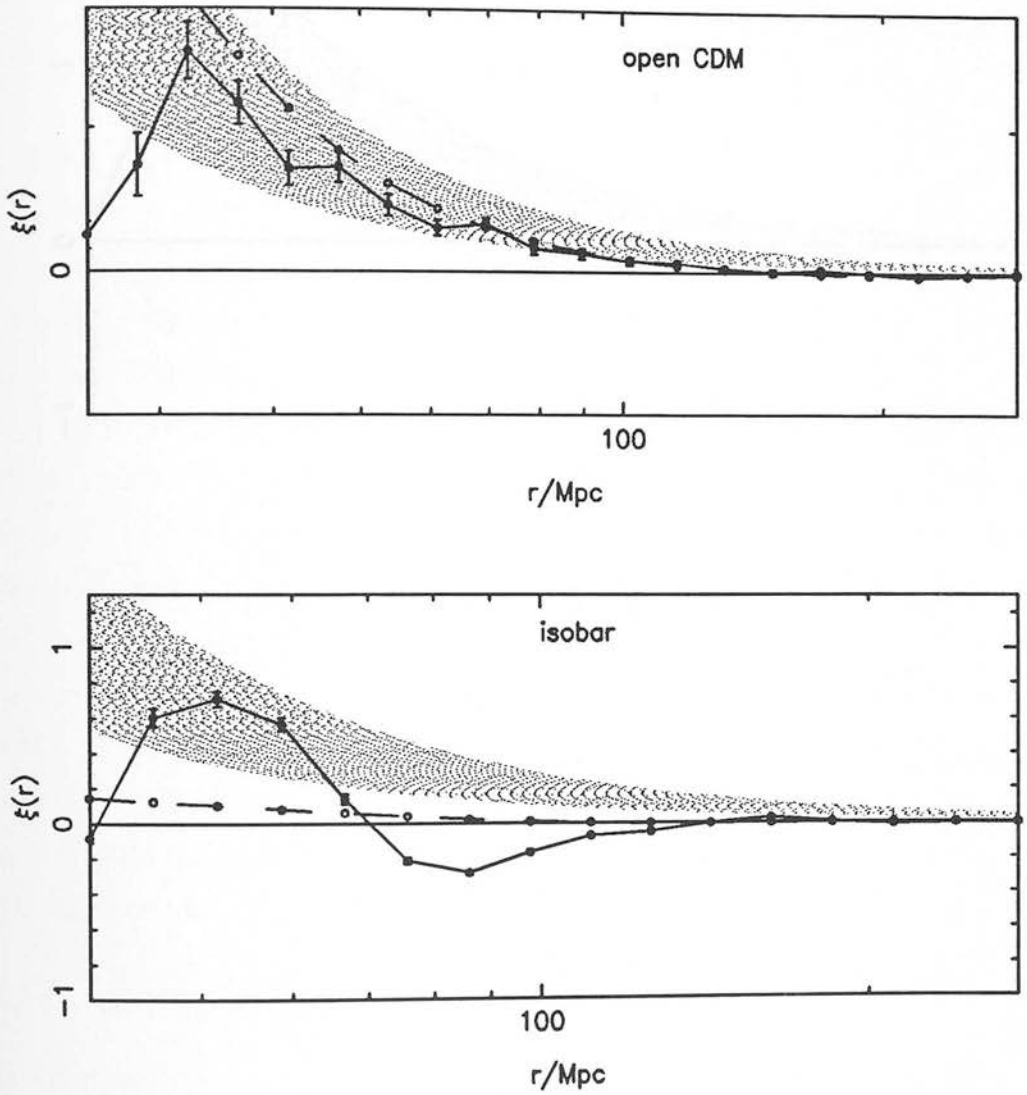

Figure 4.4: (*cont.*)

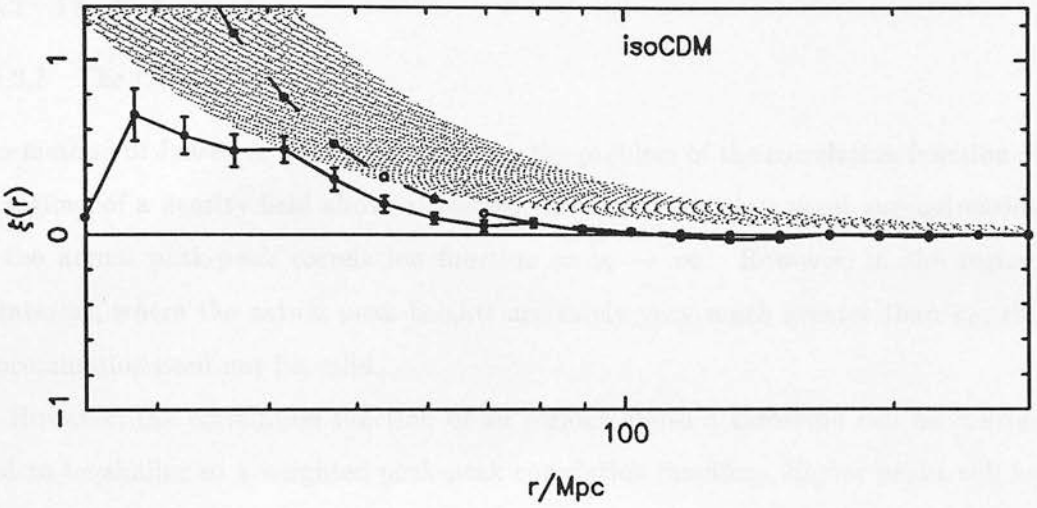

Figure 4.4: (*cont.*)

ply connected and any peak in a slice should lie close to a true three-dimensional peak. ξ_{pk-pk} should therefore be a useful asymptotic approximation to the full result.

The approximation based on the extension of the JS result is described in sections 4.4.2 and 4.4.3 and that based on the slice method in sections 4.4.4 and 4.4.5.

4.4.2 The JS Approach

4.4.2.1 The Concept

The method of Jensen & Szalay (1986) solves the problem of the correlation function of all regions of a density field above a selected threshold. This is a good approximation to the actual peak-peak correlation function as $\nu_t \rightarrow \infty$. However, in the regime of interest, where the actual peak heights are rarely very much greater than σ_0, the approximation need not be valid.

However, the correlation function of all regions above a threshold can be considered to be similar to a weighted peak-peak correlation function. Higher peaks will be surrounded by a larger region of the density field above the threshold than lower ones. If the peak-peak correlation function were to be weighted so that higher peaks had more weight than lower ones the result would have a greater amplitude (or at least the same) than the straightforward peak-peak correlation function. It is useful to consider a new function, the correlation function of all points above an *effective* threshold, ν_{eff}, defined below. This corrects the amplitude of the correlation function by forcing the JS model to fit the peak-peak correlation function at large separations but cannot change other factors such as where it becomes negative.

4.4.2.2 The Effective Threshold

For a Gaussian density field, the correlation function of all points in the field above a selected threshold is given by JS as

$$1+\xi_\nu(r) = \frac{1}{2\pi\left(1-\psi^2(r)\right)^{1/2}\left(\frac{1}{2}\mathrm{erfc}(\nu/\sqrt{2})\right)^2} \quad \times$$

$$\int\!\!\int_\nu^\infty e^{-(\nu_1^2+\nu_2^2-2\psi(r)\nu_1\nu_2)/2(1-\psi^2(r))}\, d\nu_1\, d\nu_2\,, \qquad (4.13)$$

where $\psi(r)$ is proportional to the autocorrelation function, normalised so that $\psi(0)=1$. JS also give the solution to this problem.

$$\xi_\nu = \sum_{m=1}^{\infty} \frac{\psi^m}{m!} A_m^2 \,, \tag{4.14a}$$

where the coefficients A_m are given by

$$A_m = \frac{2x\, H_{m-1}(x)\, 2^{-m/2}}{\sqrt{\pi}\, x\, e^{x^2} \mathrm{erfc}(x)} \,, \qquad x = \frac{\nu}{\sqrt{2}} \,, \tag{4.14b}$$

and the H_m are Hermite polynomials. Previous, partial solutions were also given by Kaiser (1984) and Politzer & Wise (1984), but these were of limited accuracy. JS discuss this matter in more detail.

In the limit that $\psi \to 0$, the correlation function reduces to:

$$\xi_\nu = A_1^2(\nu)\, \psi \,. \tag{4.14c}$$

This result is valid regardless of the dimension of the density field. A similar asymptotic result can be derived from the peak-peak correlation function. The result for a one dimensional field is outlined below.

Given the autocorrelation function in one dimension (equation C.14), it is trivial to show that, for a power spectrum which is approximately a power law with index n truncated at some minimum wavelength using a reasonably sharp filter function (such as a Gaussian or an exponential but not a sharp cut-off), the derivatives of $\psi(r)$ will fall off more quickly than $\psi(r)$ as $r \to \infty$, so these can be ignored. This result is also true in three dimensions.

Given these approximations, the covariance matrix is greatly simplified. Only the two terms involving ψ now connect the separate peaks. This makes analytical inversion of the matrix possible. With this, a new variable can be defined (*cf.* BBKS), $\langle \tilde{\nu} \rangle$:

$$\langle \tilde{\nu} \rangle \equiv \frac{1}{[(2\pi)^3 (1-\gamma^2) R_*^2]^{1/2}\, n_{pk}(\nu_t)} \int_{\nu_t}^{\infty} \int_0^{\infty} q\, \tilde{\nu}\, e^{-S_0}\, dq\, d\nu \,, \tag{4.15a}$$

where

$$\tilde{\nu} \equiv \frac{(\nu - \gamma q)}{1-\gamma^2} \,. \tag{4.15b}$$

In the limit that $\nu_t^2 \psi \ll 1$ the peak-peak correlation function reduces to (see appendix C.3):

$$\xi_{pk-pk}(r) = \langle \tilde{\nu} \rangle^2\, \psi(r) \,. \tag{4.16}$$

BBKS derive a similar result for a three dimensional density field (their equation 6.12). They give an expression for the effective threshold, $\langle \tilde{\nu} \rangle$ at fixed peak height, ν. However,

when peaks above a given threshold are selected and not just peaks at that threshold, the numerical integral in equation 6.45 of BBKS has to be evaluated, which is relatively easy.

Comparing this with equation 4.14c, in the limit that $\psi \to 0$ for fixed ν_t, ν_{eff} is defined by:

$$A_1(\nu_{eff}) = \langle \tilde{\nu}(\nu_t, \gamma\nu_t) \rangle \, . \tag{4.17}$$

The approximation then is simply to replace ν_t in equation 4.14a by the calculated value of ν_{eff}.

This implicit equation may be used to produce a plot of ν_{eff} against ν_t for various values of γ. This is shown in figure 4.5. For one dimensional spectra (figure 4.5(a)), the results indicate that $\nu_{eff} \sim \nu_t$. What small variation there is seems to be more prevalent for low values of γ and intermediate thresholds ($\nu_t \sim 1 - 2$), causing a reduction in ν_{eff} with respect to ν_t. Since the variation with γ is not great, only two values are displayed. Figure 4.5(b) shows how ν_{eff} varies as a function of ν_t and γ for the three dimensional case. It demonstrates that even for large values of ν_t, the effective threshold is somewhat less than the true threshold: for small true thresholds the discrepancy is even greater, emphasising the difficulty in associating a region above a given threshold with peaks above a given threshold. The effect is most prominent for larger values of γ.

4.4.3 Results

Tables 4.1 and 4.2 give the computed values of $\langle \tilde{\nu} \rangle$ and ν_{eff} for the one dimensional and three dimensional cases respectively. The dashed lines in figures 4.1 and 4.4 represent the approximation described in the last section.

In one dimension, as has already been noted for general values of γ, the calculated values of $\langle \tilde{\nu} \rangle$ and ν_{eff} are approximately the same as ν_t. The model which has the greatest deviation between ν_{eff} and ν_t, model a, is an example of the trend that $\nu_{eff} < \nu_t$ for low values of γ and ν_t. In contrast, model b which has the same parameters but a higher threshold, has $\nu_{eff} \sim \nu_t$. Here the regions above the threshold are rapidly becoming disconnected, so that ξ_ν should tend towards ξ_{pk-pk} in any case, at least on large scales.

In general terms, for $r \gg R_*$, the solutions are well behaved in all cases. For the

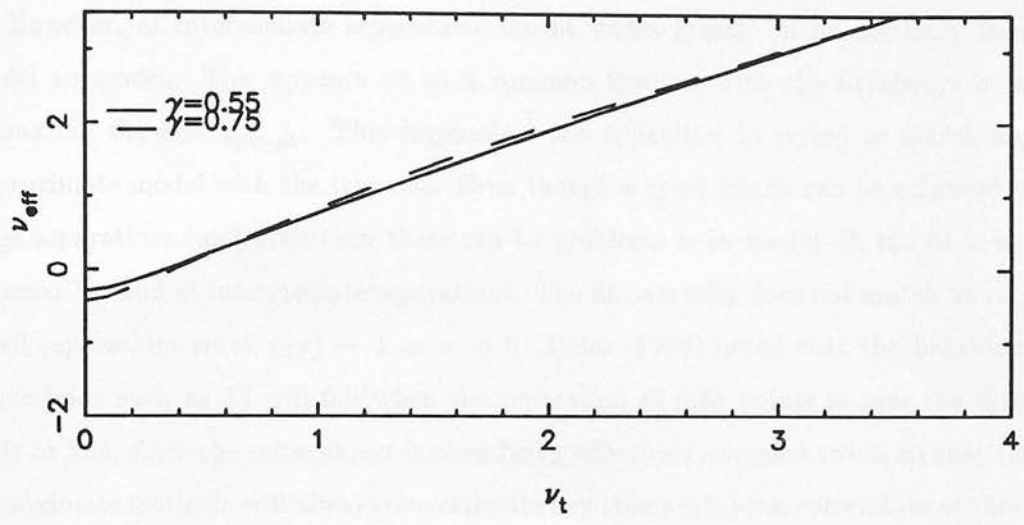

Figure 4.5: (a) The variation of the *effective* threshold, ν_{eff}, with true threshold, ν_t in one dimension. Each line represents a different value of γ.

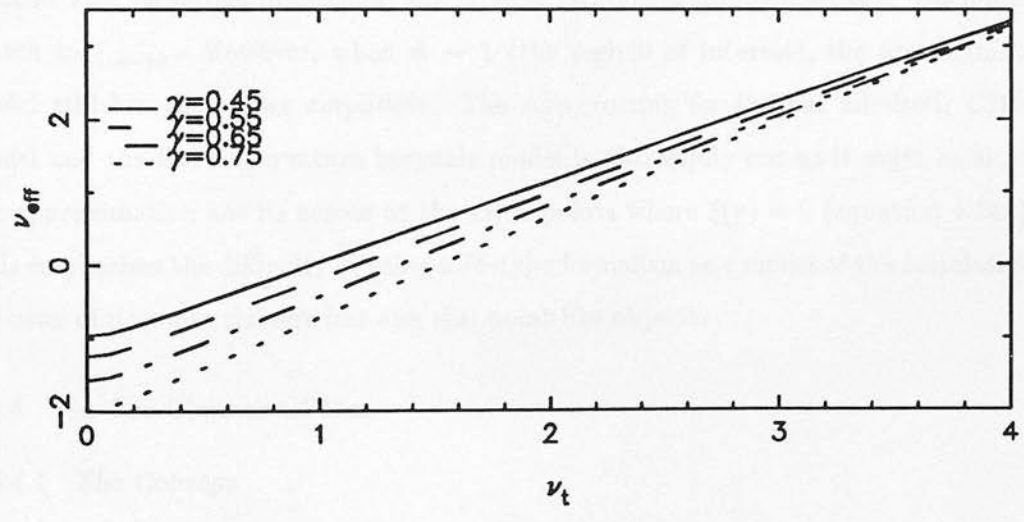

Figure 4.5: (b) The variation of the *effective* threshold, ν_{eff}, with true threshold, ν_t in three dimensions. Each line represents a different value of γ.

case of large r the peak-peak correlation function and the approximate fit should be identical, since the fit is based on matching asymptotes. All the models, excluding the anomalous case of model a, show evidence of this behaviour as $\psi \rightarrow 0$, though the match is not exact where $\psi \neq 0$ or its derivatives are still non-negligible.

However, at intermediate separations the fit varies greatly in its accuracy from model to model. This appears to be a common feature, with the fit always over-estimating the true ξ_{pk-pk}. This emphasises the difficulties in trying to match any approximate model with the true one. Even though a good match can be achieved at large separations (and even then there can be problems as in model a), the fit is not necessarily valid at intermediate separations. The fit naturally does not match at very small separations since $\psi(r) \rightarrow 1$ as $r \rightarrow 0$. Coles (1986) noted that the behaviour of methods such as JS will fail when the separation of field points is near the filter scale or less, since the same object is then being effectively sampled twice, so that the approximate methods will always overestimate any true peak-peak correlation at these separations. The same problem applies equally to the modified fit.

In three dimensions, the difference between ν_{eff} and ν_t is large for all the models. This difference is greatest as γ increases, similar to the general case described in section 4.4.2.2. Just as in one dimension, the large separation asymptotic fit is a reasonable match to ξ_{pk-pk}. However, when $\psi \sim 1$ (the regime of interest), the approximate model still has the wrong amplitude. The zero-crossing for the flat adiabatic CDM model and the flat isocurvature baryonic model is also wildly out as it must be since the approximation has its zeroes at the same points where $\xi(r) = 0$ (equation 4.14a). This emphasises the difficulty in using a JS-type formalism as a model of the correlation function of not only clusters but any real point-like objects.

4.4.4 The One Dimensional Slice

4.4.4.1 The Concept

Given a completely general three dimensional density field, it is possible to determine the power spectrum for a one dimensional slice through that field. It is therefore straightforward to use the results of section 4.2 to calculate the correlation function of peaks in this slice. If the threshold set is reasonable (*e.g.* $\nu_t > 1$), then the peaks in this slice should always fall near the real peaks in the three dimensional field.

It might be hoped therefore that the one dimensional correlation function of peaks

in the slice would be a good approximation to the correlation function of peaks in the three dimensional density field. Given that this were so, there would be an immediate advantage, namely that it would no longer be necessary to truncate the power spectrum in k-space. However, for the sake of comparison, the models considered here have identical parameters to those discussed in section 4.3.

The next section outlines how to obtain a one dimensional slice. The method of section 4.2 is then applied directly to this power spectrum.

4.4.4.2 Defining a One Dimensional Power Spectrum

Given a general three dimensional density field of the form,

$$\delta(\mathbf{x}) = (\frac{L}{2\pi})^3 \int d^3k\, \delta_{\mathbf{k}}\, e^{i\mathbf{k}.\mathbf{x}} \,, \tag{4.18a}$$

then a one dimensional form can be defined as

$$\delta(x_1) = (\frac{L}{2\pi})^3 \int d^3k\, \delta_{\mathbf{k}}\, e^{ik_1x_1} \,, \tag{4.18b}$$

corresponding to the density fluctuation along the line $x_2 = x_3 = 0$. The one dimensional correlation function of this density field is simply given by

$$\xi(r) = (\frac{L}{2\pi})^3 \int d^3k\, |\delta_{\mathbf{k}}|^2\, e^{ik_1r} \,. \tag{4.18c}$$

The one dimensional power spectrum is then the one dimensional Fourier transform of this.

$$P_{1D}(k_1) = \left(\frac{L}{2\pi}\right)^2 \int |\delta_{\mathbf{k}}|^2\, dk_2\, dk_3 \,. \tag{4.19}$$

Therefore

$$P_{1D}(k) = \left(\frac{L}{2\pi}\right)^2 \int_0^\infty |\delta_{\mathbf{k}}(\sqrt{k^2+m^2})|^2_{3D}\, 2\pi m\, dm \;=\; \frac{L^2}{2\pi} \int_{|k|}^\infty |\delta_{\mathbf{k}}(y)|^2_{3D}\, y\, dy \,. \tag{4.20}$$

or simply

$$|\delta_k|^2_{3D} = -\frac{2\pi}{L^2 k}\, \frac{dP_{1D}}{d|k|} \,. \tag{4.21}$$

P_{1D} must therefore be a decreasing function of $|k|$.

Moments over P_{1D} of the form

$$\tilde{g}(r) \equiv \frac{L}{2\pi} \int_{-\infty}^{\infty} P_{1D}(k)\, g(r|k|)\, dk \tag{4.22}$$

may be evaluated by inverting the order of integration:

$$\tilde{g}(r) = (\frac{L}{2\pi})^3 \int_0^\infty |\delta_k(y)|^2_{3D}\, 4\pi y \int_0^y g(rk)\, dk\, dy\ . \tag{4.23}$$

This makes it possible to express all the moments needed in section C.1 in terms of moments over the three-dimensional power spectrum. In particular, for the moments σ_j^2, where $g = k^{2j}$, then

$$\sigma^2_{j(3D)} = (2j+1)\sigma^2_{j(1D)}\ . \tag{4.24a}$$

Hence the spectral parameters R_* and γ are related by:

$$\gamma_{1D} = \frac{\sqrt{5}}{3}\gamma_{3D}\ , \tag{4.24b}$$

$$R_{*(1D)} = \frac{\sqrt{5}}{3}R_{*(3D)}\ . \tag{4.24c}$$

Note that $R_{*(3D)} = \sqrt{3}\sigma_{1(3D)}/\sigma_{2(3D)}$, giving rise to the extra factor of $\sqrt{3}$. The largest allowed value of γ in a one dimensional slice through a three dimensional field is thus 0.745.

It is also possible to compare the number density of maxima. In one dimension, $n_{pk}(-\infty) = 1/(2\pi R_*)$. The asymptotic result in three dimensions is given by BBKS equation 4.11b as $0.016R_*^{-3}$. By comparison, the cube of the cumulative total in one dimension is $0.0097R^{-3}_{*(3D)}$.

The particular case of most interest is that of a power law with a Gaussian cut-off, $|\delta_k|^2 = Ak^n e^{-k^2\sigma^2}$. In general,

$$P_{1D} = A\,\frac{L^2}{4\pi}\,\sigma^{-(n+2)}\,\Gamma\left((\frac{n}{2}+1), k^2\sigma^2\right)\ , \tag{4.25}$$

where $\Gamma(\alpha,\beta)$ is the incomplete gamma function. Alternatively, for exponential filtering, $|\delta_k|^2 = Ak^n e^{-kR}$,

$$P_{1D} = A\,\frac{L^2}{2\pi}\,R^{-(n+2)}\,\Gamma\left((n+2), kR\right)\ , \tag{4.26}$$

Useful special cases are given by $\Gamma(\frac{1}{2}, x^2) = \sqrt{\pi}(1 - \mathrm{erf}x)$, $\Gamma(1,x) = \exp(-x)$, $\Gamma(\alpha+1,x) = \alpha\Gamma(\alpha,x) + x^\alpha \exp(-x)$.

4.4.5 Results

Figure 4.6 shows the results of the one dimensional slice method (solid line) and, for comparison, the results of the Monte-Carlo technique. The threshold chosen for the one dimensional slice is exactly the same as in the three dimensional Monte-Carlo simulations. For most of the models, the agreement is quite good. The zero-crossing point

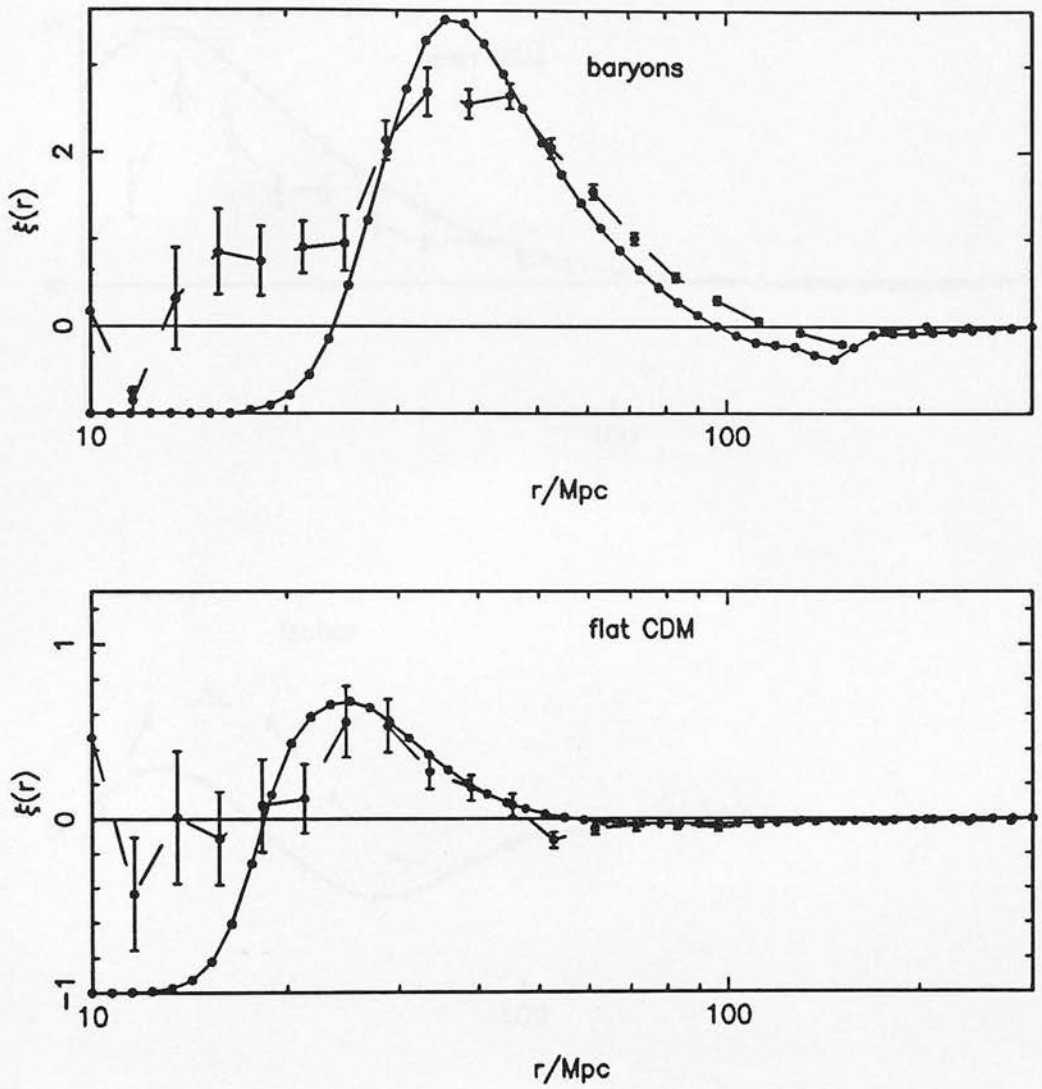

Figure 4.6: The three dimensional correlation functions of figure 4.4 approximated via a one-dimensional slice. The same k-space truncation used for the three-dimensional simulations has been applied here. The solid line is the one dimensional peak-peak correlation function and the dashed line the result of the Monte-Carlo methods of section 4.3.

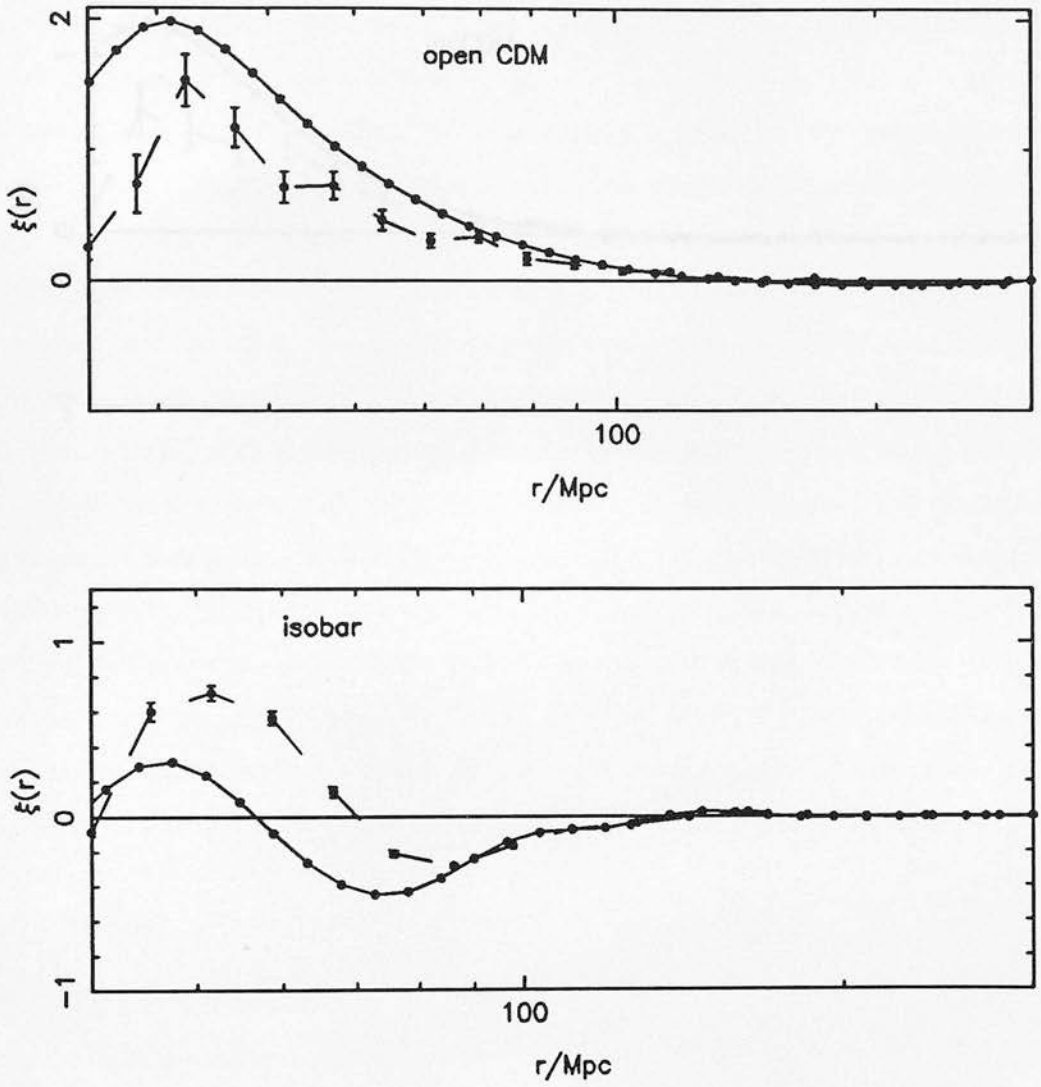

Figure 4.6: (*cont.*)

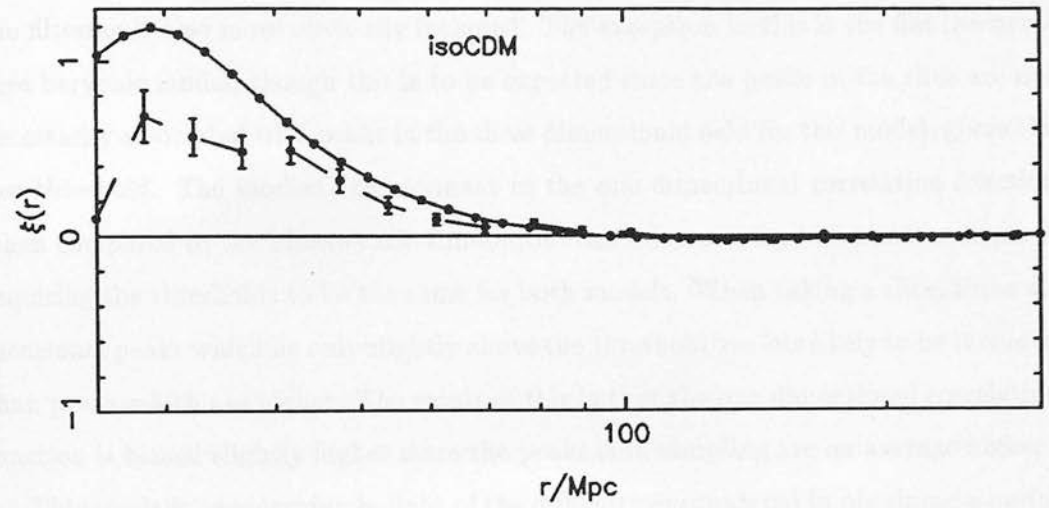

Figure 4.6: (*cont.*)

for the $\Omega = 1$ CDM model appears to be slightly further out in the one-dimensional case, though the difference is not unreasonable when the errors from the Monte-Carlo simulation are considered. The crossing point is still within that predicted by $\xi(r)$ though. Certainly, the overall amplitude of clustering in these calculations is close to that seen in three dimensions, though slightly enhanced in most cases, and the effect of the filtering is also more obviously included. The exception to this is the flat isocurvature baryonic model, though this is to be expected since the peaks in the slice are not necessarily associated with peaks in the three dimensional field for this model, given the low threshold. The modest enhancement in the one dimensional correlation function when compared to the Monte-carlo simulations can be understood as a consequence of requiring the thresholds to be the same for both models. When taking a slice, three dimensional peaks which lie only slightly above the threshold are less likely to be included than peaks which are higher. The result of this is that the one dimensional correlation function is biased slightly higher since the peaks it is sampling are on average higher.

This result is encouraging in light of the difficulty encountered in obtaining a useful approximation to ξ_{pk-pk} using the thresholded region approach; it seems that the one-dimensional slice calculation may provide in practice a much closer approximation. It is not hard to see why this should be so. Even for moderate thresholds the density contour surfaces quickly become simply connected 'bags' surrounding peaks (see BBKS), so that any maximum above this threshold in a one-dimensional slice will tend to lie on a 'shoulder' of a true three-dimensional peak.

4.5 Caveat: The Choice of Filter

4.5.1 Varying the Filter Scale

The value of R_f used in this chapter has been kept at the constant value of $5h^{-1}$ Mpc. However, there is no reason why other values should not be used when modelling clusters. The effects of filter size can be summed up fairly simply: increasing R_f will require a lower threshold and will push the first zero out to larger scales (though the dependence is not that strong). That this is true can be seen from the galaxy-galaxy correlation function as presented by BBKS: this uses the same underlying density field but a smaller filter scale and becomes negative at much smaller scales (about $10h^{-1}$ Mpc). The problem with increasing the filter length, which is what would be required

to save the flat CDM model as presented here, is that there is a limit to the filter scale that can be chosen given that $\nu_t > 0$; the maximum filter scale possible is about 12 h^{-1} Mpc for the case of flat CDM. This model will have the zero-crossing at somewhere near 55 h^{-1} Mpc but the threshold ensures that the statistical clustering will be insignificant. The flat CDM model suffers from a crucial combination of problems in that not only does ξ_{pk-pk} become zero at very small separations for any reasonable filter scale but it also has a very small amount of intrinsic clustering in any case. In attempting to ameliorate the first problem, the second is only enhanced.

4.5.2 The Effect of Using Truncated Power Spectra

Since the one dimensional slice gives a good approximation to the true ξ_{pk-pk} for the three dimensional models, it can be used to test other features. The models considered so far all include some element of truncation in k-space. It is important to calculate the effect that this might have on the results. Therefore, one dimensional slices for all five models were considered in which there is no effective truncation (in practice, since a Gaussian filter has been applied, a lower cut-off is necessary to avoid problems with the integration routines: since the filter length is 10 Mpc, the adopted lower cut-off of 0.1 Mpc will sample scales smaller than which there is no power. A long wavelength cut-off is also applied on the scale of 10^8 Mpc: again this should sample scales with no power.)

The threshold for each of these models was recalculated to ensure that the truncation did not grossly affect the number densities. Only the flat isocurvature baryonic model failed this test. A new threshold of $\nu_t = 1.1$ was found to apply when the truncation was removed. This highlights the problems with trying to use Monte-Carlo methods when power extends over a wide range of scales. Using this new threshold gives rise to a ξ_{pk-pk} which is slightly more clustered than the original one dimensional slice calculation (though this is still less than the clustering predicted by the Monte-Carlo simulation) and which has a zero crossing at slightly larger separations.

The resulting correlation functions for the other models are all very similar to those shown in figure 4.6. The effect of removing the truncation is to shift the first zero crossing (excluding the crossing from negative to positive near the filter scale) further out by no more than 10% from the original position. Therefore, it seems reasonable to conclude that the truncation does not seriously affect the results presented in the

previous sections. Moving the zero crossing by less than 10% does not change the conclusions presented in section 4.6. The *type* of filter however can affect the results.

4.5.3 Other Types of Filters

The conclusions presented in section 4.6 are based on the assumption that linear theory with a filtered power spectrum can be used to locate clusters. The detailed calculation presented here shows what would be expected for the clustering via the common assumption of a Gaussian filter, but it is by no means clear that this is the appropriate choice. BBKS consider the spherical top-hat filter, on the grounds that the spherical model predicts collapse when the overdensity averaged over a sphere reaches a critical value. However, this is clearly an impractical choice: the corresponding k-space filter rings strongly and decays so slowly to large k that a power spectrum with an effective index $n < -3$ is required for convergence of the σ_2^2 moment. Such filtering clearly retains small-scale structure in the initial density field to an undesirable extent. It is however possible to think of a variety of filter functions which avoid such unphysical behaviour, but which lead to rather different clustering properties. It will suffice to consider three examples:

$$\text{Gaussian} \qquad |\delta_k|^2 \rightarrow |\delta_k|^2 \exp(-k^2\sigma^2), \tag{4.27}$$

$$\text{Exponential} \qquad |\delta_k|^2 \rightarrow |\delta_k|^2 \exp(-kR), \tag{4.28}$$

$$\text{Power-law} \qquad |\delta_k|^2 \rightarrow |\delta_k|^2 (1 + k^2a^2)^{-4}\ . \tag{4.29}$$

These correspond to spatial filtering functions proportional to respectively $\exp(-r^2/[2\sigma^2])$, $(1 + [2r/R]^2)^{-2}$ and $\exp(-r/a)$.

Figure 4.7 shows $\psi(r)$ and ξ_{pk-pk} for these three filters applied to $\Omega = 1$ CDM. The relative values of the filter lengths have been chosen to keep the same value of R_* as for the Gaussian filter ($\sigma = 10$ Mpc; $R = 31$ Mpc; $a = 10.5$ Mpc). The threshold is then given by the requirement that the same number density should apply for all three models. This gives $\nu_t = 2.81$ for the Gaussian filter, $\nu_t = 2.61$ for the spatial power-law filter and $\nu_t = 2.46$ for the spatial exponential filter. No truncation is applied to any of these models, so the Gaussian filter shown in figure 4.7b also demonstrates the effect that this has. As noted in the last section, the general features of ξ_{pk-pk} are little different from the truncated version.

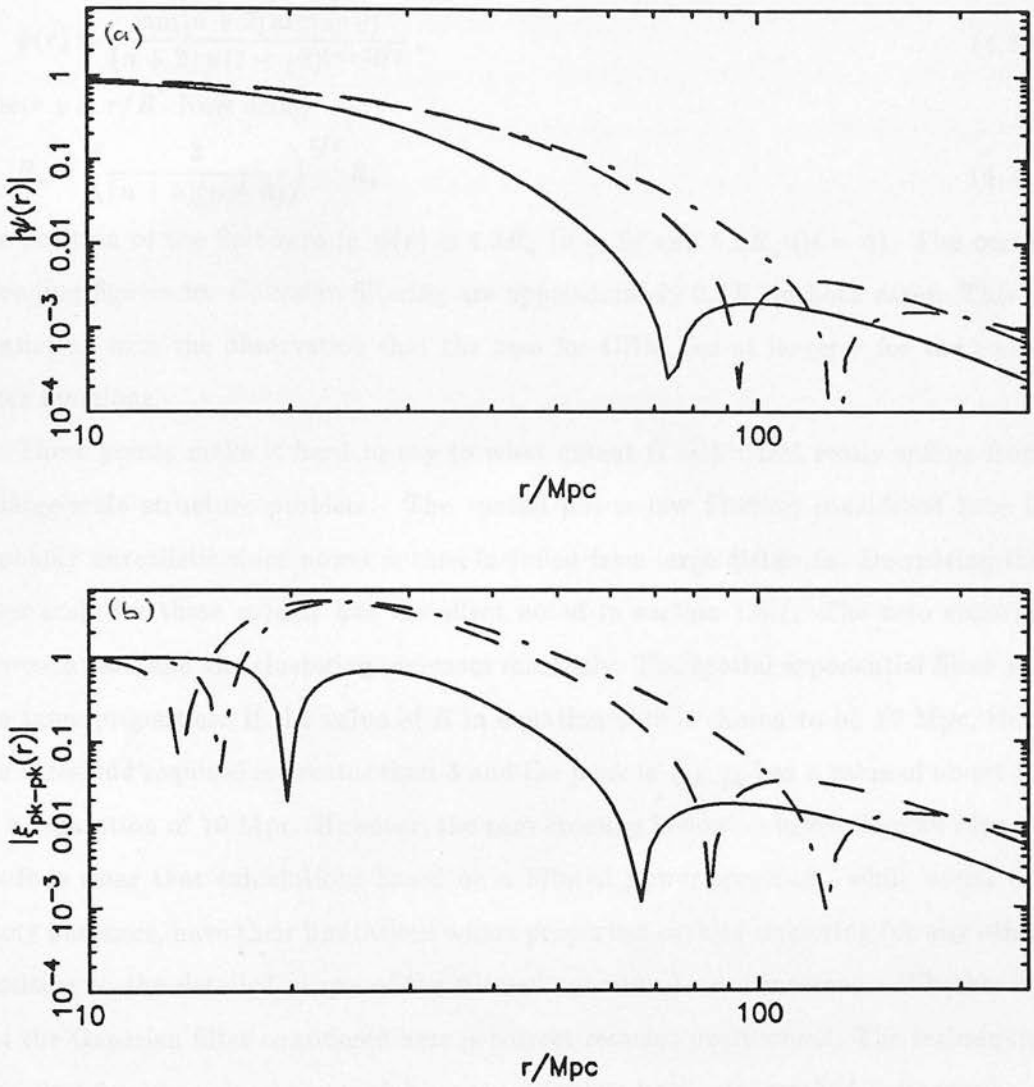

Figure 4.7: The correlations of $\Omega = 1$ $h = \frac{1}{2}$ CDM under Gaussian (solid line), exponential (dashed line) and power-law (dot-dash line) spatial filtering, without truncation in k-space. (a) The autocorrelation function $\psi(r)$; (b) the three-dimensional ξ_{pk-pk} approximated via a one-dimensional slice. All filters have been scaled to produce the same value of R_*. The threshold $\nu_t = 2.81$ in all cases.

However, when less abrupt filtering functions are used two trends are noticeable: the position of the first zero moves to larger r and the total amount of clustering of peaks increases. That this behaviour is reasonable can be seen via an analysis of power-law spectra. For exponential filtering, the correlation function is (Peebles 1980, equation 42.6):

$$\psi(r) = \frac{\sin([n+2]\arctan y)}{(n+2)\,y\,(1+y^2)^{(n+2)/2}}\,, \tag{4.30}$$

where $y \equiv r/R$. Now using

$$R_* = \left(\frac{3}{(n+5)(n+6)}\right)^{1/2} R, \tag{4.31}$$

the position of the first zero in $\psi(r)$ is $4.3R_*$ ($n = 2$) and $5.5R_*$ ($n = 4$). The corresponding figures for Gaussian filtering are approximately $2.7R_*$ in both cases. This is consistent with the observation that the zero for CDM lies at larger r for the softer filter functions.

These points make it hard to say to what extent $\Omega = 1$ CDM really suffers from a large-scale structure problem. The spatial power law filtering considered here is probably unrealistic since power is then included from large distances. Decreasing the filter scale for these models has the effect noted in section 1.5.1. The zero crossing moves inward and the clustering increases markedly. The spatial exponential filter has the same properties. If the value of R in equation 4.28 is chosen to be 10 Mpc, then the threshold required is greater than 3 and the peak in ξ_{pk-pk} has a value of about 55 at a separation of 10 Mpc. However, the zero crossing is now lower than 50 Mpc.

It is clear that calculations based on a filtered power spectrum, while useful for many purposes, have their limitations where properties such as clustering (or any other sensitive to the detailed shape of the filtered spectrum) are concerned. Whether or not the Gaussian filter considered here is correct remains unanswered. The techniques described here are clearly powerful in principle, but have now reached a stage where calibration against N-body simulations may be required to make further progress. This, however, relies on such simulations being expanded to cover a much larger range of scales than they currently do.

4.6 Conclusions

Various models of the peak-peak correlation function have been examined in both one and three dimensions. In general, the major features of the results are independent

of the dimension considered. The use of methods which give the correlation function of regions above a given threshold all give results at variance with the true peak-peak correlation function, in the regime of interest where $\xi(r)/\xi(0) \sim 1$, even in one dimension where the value of ν_{eff}, the *effective* threshold, is similar to the true threshold, ν_t. These models, when corrected to take account of their excessive amplitude are reasonable approximations for separations larger than the filter scale if they do not fall into the category defined in section 4.4.3 as 'steep'. Hence the use of these simpler methods to model true correlation functions (as in Silk & Vittorio 1987) must still be regarded with caution: the direct application of the JS method, or any of its approximate forms, to the problem of modelling the cluster-cluster correlation function will not give a useful solution in three dimensions unless the excessive amplitude is taken into account as has been attempted here.

It has also been shown how the zeroes of the peak-peak correlation function need not coincide with the zeroes of the autocorrelation function. The coincidence is true if the autocorrelation function is in some sense 'flat', so that its derivatives can be ignored. The alternative case was demonstrated quite well by the $\Omega = 1$ CDM model of the cluster-cluster correlation function. For models such as this the simple fit only applies away from the points where ψ crosses zero. Otto, Politzer & Wise (1986) noted the same behaviour in principle, though their attempt to derive analytical solutions to the difficult three dimensional case they considered was flawed.

With particular reference to the models (all of which had $h = \frac{1}{2}$) of the true cluster-cluster correlation function it was found that ξ_{pk-pk} for a flat adiabatic CDM model goes negative at about 50 Mpc. If the current observational measure of the first zero crossing is accurate (*i.e.* it lies at scales greater than this), then the flat CDM model fails on this test. Similarly, a flat baryonic isocurvature model goes negative at 70 Mpc. Both these models also suffer from a lack of statistical clustering on smaller scales. The flat adiabatic baryonic model, the flat isocurvature CDM model and the open adiabatic CDM model all remain positive out to beyond 100 Mpc. They have correlation lengths of about 60 Mpc, 35 Mpc and 40 Mpc respectively. The open CDM model agrees quite well with the observed cluster-cluster correlation function. The flat isocurvature CDM model appears to lack some clustering on small scales and the baryonic model has more clustering at all scales than is currently observed. It would be possible to have a flat CDM model which becomes negative at larger separations if h was less than 0.5. The

scale lengths involved all have a h^{-2} dependence, whereas the observations all scale as h^{-1}. A lower value of h also gives rise to a 'flatter' $\xi(r)$ so that we might expect the zero-crossing for ξ_{pk-pk} to coincide. A value of h of about 0.4 or lower would be reasonably compatible with the observations.

One problem with the results presented here is that no dynamical evolution has been included, so there is in principle a possibility that the true evolved flat CDM model will have a larger correlation length. However, if the physical overdensity on cluster scales is small, it will not affect the results significantly. BBKS (Section VI(f)) show how their peak-peak correlation functions behave under linear evolution. If, as seems likely, the density field on scales of 30 Mpc is still approximately linear then the models presented here will not be very greatly different from a better model with full dynamical evolution. This can be illustrated by using the example of the flat CDM model. Although the general problem is probably intractable (see BBKS), if the statistical part of the clustering is small then ξ_{pk-pk} will be dominated by the dynamical term (BBKS equation 6.63). Figure 4.3a shows what $\psi(r)$ is for this model under linear evolution: $\psi(50\ \mathrm{Mpc}) \sim 0.03$. The true dynamical ξ_{pk-pk} is given roughly by $\xi(r)$ at the zero-crossing. Thus, with $\xi(0) \lesssim 1$ (a conservative assumption: only 2.8σ peaks are required to have collapsed by the present) the total effect is $\xi_{pk-pk}(50\ \mathrm{Mpc}) \lesssim 0.03$. Therefore the zero-crossing should not be greatly perturbed by dynamical evolution.

Whether these results present a fatal problem for canonical CDM is open to question. Apart from the uncertainties in the observations of the cluster-cluster $\xi(r)$, it has been shown that predictions of the amount of peak-peak clustering depend to an unsatisfactory extent on the filter function assumed. If the k-space filter which best represents the non-linear process of cluster collapse is more gentle than a Gaussian cutoff, then greater clustering is predicted in CDM and there may be no large-scale structure problem after all. The solution to this problem will require detailed comparison between future non-linear simulations and the linear theory presented here.

Chapter 5

Large Scale Streaming Motions

5.1 Introduction

The observational evidence for large scale streaming motions provides a further test of linear theory. The original observations of Rubin *et al.* (1976) were initially viewed as a measurement of the peculiar velocity of the Local Group with respect to the universe as a whole. However, as more accurate measures of the dipole moment in the CBR were obtained, it became clear that this explanation was inadequate. Since the CBR dipole is significantly larger in magnitude than the upper limits on the quadrupole moment, its origin is almost certainly Doppler rather than due to intrinsic fluctuations. Unfortunately, the CBR dipole and the Rubin-Ford result are not aligned. This has led to an attempt to interpret peculiar velocities on the Rubin-Ford scale as implying a bulk motion of a shell of galaxies at that distance (Clutton-Brock & Peebles 1981).

Those original observations have been confirmed by further observations with larger samples and more accurate techniques. In particular, the observations described in Lynden-Bell *et al.* (1988), Aaronson *et al.* (1986) and Aaronson *et al* (1988b) demonstrate that there are significant motions on scales of $30h^{-1}$ Mpc and possibly greater. Most of the original theoretical work in this field constituted simple statistical tests as to whether or not a particular model could give rise to the observed motion. The work of Vittorio, Juszkiewicz & Davis (1986) and Vittorio & Turner (1987) is fairly typical of this approach.

More recently, since the complete data-sets have become available (with all the observed parameters for every galaxy; see *e.g.* Aaronson *et al.* 1988b), more powerful methods have become popular. The application of velocity correlation functions has become widespread (Groth, Juszkiewicz & Ostriker 1988, Szalay 1988, Kaiser 1988b, Gorski *et al.* 1989). However, the work presented in this chapter (which, in different form, was published as Peacock, Lumsden & Heavens 1987) is in line with the earlier methods. A consideration of the conclusions drawn by more recent work in comparison with that presented here will be given in section 5.5. More recently, it has become clear

that the velocity field is not a coherent dipole: it is still, however, meaningful to discuss the magnitude of the dipole component of the velocity field. Lynden-Bell *et al.* (1988) discuss this matter in more detail.

The earliest work was handicapped in that it considered only the probability of obtaining a given magnitude to the peculiar motion on any one scale. This fails to take account of the fact the small scale motions are misaligned with the observed streaming. Vittorio, Juszkiewicz & Davis (1986) allowed for this by considering a joint probability for the predicted velocities on two distinct scales, r_a and r_b. Unfortunately, their work is marred by several problems. The first, is their assertion that velocities on the Rubin-Ford scale can be modelled with a Gaussian window function of radius $50h^{-1}$ Mpc (see section 5.2.3 below). For the Dressler *et al.* (1987a) data, Kaiser (1988a) found that the true data was reasonably well modelled by a Gaussian window function of radius $15h^{-1}$ Mpc. Vittorio, Juszkiewicz & Davis also fail to consider the observations and their errors as an intrinsic part of the problem and instead look to see if the 95% confidence limits of observed and theoretical components overlap.

The work presented here improves upon this in several ways. Window radii that are compatible with the actual observations are used. The theoretical predictions are compared with the observations by following the method of Clutton-Brock & Peebles (1981): the theoretical and observational covariance matrices are added together. This reduces the problem to one of determining whether or not the six dimensional vector $(\mathbf{v}_a, \mathbf{v}_b)$ is normally distributed with the known covariance matrix. The choice of statistical test employed is described in section 5.3.1. Lastly, the motion of peaks is considered instead of field points. The distribution of velocities for peaks is derived in appendix C.4.

Section 5.2 presents the basic theory. Section 5.3 discusses the observations, outlines which are used to test the models and describes the statistical test used. Section 5.4 discusses possible theoretical models. Section 5.5 discusses the results obtained in the light of other work.

5.2 Modelling Large Scale Streaming Motions

5.2.1 Basics

The density field on large scales is still accurately described by linear theory as was demonstrated in the last chapter. The following convention for Fourier transforms is used:

$$\delta(\mathbf{x}) = \frac{V}{(2\pi)^3} \int \delta_{\mathbf{k}}\, e^{i\mathbf{k}.\mathbf{x}}\, d^3k \,, \tag{5.1a}$$

$$\delta_{\mathbf{k}} = \frac{1}{V} \int \delta(\mathbf{x})\, e^{-i\mathbf{k}.\mathbf{x}}\, d^3x \,, \tag{5.1b}$$

The velocity field $\mathbf{v}(\mathbf{x})$ has the following Fourier components in linear theory (Peebles 1980)

$$\mathbf{v}_{\mathbf{k}} = \frac{-if H_0 \delta_{\mathbf{k}}}{k^2}\mathbf{k} \,, \tag{5.2}$$

where $f \simeq \Omega_0^{0.6}$.

The model peculiar velocity field can then be convolved with a window function to take account of the observations (section 5.2.2 below). The actual measured velocities are all known only at our position in the universe. Hence, the probability distribution for this velocity is required to determine if the model velocities are compatible with the observations. In common with the previous chapters, the density field is assumed to be Gaussian. This then allows (as it did for clustering in chapter 4) the identification of peaks in the density field with structure in the universe. In particular, for this case, our position is assumed to be a peak.

BBKS showed how the variance for the velocity field at a peak differed from that of arbitrary field points. What is required here is that this be extended to take account of the two separate filtering scales, one of which is our local motion and the other the 'streaming' motion of a large-scale shell of galaxies surrounding us. One window scale is chosen to be representative of local motions in the universe (Vittorio, Juszkiewicz & Davis 1986 assumed that this scale was $5h^{-1}$ Mpc), and the other represents the scale size of the observed large scale motions. If these two windowed velocities are denoted $\mathbf{v}^a$ and $\mathbf{v}^b$, then since both of these quantities are Gaussian, so is the joint probability constructed from them and the density field and its first two derivatives. Fortunately, the velocities only correlate with the first derivatives of the density field, and then only

for components along the same axis. The problem therefore reduces to one of three variables, v^a, v^b and δ'.

The covariance matrix for these variables is given in appendix C.4. Moments of the density field are defined in equation C.34. Using this, for field points it is found that,

$$\left\langle v^a v^b \right\rangle = \frac{H_0^2 f^2}{3} \sigma^2_{-1ab} \cdot \tag{5.3}$$

The presence of the indices $\{a, b\}$, indicates the presence of the corresponding window function in the integral, equation C.34. The case $a = b$ is allowed. Inverting the full covariance matrix and setting the first derivatives of the density field to zero to give the constraint of being at a maximum, gives rise to a quadratic form equivalent to equation 4.23 of BBKS. The resulting distribution is still a Gaussian with zero mean, but has the altered variance,

$$\left\langle v^a v^b \right\rangle = \frac{H_0^2 f^2}{3} \left(\sigma^2_{-1ab} - \frac{\sigma^2_{0a} \sigma^2_{0b}}{\sigma_1^2} \right) \cdot \tag{5.4}$$

5.2.2 The Motion of Peaks in the Density Field

In line with BBKS, the quantity γ_{ab} is defined to be

$$\gamma_{ab} = \frac{\sigma^2_{0a} \sigma^2_{0b}}{\sigma_1^2 \sigma^2_{-1ab}} \cdot \tag{5.5}$$

Note that, just like the quantity γ defined by equation 4.7, this parameter is a measure of the 'width' of the power spectrum. Its value tends towards unity as the power spectrum tends towards a delta function. Therefore, for maxima, the peculiar velocities expected are multiplied by the factor $(1 - \gamma^2_{ab})$, and since $\gamma_{ab} \leq 1$, this means that they are effectively reduced.

As will be shown later, $\gamma_{ab} \to 0$ as the window radii tend to infinity. Hence, for large separations, the velocity tends to that expected for a field point. This is intuitively reasonable since for separations much larger than the scale size of the peaks, the peaks will appear the same as field points (c.f. the large separation limit to the peak-peak correlation function in chapter 4).

Two further points should be made here. It might be expected that this effect would depend on the height of the peak, with higher peaks showing less motion. However, γ_{ab} is independent of the peak height. The next point is that, in linear theory, the growth with time is purely local. The overdensity, $\delta(\mathbf{x})$, scales by a simple time-dependent factor in the same way for every point in the density field. This would

seem to imply that local maxima are time-independent and should therefore have zero velocity. However, that actual condition for linear theory to apply is not only $\delta \ll 1$ but (Peebles, 1980, section 9 and 10) also

$$\frac{\partial^2 \delta}{\partial t^2} \gg \frac{1}{a^2}(\nabla.\mathbf{v})^2 \,. \tag{5.6a}$$

This can be rewritten as

$$\left(\frac{ut}{d}\right)^2 \ll \delta \,, \tag{5.6b}$$

where u is a characteristic comoving velocity and d is a characteristic scale length for the perturbations. This is equivalent to saying that linear theory applies as long as particles are not convected further than the characteristic scale length of the fluctuations, which for a plane-wave decomposition would just be one wavelength.

It follows from this that linear theory does not reveal anything anything about the streaming of density maxima, but rather, the value of the velocity field at the maxima. Fortunately, it is this latter quantity that is in fact required. The observed motions of galaxies are going to be compared with cluster or supercluster sized maxima. Therefore what is wanted is not the motion of the peaks but the value of the underlying velocity field at a peak. Grinstein *et al.* (1986) discuss why these two quantities are different when the peaks are maxima of a Gaussian random field.

Lastly, there is still the matter of how long linear theory is applicable to the large scale density field. Fortunately, the Zeldovich approximation (see section 1.4.2) shows that linear velocities are very good approximations to the correct non-linear result even when $\sigma_0 \sim 1$.

5.2.3 Window Functions

The distribution of the sample of galaxies must be taken into account in any model. This is achieved by considering the convolution of the velocity field with a suitable window function. A common choice is to use a Gaussian:

$$W(\mathbf{x}) = \frac{V}{(2\pi R^2)^{3/2}} e^{-x^2/2R^2} \,. \tag{5.7a}$$

This has for its transform,

$$W_{\mathbf{k}} = e^{-k^2R^2/2} \,. \tag{5.7b}$$

Two other popular variants are a uniformly filled sphere,

$$W(\mathrm{x}) = \frac{3V}{4\pi R^3}\theta(r-R)\,, \tag{5.8a}$$

for which

$$W_{\mathbf{k}} = \frac{3}{k^3R^3}(\sin kR - kR\cos kR)\,, \tag{5.8b}$$

and an infinitely thin shell,

$$W(\mathrm{x}) = \frac{V}{4\pi R^2}\delta(r-R)\,, \tag{5.9a}$$

for which

$$W_{\mathbf{k}} = \frac{\sin kR}{kR}\,. \tag{5.9b}$$

These latter two functions can be approximated by Gaussians with $R_g = R/\sqrt{5}$ and $R_g = R/\sqrt{3}$ respectively. These functions are equivalent to second order in k and are also accurate to within 5% when $r = R$.

5.3 Comparison of Theory and Observations

5.3.1 Goodness of Fit Testing

The components of the theoretical covariance matrix, C, have already been calculated for the simple one dimensional case. For three dimensions, the matrix is no more difficult, since the density field is isotropic. Hence, the only elements in the covariance matrix C are c_{aa}, c_{bb} and c_{ab}, where $c_{ab} = \langle v_a v_b \rangle$. In order to test the theoretical predictions against the observations, the procedure used by Clutton-Brock & Peebles (1981) is followed, and the observational and theoretical covariance matrices are added. This is simply reflecting the fact that the noise in the Gaussian density field and the observed errors in the assumed Gaussian velocity field simply add. The hypothesis to be tested is that the six-dimensional vector, $\{\mathrm{v}_a, \mathrm{v}_b\}$, is normally distributed with this covariance matrix.

There are several features of this problem which ensure that it is not straightforward. There is, in general, only one data point to test against. Even though there is more than one survey, of varying depths, in the streaming picture all that is produced is a single value for the overall bulk motion. Where practical each survey will be tested individually, as well as testing a global average value. Each model is also parameterised by the values of Ω_0, H_0 and σ_0, whose real values are not known *a priori*. A general

method for treating such problems is to use maximum likelihood (see, for example, Kaiser 1988a, for such an approach to streaming motions), to set confidence limits on the allowed regions of the parameter space. However, maximum likelihood techniques require several assumptions to be made. Firstly, using this method implies using Bayes' theorem (since the probability of achieving a given observed velocity is dependent on the values of the parameters) and it is not clear what the correct priors for the parameters should be. Secondly, the likelihood method assumes that the model being tested is fundamentally correct and it is also not clear that this is necessarily true. What is desired here is some method of testing whether a given parameterised model agrees with the observations.

The method adopted here for testing the models is to try mapping a given position in the six-dimensional space defined by $\{\mathbf{v}_a, \mathbf{v}_b\}$ into a probability. One possibility is to consider the value of χ^2 given by

$$\chi^2 = \frac{1}{2}\mathbf{v}^T.C^{-1}.\mathbf{v}\ , \tag{5.10a}$$

where

$$\mathbf{v} = (\mathbf{v}_a, \mathbf{v}_b) \tag{5.10b}$$

and C is the covariance matrix

$$C_{ij} = \langle v_i v_j \rangle\ . \tag{5.10c}$$

Since $\mathbf{v}$ has six degrees of freedom, a value of $\chi^2 > 16.81$ would reject the model at the 1% level. Unfortunately, this statistic does not test whether or not the model velocities are too large, only whether they are too small. Clearly, models which predict streaming motions which are too large are just as much in error as those with very small peculiar velocities. One way round this is to consider

$$p_1 \equiv 1 - 2\left|p_{6df}(>\chi^2) - \frac{1}{2}\right|\ . \tag{5.11}$$

This statistic is uniformly distributed between 0 and 1. For very large values of χ^2 this still has $p_1 \sim 0$, but for very low values (large velocities), $p_{6df}(>\chi^2) \to 1$, and $p_1 \sim 0$ as well.

However, p_1 does not take account of the observed misalignment between $\mathbf{v}_a$ and $\mathbf{v}_b$. It assumes that for a given value of χ^2, every direction in the velocity space is equally likely. Instead of considering the value of the misalignment angle directly, another

possibility is to consider the ratio v_b/v_a. These are effectively equivalent at constant χ^2, since then requiring v_b/v_a to be correct will ensure that neither v_a or v_b are too far away from their correct values. If v_b represents the larger window scale, it would be expected that $v_b < v_a$, so large values of the ratio would allow any models to be excluded. In order to derive a probability reflecting this test consider firstly the full joint probability in the velocity space.

$$P(\mathbf{v})d^6v = \frac{1}{((2\pi)^6 \det C)^{1/2}} e^{-Q} d^6v \,, \tag{5.12a}$$

where

$$Q = \mathbf{v}^T.C^{-1}.\mathbf{v}/2 \,. \tag{5.12b}$$

The six dimensional covariance matrix, C, has a simple form since the components of the velocity only correlate along the same spatial axis. Hence, the only non-zero elements of C are given by

$$C_{11} = C_{22} = C_{33} = c_{aa} \tag{5.13a}$$

$$C_{44} = C_{55} = C_{66} = c_{bb} \tag{5.13b}$$

$$C_{14} = C_{25} = C_{36} = c_{ab} \tag{5.13c}$$

and

$$C_{ij} = C_{ji} \,. \tag{5.13d}$$

This has an equally simple inverse, given that $\Delta = c_{aa}c_{bb} - c_{ab}^2$.

$$C_{11}^{-1} = C_{22}^{-1} = C_{33}^{-1} = \frac{c_{bb}}{\Delta} \tag{5.14a}$$

$$C_{44}^{-1} = C_{55}^{-1} = C_{66}^{-1} = \frac{c_{aa}}{\Delta} \tag{5.14b}$$

$$C_{14}^{-1} = C_{25}^{-1} = C_{36}^{-1} = \frac{c_{ab}}{\Delta} \,. \tag{5.14c}$$

If the x-axis is chosen so that $\mathbf{v}_a$ lies along it, and the velocity components are expressed in terms of spherical co-ordinates then the quadratic form in the joint probability is given by

$$Q = \frac{1}{2\Delta}\left(v_a^2 c_{bb} + v_b^2 c_{aa} - 2v_a v_b c_{ab}\cos\theta\right) \,. \tag{5.15a}$$

Hence, integrating out the redundant angular dependences leaves

$$P(v_a, v_b, \cos\theta) dv_a dv_b d(\cos\theta) = \frac{1}{\pi\Delta^{3/2}} e^{-Q} d^6 v \,, \tag{5.15b}$$

This expression is valid for the theoretical distribution since the linear density field is isotropic. It also applies to the observed distributions as long as the covariance matrices for both $\mathbf{v}_a$ and $\mathbf{v}_b$ are isotropic. Although this is not true in practice, treating a full covariance matrix would give very little extra from approximating in the this manner. An example of the possible effect is illustrated later by considering an *ad hoc* doubling of the errors. With this approximation, the observed variances are simply added to the theoretical components c_{aa} and c_{bb}.

The $\cos\theta$ integration can be carried out trivially to give

$$p(v_a, v_b) dv_a dv_b = \frac{v_a v_b}{\pi\Delta^{1/2} c_{ab}} e^{-(c_{bb}v_a^2 + c_{aa}v_b^2)/2\Delta} \left\{ e^{c_{ab}v_a v_b/\Delta} - e^{-c_{ab}v_a v_b/\Delta} \right\} dv_a dv_b$$

To proceed further, the change of variables $(v_a, v_b) \rightarrow (v_a, y)$ is used, where $y = v_b/v_a$. The Jacobian of this transformation contributes an extra factor of v_a, so

$$p(v_a, y) dv_a dy = \frac{v_a^3 y}{\pi\Delta^{1/2} c_{ab}} e^{-v_a^2(c_{bb} + c_{aa}y^2)/2\Delta} \left\{ e^{c_{ab}v_a^2 y/\Delta} - e^{-c_{ab}v_a^2 y/\Delta} \right\} .$$

The semi-infinite integral over v_a is also fairly trivial since it is equivalent to

$$\int_0^\infty dv v^3 e^{-Av^2} \equiv \frac{1}{2A^2} \,,$$

so

$$p(y) dy = \frac{2\Delta^{3/2}}{\pi c_{ab}} \left\{ \frac{y}{(c_{bb} - 2c_{ab}y + c_{aa}y^2)^2} - \frac{y}{(c_{bb} + 2c_{ab}y + c_{aa}y^2)^2} \right\} .$$

The indefinite integral of this function is of a standard form (see Gradshteyn & Ryzhik 1980, section 2.103). The required probability is

$$p\left(\frac{v_b}{v_a} < x\right) = \frac{2\Delta y}{\pi} \frac{c_{aa}x^2 - c_{bb}}{(c_{aa}x^2 + c_{bb})^2 - 4c_{ab}^2 x^2} + \frac{1}{\pi}\tan^{-1}\left(\frac{c_{aa}x + c_{ab}}{\Delta^{1/2}}\right) + \frac{1}{\pi}\tan^{-1}\left(\frac{c_{aa}x - c_{ab}}{\Delta^{1/2}}\right) . \tag{5.16}$$

Using this, the probability p_2 can be defined as

$$p_2 \equiv 1 - 2\left| p\left(\frac{v_b}{v_a} < x\right) - \frac{1}{2} \right| . \tag{5.17}$$

Again, this statistic is sensible in practice since models with $v_b/v_a \sim 0$ are just as unacceptable as models with $v_b > v_a$. This can be combined with the statistic p_1, so that an acceptable model must have values of both p_1 and p_2 which are not too small. The most straightforward way of doing this would be to consider a new statistic

$$z \equiv -\ln(p_1 p_2) \tag{5.18a}$$

and using

$$p(>z) = (1+z)e^{-z} \,. \tag{5.18b}$$

This is the final statistic which will be used to decide whether or not a model is acceptable.

5.3.2 The Observations

The necessary observations can be split into two groups. The smaller window scale, denoted by the velocity v_a, will be taken to be the on small scales. Vittorio, Juszkiewicz & Davis (1986) used a Gaussian window scale of $5h^{-1}$ Mpc for their models. This a somewhat arbitrary figure given the state of the current observations. For most of the models considered here, the existence of a well defined damping cut-off in their power spectra avoids this problem, so that the streaming motions derived in the limit of zero window radius can be used. This still leaves the problem of where the local maximum is. The local group is probably not a realistic choice since it is not near the centre of the local supercluster, and its motion is strongly affected by it. However, if the peculiar velocity of Virgo itself is used, this problem also can be avoided.

There are many different values for this peculiar velocity. Early work assumed that Virgo itself was stationary, so that the infall velocity and the relative peculiar velocities were the same. In particular, it was often thought that the component of the Local Group's motion towards Virgo was simply given by the component of the Local Group's motion towards the CBR in the same direction, since this is what would be obtained for the infall velocity. The infall velocity can be affected by large scale motions however, since Virgo itself can move relative to the CBR. The relevant quantity wanted here is the actual relative peculiar velocities of Virgo and the Local Group. For this quantity, Yahil (1985) adopts a value of 250 ± 50 kms^{-1} towards $l = 284°$ and $b = 75°$, (derived from the results of Yahil, 1981, Aaronson *et al.*, 1982, Dressler, 1984 and Kraan-Korteweg, 1985). More recent results, such as Peebles (1988$_a$) who finds a motion of 160 ± 62 kms^{-1}, or Staveley-Smith & Davies (1989) who find 350 ± 90 kms^{-1}, are in reasonable agreement with this figure so it will be adopted as the true peculiar velocity.

For the larger scale, there a number of different surveys of varying depths. Some of these are unfortunately completely inconsistent. There are also differences in the methods used to derive streaming solutions from the data which lead to differences in the derived distances. Staveley-Smith & Davies (1989) demonstrate this for a sub-sample of their data which is in common with that of Aaronson *et al.* (1982). The model velocities will therefore be tested against the chosen samples independently as well as for a derived global average streaming motion.

There are now several distinct surveys of various regions of the sky. The major one is that of Lynden-Bell *et al.* (1988) (hereafter G7), which is an all-sky survey of 400 ellipticals. Distances are determined using the modified Faber-Jackson relation described in section 1.2.3.1. The basic streaming solution for the galaxies relative to the local group was 406 ± 91 kms^{-1} towards $l = 202° \pm 13°$ and $b = 31° \pm 11°$. This value is lower than their earlier estimates from an incomplete sample (Dressler *et al.* 1987b). An independent survey of seven southern clusters using essentially the same technique was carried out by Lucey & Carter (1988b). They find very similar motions (with the exception of Centaurus where they assert that the Dressler *et al.* solution is in error since they lump two possible sub-groups into a single unit without taking any relative weighting into account). There is insufficient data in their sample alone to form a streaming solution.

For spiral galaxies Aaronson *et al.* (1986) (hereafter A86) and Aaronson *et al.* (1988b) use the IRTF technique (again, see section 1.2.3.1) for a sample of, respectively, ten and six clusters. The latter sample is concentrated on the Hydra-Centaurus supercluster and thus provides another check on the motions found in the G7 sample and Lucey & Carter (1988b). The former consists of clusters visible from the Arecibo radio-telescope. This survey, although not all-sky, provides the streaming solution of 780 ± 188 kms^{-1} towards $l = 255° \pm 17°$ and $b = 18° \pm 13°$. The latter survey is again of too small a sample to give an independent streaming solution. Staveley-Smith & Davies (1989) (hereafter SS & D) use blue-band Tully-Fisher on an all-sky sample of 330 spirals. They find a streaming motion of 154 ± 54 kms^{-1} towards $l = 247° \pm 51°$ and $b = 54° \pm 25°$. For consistency with the other IRTF surveys only this value will be used and the motions given by their other indicators will be discarded.

Samples drawn on larger scales often give inconsistent results (see chapter 1.2.3 for more details). Collins, Joseph & Robertson (1986) reported motions on scales

comparable to the original Rubin-Ford streaming motion, from an incomplete all-sky sample. Collins (1989, private communication) (hereafter CJR) reports that the completed sample has a motion which is roughly 550 ± 200 kms^{-1} towards $l = 202° \pm 29°$ and $b = -11° \pm 17°$. Notice that the magnitude of the errors for this deeper sample is larger. It will however be adopted as a measure of the streaming motion on larger scales since it is all-sky, and as will be shown, is not inconsistent with the other all-sky samples.

The last measurement required is the velocity of the Local Group relative to the CBR. This is given by Lubin & Villela (1986) as 610 ± 50 kms^{-1} towards $l = 272° \pm 5°$ and $b = 30° \pm 5°$. In order to compare these observations correctly, the full covariance matrix for each measurement is required. Unfortunately, most of the published results only quote errors in (v, l, b), $(\delta v, \delta l, \delta b)$. One way round this is to assume that orthogonal error components are uncorrelated to first order, so that the covariance matrix has the form diag $[(\delta v_1)^2, (\delta v_2)^2, (\delta v_3)^2]$. This should be a reasonable approximation: for example, the covariance matrix given by Staveley-Smith & Davis has off-diagonal elements that are very small compared to the diagonal elements, and which could, to first order, be ignored. This approximation gives, for a cartesian co-ordinate system based on Galactic co-ordinates

$$\begin{bmatrix} v^4(\delta v)^2 \\ v^6 \cos^2 b(\delta b)^2 \\ (v_1^2 + v_2^3)^3 \sin^2 l(\delta l)^2 \end{bmatrix} = \begin{bmatrix} v^2 v_1^2 & v^2 v_2^2 & v^2 v_3^2 \\ v_1^2 v_3^2 & v_2^2 v_3^2 & (v^2 - v_3^2)^2 \\ v_2^4 & v_1^2 v_2^2 & 0 \end{bmatrix} \begin{bmatrix} (\delta v_1)^2 \\ (\delta v_2)^2 \\ (\delta v_3)^2 \end{bmatrix} . \tag{5.19}$$

In some cases this solution may not be sensible. It is possible, if the observed errors on l and b are very small compared to the error in v, as is the case for the Virgocentric motion, that one or more of the $(\delta v_i)^2$ could be negative. In this case, a conservative assumption is to assume that the errors are isotropic with $(\delta v_i)^2 = (\delta v)^2$.

The large scale streaming motions given above can now be compared. The values of χ^2 for three degrees of freedom are given in table 5.1. From this, it can be seen that the G7 and SS & D samples agree with each other to a reasonable degree and are not aligned with the CBR dipole. The CJR result is reasonably consistent with all the others though it should be remembered that the large errors for this sample make this not unreasonable behaviour. The A86 result is marginally inconsistent with the two small scale results, but is more aligned with the CBR dipole. However, given the narrow declination range of the A86 sample, it is not clear whether or not the inconsistency

To counter this a slightly different weighting is applied to find the error components, basically by considering the isotropic error components for the weights as opposed to the individual components used in calculating the average velocity. This gives an average streaming motion of $(214, -410, 173) \pm (119, 104, 91)$, or 493 ± 105 kms^{-1} towards $l = 298° \pm 14°$ and $b = 21° \pm 11°$. Given the large errors of the CJR sample, the mean depth of the combined sample is effectively equivalent to that of the G7 sample. Since the adopted Virgo motion with respect to the CBR is 494 ± 70 kms^{-1} towards $l = 270° \pm 9°$ and $b = 8° \pm 9°$, these two motions are clearly in different directions. The misalignment angle is about 30° ($\mu = 0.87$). The effective Gaussian window radius for this combined sample is about 17 h^{-1} Mpc since it can be considered as a thin shell at the mean depth. This is significantly smaller than the value used by Vittorio, Juszkiewicz & Davis (1986). Even though the mean depth of the samples they considered was slightly larger, their Gaussian window radius of 50 h^{-1} Mpc appears to have no justification. The value used here is in far greater agreement with that found by Kaiser (1988a) from the G7 sample of 15 h^{-1} Mpc.

5.4 Theoretical Models

5.4.1 Gaussian Power Spectra

A simple theoretical model can be constructed using power spectra which are Gaussian filtered power-laws. This naturally gives rise to a damping model similar to that seen in a baryon or neutrino dominated model.

$$|\delta_k|^2 = Ak^n T_k^2 \tag{5.20a}$$

$$T_k = e^{-k^2/2k_D^2} \, . \tag{5.20b}$$

This power spectrum gives a simple form for the required moments. Since,

$$\int_0^\infty e^{-ak^2} k^n dk \equiv a^{-(n+1)/2} \int_0^\infty e^{-t^2} t^n dt \, ,$$

if the following variables are defined

$$x = \frac{k_D}{k_a}, \qquad y = \frac{k_D}{k_b} \, , \tag{5.21a}$$

and using integration by parts

$$\sigma_{-1ab}^2 = \left(\frac{2}{n+1}\right) \sigma_0^2 k_D^{-2} \left(1 + \frac{x^2 + y^2}{2}\right)^{-(n+1)/2} \, , \tag{5.21b}$$

$$\gamma_{ab}^2 = \left(\frac{n+1}{n+3}\right)\left(1+\frac{x^2+y^2}{2}\right)^{(n+1)/2}\left[\left(1+\frac{x^2}{2}\right)\left(1+\frac{y^2}{2}\right)\right]^{-(n+3)/2} . \qquad (5.21c)$$

Hence,

$$\langle v^a v^b\rangle = \frac{1}{3}(1-\gamma_{ab}^2) f^2 H_0^2 \sigma_0^2 k_D^{-2}\left(\frac{2}{n+1}\right)\left(1+\frac{x^2+y^2}{2}\right)^{-(n+1)/2} . \qquad (5.22)$$

This simple example also shows that, in general,

$$1-\gamma_{ab}^2 \neq \left[(1-\gamma_{aa}^2)(1-\gamma_{bb}^2)\right]^{1/2} .$$

It follows that the effect of considering peaks is not simply a scaling of the two separate velocities (though the above expressions are equivalent to second order in x and y). Also, as $r_D \to \infty$, $\gamma_{ab} \to 0$. This just confirms what was said earlier: at large enough separations it is impossible to distinguish peaks from points in the field.

It is useful to recast equation 5.22 slightly.

$$\frac{c_{ab}}{(1-\gamma_{ab}^2)} = \frac{1}{3}\left(\frac{100\text{km s}^{-1} f\sigma_0 r_D}{h^{-1}\text{ Mpc}}\right)^2\left(\frac{2}{n+1}\right)\left(1+\frac{x^2+y^2}{2}\right)^{-(n+1)/2} , \qquad (5.23)$$

where $r_D = k_D^{-1}$. This takes advantage of the fact that $f\sigma_0$ and r_D/h^{-1} Mpc are dimensionless. With this relatively straightforward form for the elements of the covariance matrix, the procedure followed in judging which areas of parameter space are most likely can be illustrated. For the case of $n = 1$, figure 5.1 demonstrates the effect of adopting the various statistics outlined previously. The adopted velocity used is the global average described in the last section. The radius of the Virgo window is taken to be zero. The contour levels are set at 0.1%, 1%, 5% and 10%.

The χ^2 test on its own (figure 5.1(a)) places only a lower bound on the $f\sigma_0 - r_D$ plane, leaving a large amount of parameter space which is acceptable but which in practice would give ridiculous answers. In particular, it is possible to generate a reasonable χ^2 for any value of r_D. This occurs since the a moderate χ^2 can result from either the Virgo velocity, or the larger shell, containing virtually all the signal. The adoption of p_1 which also requires that the streaming motions should not be too large (figure 5(b)) places an upper bound across this plane as well but still leaves an uncomfortably large allowed region, large fractions of which correspond to invalid solutions. For example, for large values of r_D and $f\sigma_0$, the p_1 test gives a reasonable probability but the two velocities are both too large. The moderate value of p_1 arises because they are completely misaligned. Similarly for small r_D (and $f\sigma_0 \sim 10$), p_1

gives a reasonable probability but the two velocities are no longer of the correct order of magnitude. The Virgo streaming is very large ($\sim$1000 kms^{-1}) whilst the other is fairly small. Using the final statistic, p, (figure 5.1(c)) takes care of such misaligned and out of proportion solutions.

Even the final statistic, however, leaves a large area of parameter space within the 0.1% contour. This region is increased even further if the window radius for the Virgo motion is given a non-zero value. The effect of this is to open up the possibility of smaller damping radii, though only at extreme values of $f\sigma_0$. Figure 5.1(d) illustrates this for a window radius of $3h^{-1}$ Mpc. The actual value adopted reflects the size of the Virgo *cluster*, since observations of the peculiar velocity of Virgo give this measurement and not not the peculiar velocity of the supercluster. A Gaussian filter for motions on the Virgo supercluster scale would be about $8.7h^{-1}$ Mpc, since the diameter of the supercluster in the plane is about $15h^{-1}$ Mpc. Clearly this is not what is wanted for the smaller filter scale since it is only marginally less than the depth of the SS & D sample. For the large scale damping models to be discussed later including a non-zero Virgo radius of $3h^{-1}$ Mpc does not have a significant effect. It is important for the CDM models however since they have no natural small scale cut-off.

The reason behind the large allowed area of parameter space is also fairly easy to understand. The adopted average velocity is in fact in agreement with the motion of Virgo (the χ^2_{3df} is only 3.4 in the CBR frame). When this is the case, all that is required of the model is to have a large enough velocity correlation length, since the two velocities are not radically misaligned. Most large scale damping models (as determined by the parameter r_D) will satisfy the statistical test for some point value of $f\sigma_0$. Using the CJR result instead shows a different behaviour. Figure 5.1(e) shows the case of $n = 1$ when the Virgo radius is taken as zero. The difference between the two motions here is far more marked (the χ^2_{3df} is 9.4, again in the CBR frame) and the allowed region of parameter space is far smaller. It is largely for this reason that the individual data-sets will also be tested against the 'real' models. Another area of concern is the effect that the error in the observations can have. However, since a reasonably conservative estimate was adopted for the average streaming motion increasing the large scale error has little effect.

Even with these qualifications, figures 5.1(c) and 5.1(e) do show that the most likely damping length, if $f\sigma_0 \sim 1$, is somewhere between $5h^{-1}$ Mpc and $100h^{-1}$ Mpc. This

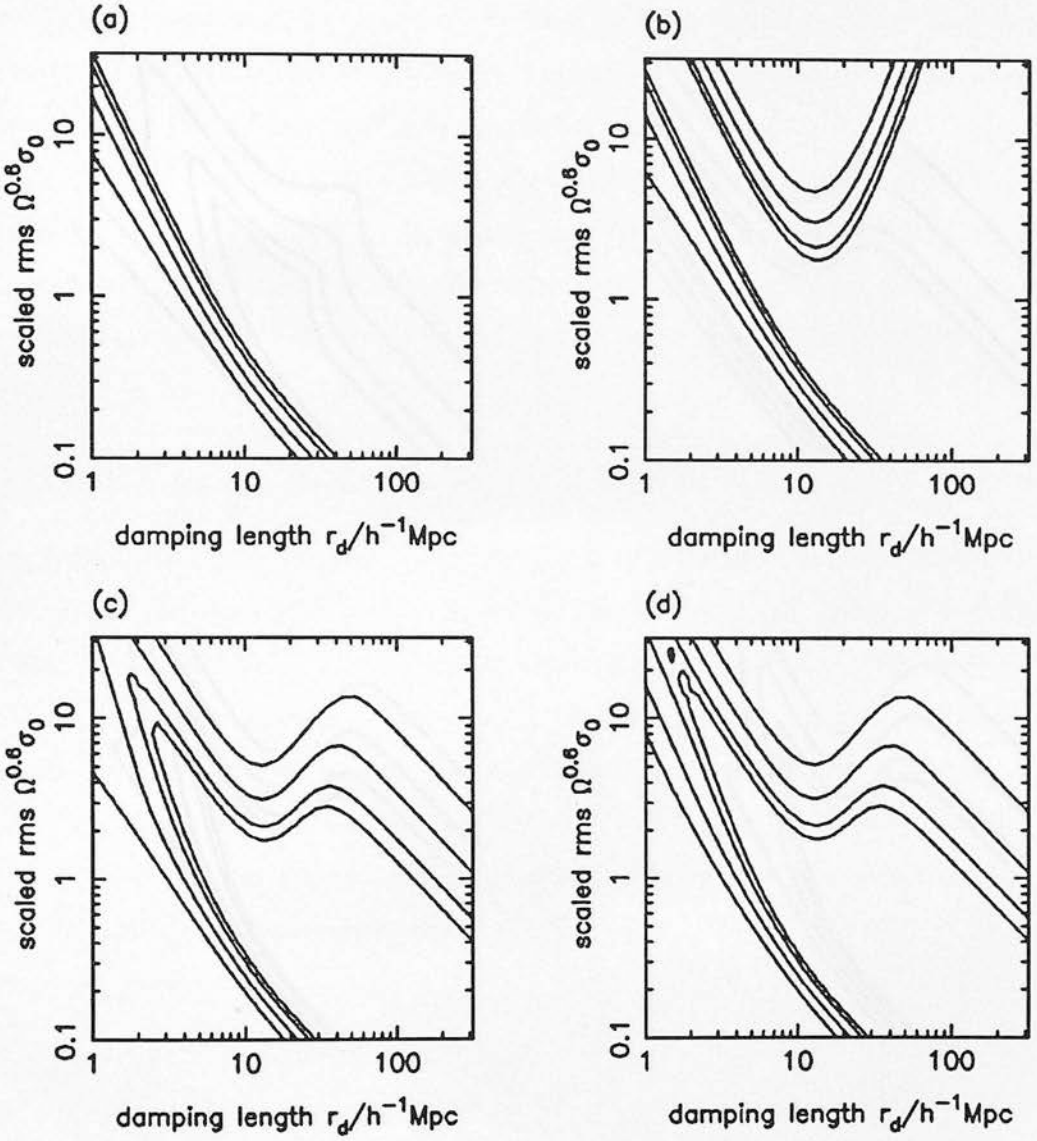

Figure 5.1: Steps involved in determining an allowed region of parameter space in the $f\sigma_0 - r_d$ plane for a generic Gaussian transfer function. The contour levels are set at 10%, 5%, 1% and 0.1%. (a) Rejecting values of χ^2 which are too large: the allowed region is to the top right. (b) Rejecting very low values of χ^2 as well using the statistic p_1. (c) The final statistic, p. (d) p with a non-zero Virgo radius.

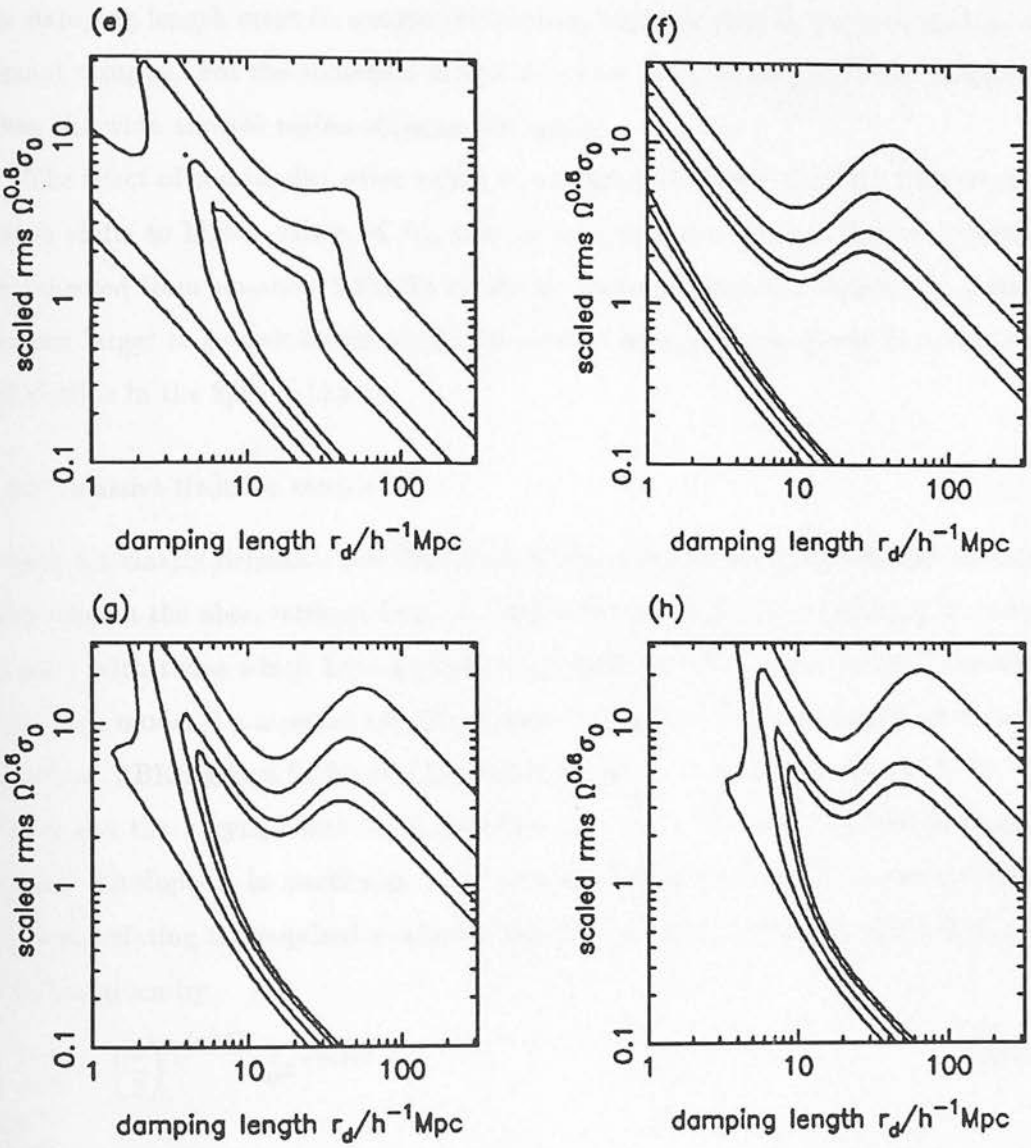

Figure 5.1: (e) Same as figure 5.1(c) but using the CJR sample. (f) As figure 5.1(c) but with $n = 0$. (g) $n = 2$. (h) $n = 4$.

places the minimum acceptable damping length at about half the scale of the combined sample. For the CJR result, the minimum is again at about half the Rubin-Ford scale, or $15h^{-1}$ Mpc. This is what would be expected intuitively for the CJR sample. For two motions to have approximately the same order of magnitude but also be misaligned, the damping length must lie somewhere between the scale sizes of the local and more distant samples. For the combined sample it is hard to make such a strong statement given the wide allowed region of parameter space.

The effect of considering other values of n is shown in figures 5.1(f-h). The allowed region shifts to higher values of $f\sigma_0$ and r_D as n increases. This is just what would be expected from equation 5.23. To obtain the same velocity as n increases, r_D must become larger to counteract the decline in the last term, and $f\sigma_0$ grows to counteract the decline in the $2/(n+1)$ term.

5.4.2 Massive Neutrino Models

Figure 5.1 clearly demonstrates that generic large scale damping models can successfully explain the observational data. To extend this work to 'real' models, it is easiest to start with those which have a physical damping cut-off on large scales. The simplest such model is a massive neutrino dominated universe with one species of massive neutrino. BBKS give a fit for this particular model. It is useful to compare both this model and the baryonic one to be described later to the generic Gaussian formalism already developed. In particular, it is possible to approximate the power spectrum when calculating the required moments. Consider equation 5.21c. The value of γ_{aa}^2 for $x \gg 1$ is given by

$$\gamma_{aa}^2 \simeq \left(\frac{1}{2}\right)^{-(n+3)} \gamma_0^2 x^{-(n+5)} , \tag{5.24a}$$

where

$$\gamma_0^2 = \left(\frac{n+1}{n+3}\right) . \tag{5.24b}$$

If the actual values of γ_{aa}^2 are calculated for the true massive neutrino power spectrum at various true window radii, r_a, then an effective Gaussian radius, r_γ, can be defined by

$$r_\gamma = r_a \left(\left(\frac{1}{2}\right)^{(n+3)} \frac{\gamma_{aa}^2}{\gamma_0^2} \right)^{1/(n+5)} . \tag{5.24c}$$

The value of r_a chosen for the fit is that which gives the closest approximation to the real values of γ_{aa}^2 when r_γ is substituted back into equation 5.24a. There is an analogous equation for when $x \ll 1$ (replacing equation 5.24a) but, in practice, the large separation limit gives the better fit.

Similarly, an effective Gaussian radius, r_v, can be defined. Ignoring the peak biasing effect, equation 5.22 gives

$$\left\langle v_a^2 \right\rangle = v_0^2 \left(1 + x^2\right)^{-(n+1)/2} , \tag{5.25a}$$

where

$$v_0^2 = \frac{1}{3} f^2 H_0^2 \sigma_0^2 r_v^2 \left(\frac{2}{n+1}\right) . \tag{5.25b}$$

Hence,

$$r_v = r_a \left(\left(\frac{v_a^2}{v_0^2} \right)^{-2/(n+1)} - 1 \right)^{-1/2} . \tag{5.25c}$$

There is no expansion used in deriving this equation so it is equally valid at small and large separations. Figure 5.2 shows the actual values of v_a and γ_{aa} for massive neutrinos and the fit using Gaussian models as outlined here. The fit is extremely good across most of the range for γ_{aa}. It is slightly poorer for v_a but still good enough at the separations required if the window radius used to derive r_v is of a similar order of magnitude to the actual real window radius. The values used in generating figure 5.2 were found by using window radii of $10(\Omega h^2)^{-1}$Mpc and $30(\Omega h^2)^{-1}$Mpc for r_v and r_γ respectively. Using smaller values for deriving r_v or larger values for deriving r_γ gave essentially the same highest probability contours although the accuracy of the fit suffered. Using window radii that were too large for deriving r_v however gave unphysical solutions since then the velocity on small scales is underestimated and the parameter Δ defined before equation 5.14 becomes negative. The accuracy of the fit when suitable window radii are used is not surprising since the power spectrum for massive neutrinos is almost Gaussian in any case, with a damping length of about $4(\Omega h^2)^{-1}$Mpc.

With suitable values for r_γ and r_v (those found in practice were $4.5(\Omega h^2)^{-1}$Mpc and $5.5(\Omega h^2)^{-1}$Mpc), the required velocities can be calculated using equations 5.24a and 5.25a. This saves having to do any numerical integration over the true power spectrum. More importantly, since these effective lengths depend on Ωh^2, and the real window lengths depend on h, it demonstrates that for massive neutrinos any model can be

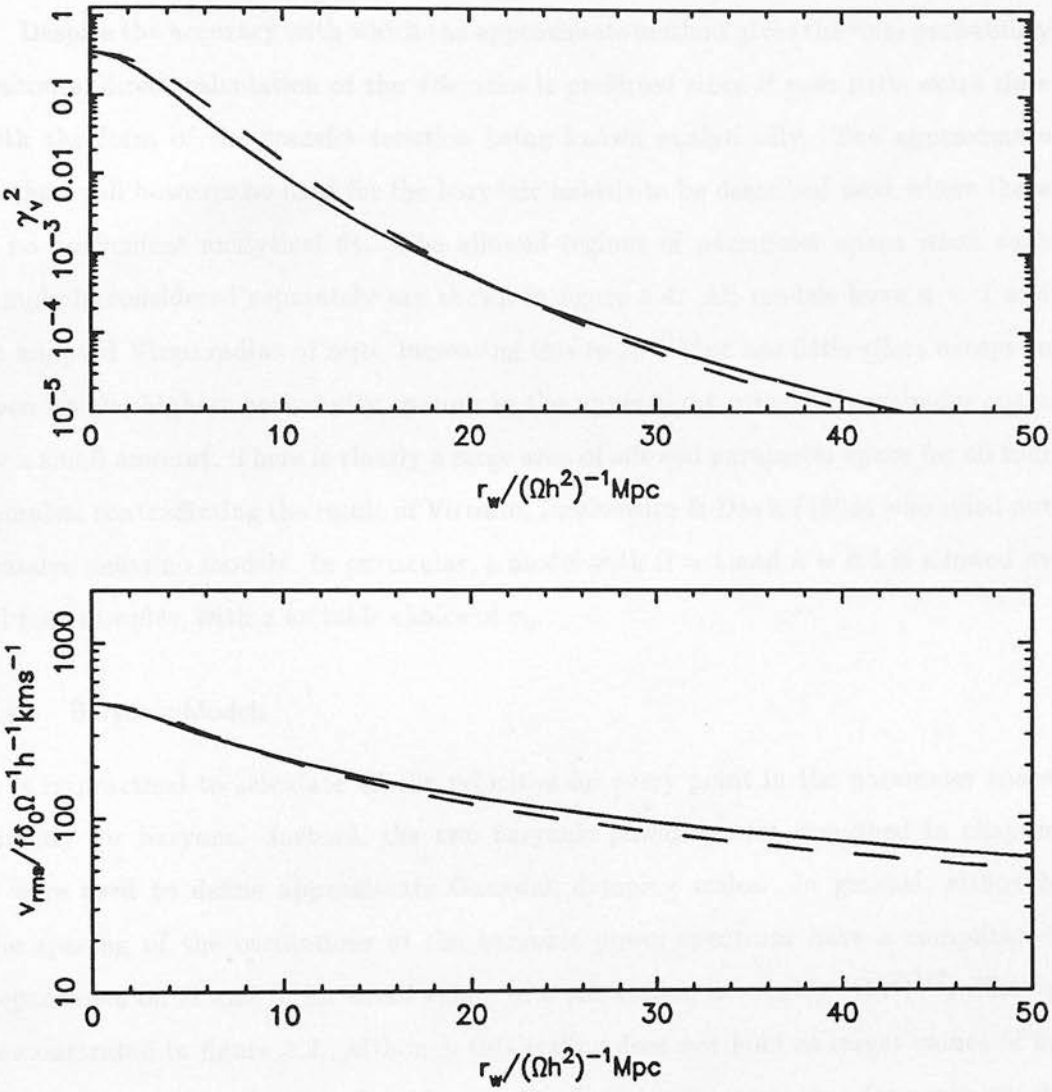

Figure 5.2: The Gaussian fits to the real neutrino power spectrum for γ_{aa}^2 and v_a. The window radii chosen for deriving the values of r_v and r_γ were $10(\Omega h^2)^{-1}$Mpc and $30(\Omega h^2)^{-1}$Mpc respectively.

parameterised by Ωh and $f\sigma_0$. Figure 5.3(a) shows the resultant probability contours (the contour levels are set at the same values as used previously) for the approximate model. Figure 5.3(b) shows the same contours where the velocities have been calculated directly. The agreement is again extremely good. Both models use a zero Virgo radius and have $n = 1$.

Despite the accuracy with which the approximate method gives the final probability contours, direct calculation of the velocities is preferred since it uses little extra time with the form of the transfer function being known analytically. The approximate method will however be used for the baryonic models to be described next where there is no convenient analytical fit. The allowed regions of parameter space when each sample is considered separately are shown in figure 5.4. All models have $n = 1$ and an adopted Virgo radius of zero. Increasing this to $3h^{-1}$Mpc has little effect except to open up the highest probability contour in the upper right corner of parameter space by a small amount. There is clearly a large area of allowed parameter space for all four samples, contradicting the result of Vittorio, Juszkiewicz & Davis (1986) who ruled out massive neutrino models. In particular, a model with $\Omega = 1$ and $h = 0.5$ is allowed by all four samples, with a suitable choice of σ_0.

5.4.3 Baryonic Models

It is impractical to calculate all the velocities for every point in the parameter space directly for baryons. Instead, the two baryonic power spectra described in chapter 3 were used to define approximate Gaussian damping scales. In general, although the spacing of the oscillations of the baryonic power spectrum have a complicated dependence on Ω and h, for small values of k the scaling is roughly $(\Omega h^2)^{1/2}$. This is demonstrated in figure 3.2. Although this scaling does not hold at larger values of k, for calculating the velocities of *field points* (*i.e.* ignoring the correction for peaks which is fairly insignificant for baryons anyway: see figure 5.5) although the part of the power spectrum near the first zero is important if $n = 1$. Figure 5.5 shows the fits to γ_{aa} and v_a using the same choices as for the neutrinos. The velocity fit is especially good. Furthermore, with a scaling of $(\Omega h^2)^{1/2}$, the final velocities scale only with $\Omega^{1/2}$, so the parameter space is defined by Ω and $f\sigma_0$.

Figure 5.6 shows the the allowed regions of this parameter space for each of the samples individually. The global average streaming gives results similar to the G7

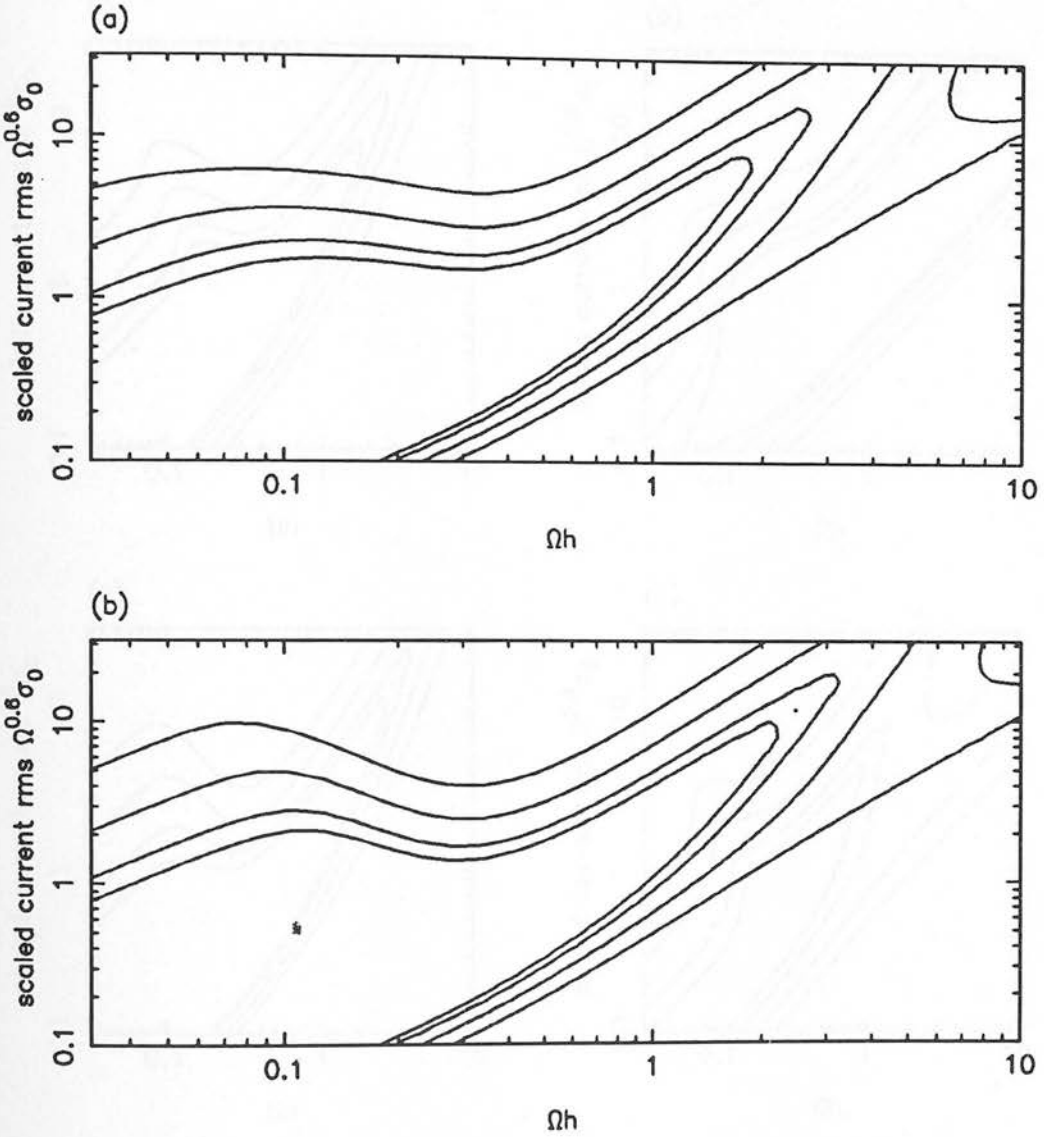

Figure 5.3: (a) The allowed region of parameter space using the approximate method outlined in section 5.4.2. (b) The allowed region of parameter space with the velocities calculated directly. The spectral index is $n = 1$, the adopted Virgo radius is zero and the model considered is massive neutrinos.

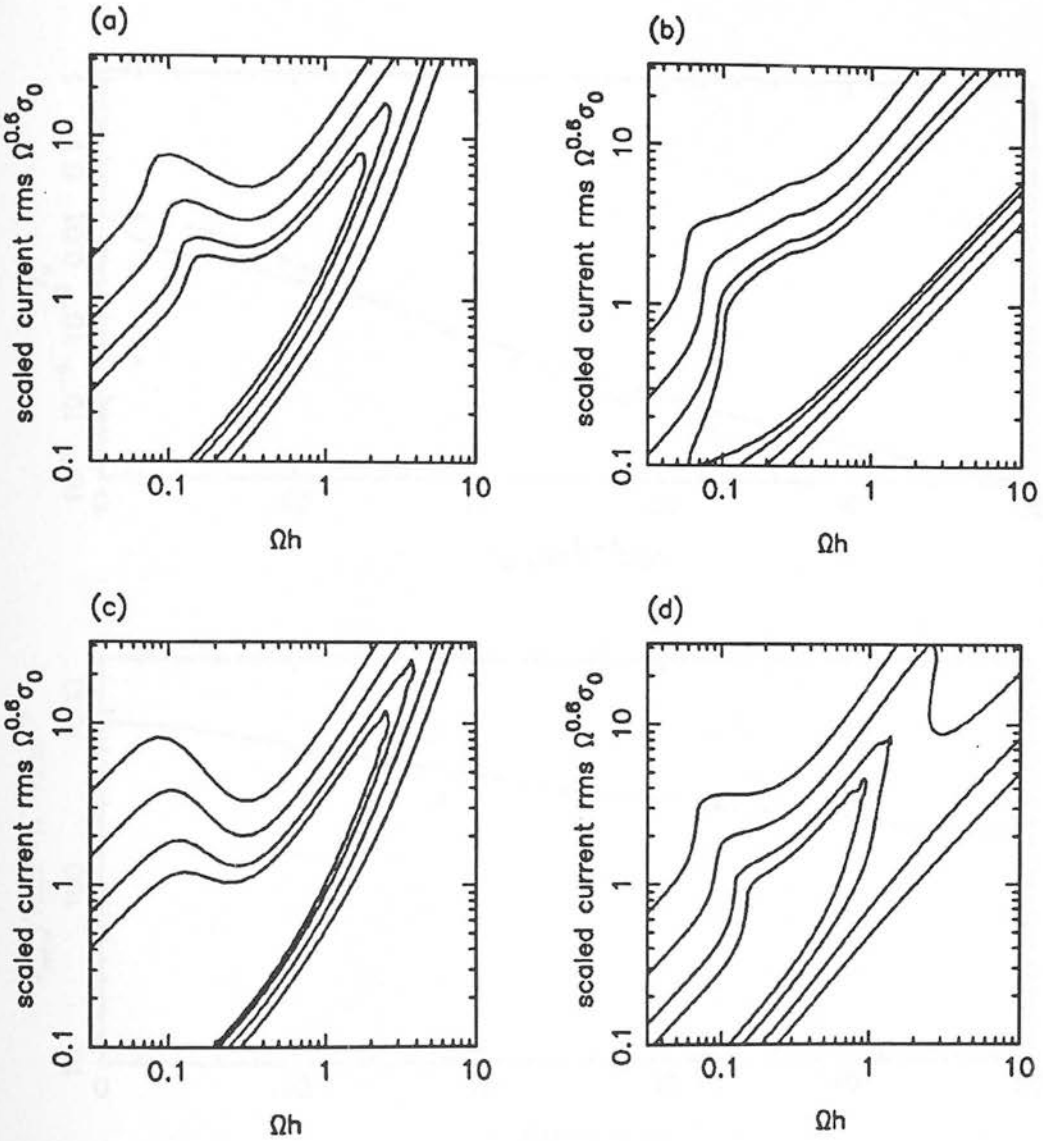

Figure 5.4: The allowed region of parameter space for every sample separately when the universe is dominated by massive neutrinos. Abbreviations are defined in the text. The spectral index is $n = 1$ and the adopted Virgo radius is zero. (a) The G7 sample. (b) The A86 sample. (c) The SS & D sample. (d) the CJR sample.

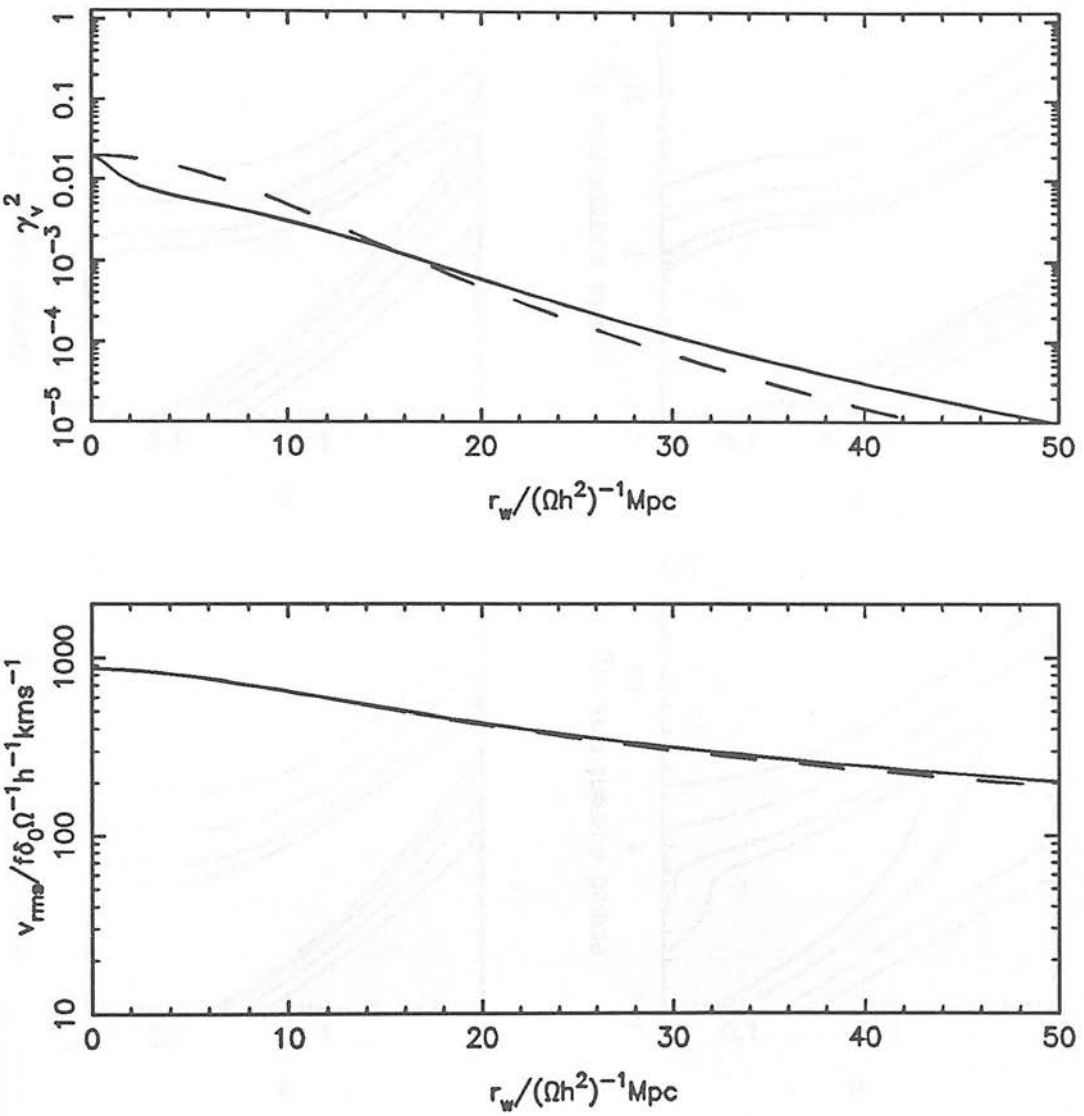

Figure 5.5: The Gaussian fits to the real baryonic power spectrum for γ_{aa}^2 and v_a. The window radii chosen for deriving the values of r_v and r_γ were $10(\Omega h^2)^{-1}$Mpc and $30(\Omega h^2)^{-1}$Mpc respectively.

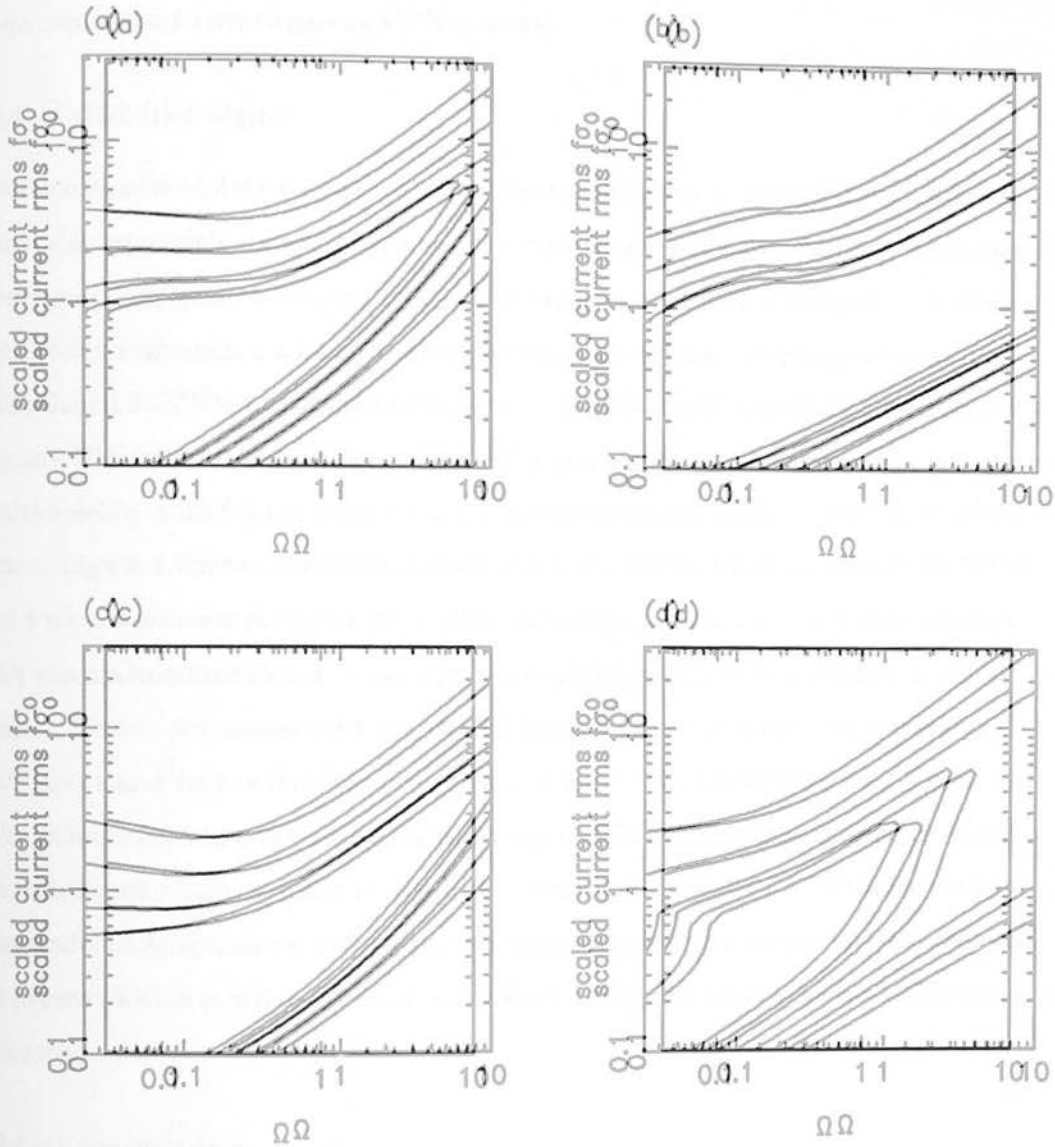

Figure 5.6: The allowed region of parameter space for every sample separately when the universe is baryon dominated. Abbreviations are defined in the text. The spectral index is $n = 1$ and the adopted Virgo radius is zero. (a) The GG sample (b) The A86 sample (c) The SS & D sample (d) the CIR sample.

and SS & D samples. The major problem with adiabatic baryon models (at least if $n = 1$ which it must for the approximate fit to work) is that the predicted streaming motions are too large unless σ_0 is small. Considering the CJR sample alone slightly improves this result but the allowed region of parameter space is still relatively small when compared to neutrino and CDM models.

5.4.4 Cold Dark Matter

For the case of cold dark matter, the approximate method is not useful since there is no physical large scale damping. Instead the velocities are calculated directly. Given the very good analytical fit to the CDM power spectrum in BBKS this is not a problem. For this set of models, a non-zero window radius for the Virgo motion must be applied. The value of $3h^{-1}$Mpc was used throughout. This, despite the lack of physical damping in the CDM model, does not actually make much difference, since most of the power in the velocity field for the scale invariant model comes from large wavelengths in any case. Figure 5.7 shows the average streaming motion with a window radius of $3h^{-1}$Mpc and with a window radius of zero. Although there is a clear shift to higher values of Ωh when a non-zero radius is used, the area of highest probability remains roughly the same. This is not unexpected since the difference in the velocities when windowed on $3h^{-1}$Mpc and zero is only about a factor of 0.75. It is however necessary to include the windowing when considering samples such as CJR where the outer window radius is much larger. Both assume that $n = 1$. Figure 5.8 shows each of the four samples separately. Again, there is definitely an allowed region of parameter space especially for lower Ω with $h = 0.5$. Flat CDM models are definitely excluded by the CJR sample however.

5.4.5 Normalisation

It is useful to consider exactly what the predicted σ_0 values are for some of the models considered. For the CDM dominated models and the baryonic ones the normalisation method used was by matching to J_3 as described in section 2.3.1.2. The massive neutrino model was normalised by assuming a collapse redshift, $z_g = 1$. This is in line with the estimates of Frenk, White & Davis (1983), who found that the collapse epoch for pancake models had to be quite late ($z \sim 2$) and correspondingly the epoch of galaxy formation is later still. This normalisation corresponds to a current *rms* density

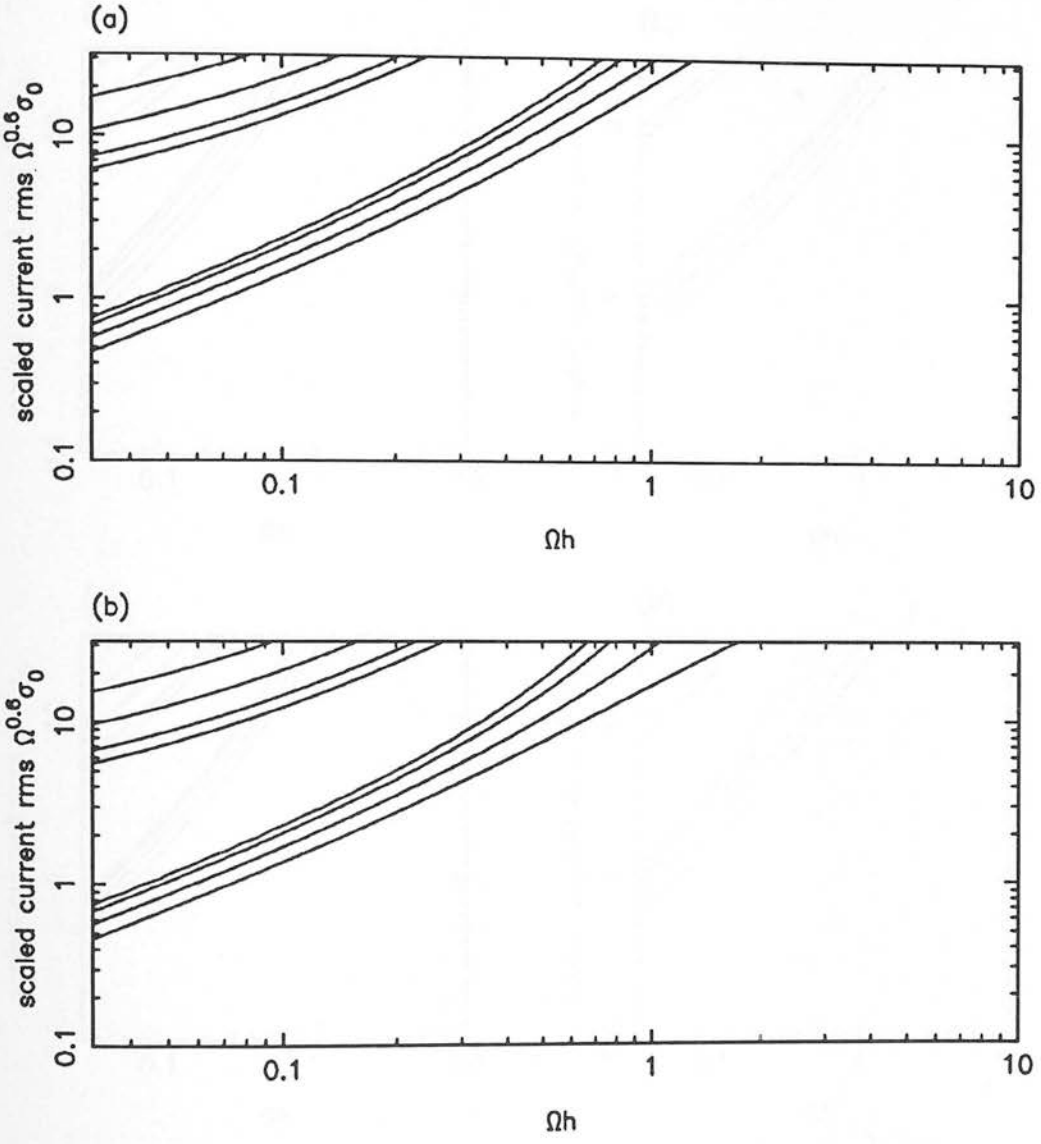

Figure 5.7: The affect of allowing the Virgo radius to be zero for CDM models. The upper figure is generated with a Virgo window of $3h^{-1}$Mpc and the lower had zero window radius.

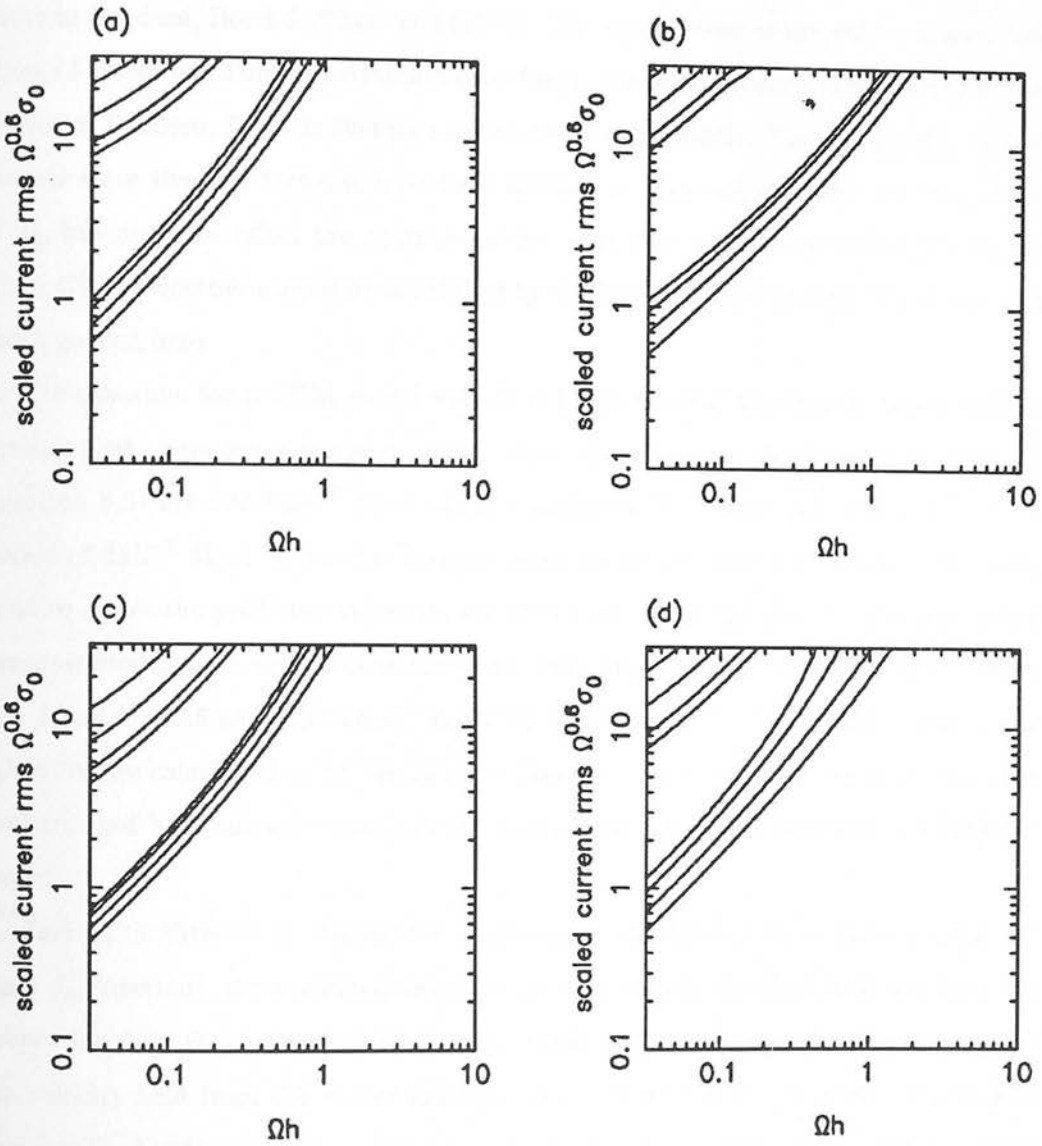

Figure 5.8: The allowed region of parameter space for every sample separately when the universe is dominated by CDM. Abbreviations are defined in the text. The spectral index is $n = 1$ and the adopted Virgo radius is $3h^{-1}$Mpc. (a) The G7 sample. (b) The A86 sample. (c) The SS & D sample. (d) the CJR sample.

fluctuation, $\sigma_0 = 2$.

The transfer functions used for the CDM and neutrino models were taken from BBKS. The fits used by Vittorio & Turner (1987) give answers which are different by up to 25% for the neutrino models. The typical velocities found here agree well with those in Bardeen, Bond & Efstathiou (1987). The comparison of typical velocities with those of Vittorio & Turner is straightforward since the normalisation criteria are similar. However, Bardeen, Bond & Efstathiou consider biased models. This affects their CDM models since the bias factor is included explicitly in comparing to the observed value of J_3, but does not affect the neutrino model since they give an explicit value for σ_0. Their CDM velocities should be multiplied by the bias factor given for comparison with those quoted here.

For example, for a CDM model with $\Omega = 1$ and $h = 0.5$ the typical *rms* velocities (noting that these are a factor $\sqrt{3}$ larger than the velocities along one axis given by equation 5.3) are 590 kms^{-1} for a window radius of $5h^{-1}$ Mpc and 253 kms^{-1} for a radius of $25h^{-1}$ Mpc. For a flat massive neutrino model with $h = 0.5$ and the same window scales the predicted velocities are 1574 kms^{-1} and 750 kms^{-1}. The two actual baryonic models have velocities on the same scales of 1884 kms^{-1} and 1300 kms^{-1} when $\Omega = 1$ and $h = 0.5$ and 1243 kms^{-1} and 1130 kms^{-1} when $\Omega = 0.2$ and $h = 0.5$. These velocities are calculated using the J_3 normalisation. The major difference between the neutrino and baryonic universes is in the much larger coherence length of the baryonic models.

Just as in Vittorio & Turner, for a constant normalisation (*e.g.* always using the same J_3 criterion), the predicted velocities on very large scales for CDM are inversely proportional to Ω. As the window radius tends to infinity the only contribution to the velocity field from the power spectrum comes from the $k = 0$ mode. Hence, the unnormalised velocity field on this scale is simply proportional to $\Omega^{0.6}$ as might be expected. However, using J_3 on a CDM model gives a normalisation constant that is roughly proportional to Ω^{-1}. The overall effect is that the normalised velocity field scales as $\Omega^{-0.4}$ at infinity. On smaller scales, the dependence is not as strong since the power spectrum also depends on Ω and h. The fits given in Vittorio & Turner for various window scales and a CDM model show this intermediate dependence on Ω and h though when compared with the velocities calculated here their variation with Ω and h is only accurate to about 20%.

Bardeen, Bond & Efstathiou also give values for σ_0 when the density field is smoothed on galaxy scales. For the neutrino model this smoothing has a negligible effect. For the CDM models it is important however. What is required here though is the value of σ_0 for the unsmoothed power spectrum. Smoothing the density field does not strongly affect the overall normalisation however since the J_3 integral is insensitive to structure on such small scale sizes.

Typical values for σ_0 with the normalisations given above vary quite markedly. A flat CDM model with $h = 1$ has $\sigma_0 = 49$. Reducing h to 0.5 changes this value to $\sigma_0 = 25$. A model with $h = 0.5$ and $\Omega = 0.2$ has $\sigma_0 = 8$. The *rms* density fluctuations when smoothed on galaxy scales for these models is 7.5, 6.6 and 3.4 respectively. The two known baryonic models, for which $h = 0.5$ and $\Omega = 1$ and $\Omega = 0.2$, have $\sigma_0 = 1.14$ and $\sigma_0 = 1.01$ respectively. These points provide additional constraints on all the contour plots given in this section.

5.5 Conclusions

5.5.1 Results

The method presented here provides powerful constraints on all the models considered, especially when coupled with predicted values for the *rms* density fluctuation. As already mentioned in section 5.4.1, generic large scale damping models can successfully reproduce the observed streaming motions. In this picture, the misalignment of two streaming motions of roughly similar magnitudes is caused by the real physical large scale damping. Motions within this scale will arise through non-linear processes whose direction and amplitude will not in general be related to the simpler linear motions on large scales. In particular, a simple flat massive neutrino model with $\Omega = 1$ and $h = 0.5$ agrees with all the samples except that of SS & D. Even there, the model can only be excluded at the 5% level. Given that the SS & D sample is at very small scales anyway, for a large scale damping model the bulk of the sample almost lies within the damping scale in any case so perfect agreement would perhaps be somewhat surprising. Baryonic models also fare well, though the large predicted velocities when $\Omega = 1$ are only just acceptable at the 10% level.

Perhaps more surprisingly, given the lack of large scale clustering in the model, both the standard flat CDM model and lower Ω models fit the data reasonably well.

The flat model is inconsistent with the CJR data at the 5% level. However, allowing biasing into the flat CDM models seriously affects the expected amplitude of large scale streaming. Such models are not good fits and can be excluded at the 1% level if the bias is $b \sim 1.7$ and at an even higher certainty for larger values of the bias. A low density (*e.g.* $\Omega = 0.2$, $h = 0.5$) CDM model does fit the data for all the samples.

The effect of considering peaks of the density field actually makes little difference for the baryonic and the CDM models since there power extends across a large range of scales. Only the neutrino models gain, since the factor γ_v is about 0.8. Without this, the predicted neutrino velocities would tend to be too large.

5.5.2 Comparison with Similar Work

Almost all the early work on analysing streaming motions took the form of examining model *rms* peculiar velocities windowed on a given scale. These were then tested against the observations to see if the probability of seeing the required velocity was reasonable. Vittorio & Turner (1987) consider many models using techniques of this kind, as did Bardeen, Bond & Efstathiou (1987). Vittorio & Turner give values for streaming motions when windowed with Gaussian filters on three different scales. Unfortunately, their chosen scale for comparing to the CJR and G7 samples is too large. This is in common with the error in Vittorio, Juszkiewicz & Davis (1986). It is true that the mean depth of the CJR sample is $50h^{-1}$ Mpc but as discussed in section 5.2.3 the relevant Gaussian window has a much smaller scale length. This was also demonstrated by Kaiser (1988a) for the G7 sample. Vittorio & Turner also use a window scale for Virgo of $10h^{-1}$ Mpc which for reasons outlined in section 5.4.1 is not the value used here. They conclude from their results that CDM models are still marginally feasible but that neutrino models are not. Allowing both the Virgo window and the larger scale filter to shrink would change Vittorio & Turner's conclusions dramatically. Since their predicted velocities for the various models are in agreement with those found here, it is only their choice of filter scales that leads them to differing conclusions, as well as the adoption of the probably incorrect value for the CJR sample.

Bardeen, Bond & Efstathiou choose more realistic values for their window functions. They use a scale of $15h^{-1}$ Mpc for the G7 sample. Their adopted values for the CJR sample (filter scale of $40h^{-1}$ Mpc and streaming motion of 970 kms^{-1}) are however anomalous. Their adopted small scale streaming value is that of the Local Group

which is larger than that obtained when using Virgo. Since at least part of the Local Group's motion is due to the effect of Virgo, using our motion as a test of linear theory is not strictly realistic. If, however, their small scale motions are compared to the Virgo motion relative to the CBR and their predicted values for the CJR sample are ignored, their results are again in agreement with those found here. Their inclusion of biasing into the flat CDM model shows how that seriously affects the predicted velocities, just as their inclusion of anti-biasing for the massive neutrino model results in predicted peculiar velocities that are too large.

The results of Vittorio, Juszkiewicz & Davis, whilst using a technique similar to that used here, use blatantly wrong filter scales for their small and large scale samples. Clearly the method is more powerful than simply considering the probability of obtaining the correct peculiar velocities on different scales separately but their use of incorrect sample sizes makes their work virtually useless when comparing to the known observations. Similarly, the work of Kaiser (1983) and Clutton-Brock & Peebles (1981) is no longer of much use. The streaming motions which their conclusions were based on have not survived. It is also largely for this reason that the conclusions of the work here differ from those of Peacock, Lumsden & Heavens (1987), and should act as a reminder that, even now, the actual velocity field is still not accurately known on an all-sky basis. Even the current best estimates may change again within a matter of years.

5.5.3 Other Methods

Despite the fact that techniques similar to the one used here can be used to set constraints on cosmological models, they do not make full use of the data available. The first advance on this was given by Kaiser (1988a) who used a subset of the galaxies in the G7 and A86 samples to construct a likelihood solution for streaming in a flat, CDM dominated universe. He used the observational data to generate a tensor window function which was then convolved with a model velocity field to give a predicted streaming motion. His conclusion was that a flat, unbiased CDM model could explain the observed streaming in the sub-sample. Note that this method is similar in principle to the earlier approaches. Its merit lies in using all the data to construct an accurate realisation of the window function. The final result is in good agreement with that found here since the flat unbiased CDM model has a large value of σ_0 when normalised

to J_3, as was found in section 5.4.5.

A more useful way of using the data is to consider a velocity correlation function. Various such functions have been proposed. Gorski *et al.* (1989) give a useful summary of the work done by others such as Kaiser (1988b) and Groth, Juszkiewicz & Ostriker (1989) as well as their own. A detailed comparison of the various correlation functions is beyond the scope of this chapter. What is of interest is that all groups find that the standard flat biased CDM model is incompatible with the G7 sample. This is in line with the simpler methods presented here.

5.5.4 Summary

The method used here agrees well with other work when a consistent approach is adopted. The concept that we must lie near a peak in the density field helps the neutrino models since the predicted velocities are lowered. Open, unbiased CDM models fit the data quite well. Standard, biased CDM models would appear to be excluded quite strongly. Baryonic models fit the data reasonably well, though there may be a problem in that the correlation length for such models is rather large. Overall, the constraints provided by large scale streaming motions are very similar to those posed by the large scale clustering discussed in chapter 4.

Although the work in this chapter has rested on the assumption that the observed streaming motions can be explained by a pure dipolar motion, similar conclusions were reached by Lynden-Bell *et al.* (1988) for their Great Attractor model. Since the mass concentration in the model is so large, they find that such an occurrence in a biased CDM model is extremely rare. Hence, even a distinctly separate model of the streaming motion leads to very similar conclusions.

Appendix A

Evolution of Small Perturbations

A.1 Introduction

The purpose of this appendix is to demonstrate that the derivation of the equations governing the evolution of the perturbed quantities, as outlined in Chapter 2, is relatively straightforward (if, algebraically, somewhat messy). The basic principle of introducing small perturbations into a metric is outlined in Section 10.9 of Weinberg (1972): however, since the metric used here has the opposite signature, $(+,-,-,-)$ instead of $(-,+,+,+)$, and the definition of the curvature tensor in Weinberg is also different, it is useful to present a brief recap.

Having considered the basic theory, a more detailed derivation is given showing how the actual equations given in chapter 2 are arrived at. This work is similar in principle to that of Wilson (1983) and Gouda, Sasaki & Suto (1987) but some details are different (especially with regard to the bizarre notation of Wilson) and some general points can be made regarding this work by considering it in detail. A detailed derivation for the case of a flat ($\Omega = 1$) universe is given in Peebles (1980).

A.2 Basic Concepts

A.2.1 Definitions and Conventions

The 4-metric, $g_{\mu\nu}$, has signature $(+,-,-,-)$.

The determinant of $g_{\mu\nu}$ is denoted by g.

The 3-metric, γ_{ij}, has signature $(+,+,+)$.

Greek indices run over the range {0,1,2,3} and Latin indices over the range {1,2,3}.

The following symbols are defined:

; covariant derivative with respect to the 4-metric, $g_{\mu\nu}$.

| covariant derivative with respect to the 3-metric, γ_{ij}.

, partial derivative with respect to either metric.

The connection coefficient, $\Gamma^{\alpha}_{\beta\gamma}$:

$$\Gamma^{\alpha}_{\beta\gamma} \equiv \frac{1}{2} g^{\alpha\mu} \left(g_{\beta\mu,\gamma} + g_{\gamma\mu,\beta} - g_{\beta\gamma,\mu} \right) . \tag{A.1}$$

The corresponding connection coefficient for the 3-metric will be labelled λ^{i}_{jk}.

The curvature tensor, $R^{\alpha}{}_{\beta\gamma\delta}$:

$$R^{\alpha}{}_{\beta\gamma\delta} \equiv -\Gamma^{\alpha}_{\beta\gamma,\delta} + \Gamma^{\alpha}_{\beta\delta,\gamma} - \Gamma^{\alpha}_{\mu\delta}\Gamma^{\mu}_{\beta\gamma} + \Gamma^{\alpha}_{\mu\gamma}\Gamma^{\mu}_{\beta\delta} . \tag{A.2}$$

The Ricci tensor, $R_{\alpha\beta}$:

$$R_{\alpha\beta} \equiv R^{\mu}{}_{\alpha\mu\beta} . \tag{A.3}$$

The curvature scalar, R:

$$R \equiv g^{\alpha\beta} R_{\alpha\beta} . \tag{A.4}$$

All the curvature terms for the 3-metric will be labelled like ${}^{3}R\ldots$.

A.2.2 Spaces with Constant Curvature

It will be seen later that the 3-metric refers to a symmetric subspace. Section 13.2 of Weinberg shows that such a space has special properties. In particular, it has constant curvature throughout the whole subspace. This implies that the curvature tensor and its various contractions can only be composed of the 3-metric, γ_{ij}, and a constant, K, known as the curvature constant. Weinberg outlines these properties in more detail. The basic form of the resultant curvature terms, ${}^{3}R\ldots$, reduces to:

The curvature tensor, ${}^{3}R_{ijkl}$:

$${}^{3}R_{ijkl} = K \left(\gamma_{ik}\gamma_{jl} - \gamma_{il}\gamma_{jk} \right) . \tag{A.5}$$

The Ricci tensor, ${}^{3}R_{ij}$:

$${}^{3}R_{ij} = 2K\gamma_{ij} . \tag{A.6}$$

The curvature scalar, ${}^{3}R$:

$${}^{3}R = 6K . \tag{A.7}$$

These properties will be used extensively in what follows.

A.2.3 General Perturbations

Following Weinberg, if a small perturbation $(\delta g)_{\mu\nu}$ is introduced such that

$$g'_{\mu\nu} = g_{\mu\nu} + (\delta g)_{\mu\nu} \,, \tag{A.8a}$$

and hence,

$$g'^{\mu\nu} = g^{\mu\nu} - (\delta g)^{\mu\nu} \qquad \text{to } \mathrm{O}(\delta g) \,, \tag{A.8b}$$

then there is a corresponding change in the other quantities.

$$\Gamma'^{\alpha}_{\beta\gamma} \equiv \Gamma^{\alpha}_{\beta\gamma} + \delta\Gamma^{\alpha}_{\beta\gamma} = \frac{1}{2} g'^{\alpha\mu} \left(g'_{\beta\mu,\gamma} + g'_{\gamma\mu,\beta} - g'_{\beta\gamma,\mu} \right) \,. \tag{A.9a}$$

Expanding the form of the metric terms as given by equation A.8 results in

$$\delta\Gamma^{\alpha}_{\beta\gamma} = \frac{1}{2} g^{\alpha\mu} \left((\delta g)_{\beta\mu;\gamma} + (\delta g)_{\mu\gamma;\beta} - (\delta g)_{\beta\gamma;\mu} \right) \,, \tag{A.9b}$$

where the covariant derivatives are defined by:

$$(\delta g)_{\beta\mu;\gamma} \equiv (\delta g)_{\beta\mu,\gamma} - \Gamma^{\rho}_{\beta\gamma} (\delta g)_{\rho\mu} - \Gamma^{\rho}_{\mu\gamma} (\delta g)_{\rho\beta} \,. \tag{A.9c}$$

Note that the terms of the connection coefficient that appear in this formula refer to the unperturbed terms, and this is in general true when considering covariant derivatives of the perturbed quantities.

Similar substitutions of the primed terms into the definitions of the curvature and Ricci tensors give the following.

The perturbation to the curvature tensor, $\delta R^{\alpha}{}_{\beta\gamma\delta}$:

$$\delta R^{\alpha}{}_{\beta\gamma\delta} = -\delta\Gamma^{\alpha}_{\beta\gamma,\delta} + \delta\Gamma^{\alpha}_{\beta\delta,\gamma} - \Gamma^{\alpha}_{\mu\delta}\delta\Gamma^{\mu}_{\beta\gamma} - \delta\Gamma^{\alpha}_{\mu\delta}\Gamma^{\mu}_{\beta\gamma} + \Gamma^{\alpha}_{\mu\gamma}\delta\Gamma^{\mu}_{\beta\delta} + \delta\Gamma^{\alpha}_{\mu\gamma}\Gamma^{\mu}_{\beta\delta} \,. \tag{A.10}$$

The perturbed Ricci tensor, $\delta R_{\alpha\beta}$:

$$\delta R_{\alpha\beta} = \delta\Gamma^{\mu}_{\alpha\beta;\mu} - \delta\Gamma^{\mu}_{\alpha\mu;\beta} \,. \tag{A.11}$$

Both the perturbations to the connection coefficients and to the Ricci tensor are themselves tensors.

The final step is to consider the effect these perturbations have on the field equations:

$$R_{\alpha\beta} = \frac{8\pi G}{c^4} \left(T_{\alpha\beta} - \frac{1}{2} g_{\alpha\beta} T \right) \,. \tag{A.12}$$

The $T_{\alpha\beta}$ is the stress-energy-momentum tensor (hereafter, the stress tensor). It is also necessary to include the effects of a small perturbation in it. T is the trace of the stress tensor given by:

$$T = g^{\alpha\beta}T_{\alpha\beta} \,. \tag{A.13}$$

Using these new definitions it is trivial to see that:

$$\delta R_{\alpha\beta} = \frac{8\pi G}{c^4}\left(\delta T_{\alpha\beta} - \frac{1}{2}(\delta g)_{\alpha\beta}T - \frac{1}{2}g_{\alpha\beta}\delta T\right) \,. \tag{A.14}$$

A.2.4 Gauge Transformations and Gauge Invariance

A gauge transformation is any infinitesimal change in the coordinates of the form

$$x^\mu \rightarrow x'^\mu = x^\mu - \varepsilon^\mu(x) \,, \tag{A.15a}$$

where $\varepsilon(x)$ is an arbitrary function. It is effectively equivalent to a small perturbation in the metric of the form

$$g'_{\mu\nu}(x) = g_{\mu\nu} + \varepsilon_{\mu;\nu} + \varepsilon_{\nu;\mu} \,.$$

There is also a corresponding perturbation in the stress tensor and the new metric, $g'_{\mu\nu}$, is now a solution to the new stress tensor, $T'_{\mu\nu}$, in the field equations. However, such a small change in the metric is equivalent to including real perturbations. It is important therefore to distinguish real physical effects from spurious gauge effects.

In principle, the best method of circumventing this problem is to use a set of variables that are *gauge invariant.* Bardeen (1980) and Kodama & Sasaki (1984) consider the implications of this choice in more detail by considering general perturbations of the kind outlined in section A2.3., and using gauge invariant quantities. Then it is necessary only to relate the invariant quantities to the observed quantities on sub-horizon scales where gauge effects are unimportant, since the gravitational field is weak and Newtonian theory must be applicable.

Conventionally, however, the results of calculations involving the evolution of small fluctuations in a Friedmann universe have been carried out by *fixing* the gauge. This implies that a choice is made regarding the form of the $(\delta g)_{\mu\nu}$ in equation A.8. A particular choice of gauge that has proven popular with theorists is the *synchronous* gauge, where

$$(\delta g)_{0\mu} = 0 \,.$$

This has the obvious attraction that any constant time hypersurface is not perturbed and provides a reference point. Since part of the purpose of redoing this work is to compare the results derived with earlier work, the same choice will be made here.

Even after adopting this particular gauge there is still some freedom. Any constant can be added to the δg_{ij} without affecting the result, so the values of the δg_{ij} themselves can never be fixed exactly. Since only the time derivatives of these quantities are important in this gauge this is not problem. However, as was shown by Press & Vishniac (1980), there is also a spurious growing mode in this gauge for perturbations on super-horizon scales. Since the dominant growing mode is real, the effect of this in a numerical calculation should be unimportant. Using gauge-invariant mechanisms does not remove this problem though, since, as was pointed out by Bardeen, the gauge-invariant quantities must still be related to real observable quantities. As is shown in chapter 2, the only real value of gauge-invariant methods is in calculating the time evolution of the perturbations numerically, since the isocurvature mode is best expressed in this form for greatest accuracy.

A.3 The Field Equations

A.3.1 The Choice of Metric

Section A2.4 outlined the reasons behind choosing a specific gauge to work in. The basic metric used is the Robertson-Walker metric. This has the general form:

$$ds^2 = c^2 dt^2 - a^2(t)\left(\frac{dr^2}{1-kr^2} + r^2(d\theta^2 + \sin^2\theta d\phi^2)\right) . \tag{A.16}$$

The function $a(t)$ is called the scale factor and represents the effect of the expansion of the universe. It is normalised such that $a = 1$ at the present epoch. This metric is manifestly isotropic in its spatial sections, and is also homogeneous as well, thus fulfilling the fundamental observational criterion outlined in chapter 1. Therefore, this metric has a maximally symmetric 3-subspace. Hereafter the value of c shall be set equal to 1: it is easy to reintroduce it into the final results.

In line with section A2.2, the symmetric 3-metric will be called γ_{ij}. With this definition and the choice of the synchronous gauge, the general form of the perturbed metric is given by:

$$g_{00} = 1 \tag{A.17a}$$

$$g_{0i} = 0 \tag{A.17b}$$

$$g_{ij} = -a^2 \left(\gamma_{ij} - h_{ij}\right) . \tag{A.17c}$$

Note that $h_{ij} \equiv (\delta g)_{ij}$. The inverse metric is (to $O(h)$):

$$g^{ij} = -a^{-2} \left(\gamma^{ij} + h^{ij}\right) . \tag{A.17d}$$

Lastly, the determinant of $g_{\mu\nu}$ can be calculated.

$$g = a^6 \det \gamma_{ij} \det(1 - \gamma^{-1} h_{ij}) , \tag{A.18a}$$

using equation A.17c, and hence,

$$g = a^6 \det \gamma_{ij} (1 - \mathrm{tr}\gamma^{-1} h_{ij}) = a^6 \det \gamma_{ij} (1 - h) \tag{A.18b}$$

since $\gamma^{-1} = \gamma^{kj}$.

A.3.2 Composite Stress Tensor

For the purposes of this calculation the constituents of the universe will be taken to be baryons, photons and three species of massless neutrino. The mass density of the baryons is denoted by ρ_b, that of the photons by ε_b and that of the neutrinos by ε_ν. Since each neutrino species of is effectively equivalent for the purposes of this work, only one is included in the calculation. The effect of all three is modelled by setting $\varepsilon_\nu = \varepsilon_{\nu_e} + \varepsilon_{\nu_\mu} + \varepsilon_{\nu_\tau}$. In line with standard theory (see *e.g.* Weinberg), $\varepsilon_\nu = 0.68\varepsilon_b$.

A.3.3 The Unperturbed Field Equations

It is convenient and simpler to derive the field equations for the unperturbed terms separately from the perturbation terms. With this in mind, the following is a brief run through of the derivation of the unperturbed field equations using the techniques outlined previously.

The components of the connection coefficients:

$$\Gamma^0_{00} = 0 , \tag{A.19a}$$

$$\Gamma^0_{0i} = 0 , \tag{A.19b}$$

$$\Gamma^0_{ij} = a\dot{a}\gamma_{ij} , \tag{A.19c}$$

$$\Gamma^i_{00} = 0 \,, \tag{A.19d}$$

$$\Gamma^i_{0j} = \frac{\dot{a}}{a}\delta^i{}_j \,, \tag{A.19e}$$

$$\Gamma^i_{jk} = \lambda^i_{jk} = \frac{1}{2}\gamma^{im}\left(\gamma_{jm,k} + \gamma_{km,j} - \gamma_{jk,m}\right) \,. \tag{A.19f}$$

$\delta^i{}_j$ is the usual Kronecker delta symbol.

The components of the curvature tensor:

$$R^0{}_{000} = 0 \,, \tag{A.20a}$$

$$R^0{}_{i00} = 0 \,, \tag{A.20b}$$

$$R^j{}_{ij0} = 0 \,, \tag{A.20c}$$

$$R^i{}_{0i0} = -3\frac{\ddot{a}}{a} \,, \tag{A.20d}$$

$$R^0{}_{i0j} = a\ddot{a}\gamma_{ij} \,, \tag{A.20e}$$

$$R^k{}_{ikj} = {}^3R^k{}_{ikj} + 2\,\dot{a}^2\gamma_{ij} \,. \tag{A.20f}$$

These are all the components necessary to form the Ricci tensor. The term ${}^3R^k{}_{ikj}$ can be simplified to

$${}^3R^k{}_{ikj} = \gamma^{mk}\,{}^3R_{mikj} = 2K\gamma_{ij} \,.$$

The components of the Ricci tensor:

$$R_{00} = -3\frac{\ddot{a}}{a} \,, \tag{A.21a}$$

$$R_{0i} = 0 \,, \tag{A.21b}$$

$$R_{ij} = \gamma_{ij}\left(a\ddot{a} + 2\dot{a}^2 + 2K\right) \,. \tag{A.21c}$$

The curvature scalar:

$$R = -6\frac{\ddot{a}}{a} - 6\frac{\dot{a}^2}{a^2} - 6\frac{K}{a^2} \,. \tag{A.22}$$

For the unperturbed metric the stress tensor is that for a perfect fluid

$$T_{\mu\nu} = (\rho + p)\,u_\mu u_\nu - p g_{\mu\nu} \,, \tag{A.23}$$

where ρ is the mass density, p is the pressure and the u_μ are the components of the 4–velocity: for an unperturbed fluid in the expanding co-ordinate system, $u_i = 0$. For baryons the matter pressure is negligible: for radiation $p = \frac{1}{3}\rho$.

$$T_{00} = \rho_b + \varepsilon_b + \varepsilon_\nu \,, \tag{A.24a}$$

$$T_{0i} = 0 \,, \tag{A.24b}$$

$$T_{ij} = \frac{1}{3}(\varepsilon_b + \varepsilon_\nu)\, a^2 \gamma_{ij} \,, \tag{A.24c}$$

$$T = \rho_b \,. \tag{A.24d}$$

The field equations (A.12) therefore become:

$$\frac{\ddot{a}}{a} = -\frac{4\pi G}{3}(\rho_b + 2\varepsilon_b + 2\varepsilon_\nu) \,, \tag{A.25a}$$

$$\dot{a}^2 = \frac{8\pi G}{3} a^2 (\rho_b + \varepsilon_b + \varepsilon_\nu) - K \,. \tag{A.25b}$$

It is also necessary to use the following equation for the conservation of the stress tensor:

$$T^{\mu\nu}{}_{;\nu} = 0 \,. \tag{A.26}$$

This implies that the matter and radiation mass densities evolve as:

$$\rho_b \propto a^{-3} \,, \tag{A.27a}$$

$$\varepsilon_b \propto \varepsilon_\nu \propto a^{-4} \,. \tag{A.27b}$$

These equations completely describe the behaviour of the unperturbed model.

A.3.4 The Perturbed Field Equations I

Again following the theory outlined in section A2.3 the following terms can be derived. It will be shown later that there is in fact a simpler method of deriving the perturbed field equations.

The perturbed connection coefficients:

$$\delta\Gamma^0_{00} = 0 \,, \tag{A.28a}$$

$$\delta\Gamma^0_{0i} = 0 \,, \tag{A.28b}$$

where ρ is the mass density, p is the pressure and the u_μ are the components of the 4–velocity: for an unperturbed fluid in the expanding co-ordinate system, $u_i = 0$. For baryons the matter pressure is negligible: for radiation $p = \frac{1}{3}\rho$.

$$T_{00} = \rho_b + \varepsilon_b + \varepsilon_\nu \,, \tag{A.24a}$$

$$T_{0i} = 0 \,, \tag{A.24b}$$

$$T_{ij} = \frac{1}{3}(\varepsilon_b + \varepsilon_\nu)\, a^2 \gamma_{ij} \,, \tag{A.24c}$$

$$T = \rho_b \,. \tag{A.24d}$$

The field equations (A.12) therefore become:

$$\frac{\ddot{a}}{a} = -\frac{4\pi G}{3}(\rho_b + 2\varepsilon_b + 2\varepsilon_\nu) \,, \tag{A.25a}$$

$$\dot{a}^2 = \frac{8\pi G}{3} a^2 (\rho_b + \varepsilon_b + \varepsilon_\nu) - K \,. \tag{A.25b}$$

It is also necessary to use the following equation for the conservation of the stress tensor:

$$T^{\mu\nu}{}_{;\nu} = 0 \,. \tag{A.26}$$

This implies that the matter and radiation mass densities evolve as:

$$\rho_b \propto a^{-3} \,, \tag{A.27a}$$

$$\varepsilon_b \propto \varepsilon_\nu \propto a^{-4} \,. \tag{A.27b}$$

These equations completely describe the behaviour of the unperturbed model.

A.3.4 The Perturbed Field Equations I

Again following the theory outlined in section A2.3 the following terms can be derived. It will be shown later that there is in fact a simpler method of deriving the perturbed field equations.

The perturbed connection coefficients:

$$\delta\Gamma^0_{00} = 0 \,, \tag{A.28a}$$

$$\delta\Gamma^0_{0i} = 0 \,, \tag{A.28b}$$

$$\delta\Gamma^0_{ij} = -\frac{1}{2}\dot{h}_{ij}a^2 - a\dot{a}h_{ij} \,, \tag{A.28c}$$

$$\delta\Gamma^i_{00} = 0 \,, \tag{A.28d}$$

$$\delta\Gamma^i_{0j} = -\frac{1}{2}\dot{h}^i{}_j \,, \tag{A.28e}$$

$$\delta\Gamma^i_{jk} = -\frac{1}{2}\gamma^{im}\left(h_{jm|k} + h_{km|j} - h_{jk|m}\right) \,. \tag{A.28f}$$

It is more straightforward to derive the perturbed Ricci tensor directly from the form of the perturbed connection coefficients given above using equation A.11 than to derive all the necessary components of the perturbation to the curvature tensor first. However, it is useful to present the forms of the covariant derivatives that appear in A.11 and these are given next:

$$\delta\Gamma^\alpha_{0\alpha;0} = -\frac{1}{2}\ddot{h} \,, \tag{A.29a}$$

$$\delta\Gamma^\alpha_{00;\alpha} = \frac{\dot{a}}{a}\dot{h} \,, \tag{A.29b}$$

$$\delta\Gamma^\alpha_{0\alpha;i} = -\frac{1}{2}\dot{h}_{,i} - \frac{\dot{a}}{a}\delta\Gamma^k_{ik} \,, \tag{A.29c}$$

$$\delta\Gamma^\alpha_{0i;\alpha} = -\frac{1}{2}\dot{h}^j{}_{i|j} - \frac{\dot{a}}{a}\delta\Gamma^k_{ik} \,, \tag{A.29d}$$

$$\delta\Gamma^0_{ij;0} = -\frac{1}{2}\ddot{h}_{ij}a^2 - \dot{h}_{ij}a\dot{a} + \left(\dot{a}^2 - a\ddot{a}\right)h_{ij} \,, \tag{A.29e}$$

$$\delta\Gamma^0_{i0;j} = \dot{a}^2 h_{ij} \,, \tag{A.29f}$$

$$\delta\Gamma^m_{im;j} = \frac{1}{2}a\dot{a}\dot{h}\gamma_{ij} - \dot{a}^2 h_{ij} + \delta\Gamma^m_{im|j} \,, \tag{A.29g}$$

$$\delta\Gamma^m_{ij;m} = -\frac{1}{2}a\dot{a}\dot{h}_{ij} - 3\dot{a}^2 h_{ij} + \delta\Gamma^m_{ij|m} \,. \tag{A.29h}$$

The perturbed Ricci tensor:

$$\delta R_{00} = \frac{1}{2}\ddot{h} + \frac{\dot{a}}{a}\dot{h} \,, \tag{A.30a}$$

$$\delta R_{0i} = \frac{1}{2}\left(\dot{h}_{,i} - \dot{h}^j{}_{i|j}\right) \,, \tag{A.30b}$$

$$\delta R_{ij} = -a^2\left(\left(\frac{\ddot{a}}{a} + 2\frac{\dot{a}^2}{a^2}\right)h_{ij} + \frac{3}{2}\frac{\dot{a}}{a}\dot{h}_{ij} + \frac{1}{2}\frac{\dot{a}}{a}\dot{h}\gamma_{ij} + \frac{1}{2}\ddot{h}_{ij}\right) + {}^3\delta R_{ij} \,. \tag{A.30c}$$

where ${}^3\delta R_{ij} = \delta\Gamma^m_{ij|m} - \delta\Gamma^m_{im|j}$.

The perturbed curvature scalar:

$$\delta R = \ddot{h} + 4\frac{\dot{a}}{a} + \frac{\ddot{a}}{a} + 2\frac{\dot{a}^2}{a^2}h \,. \tag{A.31}$$

It is now necessary to consider the form of the stress tensor in greater detail.

A.3.5 The Stress Tensor for Massive, Non-relativistic Particles

Massive, non-relativistic particles, such as baryons, act like an ideal fluid. The form of the stress tensor for an ideal fluid is given by equation A.23. As has already been noted, the pressure of massive, non-relativistic particles is largely negligible on the scales of interest. Therefore, for baryons the form of the stress tensor is given by:

$$T_{\mu\nu} = \rho_b(1+\delta_m)u_\mu u_\nu \,. \tag{A.32}$$

The form of the 4-velocity is given by:

$$u^0 = 1 \,, \tag{A.33a}$$

$$u^i = \frac{v^i}{a} \,. \tag{A.33b}$$

δ_m is the perturbation to the matter density and the v^i are the components of the dimensionless proper fluid velocity.

The components of the unperturbed stress tensor are given in equation A.24. The components of the *perturbed* stress tensor are:

$$\delta T_{00} = \rho_b \delta_m \,, \tag{A.34a}$$

$$\delta T_{0i} = -a\rho_b v_i \,, \tag{A.34b}$$

$$\delta T_{ij} = \mathrm{O}(h^2) = 0 \,, \tag{A.34c}$$

$$\delta T = \delta g^{\mu\nu} T_{\mu\nu} + g^{\mu\nu}\delta T_{\mu\nu} = \rho_b(1+\delta_m) \,. \tag{A.34d}$$

A.3.6 The Stress Tensor for Relativistic Particles

A.3.6.1 General Form

Photons and neutrinos are both examples of massless, relativistic particles whose behaviour can be described by a distribution function, $f(p^\alpha, q^\alpha)$, where the coordinate set (p^α, q^α) represents the canonical conjugate momenta and positions. The stress tensor for an ensemble of *massive* relativistic particles is (see *e.g.* Ehlers 1972):

$$T^{\mu\nu} = \int (-g)^{1/2}\, dp^{0123}\, 2\,\delta(g^{\alpha\beta}p_\alpha p_\beta - m^2)\, p^\mu p^\nu\, f(p^\alpha, q^\alpha) \,. \tag{A.35}$$

$(-g)^{1/2}dp^{0123}$ is an invariant 4-volume measure and the delta function imposes the mass-shell constraint on the particles.

The 4-tensor $\varepsilon_{\alpha\beta\gamma\delta}$ is the Levi-Civita pseudo-tensor in an arbitrary 4-space. Weinberg shows that it has the following properties:

$$\varepsilon_{\alpha\beta\gamma\delta} = -g\varepsilon^{\alpha\beta\gamma\delta} ,$$

$$\varepsilon_{0123} = (-g)^{1/2} .$$

Therefore

$$(-g)^{1/2}\, dp^{0123} \equiv (-g)^{-1/2}\, dp_{0123} .$$

The volume element can now be rewritten, since $dp_{0123} = dp_0 dp_{123}$, and the integral over dp_0 can be done immediately using the delta function. The resultant stress tensor has the form

$$T^{\mu\nu} = \int \frac{dp_{123}}{(-g)^{1/2}} \frac{p^\mu p^\nu}{p_0} f(p^\alpha, q^\alpha) . \tag{A.36}$$

where p_0 is now constrained to lie on the mass-shell.

It is useful to define new momenta.

$$p_i \equiv -pae\gamma_i , \tag{A.37a}$$

$$p \equiv \left(p_0^2 - m^2\right)^{1/2} . \tag{A.37b}$$

The γ_i are direction cosines defined such that $\gamma^{ij}\gamma_i\gamma_j = 1$, p is the particles comoving momenta and e represents to perturbation to the momentum. Using these new variables the mass-shell constraint can be rewritten.

$$p_0^2 = m^2 - g^{ij}p_i p_j = m^2 + p^2 e^2 \left(\gamma^{ij}\gamma_i\gamma_j + h^{ij}\gamma_i\gamma_j\right) . \tag{A.38}$$

A.3.6.2 Massless Limit

From now on it is simpler to consider only massless particles. In particular the notation in this subsection will refer to photons though the theory is identical for the neutrinos. Then $p = p_0$ and the constraint reduces to a condition on e.

$$p^2 \left(1 - e^2 \left(1 + h^{ij}\gamma_i\gamma_j\right)\right) = 0 , \tag{A.39a}$$

$$\text{or} \qquad e = 1 - \frac{1}{2}h^{ij}\gamma_i\gamma_j . \tag{A.39b}$$

In terms of these new variables the volume element becomes:

$$dp_{123} = a^3\, e^3\, p^2\, dp\, d\Omega . \tag{A.40}$$

Hence the stress tensor has the form:

$$T^{\mu\nu} = \left(1 + \frac{h}{2}\right) \int \frac{p^2\, dp\, d\Omega}{\det(\gamma_{ij})^{1/2}} \left(1 - \frac{3}{2} h^{ij} \gamma_i \gamma_j\right) \frac{p^\mu p^\nu}{p} f \,. \tag{A.41}$$

Just as $d^4 p_\mu / (-g)^{1/2}$ is an invariant volume element in the 4-momentum space, then $d^3 p_i / (\det \gamma_{ij})^{1/2}$ is an invariant volume element in the analogous 3-momentum space and $d\Omega / (\det \gamma_{ij})^{1/2}$ is similarly an invariant element on the 2-space.

The direction cosines defined above can be integrated over the invariant volume element as defined above relating to the angular dependence in the momentum to give the following results.

$$\int \gamma_i \gamma_j d\Omega' = \frac{4\pi}{3} \gamma_{ij} \,, \tag{A.42a}$$

$$\int \gamma_i \gamma_j \gamma_k \gamma_m d\Omega' = \frac{4\pi}{15} \left(\gamma_{ij}\gamma_{km} + \gamma_{ik}\gamma_{jm} + \gamma_{im}\gamma_{jk}\right) \,, \tag{A.42b}$$

$$\int \text{any odd number of } \gamma_i d\Omega' = 0 \,. \tag{A.42c}$$

The element $d\Omega'$ is simply the invariant element of solid angle $d\Omega / \det(\gamma_{ij})^{1/2}$.

It is also possible to define an integral over the momentum p.

$$\int p^3 f\, dp = \frac{\mathcal{E}_b}{4\pi} (1 + \delta(\Omega)) \,, \tag{A.43}$$

The total perturbation to the density field is contained within the term $\delta(\Omega)$. Note that by definition the background field $\mathcal{E}_b$ is isotropic since it is a solution to the unperturbed field equations. It is useful to define some new quantities which are the integrals of the angular dependence of this perturbation.

$$\delta_0 = \int \delta(\Omega) \frac{d\Omega'}{4\pi} \,, \tag{A.44a}$$

$$f_j = \int \gamma_j \delta(\Omega) \frac{d\Omega'}{4\pi} \,, \tag{A.44b}$$

$$\eta_{ij} = \int \left(\gamma_i \gamma_j - \frac{1}{3}\gamma_{ij}\right) \delta(\Omega) \frac{d\Omega'}{4\pi} \,. \tag{A.44c}$$

These definitions and properties allow the elements of the stress tensor to be simplified.

A.3.6.3 Elements of $T^{\mu\nu}$ for Massless Particles

Using the new variables and their properties, as outlined in the last section, the elements of the stress tensor are found as follows.

$$T_{00} = \frac{1 + h/2}{4\pi} \int d\Omega' \mathcal{E}_b (1 + \delta) \left(1 - \frac{3}{2} h^{ij} \gamma_i \gamma_j\right)$$

$$= \varepsilon_b(1+\delta_0) \,. \tag{A.45}$$

$$T_{0m} = -\frac{1+h/2}{4\pi} a \int d\Omega' \varepsilon_b(1+\delta)\left(1-2h^{ij}\gamma_i\gamma_j\right)\gamma_m$$

$$= -\varepsilon_b a f_m \,. \tag{A.46}$$

$$T_{ij} = \frac{1+h/2}{4\pi} a^2 \int d\Omega' \varepsilon_b(1+\delta)\left(1-\frac{5}{2}h^{mn}\gamma_m\gamma_n\right)\gamma_i\gamma_j$$

$$= a^2\varepsilon_b\left(\frac{1}{3}(\gamma_{ij}-h_{ij})+\eta_{ij}+\frac{1}{3}\gamma_{ij}\delta_0\right) \,. \tag{A.47}$$

These elements can be decomposed into an unperturbed part and a perturbation term. The unperturbed elements are given by equation A.24. Examination of the above elements show that the simple theory outlined in section A3.2 for the unperturbed model was correct. The perturbation terms are:

$$\delta T_{00} = \varepsilon_b\delta_0 \,, \tag{A.48a}$$

$$\delta T_{0m} = -\varepsilon_b a f_m \,, \tag{A.48b}$$

$$\delta T_{ij} = \varepsilon_b a^2\left(\eta_{ij}+\frac{1}{3}\gamma_{ij}\delta_0-\frac{1}{3}h_{ij}\right) \,, \tag{A.48c}$$

$$\delta T = \delta g^{\mu\nu}T_{\mu\nu} + g^{\mu\nu}\delta T_{\mu\nu} = 0 \,. \tag{A.48d}$$

The last term follows from the fact that $\gamma^{ij}\eta_{ij} = 0$.

A.3.7 The Perturbed Field Equations II

All the elements of the Ricci tensor and the stress tensor for both massive, non-relativistic particles and massless, relativistic particles have now been determined. Equation A.14 gives the general form for the perturbed field equations: equation A.30 gives all the elements of the perturbed Ricci tensor, equation A.24 gives the trace of the unperturbed stress tensor and equations A.34 and A.48 give the terms for the perturbed stress tensor. Plugging these components into equation A.14 gives:

The 00 component:

$$\frac{1}{2}\ddot{h} + \frac{\dot{a}}{a}\dot{h} = 4\pi G\left(\rho_b\delta_m + 2\varepsilon_b\delta_0 + 2\varepsilon_\nu\delta_{\nu 0}\right) \,. \tag{A.49a}$$

The $0i$ component:

$$\dot{h}_{,i} - \dot{h}^j{}_{i|j} = -16\pi G a\left(\rho_b v_i + \varepsilon_b f_i + \varepsilon_\nu f_{\nu i}\right) \,. \tag{A.49b}$$

The ijth component is not needed.

A.3.8 The Perturbed Field Equations III: The Easy Method

All of the preceding part of section A.3 has been based on a general Robertson-Walker metric with no assumptions as to its curvature. Peebles (1980) derives the same field equations for the case of a flat spatial section (*i.e.* $K = 0$). This derivation is naturally much simpler since all the covariant derivatives with regard to the 3-metric, γ_{ij}, are replaced by ordinary partial derivatives. In fact, the procedure is exactly equivalent to the replacement of covariant derivatives with ordinary derivatives when going from a full general relativistic theory to a special relativistic one. The same holds true in reverse: this is just the principle of covariance in a normal 4-space. If the 3-metric was thought of as akin to a special relativistic 3-metric when $K = 0$, then for the case of $K \neq 0$ all that is required is to replace the ordinary *spatial* derivatives in the field equations in Peebles with full covariant derivatives. Examination of equation 82.9 of Peebles demonstrates that this is the case (although there is some confusion over the placing of the indices in Peebles that could easily have been avoided).

Just as the principle of covariance allows the metric terms in the field equations to be derived by considering only a flat space, the form of the stress tensor can be derived similarly since the volume element is invariant under coordinate changes. Since the stress tensor is a local property, the metric at a point can be transformed to be flat *at* that point. Hence the stress tensor derived for curved space is exactly the same as that derived in a flat space. It will be shown later that the other equations governing the perturbations can also be derived (with care) from the simpler $K = 0$ case.

A.4 Dynamical Equations

A.4.1 Relativistic Particles

A.4.1.1 The Relativistic Boltzmann Equation

As has already been discussed, the behaviour of the relativistic particles can be described by a distribution function, f. The dynamical evolution of such a function is described by the relativistic Boltzmann equation.

$$\frac{Df}{D\lambda} = S(f)\,. \tag{A.50}$$

The derivative is a total derivative along the path (parameterised by λ) and $S(f)$ is a source function. For the moment only the case $S = 0$ will be considered. Then:

$$\frac{Df}{D\lambda} = \frac{\partial f}{\partial x^\alpha}\frac{dx^\alpha}{d\lambda} + \frac{\partial f}{\partial p^\alpha}\frac{dp^\alpha}{d\lambda} \,. \tag{A.51}$$

The path derivative of the 4-momenta is:

$$\frac{dp^\alpha}{d\lambda} = -\Gamma^\alpha_{\beta\gamma} p^\beta u^\gamma \,. \tag{A.52}$$

It is also possible to define a 4-velocity, u^α:

$$u^\alpha = \frac{dx^\alpha}{d\lambda} \,. \tag{A.53}$$

These 4-vectors are related by:

$$\frac{p^i}{p_0} = \frac{u^i}{u_0} \,. \tag{A.54}$$

(It is easiest to see this by considering massive particles: in the limit in which $m \to 0$, equation A.54 is still well defined.)

Utilising these simple properties gives the following form for the Boltzmann equation (restoring $S(f)$):

$$\frac{1}{u_0}\frac{Df}{D\lambda} = \frac{\partial f}{\partial t} + \frac{\partial f}{\partial x^i}\frac{p^i}{p_0} - \frac{\partial f}{\partial p_0}\Gamma^0_{\beta\gamma}\frac{p^\beta p^\gamma}{p_0} - \frac{\partial f}{\partial p^i}\Gamma^i_{\beta\gamma}\frac{p^\beta p^\gamma}{p_0} = \frac{S(f)}{u_0} \,. \tag{A.55}$$

The distribution function can be split into a homogeneous, isotropic background function, f_b, and a perturbation term, δf. The Boltzmann equation for the background field simplifies considerably since ,

$$\frac{\partial f_b}{\partial x^i} = \frac{\partial f_b}{\partial \gamma^i} = 0 \,, \tag{A.56}$$

where the momenta variables have been transformed into the set defined by equation A.37. Using this, and substituting in the unperturbed connection coefficient gives the following simple differential equation.

$$\frac{\partial f_b}{\partial t} - \frac{\dot{a}}{a}\frac{\partial f_b}{\partial p} p = 0 \,. \tag{A.57}$$

Multiplying through by p^3 and integrating with respect to p just gives back equation A.27b. Hence the unperturbed background does behave just like an ideal fluid.

The equation for the evolution of the perturbation term is:

$$\frac{\partial(\delta f)}{\partial t} + \frac{\partial(\delta f)}{\partial x^i}\frac{p^i}{p_0} - \frac{\partial f}{\partial p_0}\delta(\Gamma^0_{\beta\gamma}\frac{p^\beta p^\gamma}{p_0}) - \frac{\partial(\delta f)}{\partial p_0}\Gamma^0_{\beta\gamma}\frac{p^\beta p^\gamma}{p_0} - \frac{\partial(\delta f)}{\partial p^i}\Gamma^i_{\beta\gamma}\frac{p^\beta p^\gamma}{p_0}$$

$$= \frac{S(f)}{u_0} \,. \tag{A.58}$$

In principle, it is necessary only to multiply throughout by p^3 and then integrate, just as in the unperturbed case. It is better however to simplify the third and last terms first.

$$\delta\left(\Gamma^0_{\beta\gamma}\frac{p^\beta p^\gamma}{p_0}\right) = \delta\Gamma^0_{\beta\gamma}\frac{p^\beta p^\gamma}{p_0} + 2\Gamma^0_{\beta\gamma}\frac{\delta p^\beta p^\gamma}{p_0}\,.$$

Note that $\delta p_0 = 0$ (since the effect of the perturbation to the momentum was included in the e term), and that symmetry in $\beta \leftrightarrow \gamma$ contributes the factor of 2. It is useful to consider the form of δp^i next.

$$p^i = g^{ij}p_j = \frac{p}{a}\left(\gamma^i + h^{ij}\gamma_j - \frac{1}{2}\gamma^i h^{mn}\gamma_m\gamma_n\right)\,.$$

Hence,

$$\delta p^i = \frac{p}{a}\left(h^{ij}\gamma_j - \frac{1}{2}\gamma^i h^{mn}\gamma_m\gamma_n\right)\,.$$

Substituting the values for the momenta and the connection coefficients gives:

$$\delta\left(\Gamma^0_{\beta\gamma}\frac{p^\beta p^\gamma}{p_0}\right) = -\frac{1}{2}\dot{h}_{ij}p\gamma^i\gamma^j\,.$$

The last term is:

$$-\frac{\partial(\delta f)}{\partial p^i}\Gamma^i_{\beta\gamma}\frac{p^\beta p^\gamma}{p_0} \equiv \frac{1}{u_0}\frac{\partial(\delta f)}{\partial p^i}\frac{dp^i}{d\lambda} \equiv \frac{\partial(\delta f)}{\partial\gamma^i}\frac{d\gamma^i}{d\lambda}\,.$$

Since the final equation is to defined in terms of γ^i and not p^i, the latter form will be used. In order to determine what $d\gamma^i/d\lambda$ is it is necessary to go back a step however.

$$\frac{1}{u_0}\frac{dp^i}{d\lambda} = -\Gamma^i_{\beta\gamma}\frac{p^\beta p^\gamma}{p_0} = -2\frac{\dot{a}}{a^2}p\gamma^i - \lambda^i_{jk}\frac{p}{a^2}\gamma^j\gamma^k$$

$$\equiv \frac{1}{u_0}\frac{d}{d\lambda}\left(\frac{p}{a}\gamma^i\right) = \frac{1}{u_0}\left(\frac{dp}{d\lambda}\frac{\gamma^i}{a} - \frac{da}{d\lambda}\frac{p}{a^2}\gamma^i + \frac{p}{a}\frac{d\gamma^i}{d\lambda}\right)\,.$$

Since,

$$\frac{1}{u_0}\frac{dp}{d\lambda} = -\Gamma^0_{\beta\gamma}\frac{p^\beta p^\gamma}{p_0} = \frac{\dot{a}}{a}p\,,$$

and

$$\frac{1}{u_0}\frac{da}{d\lambda} = \dot{a}\,,$$

it can be seen that

$$\frac{1}{u_0}\frac{d\gamma^i}{d\lambda} = -\frac{1}{a}\lambda^i_{jk}\gamma^j\gamma^k\,.$$

Finally, since,

$$\int p^3 \delta f dp = \frac{\varepsilon \delta}{4\pi} ,$$

and,

$$\int p^4 \frac{\partial f}{\partial p} dp = -4 \int p^3 f dp ,$$

the relativistic Boltzmann equation is:

$$\dot{\delta} + \frac{\partial \delta}{\partial x^i}\frac{\gamma^i}{a} - \frac{1}{a}\lambda^i_{jk}\gamma^j\gamma^k\frac{\partial \delta}{\partial \gamma^i} - 2\dot{h}_{ij}\gamma^i\gamma^j = \frac{4\pi}{\varepsilon}\int p^3 \frac{S(f)}{u_0} dp . \tag{A.59}$$

A.4.1.2 The Source Function

If the particles are truly collisionless then the source function is zero. For example, massless neutrinos obey an equation like

$$\dot{\delta_\nu} + \frac{\partial \delta_\nu}{\partial x^i}\frac{\gamma^i}{a} - \frac{1}{a}\lambda^i_{jk}\gamma^j\gamma^k\frac{\partial \delta_\nu}{\partial \gamma^i} = 2\dot{h}_{ij}\gamma^i\gamma^j . \tag{A.60}$$

For photons, the source function represents the effect of Thomson scattering from electrons. In the rest frame of the matter, the differential cross-section for Thomson scattering is:

$$\frac{d\sigma}{d\Omega} = \frac{3}{16\pi}\sigma_T \left(1 + \cos^2\theta\right) .$$

The change in the distribution function along the path as seen by an observer is:

$$\delta f' = n_e \sigma_T \, \delta t' \, \frac{3}{16\pi}\int d\Omega' \left(f'(p') - f(p)\right)\left(1 + \cos^2\theta\right) . \tag{A.61}$$

The primes refer to quantities in the matter rest frame. To avoid confusion with the notation previously adopted, the element of solid angle $d\Omega$ should hereafter be taken to mean the invariant element as defined in section A.3.6.2. The term involving $f'(p')$ in the integrand represents scattering into/out of the beam and the term involving $f(p)$ represents unscattered particles. Note that $\int d\Omega' f(p) = f(p)\int d\Omega'$. The scattering frequency for Thomson scattering is $n_e\sigma_T(c)$.

The matter rest frame is defined by:

$$u_m^{\alpha\,\prime} = (1, \mathbf{0}) \qquad\qquad (u_m^\alpha = (1, \frac{v^i}{a}) \text{ generally}) .$$

Since $p'_\alpha u_m^{\alpha\,\prime} = p_\alpha u_m^\alpha$, the following relation holds:

$$p'_0 = p_0(1 - \gamma_i v^i) .$$

Now,

$$\frac{1}{u_0}\frac{\delta f}{\delta \lambda} = \frac{\delta f}{\delta t} ,$$

and,

$$\delta t' = \frac{\partial t'}{\partial x^i}\frac{dx^i}{dt}\delta t = \frac{p'}{p}\delta t .$$

Therefore:

$$\frac{S(f)}{u_0} \equiv \frac{\delta f}{\delta t} = \frac{3}{16\pi} n_e \sigma_T \frac{p'}{p} \int d\Omega' \left(f'(p') - f(p) \right) \left(1 + \cos^2\theta \right) . \tag{A.62}$$

The ratio p'/p is only needed to zeroeth order since the scattering terms are first order in the perturbation: therefore $p'/p = 1$. $\cos\theta$ is defined by

$$\cos\theta = \gamma_i \gamma^{i'} = \gamma_{ij}\gamma^i \gamma^{j'} ,$$

so,

$$\begin{aligned} \int (1 + \cos^2\theta) d\Omega' &= \int \left(1 + \gamma_{ij}\gamma_{mn}\gamma^i\gamma^m\gamma^{j'}\gamma^{n'} \right) d\Omega' \\ &= 4\pi \left(1 + \frac{1}{3}\gamma_{im}\gamma^i\gamma^m \right) = \frac{16\pi}{3} . \end{aligned}$$

This is a scalar quantity, as is f, so this is true in any frame. If we substitute A.62 into A.59, then

$$\frac{4\pi}{\varepsilon_b} \int p^3 \frac{S(f)}{u_0} dp = \frac{3}{16\pi} n_e \sigma_T \left\{ \int p^3 dp \int d\Omega' f(p')(1 + \cos^2\theta) - \frac{16\pi}{3} \int p^3 f(p) dp \right\} .$$

The first integral can be simplified by transforming $p^3 dp$ to $p'^3 dp'(1 + 4\gamma_i v^i)$. Then carrying out the p and p' integrals gives

$$\begin{aligned} &\frac{4\pi}{\varepsilon_b} \int p^3 \frac{S(f)}{u_0} dp \\ &\quad = \frac{3}{16\pi} n_e \sigma_T \left\{ \frac{1}{4\pi}(1 + 4\gamma_i v^i) \int d\Omega' \varepsilon_b (\delta(\Omega') + 1)(1 + \cos^2\theta) - \frac{4\pi}{3}\varepsilon_b (1 + \delta) \right\} . \end{aligned}$$

The integral over $d\Omega'$ is relatively straightforward given the result derived above for the integral of $\cos^2\theta$ and the previously defined quantities representing integrals of δ over Ω.

$$\int d\Omega' (1 + \cos^2\theta)(\delta + 1) = 4\pi \left(\delta_0 + \left(\eta_{ij} + \frac{1}{3}\gamma_{ij}\delta_0 \right) \gamma^i\gamma^j + \frac{4}{3} \right) .$$

Hence, finally,

$$\frac{4\pi}{\varepsilon_b} \int p^3 \frac{S(f)}{u_0} dp = n_e \sigma_T \left(\delta_0 + \frac{3}{4}\eta_{ij}\gamma^i\gamma^j + 4\gamma_i v^i - \delta \right) .$$

As expected the scattering term is of order h.

The equation for the dynamical evolution of photons is therefore:

$$\dot{\delta} + \frac{\partial \delta}{\partial x^i}\frac{\gamma^i}{a} - \frac{1}{a}\lambda^i_{jk}\gamma^j\gamma^k \frac{\partial \delta}{\partial \gamma^i} = 2\dot{h}_{ij}\gamma^i\gamma^j + n_e\sigma_T \left(\delta_0 + \frac{3}{4}\eta_{ij}\gamma^i\gamma^j + 4\gamma_i v^i - \delta \right) . \tag{A.63}$$

A.4.2 The Coupling of Matter and Radiation

The scattering of the photons from the electrons in the primeval plasma induces a force on the baryonic component. This leads to a force equation of the form

$$T_{m}^{\mu\nu}{}_{;\nu} = K^{\mu} , \tag{A.64}$$

where K^{μ} is the applied 4-force density and the stress tensor represents the contribution of the baryons only. The 4-force density is defined in the standard manner,

$$K^{\mu} = (u_i k^i, k^i) ,$$

where k^i is the 3-force density. For Thomson scattering the 3-force density is

$$k^i = \frac{1}{4\pi a} \int d\Omega \sigma_T n_e \gamma^i (I - I_+) ,$$

where I is the unperturbed brightness and I_+ is the scattered brightness. The presence of the scale factor takes account of the fact that the other terms represent comoving quantities. But from equation A.63,

$$I - I_+ = -\varepsilon_b \left(\delta_0 + \frac{3}{4} \eta_{ij} \gamma^i \gamma^j + 4\gamma_i v^i - \delta \right) .$$

Therefore the 3-force density is given by

$$k^i = \frac{\sigma_T n_e \varepsilon_b}{a} \left(f^i - \frac{4}{3} v^i \right) . \tag{A.65}$$

Since k^i is of order h and so is u_i, $K^0 \sim \mathrm{O}(h^2)$.

Therefore,

$$T_{m}^{0\nu}{}_{;\nu} = 0 ,$$

and, since the unperturbed $T^{\mu\nu}{}_{;\nu} = 0$,

$$\delta T_{m}^{0\nu}{}_{,\nu} + \Gamma^0_{\alpha\nu} \delta T_m^{\alpha\nu} + \Gamma^{\nu}_{\alpha\nu} \delta T_m^{\alpha 0} + \delta\Gamma^0_{\alpha\nu} T_m^{\alpha\nu} + \delta\Gamma^{\nu}_{\alpha\nu} T_m^{\alpha 0} = 0 .$$

Substituting for the elements of the stress tensor from equations A.23 and A.34 and for the connection coefficients from equations A.19 and A.28, and using the fact that $\dot{\rho}_b + 3\dot{a}\rho_b/a = 0$ (equation A.27a), gives the following equation.

$$\dot{\delta}_m = \frac{1}{2}\dot{h} - \frac{v^i{}_{|i}}{a} . \tag{A.66}$$

Similarly,

$$T_{m}^{i\nu}{}_{;\nu} = k^i ,$$

and again the unperturbed contribution is identically zero so,

$$\delta T^{i\nu}_{m\ ,\nu} + \Gamma^{i}_{\alpha\nu}\delta T^{\alpha\nu}_{m} + \Gamma^{\nu}_{\alpha\nu}\delta T^{\alpha i}_{m} + \delta\Gamma^{i}_{\alpha\nu}T^{\alpha\nu}_{m} + \delta\Gamma^{\nu}_{\alpha\nu}T^{\alpha i}_{m} = k^{i} \ .$$

With the form of k^i given by equation A.65 and the elements of the stress tensor and connection coefficients as before this gives,

$$\dot{v}^{i} + \frac{\dot{a}}{a}v^{i} = \sigma_T n_e \frac{\mathcal{E}_b}{\rho_b}\left(f^{i} - \frac{4}{3}v^{i}\right) \ . \tag{A.67}$$

A.4.3 Deriving the Dynamical Equations Using $K = 0$

Again returning to Peebles (1980) it can be seen that equation A.66 is just the covariant analogue (in the sense defined in section A3.8) of equation 92.14 there. Equation A.67 is exactly the same whatever the value of K (*cf.* equation 92.18 in Peebles). This leaves only the derivation of the evolution equations for relativistic particles. The explicit effect of non-zero K in equations A.59 and A.63 is confined to the connection coefficient of the 3-space, λ^{i}_{jk}. It is necessary to add the term

$$-\frac{1}{a}\lambda^{i}_{jk}\gamma^{j}\gamma^{k}\frac{\partial\delta}{\partial\gamma^{i}}$$

to equation 92.9 of Peebles (noting that his i is δ here). This is the only non-trivial part in deriving the dynamical equations for arbitrary K using the simple $K = 0$ case.

A.5 Recap: The Evolution of Perturbations in Linear Theory

The evolution of the set of perturbed variables (δ_m,v_i, δ_ν,δ,$\dot{h}$,$\dot{h}_{ij}$) is completely described by the equations already derived. For convenience these are reproduced here together.

$$\dot{\delta}_m = \frac{1}{2}\dot{h} - \frac{v^{i}_{|i}}{a} \ , \tag{A.68a}$$

$$\dot{v}^{i} + \frac{\dot{a}}{a}v^{i} = \sigma_T n_e \frac{\mathcal{E}_b}{\rho_b}\left(f^{i} - \frac{4}{3}v^{i}\right) \ , \tag{A.68b}$$

$$\frac{1}{2}\ddot{h} + \frac{\dot{a}}{a}\dot{h} = 4\pi G\left(\rho_b\delta_m + 2\mathcal{E}_b\delta_0 + 2\mathcal{E}_\nu\delta_{\nu 0}\right) \ , \tag{A.68c}$$

$$\dot{h}_{,i} - \dot{h}^{j}_{\ i|j} = -16\pi G a\left(\rho_b v_i + \mathcal{E}_b f_i + \mathcal{E}_\nu f_{\nu i}\right) \ , \tag{A.68d}$$

$$\dot{\delta} + \frac{\partial\delta}{\partial x^{i}}\frac{\gamma^{i}}{a} - \frac{1}{a}\lambda^{i}_{jk}\gamma^{j}\gamma^{k}\frac{\partial\delta}{\partial\gamma^{i}} = 2\dot{h}_{ij}\gamma^{i}\gamma^{j} + n_e\sigma_T\left(\delta_0 + \frac{3}{4}\eta_{ij}\gamma^{i}\gamma^{j} + 4\gamma_i v^{i} - \delta\right) , \tag{A.68e}$$

$$\dot{\delta}_\nu + \frac{\partial\delta_\nu}{\partial x^{i}}\frac{\gamma^{i}}{a} - \frac{1}{a}\lambda^{i}_{jk}\gamma^{j}\gamma^{k}\frac{\partial\delta_\nu}{\partial\gamma^{i}} = 2\dot{h}_{ij}\gamma^{i}\gamma^{j} \ . \tag{A.68f}$$

A.6 The Case of an $\Omega = 1$ Universe

Since the full theory will only be used for the case of $\Omega = 1$ in chapter 2, it is reasonable at this point to concentrate only on this special case. A full treatment of the decomposition of the perturbations into their spatial and angular dependences for arbitrary Ω would be needlessly long and involved for what is desired here. In this respect, at least, models of open universes are distinctly different from the $\Omega = 1$ model. Wilson (1983) covers the more general case. The decomposition of the perturbations into separate spatial and temporal parts is straightforward. The three-space has a set of eigenfunctions which are solutions to Laplace's equation. When $\Omega = 1$ these functions are simply plane waves, so that a general perturbation can be expressed as

$$f(\mathbf{x},t) = f(k,t)e^{i\mathbf{k}.\mathbf{x}} , \tag{A.69a}$$

if f is scalar

$$f_i(\mathbf{x},t) = f(k,t)\hat{k}_i e^{i\mathbf{k}.\mathbf{x}} , \tag{A.69b}$$

if f_i is a vector and, finally, following Wilson & Silk (1981), the perturbation in the metric will be expressed as

$$h_{ij}(\mathbf{x},t) = \left(\frac{1}{3}(h(t)+H(t))\delta_{ij} - H(t)\hat{k}_i\hat{k}_j\right) e^{i\mathbf{k}.\mathbf{x}} . \tag{A.69c}$$

Since the tensor η_{ij} is trace-free, it can be expressed as

$$\eta_{ij} = \left(\hat{k}_i\hat{k}_j - \frac{1}{3}\gamma_{ij}\right)\eta e^{i\mathbf{k}.\mathbf{x}} . \tag{A.69d}$$

Removing the spatial dependences from the set of equations, A.68, is therefore trivial. The radiation distribution, $\delta(\mathbf{x},\gamma,t)$, must also be expanded in terms of its angular dependence as expressed by the γ_i. The normal method of doing this is to expand $\delta(\mathbf{x},\gamma,t)$ in terms of a spherical harmonic distribution on the sky. Since there are no preferred directions, this reduces to an expansion in terms of Legendre polynomials. Hence

$$\delta(\mathbf{x},\gamma,t) = \sum_{l=0}^{\infty} \delta_l(t)P_l(\mu)e^{i\mathbf{k}.\mathbf{x}}, \tag{A.70}$$

where $\mu = \hat{\mathbf{k}}.\gamma$.

With these definitions, and the orthonormality relation for Legendre polynomials,

$$\int_{-1}^{1} P_l(\mu)P_m(\mu)d\mu = \frac{2}{2l+1}\delta_{lm} ,$$

where the δ_{lm} is a standard Kronecker delta symbol, it can be seen that

$$\delta_l(t) = \frac{2l+1}{2}\int_{-1}^{1} \delta(\mathbf{x},\gamma,t)P_l(\mu)d\mu \ .$$

From equations A.44 and A.69, this implies that

$$f_i\hat{k}_i = \frac{1}{3}\delta_1 \ , \tag{A.71a}$$

and (since $P_2 = (3\mu^2 - 1)/2$),

$$\eta_{ij}\hat{k}_i\hat{k}_j = \frac{2}{3}\eta = \frac{2}{15}\delta_2 \ . \tag{A.71b}$$

Therefore, $f = \delta_1/3$ and $\eta = \delta_2/5$.

Hence,

$$\dot{\delta}_m = -\frac{ik}{a}v + \frac{1}{2}\dot{h} \ , \tag{A.72a}$$

$$\dot{v} = -\frac{\dot{a}}{a}v + \frac{1}{3}\frac{\varepsilon_b}{\rho_b}n_e\sigma_T c\,(\delta_1 - 4v) \tag{A.72b}$$

and

$$\ddot{h} = -2\frac{\dot{a}}{a}\dot{h} + 8\pi G\,(\rho_b\delta_m + 2\varepsilon_b\delta_0 + 2\varepsilon_\nu\delta_{\nu 0}) \tag{A.72c}$$

are fairly straightforward to derive. Equation A.68d simplifies since

$$\hat{k}_i\left(\dot{h}_{,i} - \dot{h}^j{}_{i|j}\right) = ik\dot{h} - i\frac{k_ik_j}{k}\dot{h}^j{}_i = \frac{2}{3}ik\left(\dot{h} + \dot{H}\right) \ .$$

Using this gives

$$\dot{H} = -\dot{h} + \frac{24\pi G i}{k}\left(\rho_b v + \frac{1}{3}\varepsilon_b\delta_1 + \frac{1}{3}\varepsilon_\nu\delta_{\nu 1}\right) \ . \tag{A.72d}$$

The curvature terms in equations A.68e and A.68f are zero when $\Omega = 1$. Equation A.68e becomes

$$\sum_l \dot{\delta}_l P_l(\mu) + \frac{ik\mu}{a}\sum_l \delta_l\left(\frac{(l+1)}{(2l+1)}P_{l+1}(\mu) + \frac{l}{(2l+1)}P_{l-1}(\mu)\right) =$$

$$\frac{2}{3}\dot{h} - \frac{4}{3}P_2(\mu)\dot{H} + n_e\sigma_T\left(\delta_0 + \frac{1}{10}P_2(\mu)\delta_2 + 4\mu v - \sum_l \delta_l P_l(\mu)\right) \ .$$

The recurrence relation for Legendre polynomials,

$$\mu P_l(\mu) = \frac{(l+1)}{(2l+1)}P_{l+1}(\mu) + \frac{l}{(2l+1)}P_{l-1}(\mu) \ ,$$

has been used in deriving this formula, and factors of μ^2 have been replaced by a combination of P_0 and P_2. Multiplying this equation by P_m gives the relevant differential equation for the evolution of the mth moment of the radiation distribution.

This gives

$$\dot{\delta}_0 = -\frac{1}{3}\frac{ik}{a}\delta_1 + \frac{2}{3}\dot{h}\,, \tag{A.72e}$$

$$\dot{\delta}_1 = -n_e\sigma_T(\delta_1 - 4v) - \frac{ik}{a}\left(\delta_0 + \frac{2}{5}\delta_2\right)\,, \tag{A.72f}$$

$$\dot{\delta}_2 = -\frac{9}{10}n_e\sigma_T\delta_2 - \frac{ik}{a}\left(\frac{2}{3}\delta_1 + \frac{3}{7}\delta_3\right) - \frac{4}{3}\dot{H}\,, \tag{A.72g}$$

$$\dot{\delta}_l = -n_e\sigma_T\delta_l - \frac{ik}{a}\left(\frac{l}{2l-1}\delta_{l-1} + \frac{l+1}{2l+3}\delta_{l+1}\right)\,, l > 2\,. \tag{A.72h}$$

The fluctuation in the neutrinos is given by

$$\dot{\delta}_{\nu 0} = -\frac{1}{3}\frac{ik}{a}\delta_{\nu 1} + \frac{2}{3}\dot{h}\,, \tag{A.72i}$$

$$\dot{\delta}_{\nu 1} = -\frac{ik}{a}\left(\delta_{\nu 0} + \frac{2}{5}\delta_{\nu 2}\right)\,, \tag{A.72j}$$

$$\dot{\delta}_{\nu 2} = -\frac{ik}{a}\left(\frac{2}{3}\delta_{\nu 1} + \frac{3}{7}\delta_{\nu 3}\right) - \frac{4}{3}\dot{H}\,, \tag{A.72k}$$

$$\dot{\delta}_{\nu l} = -\frac{ik}{a}\left(\frac{l}{2l-1}\delta_{\nu l-1} + \frac{l+1}{2l+3}\delta_{\nu l+1}\right)\,, l > 2\,. \tag{A.72l}$$

These are the complete set of equations governing the evolution of small fluctuations in an $\Omega = 1$ universe containing baryons, photons and three species of massless neutrinos.

Appendix B

Analytical Solutions

B.1 The $t(a) - a$ Relation

Equation A.25b gives the relation between the scale factor, a, and time, t, for a specified content for the universe. For the purpose required here a simplified form can be used:

$$\dot{a}^2 = \frac{8\pi G}{3} a^2 (\rho_b + \varepsilon_b) - Kc^2 ,$$

where ρ_b is taken to represent all the non-relativistic matter and ε_b all the radiation (photons, massless neutrinos etc.). The following parameters can be introduced (note that the subscript 0 refers to the present epoch):

The Hubble constant, H_0:

$$H_0^2 = \left(\frac{\dot{a}}{a}\right)^2_{t=t_0} = \frac{8\pi G}{3} (\rho_{b0} + \varepsilon_{b0}) - Kc^2 . \tag{B.1}$$

The critical density, ρ_c:

$$\rho_c = 3H_0^2/8\pi G . \tag{B.2}$$

The density parameter, Ω_0, and the contribution Ω_{b0} of the non-relativistic matter to Ω_0:

$$\Omega_0 = \frac{\rho_{b0} + \varepsilon_{b0}}{\rho_c} , \qquad \Omega_{b0} = \frac{\rho_{b0}}{\rho_c} . \tag{B.3}$$

The scale factor at which matter and radiation densities are equal, a_{eq}:

$$a_{eq} = \varepsilon_{b0}/\rho_{b0} . \tag{B.4}$$

Hence, $K = H_0^2(\Omega_0 - 1)/c^2$, and with equation A.27,

$$\dot{a}^2 = H_0^2 \left(\frac{\Omega_{b0}}{a} + \frac{\Omega_{b0} a_{eq}}{a^2} - \Omega_0 + 1 \right) . \tag{B.5}$$

Note that the initial conditions are given by $t = 0$ when $a = 0$.

This simplifies considerably for $\Omega_0 = 1$, giving an integral for t.

$$t = H_0^{-1} (1 + a_{eq})^{1/2} \int_0^a \frac{a da}{\left(a + a_{eq}\right)^{1/2}} . \tag{B.6}$$

The factor of $(1+a_{eq})^{1/2}$ comes from $\Omega_{b0} = \Omega_0(1+a_{eq})^{-1}$. Using the substitution $a = a_{eq}\sinh^2\theta$, this is transformed to

$$t = 2H_0^{-1}(1+a_{eq})^{1/2}\int_{\theta(0)}^{\theta(a)} a_{eq}^{3/2}\sinh\theta(\cosh^2\theta - 1)d\theta\,.$$

This is now a straightforward integral which has the following solution:

$$t = 2H_0^{-1}(1+a_{eq})^{1/2}a_{eq}^{3/2}\left(\frac{1}{3}\left(\frac{a}{a_{eq}}+1\right)^{3/2} - \left(\frac{a}{a_{eq}}+1\right)^{1/2} + \frac{2}{3}\right)\,. \tag{B.7}$$

This has two useful limits. Consider first $a \ll a_{eq}$ when the universe is still radiation dominated. Then,

$$t = \frac{1}{2}H_0^{-1}(1+a_{eq})^{1/2}a_{eq}^{-1/2}a^2\,. \tag{B.8}$$

The other limit, $a \gg a_{eq}$, representing the matter dominated universe gives,

$$t = \frac{2}{3}H_0^{-1}(1+a_{eq})^{1/2}a^{3/2}\,. \tag{B.9}$$

Hence the age of the universe is $2H_0^{-1}(1+a_{eq})^{1/2}/3$. For the most commonly accepted values of the parameters ($\Omega_0 \simeq \Omega_{b0}$) the $(1+a_{eq})^{1/2}$ term is effectively unity. One other point which is not immediately obvious is the value of t at a_{eq}. Naively, it might be expected to lie in the range

$$\frac{1}{2} \le t_{eq}H_0a_{eq}^{-3/2} \le \frac{2}{3}\,,$$

but in fact $t_{eq} \simeq 0.39H_0^{-1}a_{eq}^{3/2}$. Therefore, a naive application of the limiting cases to the $a-t$ relation to epochs near equality would give misleading answers.

The behaviour when $\Omega_0 < 1$ is considerably more complicated.

$$t = \frac{H_0^{-1}}{(1-\Omega_0)^{1/2}}\int_0^a ada \Big/ \left(a^2 + \frac{\Omega_{b0}}{1-\Omega_0}a + \frac{a_{eq}\Omega_{b0}}{1-\Omega_0}\right)^{1/2}\,. \tag{B.10}$$

This can be split into two parts since,

$$\frac{d}{da}\left(a^2 + \frac{\Omega_{b0}}{1-\Omega_0}a + \frac{\Omega_{b0}}{1-\Omega_0}a_{eq}\right)^{1/2} = \frac{a + \frac{1}{2}\frac{\Omega_{b0}}{(1-\Omega_0)}}{\left(a^2 + \frac{\Omega_{b0}}{1-\Omega_0}a + \frac{\Omega_{b0}}{1-\Omega_0}a_{eq}\right)^{1/2}}\,,$$

so,

$$t = \frac{H_0^{-1}}{(1-\Omega_0)^{1/2}}\left\{\left[\left(a^2 + \frac{\Omega_{b0}}{1-\Omega_0}a + \frac{\Omega_{b0}}{1-\Omega_0}a_{eq}\right)^{1/2}\right]_0^a - \frac{1}{2}\frac{\Omega_{b0}}{1-\Omega_0}\mathrm{I}\right\}\,,$$

where,

$$\mathrm{I} = \int_0^a da \Big/ \left(a^2 + \frac{\Omega_{b0}}{1-\Omega_0}a + \frac{\Omega_{b0}}{1-\Omega_0}a_{eq}\right)^{1/2}\,.$$

If two constants, b and d are defined such that,

$$a^2 + \frac{\Omega_{b0}}{1-\Omega_0}a + \frac{\Omega_{b0}}{1-\Omega_0}a_{eq} = (a+b)(a+d)\,,$$

then

$$b = \frac{1}{2}\frac{1}{1-\Omega_0}\left(\Omega_{b0} - \left(\Omega_{b0}^2 - 4\Omega_{b0}(1-\Omega_0)a_{eq}\right)^{1/2}\right)\,,$$

and

$$d = \frac{1}{2}\frac{1}{1-\Omega_0}\left(\Omega_{b0} + \left(\Omega_{b0}^2 - 4\Omega_{b0}(1-\Omega_0)a_{eq}\right)^{1/2}\right)\,,$$

The following substitution then considerably simplifies the form of I.

$$a = (d-b)\tan^2\phi - b\,.$$

This gives,

$$\mathrm{I} = 2\int_{\phi(0)}^{\phi(a)} \sec\phi\, d\phi\,,$$

which has the solution

$$\mathrm{I} = 2\left[\log(\sec\phi + \tan\phi)\right]_{\phi(0)}^{\phi(a)}\,.$$

Hence, for $\Omega_0 < 1$,

$$t = \frac{H_0^{-1}}{(1-\Omega_0)^{1/2}}\left\{\left(a^2 + \frac{\Omega_{b0}}{1-\Omega_0}a + \frac{\Omega_{b0}}{1-\Omega_0}a_{eq}\right)^{1/2} - \left(\frac{\Omega_{b0}}{1-\Omega_0}a_{eq}\right)^{1/2} - \frac{\Omega_{b0}}{1-\Omega_0}\log\left(\frac{(a+d)^{1/2}+(a+b)^{1/2}}{d^{1/2}+b^{1/2}}\right)\right\}\,. \qquad \text{(B.11)}$$

Finally, another useful variable is given by the conformal time, τ, defined by

$$d\tau = \frac{dt}{a}\,. \qquad \text{(B.12a)}$$

It is straightforward to show that this has the following solution when $\Omega = 1$

$$\tau = 2H_0^{-1}(1+a_{eq})^{1/2}\left\{\left(a+a_{eq}\right)^{1/2} - a_{eq}^{1/2}\right\}\,. \qquad \text{(B.12b)}$$

Similarly, when $\Omega_0 < 1$, τ is given by $(1-\Omega_0)^{-1/2}H_0^{-1}(1+a_{eq})^{1/2}\times I$, where I is defined above.

B.2 Limiting Solutions to the Evolution Equations

B.2.1 The Tight Coupling Approximation

At high redshifts, when the matter and radiation fields are tightly coupled, attempting to solve the full set of differential equations is difficult and time consuming. A very accurate approximation can be made by expanding the equations in orders of t_c, where $t_c = 1/\sigma_T n_e c$. This quantity represents a mean free time between collisions for the photons.

Equations A.72a,A.72c and A.72(i-l) are unchanged by this approximation. Equation A.72f becomes

$$\dot{\delta}_1 = -\frac{1}{t_c}(\delta_1 - 4v) - \frac{ikc}{a}\left(\delta_0 + \frac{2}{5}\delta_2\right) . \tag{B.13}$$

Hence, to zeroeth order in t_c, $\delta_1 = 4v$. Similarly,

$$\delta_2 = -\frac{10}{9}t_c\left(\dot{\delta}_2 + \frac{4}{3}\dot{H} + \frac{ikc}{a}\left(\frac{2}{3}\delta_1 + \frac{3}{7}\delta_3\right)\right) .$$

All the factors on the right hand side should be replaced by their zeroeth order equivalents. In this case, $\dot{\delta}_2 = 0$, $\delta_1 = 4v$ and $\delta_l = 0$, $l > 2$. The latter two arise since increasing orders of δ_l depend on increasing powers of t_c. Using these gives

$$\delta_2 = -\frac{40}{27}t_c\left(\dot{H} + 2\frac{ikc}{a}v\right) . \tag{B.14}$$

Since,

$$\dot{v} + \frac{\dot{a}}{a}v = \frac{1}{3}\frac{a_g}{a}\frac{1}{t_c}(\delta_1 - 4v) ,$$

if v is required to first order in t_c, then $(\delta_1 - 4v)$ must be determined to second order. In line with Wilson & Silk (1981), the parameter Δ is introduced:

$$\delta_1 - 4v = t_c\Delta . \tag{B.15}$$

Then,

$$\dot{v} + \frac{\dot{a}}{a}v = \frac{1}{3}\frac{a_g}{a}\Delta . \tag{B.16}$$

Also, since,

$$\begin{aligned} \frac{2}{3}\dot{h} &= \frac{4}{3}\dot{\delta}_m + \frac{4}{3}\frac{ikc}{a}v , \\ \dot{\delta}_0 &= \frac{4}{3}\dot{\delta}_m - \frac{1}{3}\frac{ikc}{a}t_c\Delta . \end{aligned} \tag{B.17}$$

All the other equations are unchanged. All that is required is to derive a form for Δ. Equations B.13, B.15 and B.16 give

$$\Delta = 4\frac{\dot{a}}{a}v - \frac{4}{3}\frac{a_g}{a}\Delta - \dot{t}_c\Delta^{(0)} - t_c\dot{\Delta}^{(0)} - \frac{ikc}{a}\left(\delta_0 + \frac{2}{5}\delta_2\right) .$$

To lowest order in t_c this gives

$$\Delta^{(0)} = \left(4\frac{\dot{a}}{a}v - \frac{ikc}{a}\delta_0\right) / \left(1 + \frac{4}{3}\frac{a_g}{a}\right) , \tag{B.18a}$$

and the first order term is given by

$$\Delta^{(1)} = -\frac{\dot{t}_c\Delta^{(0)} + t_c\dot{\Delta}^{(0)} + \frac{2}{5}\frac{ikc}{a}\delta_2}{1 + \frac{4}{3}\frac{a_g}{a}} . \tag{B.18b}$$

Now,

$$\dot{t}_c = 3t_c\frac{\dot{a}}{a} \qquad \text{since } n_e \propto a^{-3}$$

$$\dot{\Delta}^{(0)} = \frac{4\frac{d}{dt}\left(\frac{\dot{a}}{a}\right)v + 4\frac{\dot{a}}{a}\dot{v} - \frac{ikc}{a}\dot{\delta}_0 + \frac{ikc}{a}\frac{\dot{a}}{a}\delta_0 + \frac{4}{3}\frac{a_g}{a}\frac{\dot{a}}{a}\left(1 + \frac{4}{3}\frac{a_g}{a}\right)^{-1}\left(4\frac{\dot{a}}{a}v - \frac{ikc}{a}\delta_0\right)}{1 + \frac{4}{3}\frac{a_g}{a}}$$

Using these properties and the values of $\dot{v}$ and $\dot{\delta}_0$ to lowest order in t_c gives the following

$$\Delta^{(1)}\left(1 + \frac{4}{3}\frac{a_g}{a}\right) = t_c\left(\frac{16}{27}\frac{ikc}{a}\left(\dot{H} + 2\frac{ikc}{a}v\right) + \left(1 + \frac{4}{3}\frac{a_g}{a}\right)^{-1}\left(\frac{4}{3}\frac{k^2c^2}{a^2}v + \frac{2}{3}\frac{ikc}{a}\dot{h} - 4\frac{d}{dt}\left(\frac{\dot{a}}{a}\right)v - 2\frac{\dot{a}}{a}\left(4\frac{\dot{a}}{a}v - \frac{ikc}{a}\delta_0\right)\left(1 + \frac{4}{3}\frac{a_g}{a}\right)^{-1}\left(1 + \frac{8}{3}\frac{a_g}{a}\right)\right)\right)$$

The modified set of equations are thus given by equations B.14, B.15, B.16, B.17 and

$$\Delta = \Delta^{(0)} + \Delta^{(1)} . \tag{B.19}$$

B.2.2 The Initial Conditions and Super-Horizon Fluctuations

B.2.2.1 Outline

At high redshifts, when it is assumed that any initial fluctuation pattern is laid down, various simplifying assumptions can be made. Firstly, the spatial curvature can be neglected since this does not affect the dynamics at this epoch. The equations derived in the last section can also be simplified. Initially, it is assumed that all wavelengths of interest are well outside the horizon. This implies that, for these wavelengths, $kct/a \ll 1$, so all terms of order kc/a can be ignored. Further, the matter and radiation coupling is such that only terms to zeroeth order in t_c need be kept. It is also convenient to change the independent variable in what follows to a. Then,

$$\delta_m' = \frac{1}{2}h' \tag{B.20a}$$

$$\delta_0' = \delta_{\nu 0}' = \frac{4}{3}\delta_m' \tag{B.20b}$$

$$\dot{v} = \left(1 + \frac{4}{3}\frac{a_g}{a}\right)^{-1} v \tag{B.20c}$$

$$\delta_{\nu 2}' = \frac{4}{3}h' \tag{B.20d}$$

$$a^2 h''\left(a + a_{eq}\right) + ah'\left(\frac{3}{2}a + a_{eq}\right) = 3\left(\delta_m a + 2a_\gamma \delta_0 + 2a_\nu \delta_{\nu 0}\right) . \tag{B.20e}$$

Equation B.5 has been used in deriving these equations. The initial value for v is taken to be zero (no initial bulk velocity), and hence remains zero in this limit. There are then two distinct sets of initial conditions which are considered separately below.

B.2.2.2 The Isocurvature Mode

The basis of the isocurvature initial condition is that there is no net perturbation to the local energy density. This implies that

$$\rho_T \delta_t = (\rho_b \delta_m + \varepsilon_\nu \delta_{\nu 0} + \varepsilon_b \delta_0) = 0 \tag{B.21a}$$

$$h_{ij} = 0 \tag{B.21b}$$

$$h' = 0 . \tag{B.21c}$$

The last condition arises when equation A.30c is used to give another Einstein equation, which in conjunction with equation A.49a gives

$$\frac{k^2 c^2}{a^2} h_{11} + \frac{\dot{a}^2}{a}\dot{h} + 8\pi G \rho_T \delta_T = 0 .$$

(This is equivalent to equation 86.15 in Peebles 1980). The ratio of $\delta_0/\delta_{\nu 0}$ must also be constant since there is no particle creation. Hence, given some initial value for δ_m, δ_{mi}, this equation reduces to

$$\delta_{0i} = \delta_{\nu 0 i} = -\frac{a_i}{a_{eq}}\delta_{mi} . \tag{B.21d}$$

With these initial conditions, a solution for the evolution of the perturbations can be obtained. Firstly, note that equations B.20a and B.20b have the following solutions

$$\delta_m = \frac{1}{2}h + \delta_{mi} \tag{B.22a}$$

$$\delta_0 = \frac{2}{3}h + \delta_{0i} \tag{B.22b}$$

$$\delta_{\nu 0} = \frac{2}{3}h + \delta_{\nu 0i} \tag{B.22c}$$

since $h = 0$ initially.

The right hand side to equation B.20e can then be expressed solely in terms of h and the initial conditions.

$$a^2h''\left(a + a_{eq}\right) + ah'\left(\frac{3}{2}a + a_{eq}\right) - h\left(\frac{3}{2}a + 4a_{eq}\right) = 3\delta_{mi}\left(a - 2a_i\right) \tag{B.23}$$

This equation does have an explicit solution (see Mészáros 1980, Efstathiou & Bond 1986) but the behaviour of the solution is most clearly seen in the two limits, $a \ll a_{eq}$ and $a \gg a_{eq}$.

$\underline{a \ll a_{eq}}$

Equation B.23 reduces to

$$a_{eq}\left(a^2h'' + ah' - 4h\right) = 3\delta_{mi}\left(a - 2a_i\right) \ . \tag{B.24a}$$

The homogeneous equation has a simple power law solution ($h \propto a^{\pm 2}$). The full solution is therefore

$$h = \frac{\delta_{mi}}{a_{eq}}\left(\frac{3}{2}a_i - a\right) + c_1a^2 + c_2a^{-2} \ . \tag{B.24b}$$

One of the initial conditions has already been used in deriving equation B.23. The other two initial conditions (equations B.21b and B.21c)give the two constants c_1 and c_2:

$$c_1 = 0 \ , \qquad c_2 = -\frac{1}{2}\frac{a_i^3}{a_{eq}}\delta_{mi} \ .$$

Hence, the following solutions are valid in this limit:

$$h = \frac{\delta_{mi}}{a_{eq}}\left(\frac{3}{2}a_i - a\right) - \frac{1}{2}\delta_{mi}\frac{a_i^3}{a_{eq}a^2} \tag{B.25a}$$

$$\delta_m = \frac{1}{2}\frac{\delta_{mi}}{a_{eq}}\left(\frac{3}{2}a_i - a\right) - \frac{1}{4}\delta_{mi}\frac{a_i^3}{a_{eq}a^2} + \delta_{mi} \tag{B.25b}$$

$$\delta_{\nu 0} = \delta_0 = -\frac{2}{3}\frac{a}{a_{eq}}\delta_{mi} - \frac{3}{4}\delta_{mi}\frac{a_i^3}{a_{eq}a^2} \ . \tag{B.25c}$$

Equations B.21d and B.22 have been used in deriving these solutions.

As $a \to a \gg a_i$ then

$$\delta_m \to \delta_{mi}\left(1 - \frac{1}{2}\frac{a}{a_{eq}}\right) \tag{B.26a}$$

$$\delta_{\nu 0} = \delta_0 \to -\frac{2}{3}\frac{a}{a_{eq}}\delta_{mi} \,. \tag{B.26b}$$

As a increases, the fluctuation in the matter dissipates and those in the relativistic components increase. The fluctuation in the local energy density is therefore (noting that $\rho_T \simeq \mathcal{E}_b + \mathcal{E}_\nu$)

$$\rho_T \delta_T = \frac{1}{3}\frac{a}{a_{eq}}\rho_T \delta_{mi} \tag{B.26c}$$

which is approximately zero at large redshifts as required (c.f. Peebles 1980, section 94).

$\underline{a \gg a_{eq}}$

The differential equation B.23 reduces to

$$a^2 h'' + \frac{3}{2}ah' - \frac{3}{2}h \simeq 3\delta_{mi} \,. \tag{B.27}$$

Again, the homogeneous part has a power law solution, $h \propto a$ and $h \propto a^{-3/2}$, but the growing mode solution is not present with the initial conditions given as already shown. Hence, as $a \to a \gg a_{eq}$,

$$h \to -2\delta_{mi} \tag{B.28a}$$

so

$$\delta_m \to 0 \tag{B.28b}$$

$$\delta_0 = \delta_{\nu 0} \to -\frac{4}{3}\delta_{mi} \,. \tag{B.28c}$$

At late times, the perturbation to the local energy density

$$\rho_T \delta_T \to -\frac{4}{3}\frac{a_{eq}}{a}\rho_b \delta_{mi} \,. \tag{B.29}$$

Therefore, at late times the perturbation to the local energy density disappears and the fluctuation in the curvature remains fixed. This calculation assumes that the curvature at late times is negligible. However, when the curvature becomes dominant, the universe enters a free expansion phase and all perturbation terms freeze out in any case, so the conclusion that the fluctuation remains largely isocurvature on super-horizon scales still holds.

B.2.2.3 *The Adiabatic Mode*

For adiabatic perturbations, there is a net injection of energy into the particles, giving rise to fluctuations in their densities. By equipartition, all the particles must share the energy equally, so

$$\frac{\delta\mathcal{E}_b}{\mathcal{E}_b} = \frac{\delta\mathcal{E}_\nu}{\mathcal{E}_\nu} = \frac{\delta\rho_b}{\rho_b} \, .$$

This gives the simple adiabatic initial conditions,

$$\delta_{0i} = \delta_{\nu 0i} = \frac{4}{3}\delta_{mi} \, . \tag{B.30}$$

Hence, by equation B.20b, these equalities must hold at all epochs when the simplifying approximations assumed are valid. This property can be used to recast equation B.20e into the form

$$a^2\delta_m'' \left(a + a_{eq}\right) + a\delta_m' \left(\frac{3}{2}a + a_{eq}\right) - \delta_m \left(\frac{3}{2}a + 4a_{eq}\right) = 0 \, . \tag{B.31}$$

This equation has the same solution as the homogeneous part of equation B.23. As before, it is easiest to see the behaviour of these fluctuation in the two limits, $a \ll a_{eq}$ and $a \gg a_{eq}$.

$\underline{a \ll a_{eq}}$

In this regime,

$$\delta_m = c_1 a^2 + c_2 a^{-2} \tag{B.32a}$$

$$\delta_0 = \delta_{\nu 0} = \frac{4}{3}\delta_m \tag{B.32b}$$

$$h' = \frac{4}{a}\delta_m \, . \tag{B.32c}$$

These three equations specify all the initial conditions. It is not necessary to solve for the constants, c_1 and c_2, since the fluctuations are dependent only on δ_{mi}, and not on the decomposition of that quantity into growing and decaying modes.

$\underline{a \gg a_{eq}}$

In this regime,

$$\delta_m = c_1 a + c_2 a^{-3/2} \, . \tag{B.33a}$$

This implies that the gravitational term tends towards

$$h' \to 2c_1 \tag{B.33b}$$

at late times. Again, this assumes the curvature is negligible.

B.2.3 The Post-Recombination Epoch

After recombination is completed, the full set of equations can be simplified by ignoring all scattering terms. This approximation is valid for all wavelengths within the horizon at that time since the mean free path for the photons increases greatly as the ionisation fraction in the universe drops sharply after recombination. For simplicity, a flat ($\Omega = 1$) universe in considered in this section. At this epoch, although the perturbation terms for the radiation can be ignored the effect of the background radiation in driving the expansion of the universe can still have an effect. This is known as the Mészáros effect (Mészáros 1975).

Firstly, consider that the values of the various components sometime after recombination are known and can be denoted by δ_{mr}, v_r, etc. Then, noting that

$$\dot{v} = -\frac{\dot{a}}{a} v \,, \tag{B.34a}$$

it is clear that

$$v = \frac{a_r}{a} v_r \,. \tag{B.34b}$$

Hence, using equation B.34a, A.72a and A.72c, ignoring all terms proportional to δ_0 or $\delta_{\nu 0}$, gives

$$\ddot{\delta}_m + 2\frac{\dot{a}}{a}\dot{\delta}_m - 4\pi G \rho_{b0} a^{-3} \delta_m = 0 \,. \tag{B.35a}$$

Changing to a as the independent variable therefore gives a form similar to that of equation B.20e.

$$a^2 \delta_m'' \left(a + a_{eq}\right) + a\delta_m' \left(\frac{3}{2}a + a_{eq}\right) - \frac{3}{2}\delta_m a = 0 \,. \tag{B.35b}$$

One solution to this equation is gained by considering $\delta_m'' = 0$.

$$\delta_m \propto 1 + \frac{3}{2} y \,, \tag{B.36a}$$

where

$$y = \frac{a}{a_{eq}} \,. \tag{B.36b}$$

This is the Mészáros solution. Until $a \gg a_{eq}$, the growth of the matter perturbation is held back since the collapse timescale is comparable to the timescale of the expansion of the universe. The corresponding decaying solution is given by Peebles (1980) equation 12.9 and is derived by considering $\delta_m = \mathcal{F}(\dagger)\mathcal{D}_\infty$ and solving equation B.35b for $\mathcal{F}$, where D_1 is the growing mode. Therefore, the full solution is

$$\delta_m = c_1\left(1+\frac{3}{2}y\right) + c_2\left[\left(1+\frac{3}{2}y\right)\log\left(\frac{\sqrt{1+y}+1}{\sqrt{1+y}-1}\right) - 3\sqrt{1+y}\right] . \tag{B.36c}$$

A set of joining conditions can be derived which gives the constants c_1 and c_2. Suppose, for clarity, that the full solution is denoted

$$\delta_m = c_1\left(1+\frac{3}{2}y\right) + c_2 f(y) . \tag{B.37a}$$

Then,

$$\delta_m' = \frac{3}{2}c_1 + c_2 f'(y) .$$

Here, $f' \equiv df/dy$. This gives c_1 as

$$c_1 = \left(\ \delta_{mr} f'(y) - \delta_{mr}' f(y)\right) \Big/ \left(\left(1+\frac{3}{2}y\right) f'(y) - \frac{3}{2}f(y)\right) . \tag{B.37b}$$

The value of δ_{mr}' can be derived from

$$\delta_m' = -\frac{ikca_{eq}}{a_r\dot{a}_r}v_r + \frac{1}{2}h_r' .$$

The value of c_2 can then trivially be derived from equation B.37. Finally, the solution for h' is given by

$$h' = 3c_1 + 2c_2 f'(y) + 2\frac{ikc}{a^2}\frac{a_{eq}}{\dot{a}}v_r a_r . \tag{B.38}$$

The radiation can also be followed analytically in the post-recombination epoch given a few more assumptions. Consider equation A.68e. For a flat space it gives

$$\dot{\delta}(\mu,t) + \frac{ikc\mu}{a}\delta(\mu,t) = -2\mu^2\dot{H} , \tag{B.39}$$

where $\mu = \hat{k}_i\gamma_i$. In order to proceed further, the following assumptions are necessary

$$h' = -H' \tag{B.40a}$$

$$h' = 3c_1 . \tag{B.40b}$$

The first of these conditions is generally true after recombination for modes within the horizon if the universe is also mostly matter dominated. For a flat universe this is true at even higher redshifts. The second condition is true for adiabatic modes after recombination since there the growing mode of the density field dominates. For isocurvature perturbations however, the dominant term on the right hand side of equation B.38 is not the growing mode. Hence, until this condition is fulfilled (which does happen eventually since the other two terms are both decaying), what follows cannot be applied

to isocurvature perturbations. Their evolution must be followed numerically, unless the modes concerned are always well within the horizon so that the right hand side of equation B.39 is effectively zero.

Given the validity of the assumptions,

$$\delta'(\mu,t) + \frac{iA\mu}{\sqrt{1+y}}\delta(\mu,t) = 6\mu^2 c_1 \ , \tag{B.41a}$$

where,

$$A = kcH_0^{-1}a_{eq}^{1/2} \ . \tag{B.41b}$$

Using the substitution, $x = \sqrt{1+y}$, this equation becomes

$$\frac{d\delta(\mu,x)}{dx} + 2iA\mu\delta(\mu,x) = 12\mu^2 c_1 x \ . \tag{B.41c}$$

The variable x is related to conformal time in a flat universe.

$$\tau = \int \frac{dt}{a} = 2H_0^{-1}a_{eq}^{1/2}(x-1) \ . \tag{B.42}$$

Hence, equation B.41c here is comparable to equation 4.3 in Bond & Efstathiou (1987). However, the presence of the extra constant term in the definition of conformal time implies that $dh/d\tau \not\propto \tau$ until $x \gg 1$. For instance, if $h = 0.5$ then $x = 10$ at a redshift of about 70. The use of the variable x however overcomes this, and is therefore preferred here.

Equation B.41 can be cast into a simpler form by considering a new function $\tilde{\delta}$:

$$\tilde{\delta} = \delta - 3\frac{c_1}{A^2} + 6i\frac{c_1}{A}x\mu \ . \tag{B.43a}$$

This obeys the equation

$$\frac{d\tilde{\delta}(\mu,x)}{dx} + 2iA\mu\tilde{\delta}(\mu,x) = 0 \ , \tag{B.43b}$$

which has the solution

$$\tilde{\delta}(\mu,x_0) = \tilde{\delta}(\mu,x_1)e^{2iA\mu(x_1-x_0)} \ . \tag{B.43c}$$

However, the Legendre decomposition of this function is required rather than the function itself. Since,

$$\delta(\mu,x) = \sum_{l=0}^{\infty}\delta_l(x)P_l(\mu) \ ,$$

it is clear that

$$\tilde{\delta}_l(x_0) = \left(\frac{2l+1}{2}\right) \sum_{n=0}^{\infty} \int_{-1}^{1} \tilde{\delta}_n(x_1) P_n(\mu) P_l(\mu) e^{2iA\mu(x_1 - x_0)} d\mu \,. \tag{B.44a}$$

The product of two Legendre polynomials is given by Gradshteyn & Ryzhik (1980) equation 8.915 as

$$P_l(\mu) P_n(\mu) = \sum_{p=0}^{\min(l,n)} c_{lnp} P_{l+n-2p}(\mu) \,,$$

where

$$c_{lnp} = \left(\frac{2l+2n-4p+1}{2l+2n-2p+1}\right) \frac{a_{l-p} a_{n-p} a_p}{a_{l+n-p}}$$

and

$$a_n = \frac{(2n-1)!!}{n!} \,.$$

Hence, since

$$\frac{(-i)^l}{2} \int_{-1}^{1} e^{ic\mu} P_l(\mu) d\mu = j_l(c) \,,$$

and $j_l(-c) = (-1)^l j_l(c)$, the final form is

$$\tilde{\delta}_l(x_0) = (2l+1) \sum_{n=0}^{\infty} \sum_{p=0}^{\min(l,n)} \tilde{\delta}_n(x_1) c_{lnp} (-i)^{l+n-2p} j_{l+n-2p}(2A(x_0 - x_1)) \,. \tag{B.44b}$$

Note that the upper limit on the sum over n is effectively set by $n \sim 2A(x_0 - x_1)$, since $j_n(c)$ is effectively zero when $n > c$.

Appendix C

One Dimensional Gaussian Fields

C.1 Introduction

The basic theory relating to a one dimensional Gaussian field was first given by Rice (1954). Although the original work was related to the statistics of noise in electrical lines, it is equally applicable to a general one dimensional density field. The basic properties of the field are dependent on the density, δ, its first spatial derivative, δ', and its second spatial derivative, δ''. If a vector $\mathbf{y}_{(0)}$ is defined such that:

$$\mathbf{y}_{(0)}^{\mathbf{T}} \equiv (\delta, \delta', \delta'') \,, \tag{C.1a}$$

then the associated covariance matrix, $\mathbf{m}$, is given by

$$m_{ij} \equiv \langle y_{(0)i} y_{(0)j} \rangle \,. \tag{C.1b}$$

The joint probability distribution for a one dimensional random Gaussian field is then

$$P(\mathbf{y}_{(0)})\, d^3 y_{(0)} = \frac{e^{-Q_{(0)}}}{[(2\pi)^3 \det M]^{1/2}}\, d^3 y_{(0)} \,, \tag{C.2a}$$

where,

$$Q_{(0)} \equiv \frac{1}{2}\, \mathbf{y}_{(0)}^{\mathbf{T}} . \mathbf{m}^{-1} . \mathbf{y}_{(0)} \,. \tag{C.2b}$$

Using the definition for the Fourier transform (equation 4.4),

$$\langle y_{(0)i} y_{(0)j} \rangle = \frac{L}{2\pi} \int_{-\infty}^{\infty} \delta_k^{(i-1)} \delta_k^{(j-1)} dk \,, \tag{C.3}$$

where

$$\delta^{(m)} = \frac{d^m \delta}{dx^m} \,. \tag{C.3a}$$

In particular, the mean square density fluctuation is

$$\sigma_0^2 = \frac{L}{2\pi} \int_{-\infty}^{\infty} |\delta_k|^2 \, dk \,, \tag{C.4}$$

and there is a corresponding set of spectral moments of higher order

$$\sigma_j^2 = \frac{L}{2\pi} \int_{-\infty}^{\infty} |\delta_k|^2 \, k^{2j} \, dk \, . \tag{C.5}$$

It is also convenient to introduce the spectral parameters γ and R_*:

$$\gamma = \frac{\sigma_1^2}{\sigma_2 \sigma_0} \, , \qquad R_* = \frac{\sigma_1}{\sigma_2} \, . \tag{C.6}$$

The value of γ indicates over what range the power spectrum has significant structure (see BBKS Section IV(b)). Thus, as the power spectrum tends towards a δ-function, $\gamma \to 1$, and, conversely, low values of γ indicate that there is significant power over a large range of scales.

The elements of the covariance matrix, $\mathbf{m}$, are (noting that $\mathbf{m} = \mathbf{m^T}$):

$$m_{11} = \sigma_0^2 \, , \tag{C.7a}$$

$$m_{22} = -m_{13} = \sigma_1^2 \, , \tag{C.7b}$$

$$m_{33} = \sigma_2^2 \, . \tag{C.7c}$$

Near a maxima in the density field, $\delta'(x_{max} + dx) = \delta''(x_{max})dx$. So, the global number density of peaks above a given threshold ν_t is (Rice 1954):

$$n_{pk}(\nu_t) = - \int_{\nu_t}^{\infty} \int_{-\infty}^{0} P(\delta, \delta' = 0, \delta''; m) \, \delta'' \, d\delta'' \, d\delta \, . \tag{C.8}$$

Introducing the variables $\nu = \delta/\sigma_0$ and $q = -\delta''/\sigma_2$ helps simplify the problem. Note that in linear theory these variables are time-independent, as are γ and R_*. The number density above a threshold, ν_t, in terms of these parameters is

$$n_{pk}(\nu_t) = \frac{1}{[(2\pi)^3 (1-\gamma^2) R_*^2]^{1/2}} \int_{\nu_t}^{\infty} \int_0^{\infty} q \, dq \, d\nu \, e^{-S_0} \, , \tag{C.9a}$$

where

$$2S_0 = (\nu^2 - 2\gamma\nu q + q^2)/(1-\gamma^2) \, . \tag{C.9b}$$

Both integrals can in fact be done analytically (Cartwright & Longuet-Higgins 1956).

C.2 Derivation of the Peak-Peak Correlation Function

The joint probability distribution for a one dimensional Gaussian random field considered at two distinct field points is (*cf* equation C.2a)

$$P(\mathbf{y}) \, d^6y = \frac{e^{-Q}}{[(2\pi)^6 \det M]^{1/2}} \, d^6y \, , \tag{C.10}$$

where:

$$Q \equiv \frac{1}{2}\,\mathbf{y^T}.\mathbf{M^{-1}}.\mathbf{y}\,, \tag{C.11a}$$

$$M_{ij} \equiv \langle y_i y_j \rangle\,, \tag{C.11b}$$

$$\mathbf{y^T} \equiv (\delta_1, \delta_1', \delta_1'', \delta_2, \delta_2', \delta_2'')\,. \tag{C.11c}$$

M_{ij} is the covariance matrix of the set of random variables $\{y_i\}$ and the indices refer to the separate field points.

The covariance matrix for this field can be generated from the following:

$$\left\langle \delta_i^{(m)}(x)\,\delta_j^{(n)}(x+r_{ij}) \right\rangle = \frac{L}{2\pi}\int_{-\infty}^{\infty} dk\,k^{m+n}\,|\delta(k)|^2 \begin{cases} \cos(kr_{ij}) & m+n \text{ even} \\ \sin(kr_{ij}) & m+n \text{ odd} \end{cases}\,, \tag{C.12}$$

where

$$\delta^{(m)} = \frac{d^m\delta}{dx^m}\,, \tag{C.13a}$$

$$r_{ij} = \begin{cases} 0 & i = j \\ r_{12} & i \neq j \end{cases}\,. \tag{C.13b}$$

Hence the one dimensional autocorrelation function is given by

$$\xi(r_{12}) = \frac{L}{2\pi}\int_{-\infty}^{\infty} dk\,|\delta(k)|^2\cos(kr_{12}) \tag{C.14}$$

and the mean square density fluctuation is given by $i = j$ and $m = n = 0$. If the following notation for the elements of the covariance matrix is adopted,

$$\sigma^2_{\frac{m+n}{2}}(r_{ij}) = \left\langle \delta_i^{(m)}(x)\,\delta_j^{(n)}(x+r_{ij}) \right\rangle\,, \tag{C.15}$$

then:

$$\begin{aligned} M_{11} &= M_{44} = \sigma_0^2(0)\,, \\ M_{22} &= M_{55} = \sigma_1^2(0)\,, \\ M_{13} &= M_{46} = -\sigma_1^2(0)\,, \\ M_{33} &= M_{66} = \sigma_2^2(0)\,, \\ M_{14} &= \sigma_0^2(r_{12})\,, \end{aligned} \tag{C.16}$$

$$M_{24} = -M_{15} = \sigma^2_{1/2}(r_{12}) \,,$$

$$M_{16} = M_{34} = -\sigma^2_1(r_{12}) \,,$$

$$M_{25} = \sigma^2_1(r_{12}) \,,$$

$$M_{35} = -M_{26} = \sigma^2_{3/2}(r_{12}) \,,$$

$$M_{36} = \sigma^2_2(r_{12}) \,.$$

Using the standard definition of the correlation function (Peebles 1980), in which the probability of having two distinct objects in line elements dx_1 and dx_2 separated by distance r is

$$P = n_1 \, n_2 \, dx_1 \, dx_2 \, (1 + \xi_{12}(r)) \,, \tag{C.17}$$

then the correlation function for peaks in the Gaussian field can be derived in a straightforward manner. The probability of having two peaks in line elements dx_1 and dx_2 separated by distance r is

$$P = \int\int_{\nu_t\sigma_0}^{\infty} \int\int_{-\infty}^{0} P(\delta_i, \delta_i' = 0, \delta_i''; i = 1,2) \, \delta_1'' \, \delta_2'' \, d\delta_1'' \, d\delta_2'' \, d\delta_1 \, d\delta_2 \, dx_1 \, dx_2 \,. \tag{C.18}$$

Hence the correlation function of peaks in a one dimensional field is:

$$1 + \xi_{12}(r) = \frac{1}{n^2_{pk}(\nu_t)} \int\int_{\nu_t}^{\infty} \int\int_{-\infty}^{0} P(\mathbf{y}; \delta_i' = 0) \, \delta_1'' \, \delta_2'' \, d\delta_1'' \, d\delta_2'' \, d\delta_1 \, d\delta_2 \,. \tag{C.19}$$

In principle the threshold for the two sets of heights, δ_1 and δ_2, could be different, but the constraint that ν_t should be the same for both has been applied.

Since the same density threshold applies for both sets of peaks, there is a symmetry in the indices $1 \leftrightarrow 2$. Since the original covariance matrix is symmetric, there are only six distinct elements in the inverse. The quadratic form can therefore be simplified to give (M^{-1}_{ij} is the ijth element of the inverse of the covariance matrix):

$$\begin{aligned} \mathbf{y^T . M^{-1} . y} \;=\; & M^{-1}_{11} \sigma^2_0 (\nu_1^2 + \nu_2^2) + 2 M^{-1}_{14} \sigma^2_0 \, \nu_1 \nu_2 + \\ & M^{-1}_{33} \sigma^2_2 (q_1^2 + q_2^2) + 2 M^{-1}_{36} \sigma^2_2 \, q_1 q_2 - \\ & 2\sigma_0 \sigma_2 \left(M^{-1}_{13} (\nu_1 q_1 + \nu_2 q_2) + M^{-1}_{16} (\nu_1 q_2 + \nu_2 q_1) \right) \,. \end{aligned} \tag{C.20}$$

Defining the two new forms:

$$Q_0 = M_{11}^{-1}\sigma_0^2(\nu_1^2+\nu_2^2) + 2M_{14}^{-1}\sigma_0^2\,\nu_1\nu_2 + M_{33}^{-1}\sigma_2^2\,q_2^2 - 2\sigma_0\sigma_2\left(M_{13}^{-1}\nu_2 q_2 + M_{16}^{-1}\nu_1 q_2\right)\,, \tag{C.21a}$$

$$Q' = M_{33}^{-1}\sigma_2^2\,q_1^2 + 2M_{36}^{-1}\sigma_2^2\,q_1 q_2 - 2\sigma_0\sigma_2\left(M_{13}^{-1}\nu_1 q_1 + M_{16}^{-1}\nu_2 q_1\right)\,. \tag{C.21b}$$

the correlation function can be rewritten as:

$$1+\xi_{12}(r) = \frac{\sigma_0^2\sigma_2^4}{(2\pi)^3(\det M)^{1/2}\,n_{pk}^2(\nu_t)} \quad \times$$
$$\int\!\!\int_{\nu_t}^{\infty}\int_0^{\infty} q_2\,e^{-Q_0/2}\int_0^{\infty} q_1\,e^{-Q'/2}\,dq_1\,dq_2\,d\nu_1\,d\nu_2\,. \tag{C.22}$$

The inner integral is of a standard form, so the number of integrals it is necessary to do numerically can be reduced from four to three. The correlation function then has the form:

$$1+\xi_{12}(r) = \frac{\sigma_0^2\sigma_2^2}{(2\pi)^3 M_{33}^{-1}(\det M)^{1/2}\,n_{pk}^2(\nu_t)} \quad \times$$
$$\int\!\!\int_{\nu_t}^{\infty}\int_0^{\infty} q_2\,e^{-Q_0/2}\left(1-\frac{\sqrt{2\pi}}{2}\,e^{-a^2/2}\,a\,\mathrm{erfc}(a/\sqrt{2})\right)dq_2\,d\nu_1\,d\nu_2\,, \tag{C.23}$$

where

$$a = \sigma_0^2(M_{13}^{-1}\,\nu_1 + M_{16}^{-1}\,\nu_2 + \frac{\sigma_2}{\sigma_0}\,M_{36}^{-1}q_2)^2/M_{33}^{-1}\,. \tag{C.24}$$

C.3 Asymptotic Form of the Correlation Function

Given the autocorrelation function in one dimension (equation C.15), it is trivial to show that, for a power spectrum which is approximately a power law with index n truncated at some minimum wavelength using a reasonably sharp filter function (such as a Gaussian or an exponential but not a sharp cut-off), the derivatives of $\psi(r)$ will fall off more quickly than $\psi(r)$ as $r \to \infty$, so we can ignore these. This greatly simplifies the correlation matrix, since the only cross term of the form $< \delta_1^{(m)}\delta_2^{(n)} >$ is ξ itself. Asymptotically, we also have $\psi \ll 1$, so we can also ignore terms of order ψ^2. The covariance matrix then has as its inverse:

$$
\begin{aligned}
M_{11}^{-1} &= \sigma_1^4\sigma_2^2(\sigma_0^2\sigma_2^2 - \sigma_1^4)/\det M \ , \\
M_{33}^{-1} &= \sigma_0^2\sigma_1^4(\sigma_0^2\sigma_2^2 - \sigma_1^4)/\det M \ , \\
M_{13}^{-1} &= \sigma_1^6(\sigma_0^2\sigma_2^2 - \sigma_1^4)/\det M \ , \\
M_{16}^{-1} &= -\sigma_0^2\sigma_1^6\sigma_2^2\psi/\det M \ , \\
M_{14}^{-1} &= -\sigma_0^2\sigma_1^4\sigma_2^4\psi/\det M \ , \\
M_{36}^{-1} &= -\sigma_0^2\sigma_1^8\psi/\det M \ , \\
\det M &= \sigma_1^4(\sigma_0^2\sigma_2^2 - \sigma_1^4)^2 = (\det m)^2 \ .
\end{aligned}
\tag{C.25}
$$

The quadratic form can be decomposed into two parts, this time splitting the full form $\mathbf{y^T}.\mathbf{M^{-1}}.\mathbf{y}$ into S_0 and S', where the latter form contains all the terms linking the separate peaks.

$$
S_0 = \frac{1}{2}\sum_{i=1,2}\left\{\nu_i^2 + \frac{(q_i - q_{*i})^2}{(1-\gamma^2)}\right\} = \sum_{i=1,2} S_{0(i)} \ , \tag{C.26a}
$$

$$
S' = -\psi\,\tilde{\nu}_1\,\tilde{\nu}_2 \ , \tag{C.26b}
$$

where we have also defined two new variables, $\tilde{\nu}$ and q_*.

$$
\tilde{\nu}_i = \frac{\nu_i - \gamma q_i}{1-\gamma^2} \ , \tag{C.27a}
$$

$$
q_{*i} = \gamma\nu_i \ . \tag{C.27b}
$$

Using these simplifications, the correlation function can be written as (*c.f.* BBKS equation 6.8 for the three dimensional case):

$$
1 + \xi(r) = \frac{1}{n_{pk}^2\,R_*^2\,(2\pi)^3\,(1-\gamma^2)}\left\{\prod_{i=1,2}\int_{\nu_t}^{\infty}\int_0^{\infty} q_i\,dq_i\,d\nu_i\,e^{-S_{0(i)}}\right\}e^{-S'} \ . \tag{C.28}
$$

We have already assumed that $\psi \ll 1$ as $r \to \infty$. If we add the further assumption that $\nu_t^2\psi \ll 1$, which in practice will tend to be reasonable as long as $\nu_t \sim 1$, then we can expand the final exponential as

$$
e^{-S'} \simeq 1 + \psi\tilde{\nu}_1\tilde{\nu}_2 \ . \tag{C.29}
$$

Hence, we arrive at the result:

$$
\xi(r) = \langle\tilde{\nu}\rangle^2\psi(r) \ . \tag{C.30}
$$

C.4 The Velocities of Peaks

The properties of three dimensional density fields are well described by BBKS (1986). The velocities of peaks in such a field can be derived in a similar fashion to the techniques already used in this chapter. Given a three dimensional density field, δ, then

$$\delta(\mathbf{x}) = \frac{V}{(2\pi)^3} \int \delta_{\mathbf{k}}\, e^{i\mathbf{k}.\mathbf{x}}\, d^3k \,, \tag{C.31a}$$

$$\delta_{\mathbf{k}} = \frac{1}{V} \int \delta(\mathbf{x})\, e^{-i\mathbf{k}.\mathbf{x}}\, d^3x \,. \tag{C.31b}$$

The velocity of any field point in linear theory is given by (Peebles 1980):

$$\mathbf{v}_{\mathbf{k}} = \frac{-ifH\delta_{\mathbf{k}}}{k^2}\mathbf{k} \,, \tag{C.32}$$

where $f \simeq \Omega^{0.6}$.

In three dimensions, the probability distribution for the velocities of peaks is dependent on the density, δ, its three first derivatives, $\nabla_i\delta$, the six distinct elements of the second derivatives, $\nabla_i\nabla_j\delta$, and the three components of the velocity, v_i.

However, peculiar velocities only correlate with first derivatives of the density field along the same axis. Following appendix A of BBKS then, the problem of inverting the covariance matrix can be simplified to the problem of inverting the sub-matrix composed of the correlations of $\mathbf{x}^T = (\nabla_i\delta, v_i^a, v_i^b)$. Here, $\mathbf{v}^a$ and $\mathbf{v}^b$ are the peculiar velocities windowed on two scales r_a and r_b. Since components along different axes do not correlate the problem reduces to the distribution of only three variables. With this in mind the variables will be relabelled as $\mathbf{x}^T = (\eta, v_a, v_b)$.

The covariance matrix, $\mathbf{C}$, for the elements of the sub-matrix are:

$$\left\langle \eta^2 \right\rangle = \frac{\sigma_1^2}{3} \tag{C.33a}$$

$$\langle v_a \eta \rangle = \frac{H_0 f}{3}\sigma_{0a}^2 \tag{C.33b}$$

$$\langle v_a v_b \rangle = \frac{H_0^2 f^2}{3}\sigma_{-1ab}^2 \,, \tag{C.33c}$$

where,

$$\sigma_{nab}^2 = \frac{4\pi V}{(2\pi)^3}\int_0^\infty W_k^a W_k^b\, |\delta_k|^2\, k^{2n+2}\, dk \,. \tag{C.34}$$

The extension of this notation to fewer indices and the case where $a = b$ is obvious. The W_k are the Fourier components of an isotropic window function. Although such a window function is never realised in practice, it is a reasonable approximation (see Kaiser 1988a).

All that is required now is to invert this covariance matrix to find the quadratic term that occurs in the probability distribution ($\mathbf{x}^T.\mathbf{C}^{-1}.\mathbf{x}$). For maxima of the density field, the additional constraint that $\eta = 0$ can be applied.

There are six independent terms in the inverse of the covariance matrix, of which only three are required here. Then,

$$\mathbf{x}^T.\mathbf{C}^{-1}.\mathbf{x}\Big|_{\eta=0} = \frac{1}{\det C}\left(m_{11}v_a^2 - 2m_{12}v_a v_b + m_{22}v_b^2\right) , \tag{C.35}$$

where

$$m_{11} = \left(\frac{fH_0}{3}\right)^2 \left(\sigma_1^2\sigma^2_{-1b^2} - \sigma^4_{0b}\right) \tag{C.36a}$$

$$m_{12} = \left(\frac{fH_0}{3}\right)^2 \left(\sigma_1^2\sigma^2_{-1ab} - \sigma^2_{0a}\sigma^2_{0b}\right) \tag{C.36b}$$

$$m_{22} = \left(\frac{fH_0}{3}\right)^2 \left(\sigma_1^2\sigma^2_{-1a^2} - \sigma^4_{0a}\right) \tag{C.36c}$$

$$\det C = m_{11}m_{22} - m_{12}^2 . \tag{C.36d}$$

Hence,

$$\left\langle v^a v^b | \eta = 0 \right\rangle = \frac{H_0^2 f^2}{3}\left(\sigma^2_{-1ab} - \frac{\sigma^2_{0a}\sigma^2_{0b}}{\sigma_1^2}\right) . \tag{C.37}$$

References

Aaronson, M., 1986. In: *Galaxy Distances and Deviations from the Hubble Flow,* p55, eds Madore, B.F. & Tully, R.B., Reidel, Dordrecht, Holland.

Aaronson, M., Huchra, J. & Mould, J., 1979. *Astrophys. J.,* **229**, 1.

Aaronson, M., Huchra, J., Mould, J., Schecter, P.L. & Tully, R.B., 1982. *Astrophys. J.,* **258**, 64.

Aaronson, M., Bothun, G., Mould, J., Huchra, J., Schommer, R.A. & Cornell, M.E., 1986. *Astrophys. J.,* **302**, 536.

Aaronson, M., Bothun, G.D., Budge, K.G., Dawe, J.A., Dickens, R.J., Hall, P.J., Lucey, J.R., Mould, J.R., Murray, J.D., Schommer, R.A. & Wright, A.E., 1988a. In: *Large Scale Structures of the Universe, IAU Symp. No. 130,* p. 185, eds Audouze, J., Pelletan, M. & Szalay, A., Kluwer, Dordrecht, Holland.

Aaronson, M., Bothun, G.D., Dawe, J.A., Dickens, R.J., Han Ming Sheng, Hall, P.J., Huchra, J., Lucey, J.R., Mould, J.R., Murray, J.D., Schommer, R.A. & Wright, A.E., 1988b. preprint.

Abell, G.O., 1958. *Astrophys. J. Suppl.,* **3**, 211.

Abell, G.O., Corwin, H.G. & Olowin, R.P., 1989. *Astrophys. J. Suppl.,* **70**, 1.

Applegate, J.H., Hogan, C.J. & Scherrer, R.J., 1987. *Phys. Rev. D,* **35**, 1151.

Arfken, G., 1970. *Mathematical Methods for Physicists,* Academic Press, New York.

Bahcall, N.A. & Soneira, R.M., 1983. *Astrophys. J.,* **270**, 20.

Bardeen, J.M., 1980. *Phys. Rev. D,* **22**, 1882.

Bardeen, J.M., Bond, J.R., Kaiser, N. & Szalay, A.S., 1986. *Astrophys. J.,* **304**, 15.

Bardeen, J.M., Bond, J.R. & Efstathiou, G., 1987. *Astrophys. J.,* **321**, 28.

Blumenthal, G.R., Dekel, A. & Primack, J.R., 1988. *Astrophys. J.,* **326**, 539.

Bond, J.R., 1988a. In: *The Early Universe,* p. 283, eds Unruh, W.G. & Semenoff, G.W., Reidel, Dordrecht, Holland.

Bond, J.R., 1988b. In: *Large Scale Structures of the Universe, IAU Symp. No. 130,* p. 93, eds Audouze, J., Pelletan, M. & Szalay, A., Kluwer, Dordrecht, Holland.

Bond, J.R. & Szalay, A.S., 1983. *Astrophys. J.,* **274**, 443.

Bond, J.R. & Efstathiou, G., 1984. *Astrophys. J.,* **285**, L45.

Bond, J.R., Carr, B.J. & Hogan, C.J., 1986. *Astrophys. J.,* **306**, 428.

Bond, J.R. & Efstathiou, G., 1987. *Mon. Not. R. astr. Soc.,* **226**, 655.

Bothun, G.D. & Mould, J.R., 1987. *Astrophys. J.,* **313**, 629.

Cartwright, D.E. & Longuet-Higgins, M.S., 1956. *Proc. Roy. Soc. A.,* **237**, 212.

Clutton-Brock, M. & Peebles, P.J.E., 1981. *Astr. J.,* **86**, 1115.

Coles, P., 1986. *Mon. Not. R. astr. Soc.,* **222**, 9P.

Collins, C.A., Joseph, R.D. & Robertson, N.A., 1986. *Nature,* **320**, 506.

Collins, C.A., Heydon-Dumbleton, N.H. & MacGillivray, H.T., 1988 *Mon. Not. R. astr. Soc.,* **236**, 7P.

Couchman, H.M.P., McGill, C. & Olowin, R.P., 1989. *Mon. Not. R. astr. Soc.,* **239**, 513.

Crane, P., 1988. *ESO Messenger,* **53**, 43.

Crane, P., Hegyi, D.J., Mandolesi, N. & Danks, A.C., 1986. *Astrophys. J.,* **309**, 822.

Davis, M. & Boynton, P.E., 1980. *Astrophys. J.,* **237**, 365.

Davis, M. & Peebles, P.J.E., 1983. *Astrophys. J.,* **267**, 465.

Davis, M., Efstathiou, G., Frenk, C. & White, S., 1985. *Astrophys. J.,* **292**, 371.

Davies, R.D., Lasenby, A.N., Watson, R.A., Daintree, E.J., Hopkins, J., Beckman, J., Sanchez-Almeida, J. & Rebolo, R., 1987. *Nature,* **326**, 462.

De Amici, G., Smoot, G., Friedman, S.D. & Witebsky, C., 1985. *Astrophys. J.*, **298**, 710.
De Amici, G., Smoot, G.F., Aymon, J., Bersanelli, M., Kogut, A., Levin, S.M. & Witebsky, C., 1988. *Astrophys. J.*, **329**, 556.
Dekel, A. & Rees, M.J., 1987. *Nature*, **326**, 455.
De Lapparent, V., Geller, M.J. & Huchra, J.P., 1988. *Astrophys. J.*, **332**, 44.
de Vaucouleurs, G.H. & Peters, W.L., 1984. *Astrophys. J.*, **287**, 1.
de Vaucouleurs, G.H., 1986. In: *Galaxy Distances and Deviations from the Hubble Flow*, p55, eds Madore, B.F. & Tully, R.B., Reidel, Dordrecht, Holland.
Dimopoulous, S., Esmailzadeh, R., Hall, R.J. & Starkman, G.D., 1988. *Astrophys. J.*, **330**, 545.
Djorgovski, S. & Davis, M., 1987. *Astrophys. J.*, **313**, 59.
Doroshkevich, A.G., Zel'dovich, Ya. B. & Sunyaev, R.A., 1978. *Sov. Astron.*, **22**, 523.
Dressler, A., 1984. *Astrophys. J.*, **281**, 512.
Dressler, A., Lynden-Bell, D., Burstein, D., Davies, R.L., Faber, S.M., Terlevich, R.J. & Wegner, G., 1987a. *Astrophys. J.*, **313**, 42.
Dressler, A., Faber, S.M., Burstein, D., Davies, R.L., Lynden-Bell, D., Terlevich, R.J. & Wegner, G., 1987b. *Astrophys. J.*, **313**, L37.
Dunlop, J.S., 1987.PhD. thesis, University of Edinburgh.
Efstathiou, G., 1988. In: *Large Scale Motions in the Universe: A Vatican Study Week*, p. 299, eds Rubin, V.C. & Coyne, G.V., Princeton University Press, Princeton.
Efstathiou, G. & Silk, J., 1983. *Fund. Cosmic Phys.*, **9**, 1.
Efstathiou, G., Davis, M., Frenk, C.S. & White, S.D.M., 1985. *Astrophys. J. Suppl.*, **57**, 241.
Efstathiou, G. & Bond, J.R., 1986. *Mon. Not. R. astr. Soc.*, **218**, 103.
Efstathiou, G. & Bond, J.R., 1987. *Mon. Not. R. astr. Soc.*, **227**, 33P.
Ehlers, J., 1971. In: *Proceedings of the International School of Physics, 'Enrico Fermi', course 47, 'General Relativity and Cosmology'*, p. 1, ed Sachs, R.K., Academic Press, New York.
Faber, S.M. & Jackson, R.E., 1976. *Astrophys. J.*, **204**, 668.
Faber, S.M., Burstein, D., Davies, R.L., Dressler, A., Lynden-Bell, D., Terlevich, R. & Wegner, G., 1988. In: *Large Scale Structures of the Universe, IAU Symp. No. 130*, p. 169, eds Audouze, J., Pelletan, M. & Szalay, A., Kluwer, Dordrecht, Holland.
Fixsen, D.J., Cheng, E.S. & Wilkinson, D.T., 1983. *Phys. Rev. Lett.*, **50**, 620.
Fomalont, E.B., Kellerman, K.I. & Wall, J.V., 1984. *Astrophys. J.*, **277**, L23.
Frenk, C.S., 1988. In: *Large Scale Structures of the Universe, IAU Symp. No. 130*, p. 259, eds Audouze, J., Pelletan, M. & Szalay, A., Kluwer, Dordrecht, Holland.
Frenk, C.S., White, S.D.M. & Davis, M., 1983 *Astrophys. J.*, **271**, 417.
Gear, W.C., 1971 *Numerical Initial Value Problems in Ordinary Differential Equations*, Prentice-Hall, Englewood Cliffs, New Jersey.
Gorski, K., Davis, M., Strauss, M.A., White, S.D.M. & Yahil, A., 1989 *Astrophys. J.*, , in press.
Gouda, N., Sasaki, M. & Suto, Y., 1987. *Astrophys. J.*, **321**, L1.
Gradshteyn, I.S. & Ryzhik, I.M., 1980. *Table of Integrals, Series and Products*, Academic Press, New York.
Grinstein, B., Politzer, H.D., Rey, S.-J. & Wise, M.B., 1986. *Astrophys. J.*, **314**, 431.
Groth, E.J. & Peebles, P.J.E., 1977. *Astrophys. J.*, **217**, 385.
Groth, E.J., Juszkiewicz, R. & Ostriker, J.P., 1988. *Astrophys. J.*, , submitted.

Halpern, M., Benford, R., Meyer, S., Muehlner, D. & Weiss, R., 1988. *Astrophys. J.*, **332**, 596.
Hart, L. & Davies, R.D., 1982. *Nature,* **297**, 191.
Heydon-Dumbleton, N.H., 1989.PhD. thesis, University of Edinburgh.
Hoessel, M.G., Gunn, J.E. & Thuan, T.X., 1980. *Astrophys. J.,* **241**, 486.
Hoffman, Y., 1988. *Astrophys. J.,* **329**, 8.
Hogan, C.J., 1984. *Astrophys. J.,* **284**, L1.
Hogan, C.J. & Rees, M.J., 1987. *Nature,* **311**, 109.
Ikeuchi, S., 1981. *Publ. Astron. Soc. Japan.,* **33**, 211.
James, P.A., Joseph, R.D. & Collins, C.A., 1987. *Mon. Not. R. astr. Soc.,* **229**, 53.
Jensen, L.G. & Szalay, A.S., 1986. *Astrophys. J.,* **305**, L5.
Johnson, D.G. & Wilkinson, D.T., 1987. *Astrophys. J.,* **313**, L1.
Jones, B.J.T. & Wyse, R.F.G., 1985. *Astr. Astrophys.,* **149**, 144.
Kaiser, N., 1983. *Astrophys. J.,* **273**, L17.
Kaiser, N., 1984. *Astrophys. J.,* **284**, L9.
Kaiser, N., 1986. *Mon. Not. R. astr. Soc.,* **219**, 785.
Kaiser, N., 1988a. *Mon. Not. R. astr. Soc.,* **231**, 149.
Kaiser, N., 1988b. , preprint.
Kaiser, N., 1988c. In: *Large Scale Structures of the Universe, IAU Symp. No. 130,* p. 43, eds Audouze, J., Pelletan, M. & Szalay, A., Kluwer, Dordrecht, Holland.
Kaiser, N. & Silk, J., 1986. *Nature,* **324**, 529.
Kaiser, N. & Stebbins, A., 1984. *Nature,* **310**, 391.
Klypin, A.A. & Shandarin, S.F., 1983. *Mon. Not. R. astr. Soc.,* **204**, 891.
Knoke, J.E., Partridge, R.B., Ratner, M.I. & Shapiro, I.I., 1984. *Astrophys. J.,* **284**, 479.
Kodama, H. & Sasaki, M., 1984. *Prog. Theor. Phys. Suppl.,* **78**, 1.
Kodama, H. & Sasaki, M., 1986. *Int. J. mod. Phys.,* **1**, 265.
Kraan-Korteweg, R.C., 1985. In: *The Virgo Cluster of Galaxies,* p. 397, eds Richter, O.G. & Bingelli, B., ESO, Munich.
Lasenby, A.N., 1981.PhD. thesis, University of Manchester.
Lifshitz, E.M., 1946. *JETP Lett.,* **16**, 587.
Ling, E.N., Frenk, C.S. & Barrow, J.D., 1986. *Mon. Not. R. astr. Soc.,* **223**, 21P.
Lubin, P., Epstein, G. & Smoot, G., 1983. *Phys. Rev. Lett.,* **50**, 616.
Lubin, P. & Villela, T., 1986. In: *Galaxy Distances and Deviations from the Hubble Flow,* p.169, eds Madore, B.F. & Tully, R.B., Reidel, Dordrecht, Holland.
Lucey, J.R. & Carter, D., 1988a. *Mon. Not. R. astr. Soc.,* **231**, 15P.
Lucey, J.R. & Carter, D., 1988b. *Mon. Not. R. astr. Soc.,* **235**, 1177.
Lynden-Bell, D., Faber, S.M., Burstein, D., Davies, R.L., Dressler, A., Terlevich, R.J. & Wegner, G., 1988 *Astrophys. J.,* **326**, 19.
Mandolesi, N., Calzolari, P., Cortglioni, S., Morigi, G., Danese, L. & De Zotti, G., 1986. *Astrophys. J.,* **310**, 561.
Matsumoto, T., Hayakawa, S., Matsuo, H., Murakami, H., Sato, S., Lange, A.E. & Richards, P.L., 1988. *Astrophys. J.,* **329**, 567.
Melchiorri, F., Melchiorri, B.O., Ceccarelli, C. & Pietranera, L., 1981. *Astrophys. J.,* **250**, L1.
Meyer, D.M. & Jura, M., 1985. *Astrophys. J.,* **297**, 119.
Meyer, D.M., Roth, K.C. & Hawkins, I., 1989. *Astrophys. J.,* **343**, L1.
Mészáros, P., 1975. *Astr. Astrophys.,* **38**, 5.
Mészáros, P., 1980. *Astrophys. J.,* **238**, 781.

Mitchell, P.S., 1989.PhD. thesis, University of Edinburgh.
More, J.M., Heavens, A.F. & Peacock, J.A., *Mon. Not. R. astr. Soc.*, **220**, 189.
Oort, J.H., 1983. *Ann. Rev. Astron. Astrophys.*, **21**, 373.
Ostriker, J.P., 1988. In: *Large Scale Structures of the Universe, IAU Symp. No. 130,* p. 321, eds Audouze, J., Pelletan, M. & Szalay, A., Kluwer, Dordrecht, Holland.
Ostriker, J.P. & Cowie, L.L., 1981. *Astrophys. J.*, **243**, L127.
Ostriker, J.P. & Thompson, C., 1987a *Astrophys. J.*, **323**, L97.
Ostriker, J.P. & Thompson, C., 1987b In: *Dark Matter in the Universe, Fourth Jerusalem Winter School for Theoretical Physics,* p. 90, eds Bahcall, J.N., Piran, T. & Weinberg, S., World Scientific, Singapore.
Otto, S., Politzer, H.D. & Wise, M.B., 1986. *Phys. Rev. Lett.*, **56**, 1878.
Peacock, J.A. & Heavens, A.F., 1985. *Mon. Not. R. astr. Soc.*, **217**, 805.
Peacock, J.A., Lumsden, S.L. & Heavens, A.F., 1987. *Mon. Not. R. astr. Soc.*, **229**, 469.
Peebles, P.J.E., 1968. *Astrophys. J.*, **153**, 1.
Peebles, P.J.E., 1971. *Physical Cosmology,* Princeton University Press, Princeton.
Peebles, P.J.E., 1974. *Astrophys. J.*, **189**, L51.
Peebles, P.J.E., 1980. *The Large Scale Structure of the Universe,* Princeton University Press, Princeton.
Peebles, P.J.E., 1982. *Astrophys. J.*, **258**, 415.
Peebles, P.J.E., 1987. *Astrophys. J.*, **315**, L73.
Peebles, P.J.E., 1988a *Astrophys. J.*, **332**, 17.
Peebles, P.J.E., 1988b In: *Large Scale Structures of the Universe, IAU Symp. No. 130,* p. 495, eds Audouze, J., Pelletan, M. & Szalay, A., Kluwer, Dordrecht, Holland.
Peebles, P.J.E. & Yu, J.T., 1970. *Astrophys. J.*, **162**, 815.
Peterson, J.B., Richards, P.L. & Timusk, T., 1985. *Phys. Rev. Lett.*, **55**, 232.
Politzer, H.D. & Wise, M.B., 1984. *Astrophys. J.*, **285**, L1.
Press, W.H. & Vishniac, E.T., 1980. *Astrophys. J.*, **236**, 323.
Press, W.H., Flannery, B.P., Teukolsky, S.A. & Vetterling, W.T., 1986. *Numerical Recipes,* Cambridge University Press, Cambridge, U.K.
Press, W.H. & Spergel, D.N., 1987. In: *Dark Matter in the Universe, Fourth Jerusalem Winter School for Theoretical Physics,* p. 218, eds Bahcall, J.N., Piran, T. & Weinberg, S., World Scientific, Singapore.
Readhead, A.C.S., Lawrence, C.R., Myers, S.T. & Sargent, W.L.W., 1988a. In: *Large Scale Structures of the Universe, IAU Symp. No. 130,* p. 37, eds Audouze, J., Pelletan, M. & Szalay, A., Kluwer, Dordrecht, Holland.
Readhead, A.C.S., Lawrence, C.R., Myers, S.T. & Sargent, W.L.W., 1988b. In: *The Post-Recombination Universe,* p. 167, eds Kaiser, N. & Lasenby, A.N., Reidel, Dordrecht, Holland.
Rice, S.O., 1954. *Selected papers on Noise and Stochastic Processes,* p. 133, ed. Wax, N., Dover.
Rubin, V.C., Thonnard, N., Ford, W.K. & Roberts, M.S., 1976. *Astr. J.*, **81**, 719.
Sandage, A., 1988. *Astrophys. J.*, **331**, 583.
Sandage, A. & Tammann, G.A., 1988. *Astrophys. J.*, **328**, 1.
Silk, J., 1968. *Astrophys. J.*, **151**, 459.
Silk, J. & Vittorio, N., 1987. *Astrophys. J.*, **317**, 564.
Sironi, G. & Bonelli, G., 1986. *Astrophys. J.*, **311**, 418.

Sironi, G., Bersanelli, M., Bonelli, G., Conti, G., Marcellino, M., Limon, M. & Reif, K., 1987. In: *13th Texas Symposium on Relativistic Astrophysics,* p. 245, ed Ulmer, M.P., World Scientific, Singapore.

Smoot, G.F., Bensadoun, M., Bersanelli, M., De Amici, G., Kogut, A., Levin, S. & Witebsky, C., 1987. *Astrophys. J.,* **317**, L45.

Stavely-Smith, L. & Davies, R.D., 1989. Preprint.

Struble, M.F. & Rood, H.J., 1987. *Astrophys. J. Suppl.,* **63**, 543.

Strukov, I.A., Skulachev, D.P., Klypin, A.A. & Sazhin, M.V., 1988. In: *Large Scale Structures of the Universe, IAU Symp. No. 130,* p. 27, eds Audouze, J., Pelletan, M. & Szalay, A., Kluwer, Dordrecht, Holland.

Sunyaev, R.A. & Zel'dovich, Ya. B., 1970. *Astrophys. Space Sci.,* **7**, 1.

Sutherland, W., 1988. *Mon. Not. R. astr. Soc.,* **234**, 159.

Szalay, A., 1988. In: *Large Scale Motions in the Universe: A Vatican Study Week,* p. 323, eds Rubin, V.C. & Coyne, G.V., Princeton University Press, Princeton.

Tully, R.B. & Fisher, J.R., 1977. *Astr. Astrophys.,* **54**, 661.

Turner, M.S., 1986. In: *Intersection Between Particle Physics and Cosmology, First Jerusalem Winter School for Theoretical Physics,* p. 100, eds Piran, T. & Weinberg, S., World Scientific, Singapore.

Turner, M.S., Villumsen, J.V., Vittorio,N., Silk, J. & Juszkiewicz, R., 1987. *Astrophys. J.,* **323**, 423.

Turok, N., 1985. *Phys. Rev. Lett.* **55**, 1801.

Uson, J.M. & Wilkinson, D.T., 1984a. *Astrophys. J.,* **277**, L1.

Uson, J.M. & Wilkinson, D.T., 1984b. *Astrophys. J.,* **283**, 471.

Uson, J.M. & Wilkinson, D.T., 1985. *Nature,* **312**, 427.

Vishniac, E.T., 1987. *Astrophys. J.,* **322**, 597.

Vishniac, E.T. & Ostriker, J.P., 1986. *Soc. Ital. Fis.,* **1**, 157

Vittorio, N. & Silk, J., 1984 *Astrophys. J.,* **285**, L39.

Vittorio, N., Juszkiewicz, R. & Davis, M., 1986. *Nature,* **323** ,132.

Vittorio, N. & Turner, M.S., 1987. *Astrophys. J.,* **316**, 475.

Warren, S.J., Hewett, P.C. & Osmer, P.S., 1989. In: *The Epoch of Galaxy Formation,* p.135, eds Frenk, C.S., Ellis, R.S., Shanks, T., Heavens, A.F. & Peacock, J.A., Kluwer, Dordrecht, Holland.

Webster, A., 1977. In: *Radio Astronomy and Cosmology, IAU Symp. No. 74,* p. 75, ed Jauncey, D.L., Reidel, Dordrecht, Holland.

Weinberg, S., 1972. *Gravitation and Cosmology,* Wiley, New York.

White, S.D.M., Davis, M., Efstathiou, G. & Frenk, C.S., 1987a. *Nature,* **330**, 451.

White, S.D.M., Frenk, C.S., Davis, M. & Efstathiou, G., 1987b. *Astrophys. J.,* **313**, 505.

Wilkinson, D.T., 1988. In: *Large Scale Structures of the Universe, IAU Symp. No. 130,* p. 7, eds Audouze, J., Pelletan, M. & Szalay, A., Kluwer, Dordrecht, Holland.

Wilson, M.L., 1983. *Astrophys. J.,* **273**, 2.

Wilson, M.L. & Silk, J., 1981. *Astrophys. J.,* **243**, 14.

Yahil, A., 1985. In: *The Virgo Cluster of Galaxies,* p. 359, eds Richter, O.G. & Bingelli, B., ESO, Munich.

Yahil, A., 1981. In: *10th Texas Symposium on Relativistic Astrophysics,* **375**, p.169, eds Ramaty, R. & Jones, F.C., Ann. N.Y. Acad. Sci., New York.

Yang, J., Turner, M.S., Steigman, G., Schramm, D.N. & Olive, K.A., 1984. *Astrophys. J.,* **281**, 493.

Yashioka, A. & Ikeuchi, S., 1987. *Astrophys. J.,* **323**, L7.

Zel'dovich, Ya.B., 1970. *Astr. Astrophys.*, **5**, 84.

Zurek, W.H. & Hoffman, Y., 1988. In: *Large Scale Structures of the Universe, IAU Symp. No. 130,* p. 568, eds Audouze, J., Pelletan, M. & Szalay, A., Kluwer, Dordrecht, Holland.

Aaronson, M. & Mould, J., 1986. Astrophys. J. 303. 1.

Lawrence, C.R., Readhead, A.C.S. & Myers, S.T. 1988. In: The Post Recombination Universe. P.173, eds Kaiser N & Lasenby, A.N. Reidel, Dordrecht, Holland.